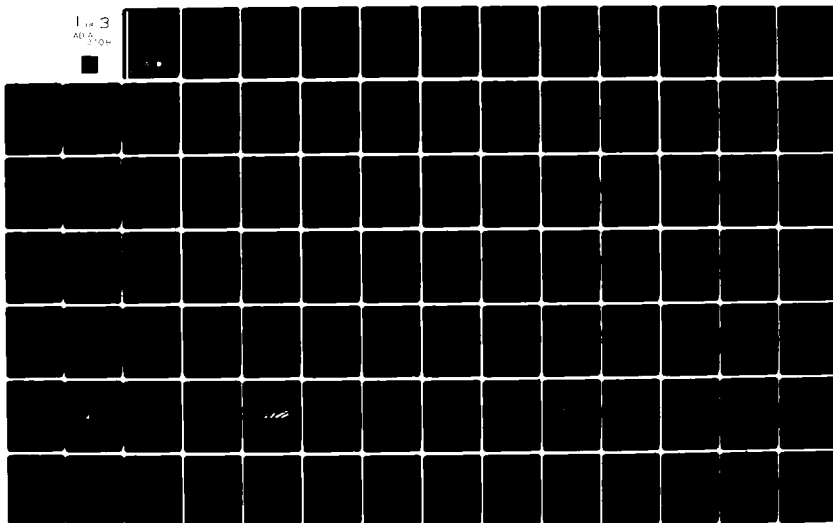


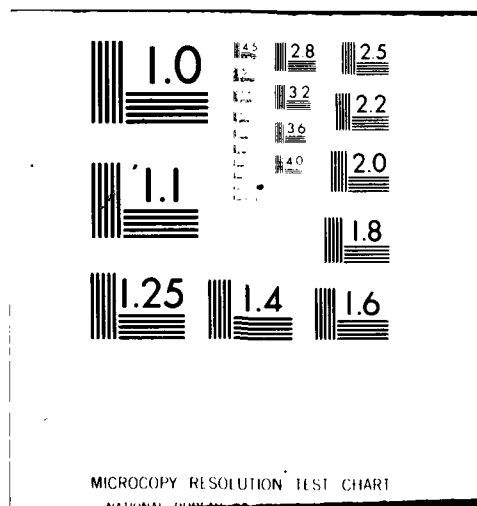
AD-A112 708

TEXAS UNIV AT AUSTIN APPLIED RESEARCH LABS  
SOME APPROACHES TO THE ANALYSIS AND INTERPRETATION OF WIDE-ANGL-ETC(U)  
FEB 82 G D INGRAM  
N00014-78-C-0329  
ARL-TR-82-11  
NL

UNCLASSIFIED

1 of 3  
AD-A112 708





405

2

ARL-TR-82-11

Copy No. 61

**SOME APPROACHES TO THE ANALYSIS AND INTERPRETATION OF  
WIDE-ANGLE BOTTOM LOSS DATA**

Gregory D. Ingram

**APPLIED RESEARCH LABORATORIES  
THE UNIVERSITY OF TEXAS AT AUSTIN  
POST OFFICE BOX 8028, AUSTIN, TEXAS 78712-8028**

15 February 1982

Technical Report

**APPROVED FOR PUBLIC RELEASE;  
DISTRIBUTION UNLIMITED.**

*Prepared for:*

**NAVAL OCEAN RESEARCH  
AND DEVELOPMENT ACTIVITY  
NSTL STATION, MS 39529**

DTIC FILE COPY



**DTIC  
ELECTE  
MAR 31 1982  
E**

82 03 31 017

UNCLASSIFIED

SECURITY CLASSIFICATION OF THIS PAGE (When Data Entered)

REPORT DOCUMENTATION PAGE		READ INSTRUCTIONS BEFORE COMPLETING FORM
1. REPORT NUMBER	2. GOVT ACCESSION NO. AD A112 708	3. RECIPIENT'S CATALOG NUMBER
4. TITLE (and Subtitle)  SOME APPROACHES TO THE ANALYSIS AND INTERPRETATION OF WIDE-ANGLE BOTTOM LOSS DATA		5. TYPE OF REPORT & PERIOD COVERED  technical report
7. AUTHOR(s)  Gregory D. Ingram		6. PERFORMING ORG. REPORT NUMBER ARL-TR-82-11
9. PERFORMING ORGANIZATION NAME AND ADDRESS Applied Research Laboratories The University of Texas at Austin Austin, Texas 78712-8029		8. CONTRACT OR GRANT NUMBER(s)  N00014-78-C-0329
11. CONTROLLING OFFICE NAME AND ADDRESS Naval Ocean Research and Development Activity NSTL Station, Mississippi 39529		10. PROGRAM ELEMENT, PROJECT, TASK AREA & WORK UNIT NUMBERS
14. MONITORING AGENCY NAME & ADDRESS (if different from Controlling Office)		12. REPORT DATE 15 February 1982
		13. NUMBER OF PAGES 196
		15. SECURITY CLASS. (of this report)  UNCLASSIFIED
		15a. DECLASSIFICATION DOWNGRADING SCHEDULE N/A
16. DISTRIBUTION STATEMENT (of this Report)  Approved for public release; distribution unlimited.		
17. DISTRIBUTION STATEMENT (of the abstract entered in Block 20, if different from Report)		
18. SUPPLEMENTARY NOTES		
19. KEY WORDS (Continue on reverse side if necessary and identify by block number)  sediment acoustic properties      cepstrum bottom-loss analysis                  autocorrelation underwater acoustics                deconvolution signal analysis		
20. ABSTRACT (Continue on reverse side if necessary and identify by block number) Some approaches are developed to analyze and interpret wide angle bottom loss data in terms of ocean sediment acoustic properties. After a brief review of bottom loss data collection and the state-of-the-art knowledge of relevant ocean bottom properties, a filter description of the acoustic signal is developed illustrating the effects of the source waveform and ghosts on travel time versus grazing angle plots. It is shown that these effects can be identified and that, in general, they severely distort the ocean bottom impulse response.		

UNCLASSIFIED

SECURITY CLASSIFICATION OF THIS PAGE (When Data Entered)

20. (Cont'd)

The autocorrelation and power cepstrum are examined for their usefulness in extracting geoacoustic information from the multiple bottom bounce data. The autocorrelation is initially preferred due to several reasons having to do with the fact that it has the superposition property with respect to convolution:

- (1) the shape of events are more interpretable in terms of the phase of the time components,
- (2) the amplitudes of events are more predictable, and
- (3) the effects of coherent noise are more recognizable.

On the other hand, the power cepstrum is as good and better than the autocorrelation for much synthetic plane wave data, since it gives better resolution of delays between components (it produces a spike at the delays between components rather than a pulse with the crosspower spectrum of the components) and since it is better able to take advantage of infinite dynamic range. The advantage of infinite dynamic range is lost and the power cepstrum is degraded with respect to the autocorrelation by adding white uncorrelated noise to synthetics. For real data, preference of one technique over the other will be dependent on source-receiver geometry, geoacoustic structure, and signal-to-noise ratio.

An impulse response estimate was obtained from the data by using a least squares method to deconvolve an (n-1) bottom bounce waveform from an (n) bottom bounce waveform. This method, which is directly analogous to the debubbling technique of Wood et al. (1978), requires that the two waveforms correspond to equal source and receiver depths and equal bottom grazing angles. Although good results have been obtained, significant noise contamination of the deconvolved signal results for source depth difference between 3 and 7%. This noise contamination can be reduced by low pass filtering at the cost of resolution.

Application of the autocorrelation, power cepstrum, and deconvolution techniques to real data obtained in a turbidite province indicated that bottom loss in the region was largely controlled by a single reflector and refracted energy. Although ambiguity exists as to whether the reflector is a bottom or subbottom reflector, either interpretation implies a significant difference of geoacoustic structure from that previously predicted for this region. Assuming the two components of the impulse response are the specularly reflected and refracted components, the gradient for the first 180 m decreases from  $2.0 \text{ sec}^{-1}$  to  $1.3 \text{ sec}^{-1}$  with an average of about  $1.5 \text{ sec}^{-1}$  in the first 180 m. The attenuation coefficient was about 0.02 dB/m-kHz in this same depth interval. The autocorrelations and power cepstrums indicated significant reflectivity in the upper 50 m of the subbottom.

UNCLASSIFIED

SECURITY CLASSIFICATION OF THIS PAGE (When Data Entered)

# TABLE OF CONTENTS

	<u>Page</u>
LIST OF TABLES	iii
LIST OF FIGURES	vii
CHAPTER 1 BACKGROUND	1
1.1 Acoustic Propagation Experiments	1
1.2 Bottom Loss Analysis Procedure	3
1.3 Reflected and Refracted Energy in the Ocean Bottom	8
1.4 Geoacoustic Structure	13
1.5 Forward Modeling	25
1.5.1 Impulse Response Calculation	28
1.5.2 Synthetic Source Waveform	35
1.5.3 Synthesized Waveform	39
CHAPTER 2 SYSTEM FILTER EFFECTS ON ACOUSTIC DATA	41
2.1 System Filter Effects	41
2.2 T- $\theta$ Plots of Multiple Bottom Bounce Acoustic Signals	53
CHAPTER 3 CORRELATION TECHNIQUES	69
3.1 Correlation for Time Delay Detection	69
3.2 Theory of the Autocorrelation	70
3.3 Theory of the Power Cepstrum	72



Accession For	
NTIS GSA&I	<input checked="" type="checkbox"/>
DTIC TAB	<input type="checkbox"/>
Unannounced	<input type="checkbox"/>
Justification	
Ex	
Distribution/	
Availability Codes	
Avail and/or	
Dist	Special
<b>A</b>	

	<u>Page</u>
3.4 Synthetic Results	74
3.5 Data Autocorrelogram and Power Cepstra	99
CHAPTER 4 IMPULSE RESPONSE ESTIMATION USING MULTIPLE BOTTOM BOUNCE SIGNALS	115
4.1 Impulse Response Estimation	115
4.2 Theory of MBB Deconvolution	117
4.3 Examples of MBB Deconvolution Technique	120
CHAPTER 5 GEOLOGIC INFERENCES	151
CHAPTER 6 CONCLUSIONS AND RECOMMENDATIONS	171
6.1 Conclusions	171
6.2 Recommendations	175
APPENDIX I	179
APPENDIX II	183
BIBLIOGRAPHY	185

# LIST OF TABLES

<u>Table No.</u>		<u>Page</u>
I	Geoacoustic Model for Figs. 20, and 68-89	37
II	Geoacoustic Model for Figs. 41-48	79
III	Geoacoustic Model for Figs. 49-54	93
IV	New Acoustic Model Derived from Multiple Bottom Bounce Acoustic Data	158
V	Geoacoustic Model Suggested a priori (Shear Waves Ignored)	159



## LIST OF FIGURES

<u>Figure No.</u>		<u>Page</u>
1	Experimental Geometry	2
2	Bottom Loss Processing Flowchart	5
3	Comparison of Measured and Predicted Arrival Structure	6
4	Ray Tracing Model Illustrating Refracted Energy in Ocean Bottom	10
5	Ray Paths of Multiple Bottom Bounce Signals	11
6	Cross Section Illustrating the Depth and Roughness of the Basement Beneath the Sediment Cover in the Philippine Sea	14
7	Instantaneous Velocity versus Depth Curves for Different Sediment Types	17
8	Velocity versus Density for Common Marine Sediment Types	18
9	Compiled Data of Attenuation versus Depth	19
10	Attenuation versus Depth in the Bay of Bengal	20
11	Attenuation as a Function of Depth in the Sea Floor Calculated from Bottom Loss Data	21
12	Density Measurements of the DSDP in the Gulf of Mexico	23
13	Velocity versus Depth for Two Sites in the Gulf of Mexico	24
14	Bottom Loss in an Area of Thin Sediment Overlying Rough Basement	26
15	Bottom Loss Curves for Two Areas of Thick Sediment	27

<u>Figure No.</u>		<u>Page</u>
16	Plane Wave Interacting with Ocean Bottom	29
17	Impulse Response Calculation of BOTREF	30
18	Output to BOTREF	33
19	Comparison of Wave Theory and Ray Theory Predictions of Bottom Response	34
20	Synthetic Ocean Bottom Impulse Response versus Grazing Angle Aligned on Specular Reflection Calculated from BOTREF	36
21	Parameters for the Pressure-Time History of the Quasitheoretical Synthetic Source Waveform	38
22	Frequency Domain Representation of Acoustic Signal	42
23	System Filtering Effects	43
24	Source Waveforms for Different Source Depths	45
25	Calculation of Ghost Time Delay	46
26	Range of Typical Source-Receiver Ghost Delays	47
27	Synthesis of Total Ghost Response of an Acoustic Signal	49
28	Multiple Bottom Bounce Impulse Response	51
29	Multiple Bottom Bounce Impulse Response Delays versus Grazing Angle	55
30	Bubble Pulse Delays of Multiple Bottom Bounce Impulse Response	56
31	Ghost Delays of Multiple Bottom Bounce Impulse Response	57
32	Travel Time Versus Grazing Angle Plot of Time Delays Between Main Arrivals of a 5 BB Acoustic Signal with a 244 m Source and 498 m Receiver	59
33	Six Bottom Bounce Acoustic Signals with 244 m Source Depth and Nominal 498 m Receiver Depth	60

<u>Figure No.</u>		<u>Page</u>
34	Six Bottom Bounce Acoustic Signals with 244 m Source Depth and 498 m Nominal Receiver Depth Aligned at 75 msec to Reveal at Least One Arrival Before the Aligned Arrival	61
35	Six Bottom Bounce Acoustic Signals with Predicted Delays Between Main Arrivals Assuming Nominal Source Receiver Depths	63
36	Five Bottom Bounce Acoustic Signals with 18 m Source Depth and Nominal 498 m Receiver Depth	64
37	Six Bottom Bounce Acoustic Signals with Predicted Delays Between Main Arrivals Assuming Nominal Source Depth (244 m) and Receiver Depth Calculated from 18 m Source Data	67
38	The Autocorrelation Function $P_{xx} = \int_{-\infty}^{\infty} f(u) f(u-x) du$ is Represented as an Area in the Figure Above	71
39	Derivation of Log Power Spectrum of Delayed Pulse with 90° Phase Shift	75
40	Block Diagram Showing Flowchart of the Calculation of the Autocorrelation, Log Power Spectrum, and Power Cepstrums of a Signal	76
41	Time Signature, Autocorrelation, Power Spectrum, and Power Cepstrum for Plane Wave Impulse Response ( $\theta_g = 26^\circ$ )	
42	Time Signature, Autocorrelation, Power Spectrum, and Power Cepstrum of Plane Wave Impulse Response Convolved with Source Waveform (244 m Source)	81
43	Time Signature, Autocorrelation, Power Spectrum, and Power Cepstrum of Plane Wave Impulse Response Convolved with Source Waveform and Source Ghost Response	83
44	Time Signature, Autocorrelation, Power Spectrum, and Power Cepstrum of Plane Wave Impulse Response Convolved with Source Waveform and Total Ghost Response (75 m Receiver)	84

<u>Figure No.</u>		<u>Page</u>
45	Time Signature, Autocorrelation, Power Spectrum, and Power Cepstrum of 5 Bottom Bounce Plane Wave Impulse Response ( $\theta_g = 26^\circ$ )	86
46	Time Signature, Autocorrelation, Power Spectrum, and Power Cepstrum of 5 Bottom Bounce Plane Wave Impulse Response Convolved with Source Waveform and Total Ghost Response (244 m Source, 75 m Receiver)	87
47	Time Signature, Autocorrelation, Power Spectrum, and Power Cepstrum of 5 Bottom Bounce Plane Wave Impulse Response Convolved with Source Waveform and Total Ghost Response (244 m Source, 400 m Receiver)	89
48	Time Signature, Autocorrelation, Power Spectrum, and Power Cepstrum of 5 Bottom Bounce Plane Wave Impulse Response Convolved with Source Waveform and Total Ghost Response (244 m Source, 256 m Receiver)	90
49	Plot Showing the Impulse Response, Autocorrelation, Power Spectrum and Power Cepstrum with Geoacoustic Model Having Slightly Higher Sound Speeds and Lower Attenuation	91
50	Plot Showing the Effect of Bubble Pulses and Ghosts with a 5 BB Impulse Response Calculated from the 1 BB Impulse Response Shown in Fig. 49	94
51	Plot Showing the Effect of Adding White Uncorrelated Noise: 20 dB Signal Excess	96
52	Plot Showing the Effect of Adding White Uncorrelated Noise: 10 dB Signal Excess	97
53	Plot Showing the Effect of Whitening the Log Power Spectrum Before Calculating the Power Cepstrum	98
54	Plot Showing the Effect of Whitening the Log Power Spectrum Before Calculating the Power Cepstrum with the First Three Samples of the Power Cepstrum Zeroed	100
55	Autocorrelogram for a Turbidite Province	101

<u>Figure No.</u>		<u>Page</u>
56	Autocorrelogram of the Turbidite Province for Which the Time Signals are Muted Past the Source Ghost Delay Before the Auto-correlations are Calculated	104
57	Autocorrelogram with 18 m Sources and 256 m Receiver	105
58	Autocorrelogram for Which the Time Signals Were Muted Past the Receiver Ghost Before the Autocorrelations Were Calculated	106
59	Figure Showing Autocorrelations With a Bottom Angle of About $26^{\circ}$ for Different Numbers of Bottom Bounces and Their Sum	108
60	Power Cepstrum of Data in Turbidite Province	109
61	Power Spectrum Whitened Before Calculating the Power Cepstrum	110
62	Signal Muted Past Source Ghost Delay Before Calculating the Power Cepstrum	111
63	Signal Muted Past Source Ghost Delay and Power Spectrum Whitened Before Calculating the Power Cepstrum	112
64	Flowchart for Calculation of Deconvolution Filter, $D(Z)$ $X(Z)$ is the $(n-1)$ Bottom Bounce Waveform	118
65	Geometry for Deconvolving an $(n-1)$ Bottom Bounce Waveform from an $(n)$ Bottom Bounce Waveform	121
66	Recovery of the Impulse Response from Synthetic Data	122
67	Recovery of the Impulse Response from Data Obtained in Turbidite Province	123
68	Input Impulse Response for Synthetic Deconvolution	125
69	Deconvolution of $(n-1)$ from $(n)$ Bottom Bounce Waveform with Identical Source Waveforms	126

<u>Figure No.</u>		<u>Page</u>
70	Output Impulse Response for Identical Source Waveform	127
71	-1% Source Depth Error	128
72	-1% Source Depth Error	129
73	-3% Source Depth Error	130
74	-3% Source Depth Error	131
75	-5% Source Depth Error	132
76	-5% Source Depth Error	133
77	-7% Source Depth Error	134
78	-7% Source Depth Error	135
79	-9% Source Depth Error	136
80	-9% Source Depth Error	137
81	+7% Source Depth Error	138
82	+7% Source Depth Error	139
83	+7% Source Depth Error	140
84	+7% Source Depth Error	141
85	+7% Source Depth Error	142
86	-3% Source Depth Error	143
87	-3% Source Depth Error	144
88	-3% Source Depth Error	145
89	-3% Source Depth Error	146
90	Examples of Deconvolution of Five Bottom Bounce Waveforms from Six Bottom Bounce Waveforms in Turbidite Province	148
91	Velocity Profile Obtained by Inverting Time Delays Between Reflected and Refracted Events Observed in the Autocorrelations of Multiple Bottom Bounce Acoustic Signals Measured in a Turbidite Province	154

<u>Figure No.</u>		<u>Page</u>
92	Attenuation Profile Obtained from Multiple Bottom Bounce Acoustic Signals Measured in a Turbidite Province Using the Velocity Profile Shown in Fig. 91 and Bottom Loss Data	156
93	Synthetic Autocorrelogram Using a priori Geoacoustic Model Shown in Table V	158
94	Synthetic Power Cepstra Using a priori Geoacoustic Model	162
95	Synthetic Power Cepstrums Using a priori Geoacoustic Model with Whitened Power Spectra	163
96	Synthetic Autocorrelogram Using a New Geoacoustic Model Presented in Table IV Derived from Data Correlograms	166
97	Synthetic Power Cepstra Using a New Geoacoustic Model	167
98	Synthetic Power Cepstrums Using New Geoacoustic Model with Whitened Power Spectra	168
A-1	Travel Time Difference Curves for Plane Waves and Spherical Waves Assuming An Isovelocity Water Column	177
A-2	Travel Time Difference Curves for Ocean Bottom with Sound Speed Ratio at the Water-Sediment Interface Less than One Assuming Spherical Wave Fronts and Isovelocity Water Layer	181

## CHAPTER 1

### BACKGROUND

#### 1.1 Acoustic Propagation Experiments

The purpose of this work is to develop approaches to analyze and interpret wide angle multiple bottom bounce acoustic signals in terms of ocean sediment acoustic properties. This falls within the realm of the science of underwater sound which has developed as a quantitative subject in the years since World War II (Urick, 1975). Recently in underwater acoustics interest has been focused on long range propagation in deep water. Often these acoustic environments are bottom limited so that a significant fraction of the acoustic energy interacts with the ocean bottom (Hampton, 1978). It is desired to characterize the physics of this interaction with the ocean bottom and, in particular, to be able to predict the amount of loss expected at the ocean bottom boundary as a function of angle and frequency. This involves a quantitative knowledge of geoacoustic structure as a function of depth.

Experiments that have been designed to study acoustic propagation in bottom limited environments are known as bottom loss experiments. These experiments are generally long range (1-200 km), low frequency (0-600 Hz) measurements with a geometry like that shown in Fig. 1. Vertical arrays are deployed with hydrophone clusters at approximately 400 and 1900 m below the surface and 30 m above the bottom, with one hydrophone



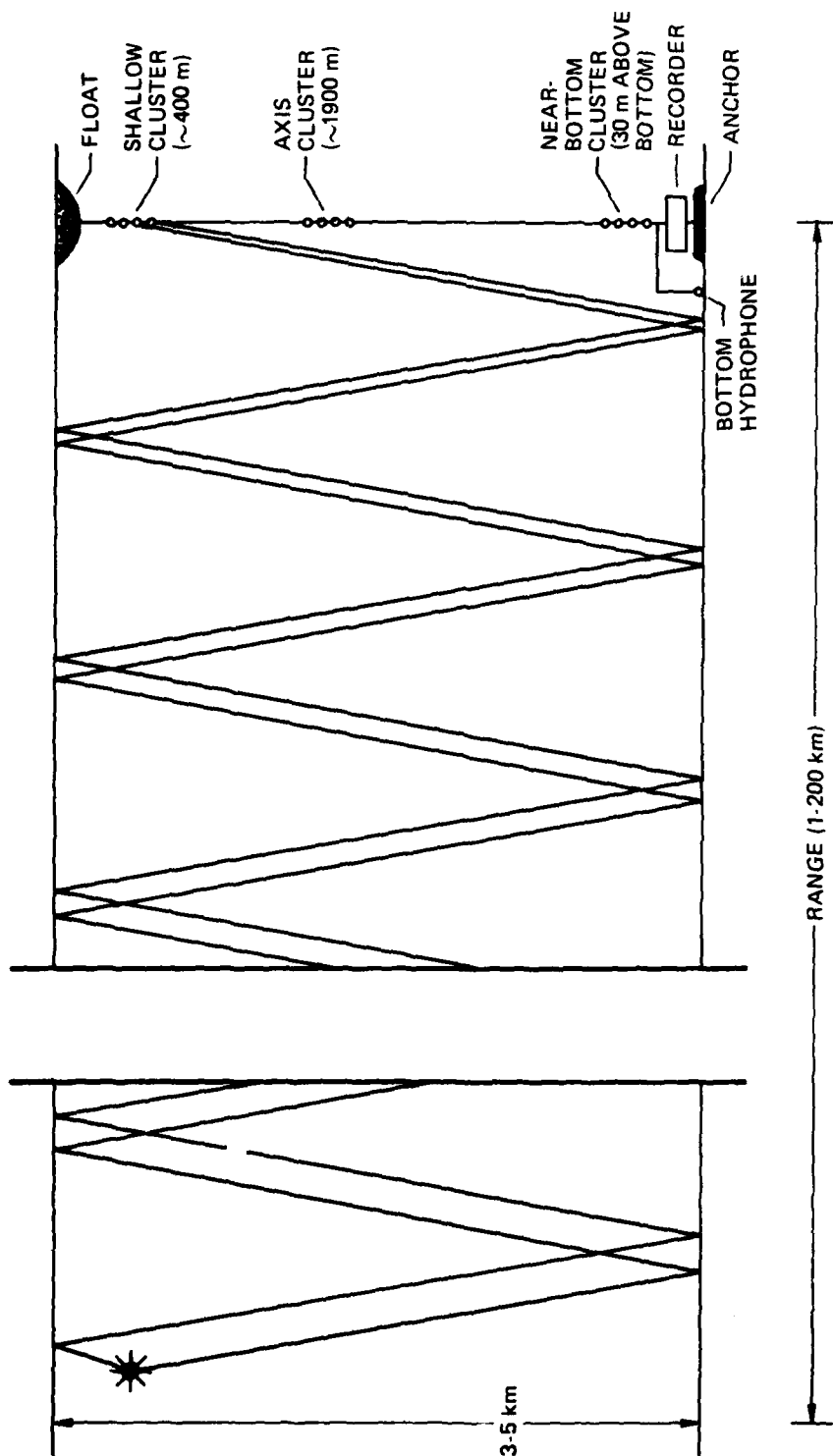


FIGURE 1  
EXPERIMENTAL GEOMETRY

ARL:UT  
AS-81-805  
GDI - GA  
7-28-81

located directly on the bottom. The arrays are anchored to the bottom and suspended by a float.

Explosive SUS (shallow underwater source) charges are then commonly deployed by a ship moving away from the receiver site and detonated at depths of approximately 18, 91, and 244 m. Figure 1 shows that for the depths of most ocean basins (3.5-5 km) most of the acoustic signals measured in the experiment have interacted with the bottom several times before reaching the receiver (Mitchell et al., 1978).

In this work it is desired to make quantitative inferences of the acoustic properties of ocean bottom sediments from these acoustic measurements.

## 1.2 Bottom Loss Analysis Procedure

From a theoretical standpoint, the interaction of acoustic signals with the ocean bottom can be described by a single function, the reflection coefficient,  $R(\theta, \omega)$ , a function of grazing angle and frequency. This function is commonly calculated using a normal mode model (Hawker and Foreman, 1978) or a ray tracing model (Mitchell and Lemmon, 1979) by considering a single frequency infinite plane wave interacting with the ocean bottom.

The ocean bottom is modeled as a series of flat, horizontal (generally fluid) layers with the variables of layer thickness, density, sound speed, sound attenuation, and sound speed gradient. If the sediments have significant rigidity then shear wave parameters versus depth must be included in the model (Vidmar and Foreman, 1978; Vidmar, 1980). Bottom loss (BL) is defined as negative twenty times the common logarithm of the plane wave reflection coefficient:

$$-20 \log R(\theta, \omega) \quad ,$$

where  $R(\theta, \omega)$  is the reflection coefficient.

The measurement of bottom loss within the constraints of this definition is virtually impossible. In practice bottom loss is obtained from propagation loss experiments in which the acoustic wave has reflected from the ocean bottom one or more times. Figure 2 is a flowchart which shows the process of deriving bottom loss from multiple bottom bounce acoustic data (Mitchell et al., 1978).

First, the recorded signals are digitized and stored on magnetic tape. Then the approximate arrival timing structure of waterborne paths is calculated from ancillary data using nominal source and receiver depths and the water sound speed structure. Third, the arrivals are plotted and the predicted arrival structure verified. Finally, the spectra of the reference structure are calculated, corrected for geometrical spreading loss, and compared with the spectra of data to obtain bottom loss. The source spectra levels for the data discussed in this report and processed at ARL:UT were assumed to be those reported by Gaspin and Shuler (1971). The ocean bottom is assumed to be flat and horizontal so the grazing angle at the ocean bottom is unique and can be calculated from the source-receiver geometry and the water sound speed structure.

Figure 3 is a plot of an intermediate step of the ARL:UT processing of bottom loss with the results of other steps summarized. The digitized multiple bottom bounce signal is plotted above the time axis with two tick marks equaling 1 sec. The top printed line documents the number of bottom bounces for each blip, which was determined on the basis of travel time information. It is seen that arrivals with less than two

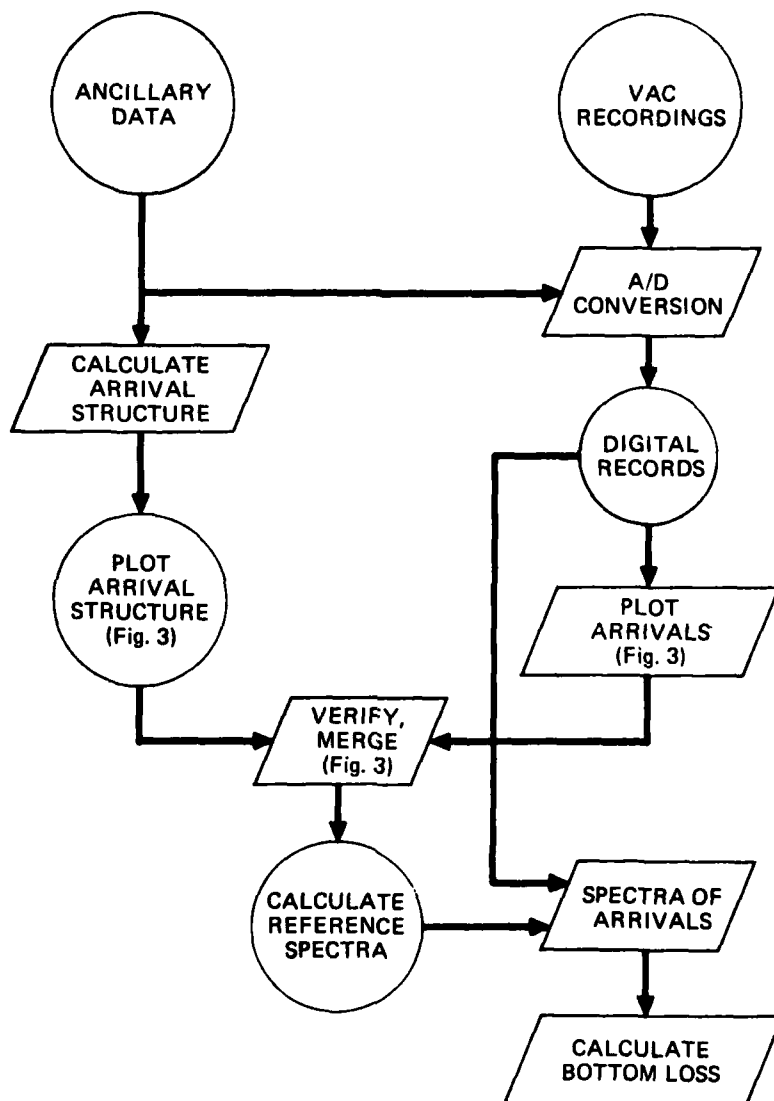


**FIGURE 2**  
**BOTTOM LOSS PROCESSING FLOWCHART**

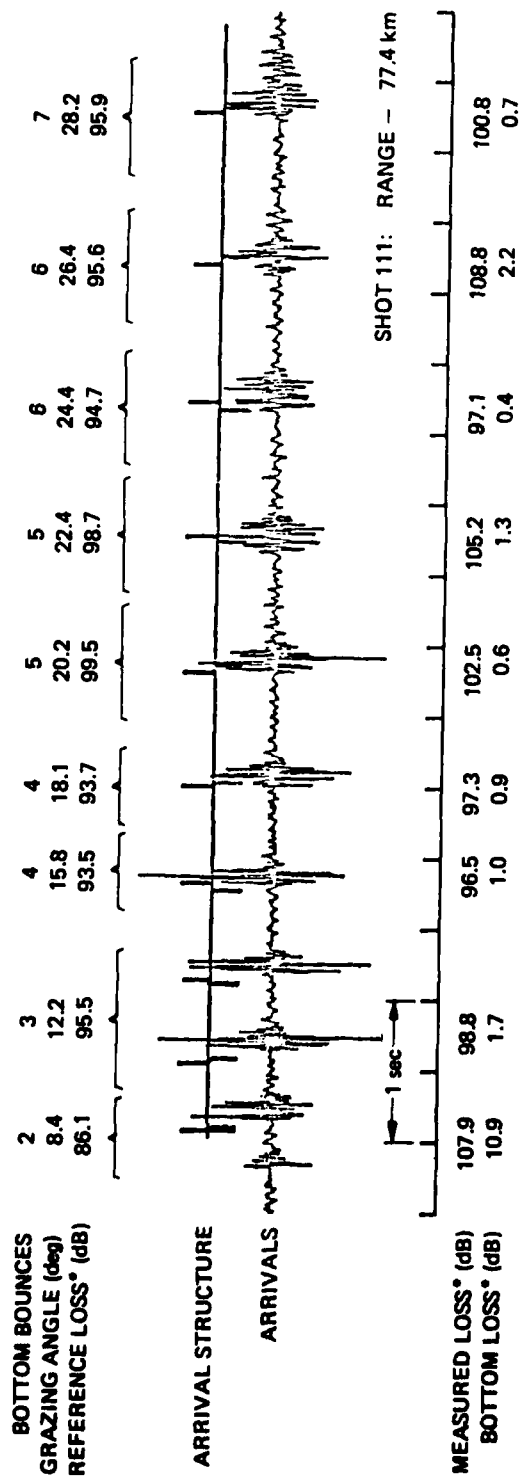


FIGURE 3  
 COMPARISON OF MEASURED AND PREDICTED ARRIVAL STRUCTURE  
 91 m SOURCE, 1685 m RECEIVER

bottom bounces are essentially canceled due to simultaneous arrival of ghosts at these times. The grazing angle for each blip is calculated from the sound speed structure in the water column and the source-receiver geometry. The reference structure is calculated from assumed source levels and the calculated arrival structure. The grazing angle for each blip and the reference loss (at 50 Hz) for each blip is tabulated in the figure. The reference loss includes the effects of geometrical spreading of the acoustic energy and absorption by the seawater. The measured loss is calculated by windowing each blip and finding the difference between the reference level and the measured level. Bottom loss is simply the difference between the reference and measured losses. The measured loss and bottom loss (both at 50 Hz) are tabulated for the signal of Fig. 3 below the time axis. Generally, bottom loss is calculated at frequencies of 25, 50, 100, 200, and 400 Hz with a 1/3 octave band average. This gives bottom loss as a function of angle and frequency.

To obtain source levels, some bottom loss experiments use measured levels of direct arrivals that have not interacted with the ocean bottom rather than assuming levels from previous work (Santaniello et al., 1979). This involves adding the predicted spreading loss of the direct arrival ( $WPL_D$ ) to the level of the direct arrival ( $RL_D$ )

$$SL = RL_D + WPL_D \quad . \quad (1.2.1)$$

Bottom loss (BL) can then be calculated by subtracting the level of the bottom arrival ( $RL_B$ ) and its predicted spreading loss ( $WPL_B$ ) from the source level.

$$BL = SL - RL_B - WPL_B \quad , \quad (1.2.2)$$

or

$$BL = (RL_D - RL_B) + (WPL_D - WPL_B) \quad (1.2.3)$$

Expression (1.2.2) is the expression used at ARL:UT to derive bottom loss using the source levels predicted by Gaspin and Shuler. Alternatively, Santaniello et al., with an experimental geometry designed to allow for indirect measurement of the source levels, use expression (1.2.3) to calculate bottom loss.

For multiple bottom bounce signals bottom loss must be normalized to the loss per bottom bounce. The bottom loss calculated from (1.2.2) or (1.2.3) for an (n) bottom bounce signal must be divided by n.

### 1.3 Reflected and Refracted Energy in the Ocean Bottom

In order to predict the amount of energy loss expected at the ocean bottom in different ocean basins a physical model is needed to predict the main energy components returned to the water column. The simplest model is one that considers the ocean bottom as a perfect absorber. In this case, all of the energy which interacts with the ocean bottom is absorbed by it. Alternatively, the ocean bottom can be modeled as a reflector with a simple Rayleigh reflection coefficient; all energy not reflected at the water-sediment interface is assumed to be absorbed into the ocean bottom. These models yield white transfer functions for the ocean bottom.

A more complex model is to consider a refracted component which returns energy to the water column due to a positive sound speed gradient. This results in a two-component model of the ocean bottom transfer function with one component reflected at the water-sediment interface and another

component transmitted at the water-sediment interface and refracted back to the water column through the sediments (see Figs. 4 and 5). The existence and the importance of this refracted arrival has been known for many years.

Apparently, Hill (1952) was the first to identify an arrival refracted through the ocean subbottom. His interpretation was later supported by a more controlled experiment conducted by Officer (1955) and by interpretations of bottom loss experiments of Morris (1970) and Hanna (1973). Christensen et al. (1975) conducted an experiment in which they were able to characterize the refracted arrivals in terms of travel times, amplitudes, and frequency content.

Since that time controlled experiments employing deconvolution processing (Dicus, 1976; Herstein et al., 1979; Santaniello et al., 1979) have revealed that the refraction arrival is a significant event especially for low frequencies. Santaniello et al. attribute the calculation of negative bottom loss to the breakdown of the plane wave assumption and the occurrence of refracted energy. The amplitude of the refracted arrival is frequency dependent due primarily to the frequency dependent attenuation of the sediments. The specular reflection, however, should contain more high frequencies and may be nearly white. The overall transfer function of this model will be colored.

The two-component model described above assumes that the impedance in the subbottom is a smooth and continuous function of depth; however, discontinuous or sharp impedance contrasts with depth yield reflectors in the subbottom besides the specular reflection. Many recent studies indicate that there are significant subbottom reflectors in



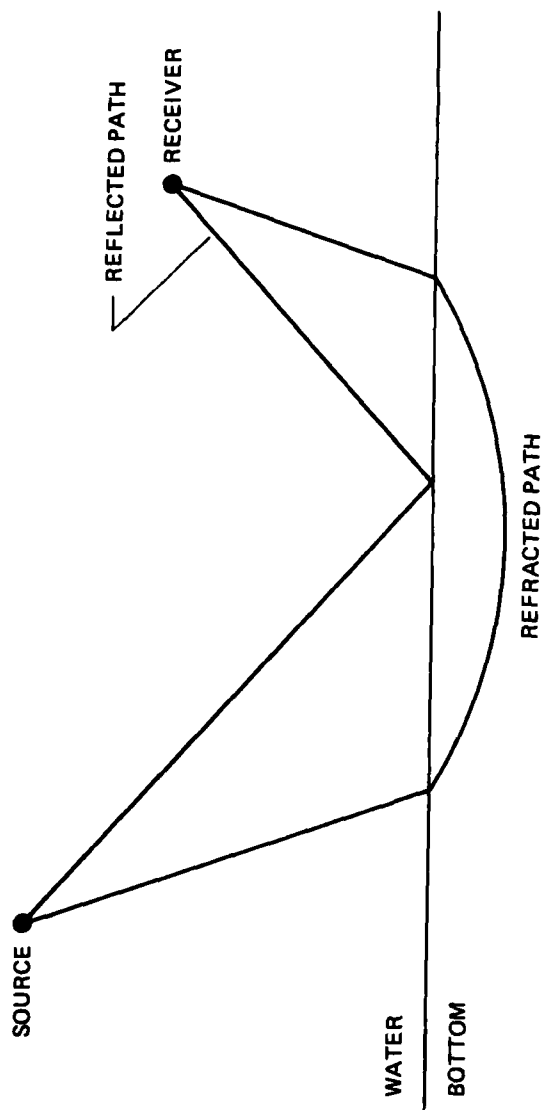


FIGURE 4  
RAY TRACING MODEL ILLUSTRATING REFRACTED ENERGY IN OCEAN BOTTOM

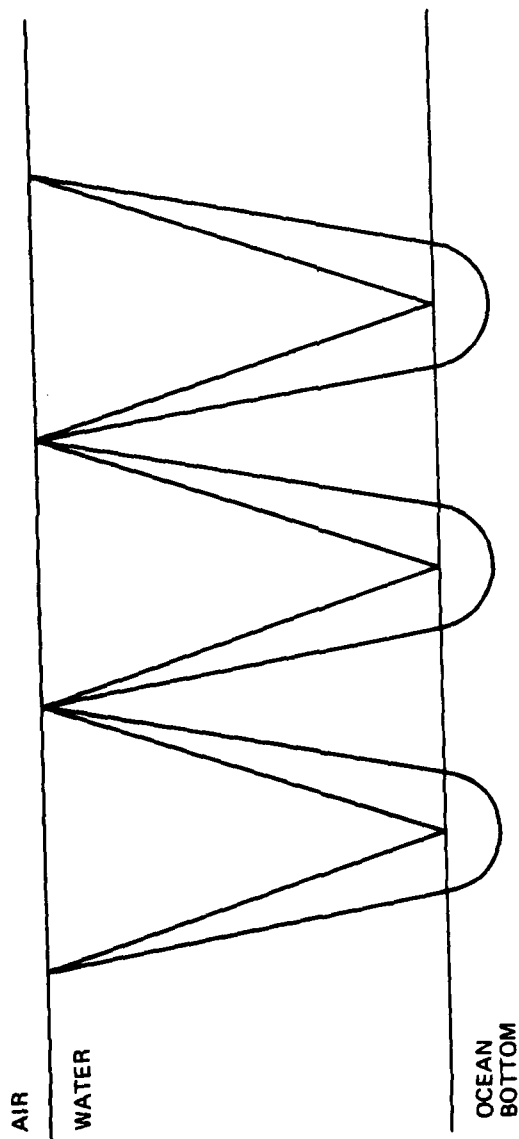
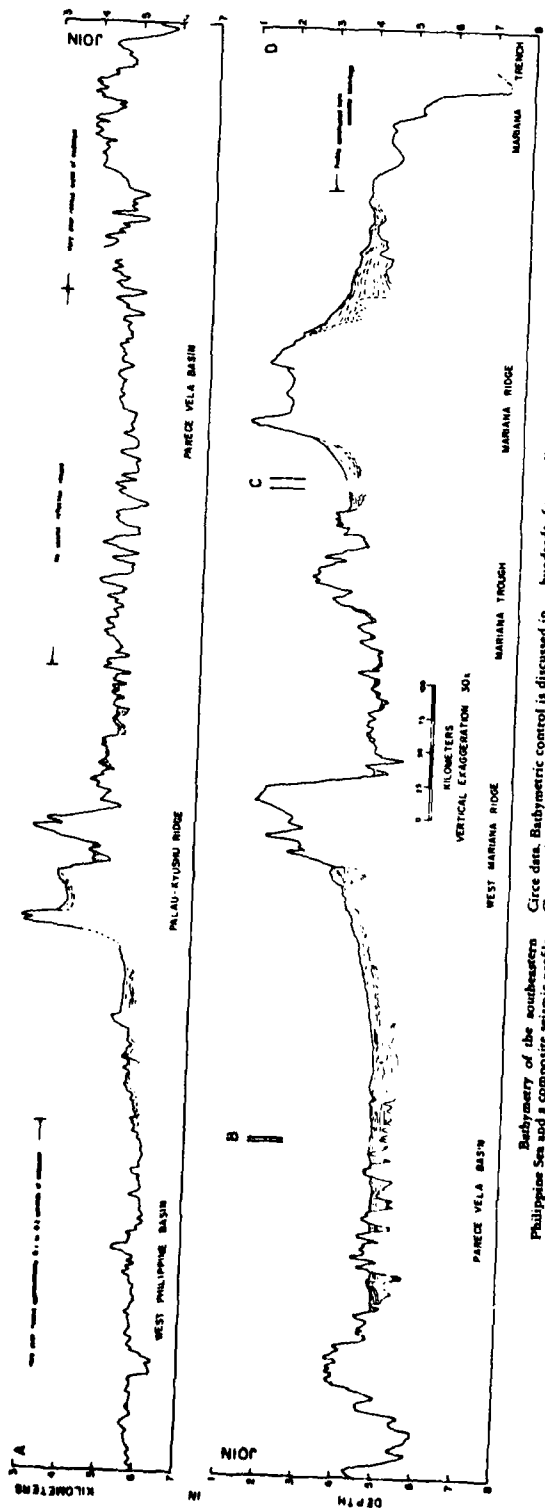


FIGURE 5  
RAY PATHS OF MULTIPLE BOTTOM BOUNCE SIGNALS

ARL:UT  
AS-81-809  
GDI - GA  
7-28-81

addition to the specularly reflected and refracted component. For instance, in the work of Herstein et al. in the Hatteras Abyssal Plain (1979) and Santaniello et al. (1979) at least one significant subbottom reflector was observed. The data presented by Dicus (1976; 1981) also showed significant subbottom reflectivity. Data obtained in the Tufts Abyssal Plain presented by Chapman (1980) indicated that the bottom loss was controlled by two major reflectors; refracted energy did not appear on the deconvolved traces. Data of Santaniello et al. (1979) also indicate that subbottom reflected energy dominates the bottom return rather than refracted energy. It appears then that the model of the ocean bottom as a specular reflection with a refracted component is not accurate for some ocean environments, and knowledge of sharp and/or discontinuous impedance contrasts with depth may be required to predict bottom reflection loss in a particular ocean basin.

A primary motivation of the work presented here is the desire to examine subbottom reflectivity for different ocean basins using existing bottom loss data. Currently, the two component model of a specularly reflected and refracted arrival is often used to match measured bottom loss to theoretical curves using geoacoustic models without sharp subbottom impedance contrasts. In what follows, two correlation techniques and a deconvolution technique are applied to multiple bottom bounce signals obtained in a turbidite province. These techniques reveal two major components; however, it is ambiguous whether the reflected component is the specular reflection or a subbottom reflection. Either interpretation implies that the geoacoustic structure in this turbidite province is significantly different from that proposed a priori (Hamilton, 1979).

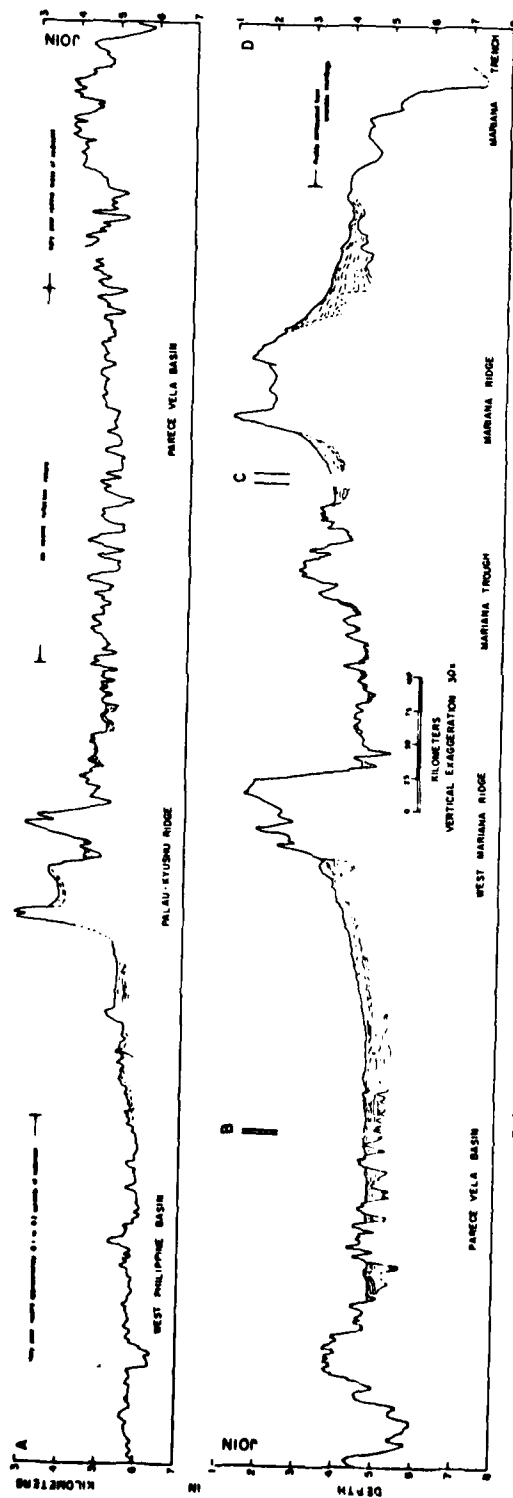


**FIGURE 6**  
**CROSS SECTION ILLUSTRATING THE DEPTH AND ROUGHNESS OF THE**  
**BASEMENT BENEATH THE SEDIMENT COVER IN THE PHILIPPINE SEA**  
 [Reproduced from Karig, (1971)]

#### 1.4 Geoacoustic Structure

There are four main parameters in the ocean bottom which affect bottom loss: the depth and nature of the basement (roughness, impedance, etc.) sound speed versus depth, density versus depth, and attenuation versus depth. The most important of these parameters is the depth and nature of the basement. If, for instance, the basement is shallow ( $<75$  m) and rough, as in much of the open ocean where the basement is basaltic and undulatory (Fig. 6), then the acoustic response of the basement will largely control the level and shape of the bottom loss curves. It would be expected that the frequency dependence of the acoustic response of the basement will be highly dependent on the spatial frequency distribution of the basement roughness and that the dependence of bottom loss on grazing angle will be dependent largely on the depth of the basement below the ocean bottom. In the case where the sediment thickness is large ( $>75$  m) and the basement is smooth and hard, then the frequency response of the basement could be considered to be white, and its effect on bottom loss curves would be seen mainly at low frequencies and high grazing angles.

The most important parameter after the depth and nature of the basement is the sound speed versus depth. The sound speed versus depth controls the "paths" that acoustic energy travels between source and receiver and, therefore, the densities and attenuations it encounters. Thus, the dependence of bottom loss on the grazing angle of the incident acoustic wave is very dependent on the sound speed structure in the subbottom.



Bathymetry of the southeastern Philippine Sea and a composite seismic profile across the region constructed from Scan and Chase and Menard (1969). Contours are in hundreds of meters, "corrected" with Marlow's tables and shown in 500 and 1000 m intervals.

**FIGURE 6**  
**CROSS SECTION ILLUSTRATING THE DEPTH AND ROUGHNESS OF THE**  
**BASEMENT BENEATH THE SEDIMENT COVER IN THE PHILIPPINE SEA**

[Reproduced from Karig, (1971)]

At low grazing angles ( $0-10^\circ$ ) bottom loss is highly dependent on the sound speed ratio at the water-sediment interface ( $c_w/c_s$ ). This is due partly to the intromission effect where (for a sound speed ratio less than one) the specular reflection amplitude goes to zero at some small grazing angle. More importantly there is an interference effect between the specularly reflected and refracted arrivals. This interference effect gives a large peak in the bottom loss curve for sound speed ratios less than one at small grazing angles. Bottom loss goes to zero as the grazing angle goes to zero for sound speed ratios greater than one.

The gradient of sound speed versus depth mainly controls the level of the bottom loss curves for grazing angles not associated with basement interaction. This is due to the fact that the gradient of sound speed controls the path lengths of the transmitted paths and the attenuation and density contrasts that the acoustic energy encounters. Discontinuities in velocity versus depth (or sharp changes) will result in reflections that also will significantly affect the level and shape of the bottom loss curves for angles not associated with bottom interaction.

Attenuation is the least well known of the geoacoustic parameters versus depth, and this is due partly to the uncertainty of the relative importance of different mechanisms which cause acoustic energy to be lost in the ocean bottom. It is, however, a very significant parameter in predicting bottom loss at all grazing angles.

The importance of the density profile on the shape and level of the bottom loss curves is important at discontinuities or sharp changes with depth which result in reflections such as at the water-sediment interface.

Edwin Hamilton, who has been greatly involved in geoacoustic modeling, has recently given a lengthy review article of the methodology and state-of-the-art knowledge of geoacoustic modeling of the ocean floor (Hamilton, 1980). Figure 7 is a set of velocity profiles presented by Hamilton for different sediment types from reflection and refraction profiling. This figure shows the approximate variability of velocity versus depth in the ocean floor. It is seen that the smallest increase in velocity with depth occurs with siliceous sediments, the largest increase occurs with calcareous sediments, and an intermediate increase occurs with terrigenous turbidites.

These profiles are obtained primarily from seismic reflection and refraction profiles. The actual velocity profile for an ocean basin is determined generally by linear regression of interval velocities obtained from seismic reflection data, which is forced through a sound speed value at the water-sediment interface obtained from physical property measurements of geologic cores.

Figure 8 shows velocity-density data indicating the relationship between velocity and density for different sediment types. In geoacoustic modeling, density versus depth is often determined by obtaining a velocity profile and converting the velocities to densities using velocity-density relationships in conjunction with known or assumed sediment types.

Figures 9-11 show published predictions of attenuation versus depth. Figure 9 is the composite of laboratory measurements, physical property measurements of cores, and other field data collected from acoustic measurements. Note that attenuation varies over a considerable range of 0.015 dB/m-kHz to 0.35 dB/m-kHz. Jacobson et al. report a similar range



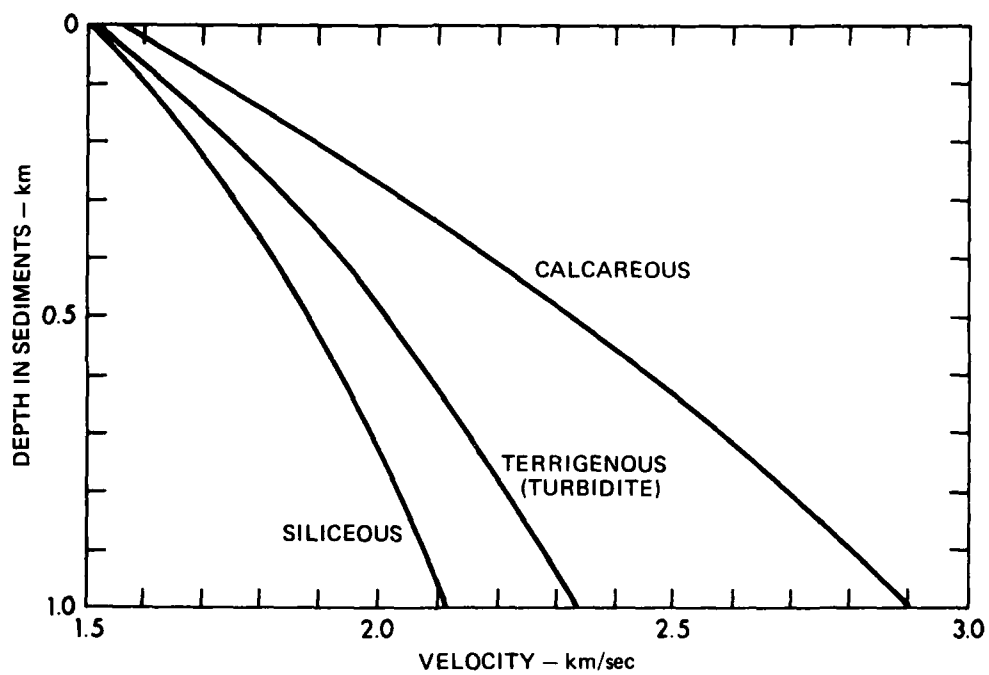
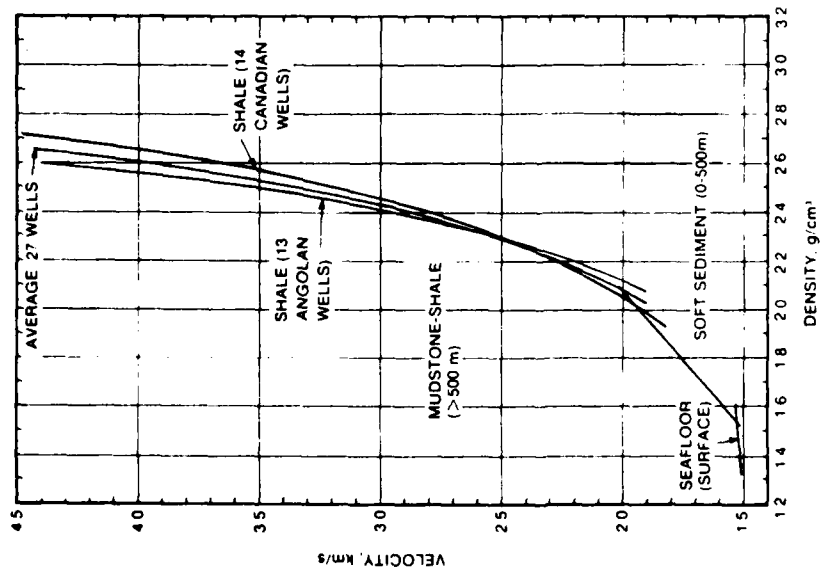
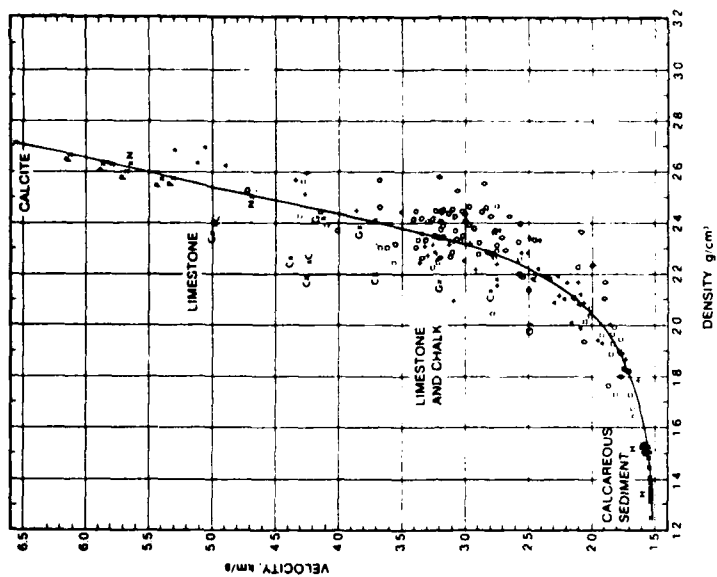


**FIGURE 7**  
**INSTANTANEOUS VELOCITY versus DEPTH CURVES**  
**FOR DIFFERENT SEDIMENT TYPES**

[Reproduced from Hamilton, (1980)]



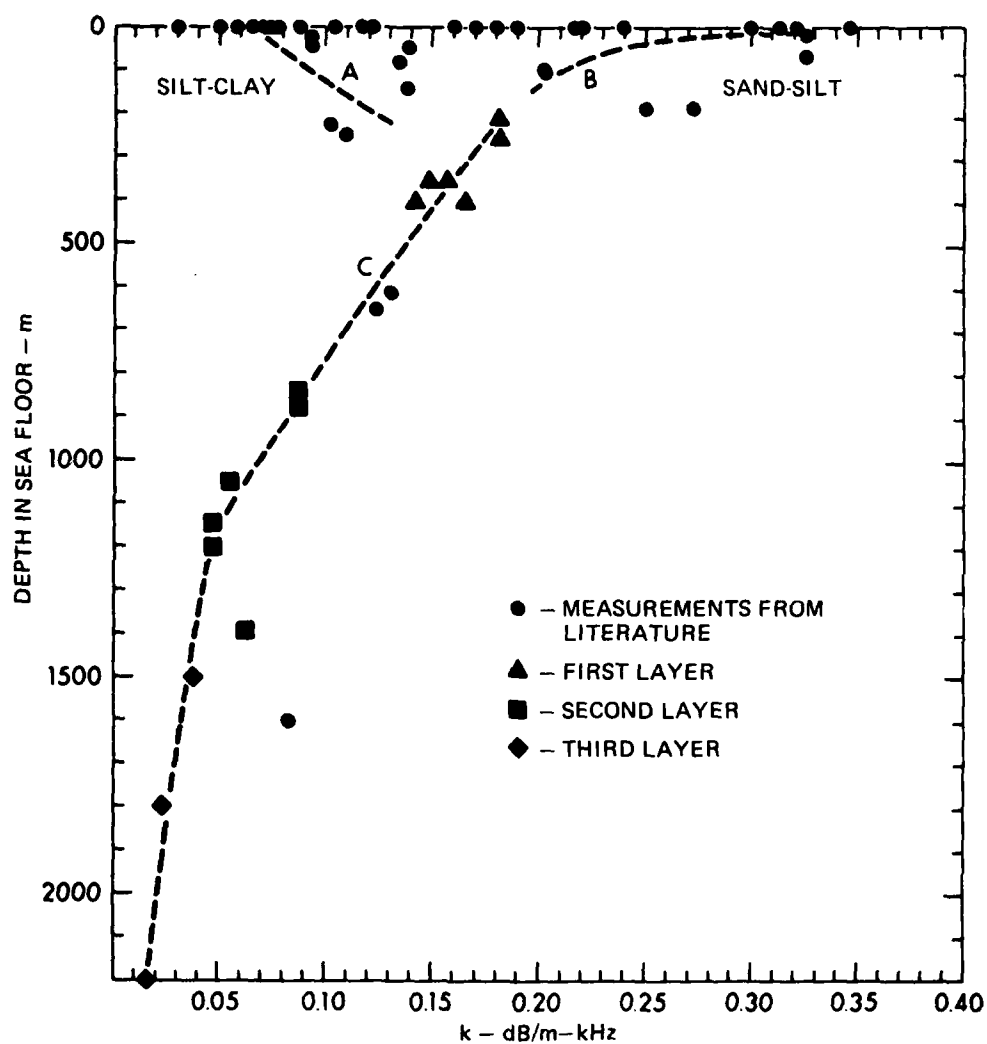
(a) TERRIGENOUS



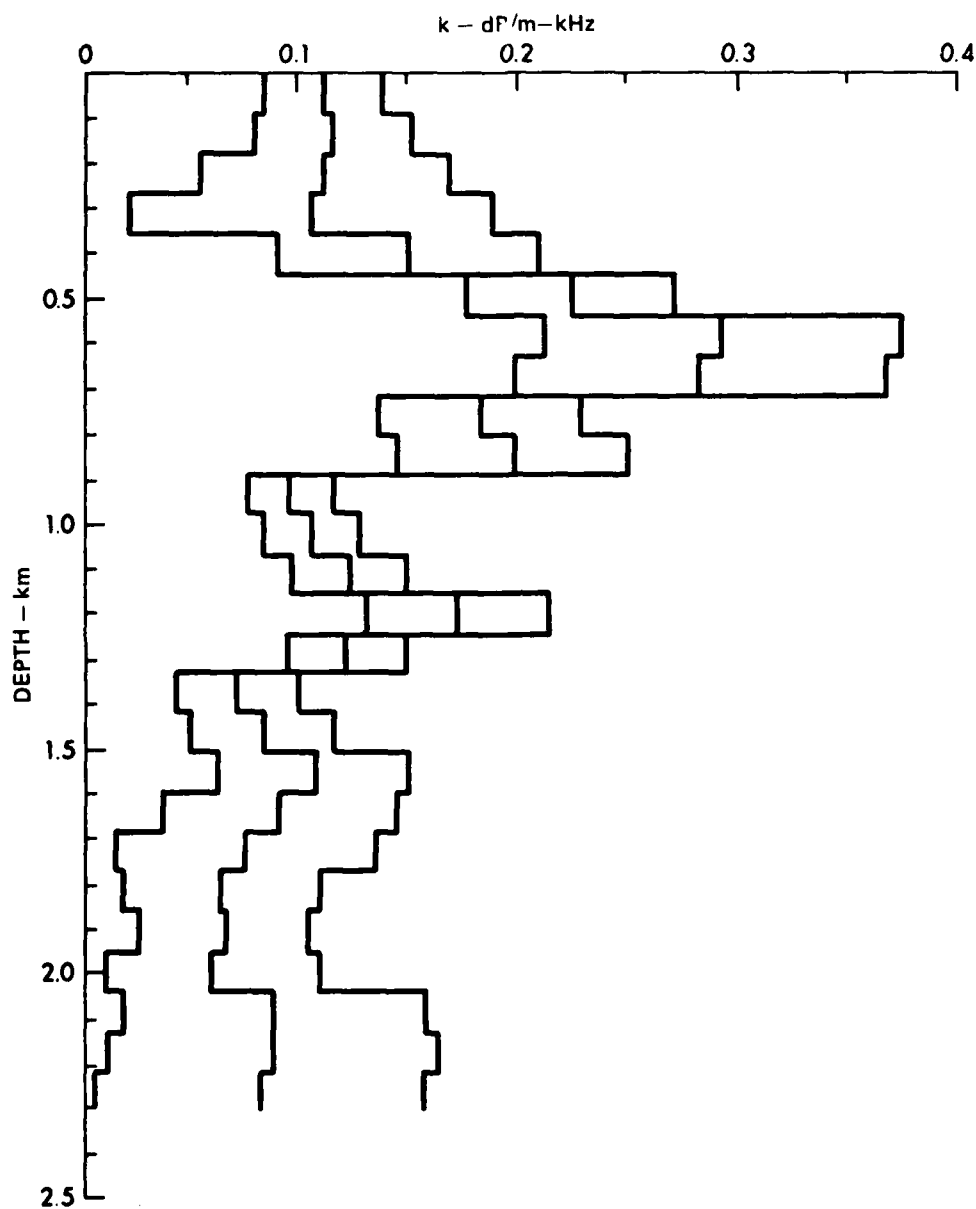
(b) CALCAREOUS

FIGURE 8  
VELOCITY versus DENSITY FOR COMMON MARINE SEDIMENT TYPES  
[Reproduced from Hamilton, (1980)]

ARL:UT  
AS-81-812  
GDI - GA  
7-28-81



**FIGURE 9**  
**COMPILED DATA OF ATTENUATION versus DEPTH**  
 [Reproduced from Hamilton, (1980)]



**FIGURE 10**  
**ATTENUATION versus DEPTH IN THE BAY OF BENGAL**  
 [Reproduced from Jacobson et al., (1981)]

ARL:UT  
 AS-81-819  
 GDI - GA  
 7-28-81

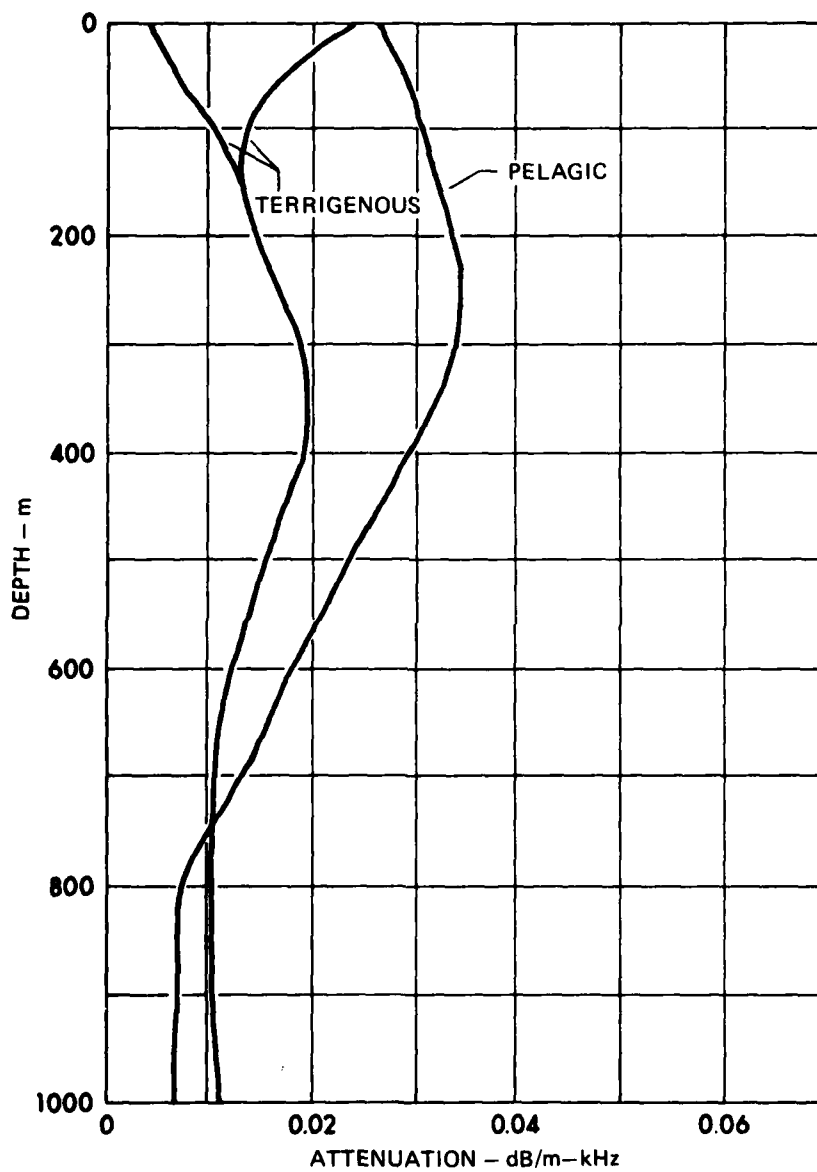


**FIGURE 11**  
**ATTENUATION AS A FUNCTION OF DEPTH IN THE**  
**SEA FLOOR CALCULATED FROM BOTTOM LOSS DATA**

[Reproduced from Mitchell and Focke, (1980)]

of values from a seismic refraction experiment in the Bay of Bengal, in good agreement with Hamilton's data (Fig. 10). On the other hand Fig. 11 shows attenuation values obtained from bottom loss data by Mitchell and Focke (1980) that are considerably lower than those obtained by Jacobson or Hamilton. At present there is no explanation for the difference in the two profiles. It could be due to actual differences in intrinsic attenuations of the sediments in the two regions or to use of erroneous assumptions in determining the attenuation values. The majority of the current literature seems to point to the lower values of attenuation at least for shallow (<300 m) depths (Bottom Interacting Acoustics, 1980).

Figures 12 and 13 illustrate the probable need for refinement of preliminary models of velocity and density versus depth. This is because preliminary geoacoustic models often do not take into account sharp impedance contrasts, and even more rarely account for lateral variability at a site. Figures 12 and 13 show data obtained from physical property measurements of the Deep Sea Drilling Project (DSDP) for cores obtained in the Gulf of Mexico. Hole 90 was drilled in the western Gulf and Hole 91 was drilled about 200 km away in the northern Gulf. Figure 12 shows density measurements obtained by the DSDP and Fig. 13 shows velocity data calculated from the density measurements using the velocity-density relationships of Hamilton and the sediment types reported from the cores.

Assuming that the variance of the errors of measurement is constant between sites, it is seen that the velocities are higher in the northern Gulf than the western Gulf and that there are more sharp impedance contrasts. The substantial agreement between the velocity profile derived from seismic measurements in the western Gulf with the DSDP measurements

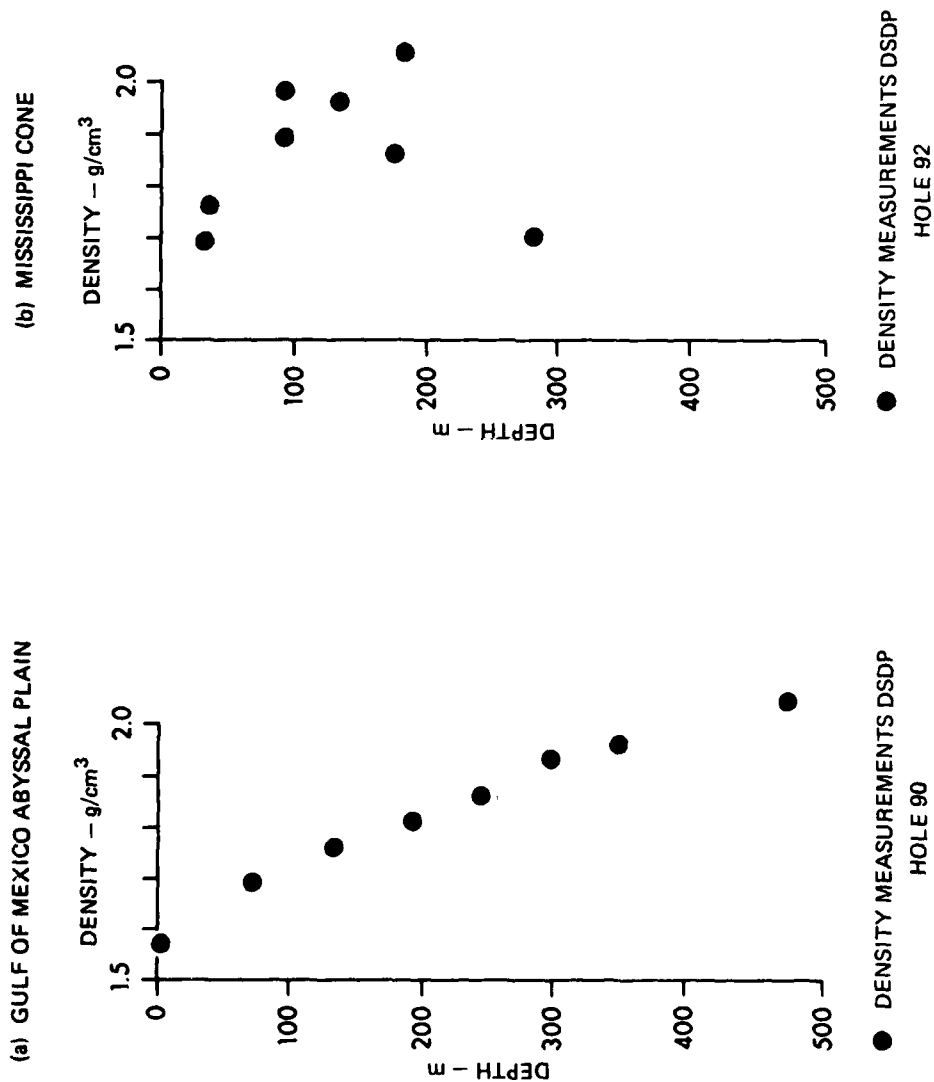


FIGURE 12  
DENSITY MEASUREMENTS OF THE DSDP IN THE GULF OF MEXICO

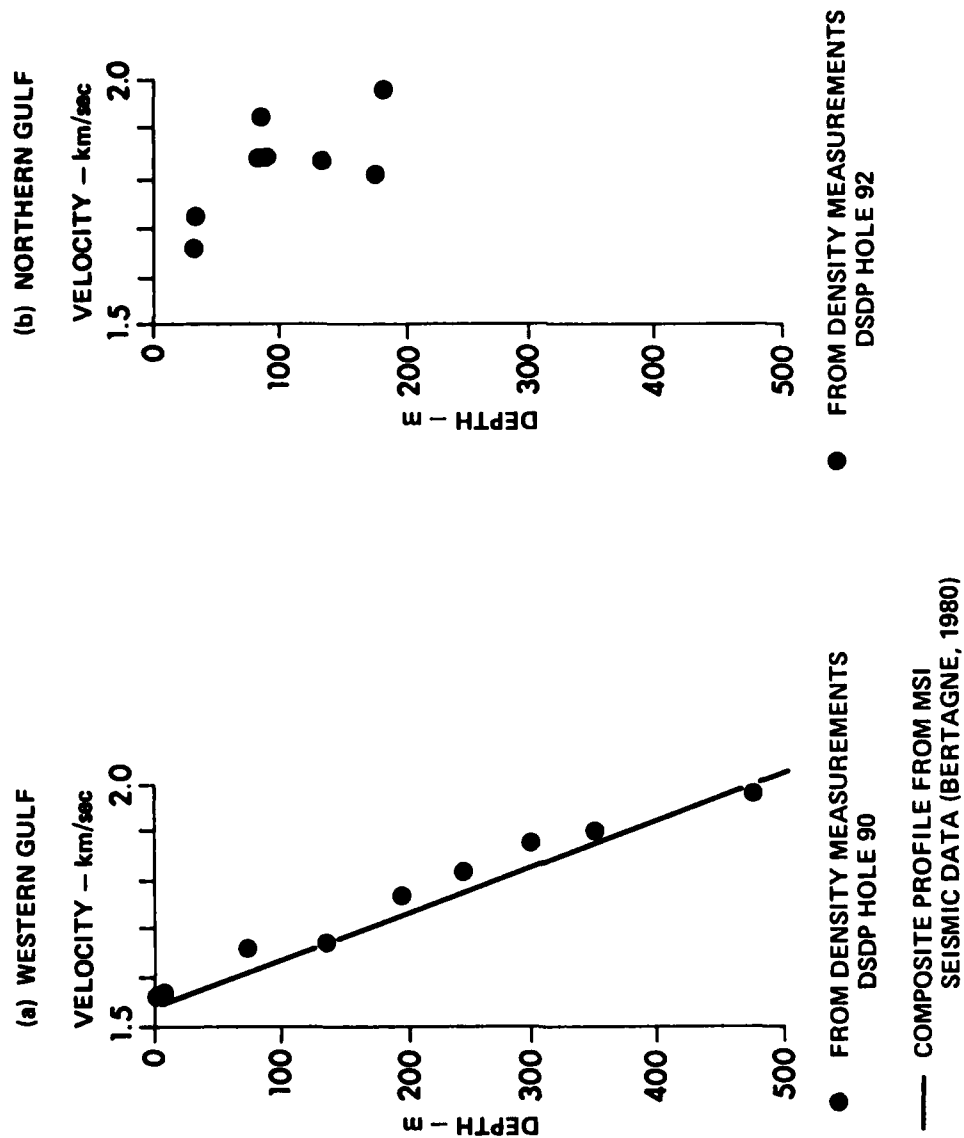


FIGURE 13  
VELOCITY versus DEPTH FOR TWO SITES IN THE GULF OF MEXICO



gives credence to both and implies that errors in the DSDP velocity values obtained from cores are small. Thus, these data illustrate significant lateral variability that occurs over a fairly small areal extent. These data, particularly Fig. 13(a), also imply the feasibility of comparing acoustic experiments and coring data and suggest the use of DSDP data for preliminary geoacoustic modeling.

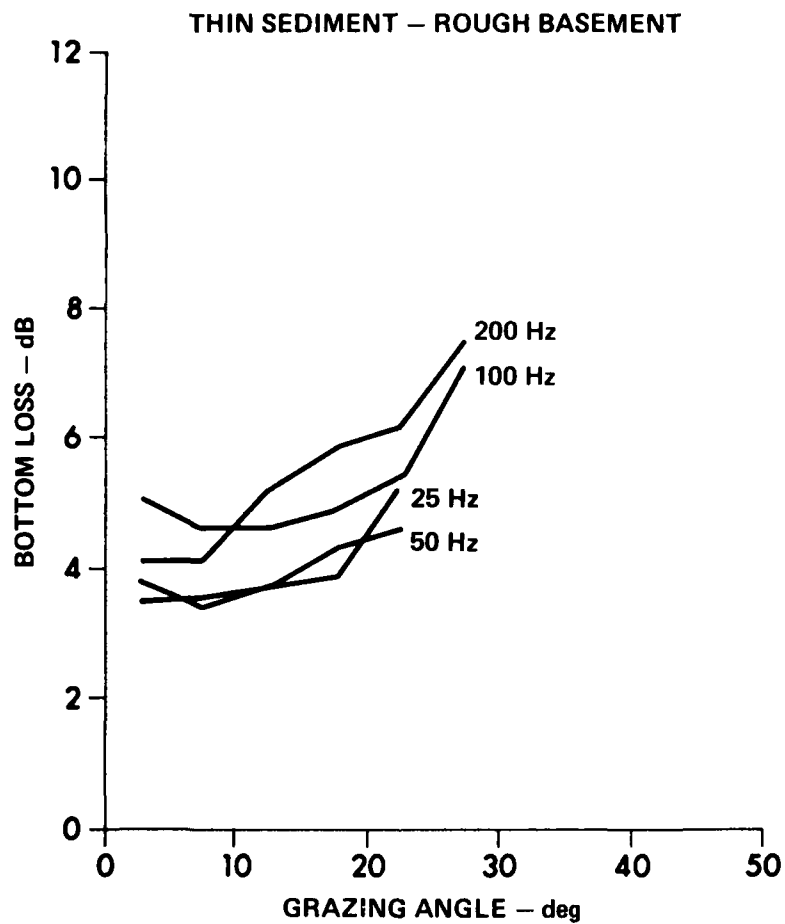
Finally, Figs. 14 and 15 show the effects of different geoacoustic environments on averaged bottom loss curves. Figure 14 shows bottom loss for an area of thin sediment overlying a rough basaltic basement. It is seen that there is relatively high loss at low angles and that the loss does not increase with frequency for all grazing angles.

Figure 15 shows two bottom loss plots for thick sediment regions. It is seen that the loss increases with frequency for all grazing angles and is lower at the low grazing angles than the thin sediment region. It is seen that there is higher loss for the calcareous ooze region than for the region of terrigenous turbidites. The reason for this difference is ambiguous. It could be due to a higher velocity gradient in the turbidite region, a higher reflectivity, or lower attenuations.

The work that follows is an attempt to develop processing techniques that could resolve the ambiguity of the bottom loss curves by identifying events of the time signal and thereby constraining the model of the geoacoustic structure.

### 1.5 Forward Modeling

In this study it was often necessary to model acoustic signals as a function of time and grazing angle. These synthetic waveforms are generated from a computer program called IMPULSE (and its feeder program



**FIGURE 14**  
**BOTTOM LOSS IN AN AREA OF THIN SEDIMENT**  
**OVERLYING ROUGH BASEMENT**

ARL:UT  
AS-81-333-S  
GDI - GA  
3 - 9 - 81

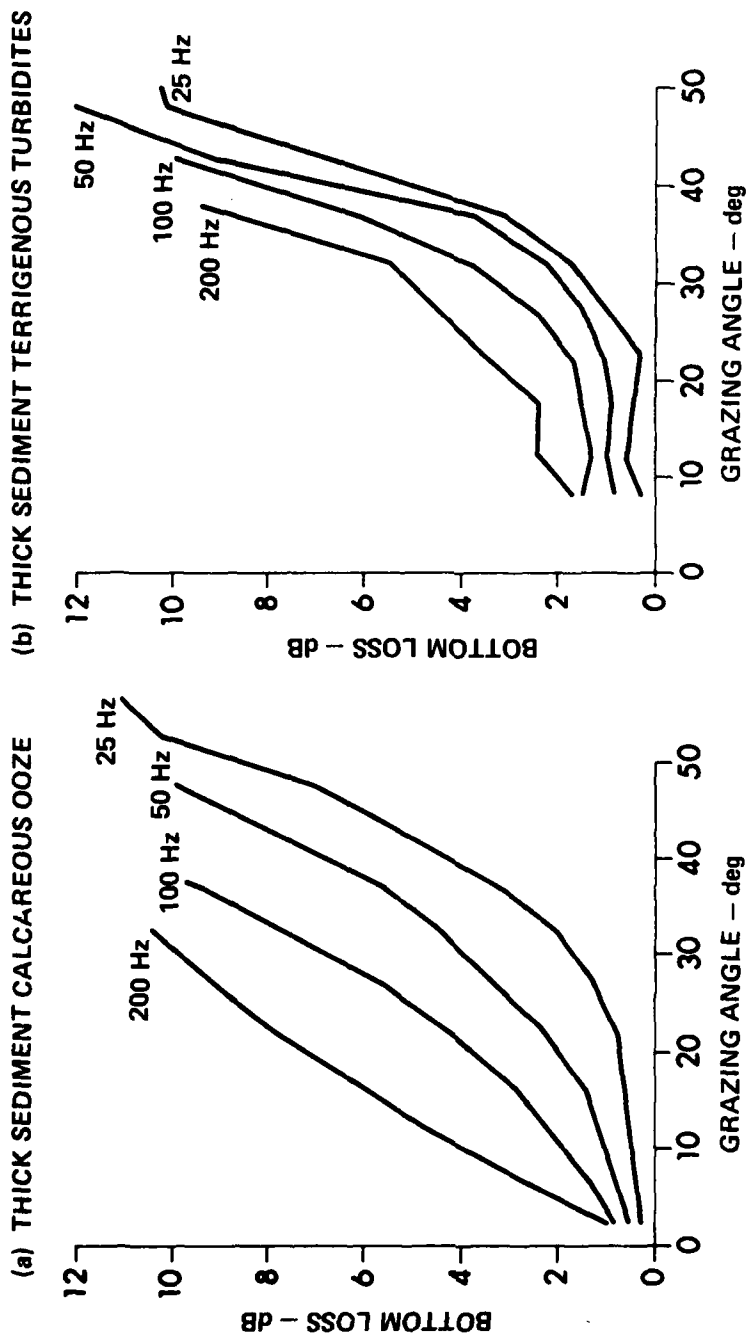


FIGURE 15  
BOTTOM LOSS CURVES FOR TWO AREAS OF THICK SEDIMENT

BOTREF), which resulted from the work of Mitchell and Lemmon. (See "A ray theory model of acoustic bottom interaction," J. Acoust. Soc. Am. 66 (1979).) IMPULSE calculates the synthetic waveforms by calculating a synthetic source waveform by the method of Gaspin and Schuler (1971), adding in ghosts at the respective ghost delays, and convolving this "total source waveform" with the plane wave ocean bottom impulse response calculated by the ray tracing model described below.

#### 1.5.1 Impulse Response Calculation

The impulse response of the synthetic waveforms discussed in this thesis were calculated by tracing rays between layers of the subbottom and calculating reflection and transmission coefficients at each interface in the subbottom with the usual fluid-fluid and fluid-solid boundary conditions (Mitchell and Lemmon, 1979). The ocean bottom is modeled as an isovelocity fluid half-space (water) above an arbitrary number of absorbing fluid layers with variable sound velocity, density, and attenuation which overlie a lower, solid half-space (basement) (see Fig. 17(a)).

A simple example of the method is shown in Fig. 16. In this case an isovelocity half-space overlies an absorbing fluid half-space with a positive velocity gradient. It is seen that there is a reflected component, a refracted component, and multiple refracted components which have reflected from beneath the interface one or more times. At any point along the interface there is an incident ray, a reflected ray, an upcoming ray, and a downgoing ray. The field can be represented by the displacement potentials,  $\phi_I$ ,  $\phi_R$ ,  $\phi_D$ , and  $\phi_U$ . Realizing that the downgoing wave at point A is the same as the downgoing wave at O to within a phase factor, taking

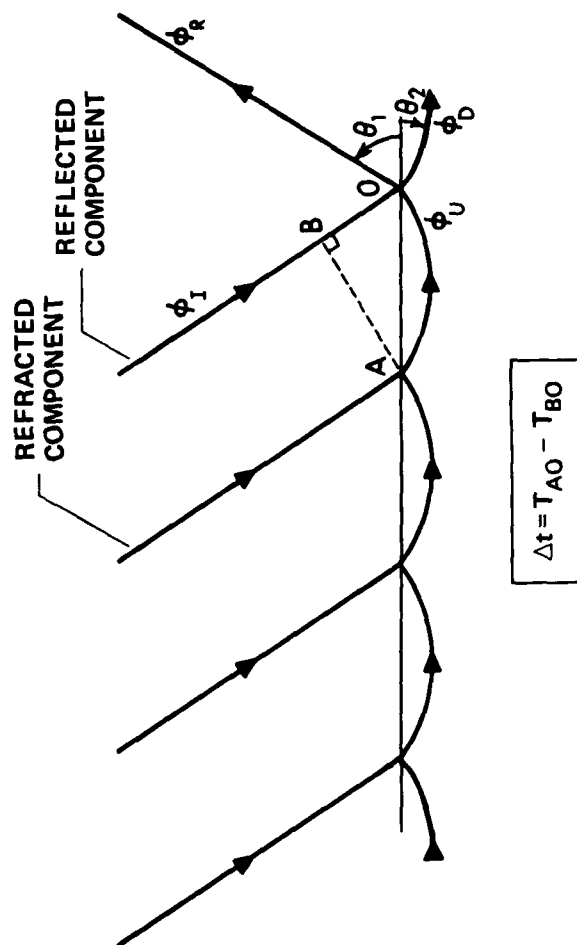
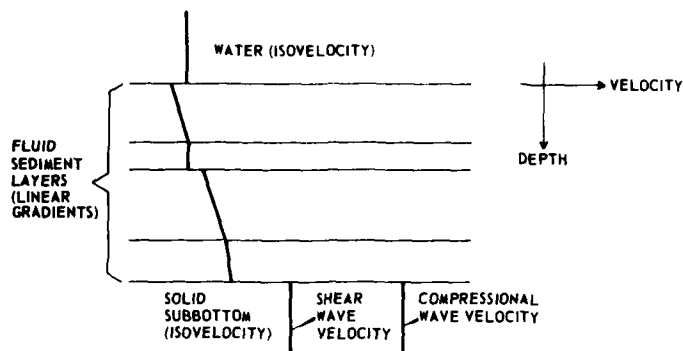
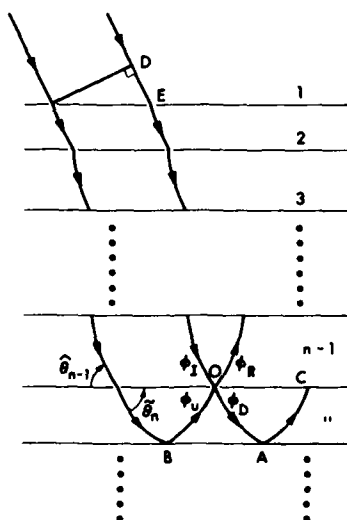


FIGURE 16  
PLANE WAVE INTERACTING WITH OCEAN BOTTOM



(a) GEOACOUSTIC MODELING FOR INPUT TO BOTREF



(b) RAY DIAGRAM ILLUSTRATING METHOD OF  
IMPULSE RESPONSE CALCULATION OF BOTREF

**FIGURE 17**  
**IMPULSE RESPONSE CALCULATION OF BOTREF**

[Reproduced from Mitchell and Lemmon, (1979)]

into account absorption, and the  $\pi/2$  phase shift associated with a plane wave passing through a turning point (Silbiger, 1968; Tolstoy, 1968; Burash, 1968), the reflected field can be found to be:

$$R = \frac{\rho_2(1+\alpha)k_1\sin\theta_1 - \rho_1(1-\alpha)k_2\sin\theta_2}{\rho_2(1+\alpha)k_1\sin\theta_1 + \rho_1(1-\alpha)k_2\sin\theta_2},$$

where

$\rho_{1,2}$  = density in upper (lower) interface

$k_{1,2}$  = wavenumber in upper (lower interface)

$\theta_{1,2}$  = incident (transmitted) angle, and

$\alpha$  is the factor which takes into account the phase shifts and attenuation of the refracted arrival relative to the reflected arrival.

$$\alpha = \exp\left(-\int B(z)dz + i\omega(\tau_{AO}-\tau_{BO}) - i\pi/2\right).$$

Mitchell and Lemmon then generalizes this result to a series of flat horizontal layers by tracing rays and solving the fluid-fluid and fluid-solid boundary conditions for a plane wave locally at each interface (see Fig. 17(b)). The results of this procedure are the recursive relations.

$$I_{n-1,n} = \frac{1}{2} \left[ (I_{(n,n+1)} / \alpha_n - R_{n,n+1} \alpha_n \gamma_n) \frac{\hat{C}_{n-1} \sin \tilde{\theta}_n}{C_n \sin \theta_{n-1}} + (I_{(n,n+1)} / \alpha_n + \alpha_n \gamma_n R_{n,n+1}) \frac{\tilde{\rho}_n}{\tilde{\rho}_{n-1}} \right],$$

and

$$R_{n-1,n} = \frac{1}{2} \left[ (I_{(n,n+1)} / \alpha_n + \alpha_n \gamma_n R_{n,n+1}) \frac{\tilde{\rho}_n}{\tilde{\rho}_{n-1}} \right]$$

$$- (I_{(n,n+1)} / \alpha_n - \alpha_n \gamma_n R_{n,n+1}) \frac{\hat{C}_{n-1} \sin \tilde{\theta}_n}{C_n \sin \tilde{\theta}_{n-1}} \Bigg] ,$$

where

$I_{n,n+1}$  = incident amplitude,

$R_{n,n+1}$  = reflected amplitude,

$\tilde{C}_n, \tilde{\rho}_n$  = velocity and density at the top of the nth interface, and

$\hat{C}_{n-1}, \hat{\rho}_{n-1}$  = velocity and density at the bottom of the (n-1)

interface,

and where  $\alpha_n, \gamma_n$  are terms which take into account attenuation and time delays between impulse response components.

Thus, the plane wave reflection coefficient of the stack of layers is

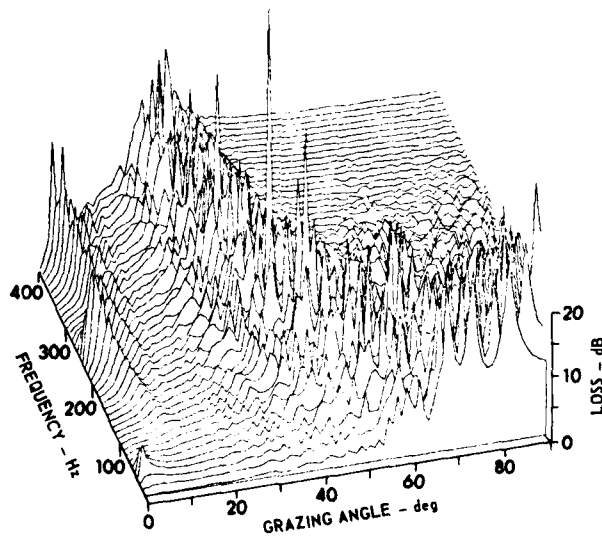
$$R = R_{1,2} / I_{1,2} .$$

Figures 18 and 19 show the results of the Mitchell and Lemmon work. Figure 18(a) shows the Fourier transform of the reflection coefficient at a particular angle of incidence. This is the transfer function of the ocean bottom. Figure 18(b) shows the bottom loss prediction from BOTREF as a function of angle and frequency. Finally, Fig. 19 shows how this ray tracing model compares to normal mode theory. Figure 19(a) shows that the ray tracing model is good for frequencies greater than about 10 Hz. Figure 19(b) shows the breakdown of the model when there is a critical angle. The advantage of the ray tracing model over the normal mode model is that the impulse response can be calculated much more rapidly on the computer.





(a) TYPICAL IMPULSE RESPONSE  
OBTAINED FROM BOTREF

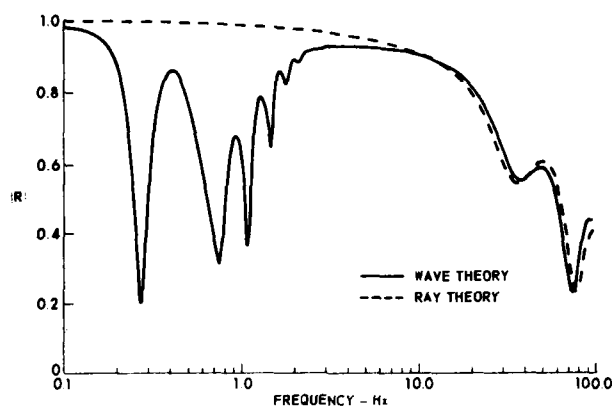


(b) BOTTOM LOSS AS A FUNCTION OF  
GRAZING ANGLE AND FREQUENCY

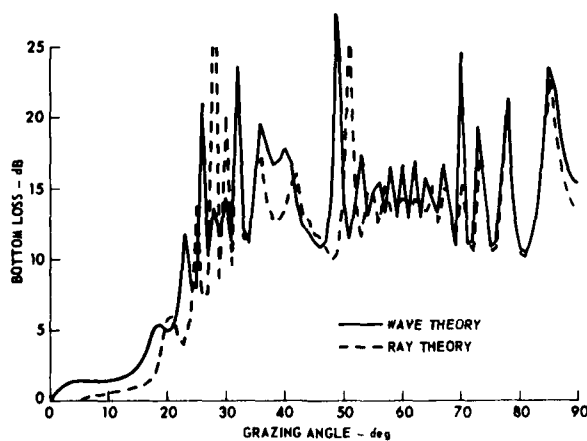
# **FIGURE 18** **OUTPUT TO BOTREF**

[Reproduced from Mitchell and Lemmon, (1979)]

ARL:UT  
AS-81-822  
GDI - GA  
7 - 28 - 81



(a) REFLECTION COEFFICIENT FOR A TURBIDITE MODEL AT 20° GRAZING ANGLE



(b) BOTTOM LOSS AT 50 Hz FOR A TURBIDITE MODEL WITH A 5° CRITICAL ANGLE

**FIGURE 19**  
**COMPARISON OF WAVE THEORY**  
**AND RAY THEORY PREDICTIONS**  
**OF BOTTOM RESPONSE**  
[Reproduced from Mitchell and Lemmon, (1979)]

ARL:UT  
AS-81-823  
GDI - GA  
7-28-81

In what follows, the synthetic ocean bottom transfer function will be modeled by the ray tracing method. Figure 20 shows the impulse response output from BOTREF using the geoacoustic model of Table I over 300 msec with the specular reflection aligned at 25 msec. In the absence of sharp impedance contrasts with depth, these specular reflected and refracted components are the only important components of the ocean bottom response, and knowledge of the time difference between these components is sufficient to obtain a velocity profile with depth.

#### 1.5.2 Synthetic Source Waveform

The source waveform that is used in synthetic modeling of acoustic signals in this report comes from the work of Gaspin and Shuler (1971), who model the source waveforms of explosive charges by fitting exponentials to the amplitudes of positive and negative peaks of the source signature. The Fourier transform of the constructed waveform provides an estimate of the source spectrum levels for bottom loss processing, and the constructed waveform itself is used in the synthetic modeling of acoustic signals. The shock pulse is modeled as an exponential pulse of the form

$$P(t) = P_0 e^{-t/\theta} ,$$

where  $P_0$  is the amplitude of the shock pulse and  $\theta$  is a decay constant evaluated from empirical relationships. The bubble pulses are modeled as double exponential decays.

The parameters involved in the formulation of the synthetic waveform are shown in Fig. 21. It is seen that if the source waveform is considered to have four significant bubble pulses, there are five

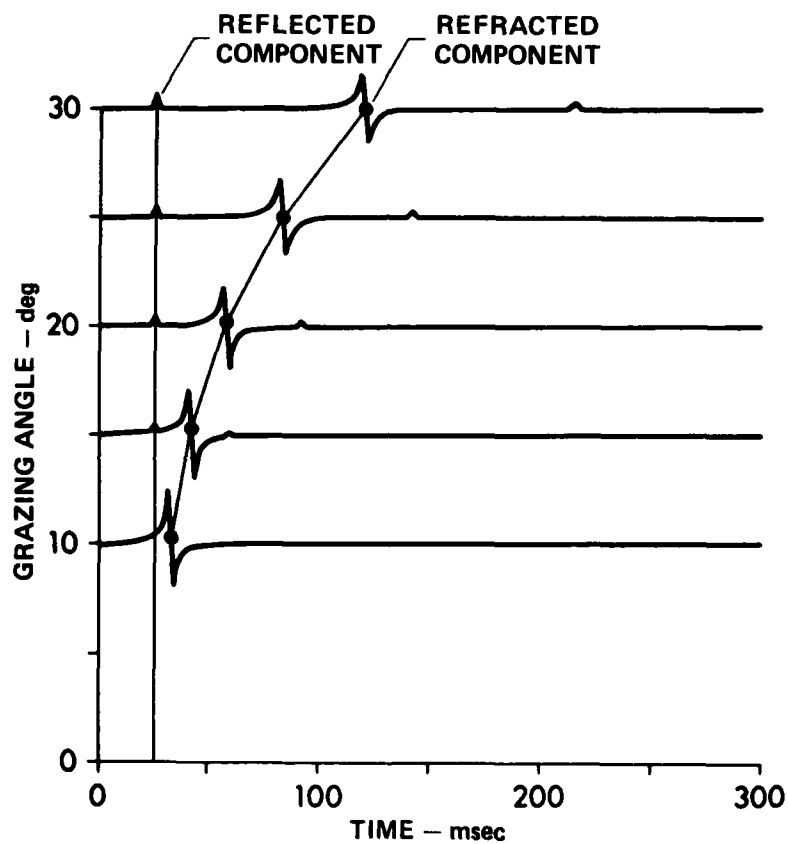
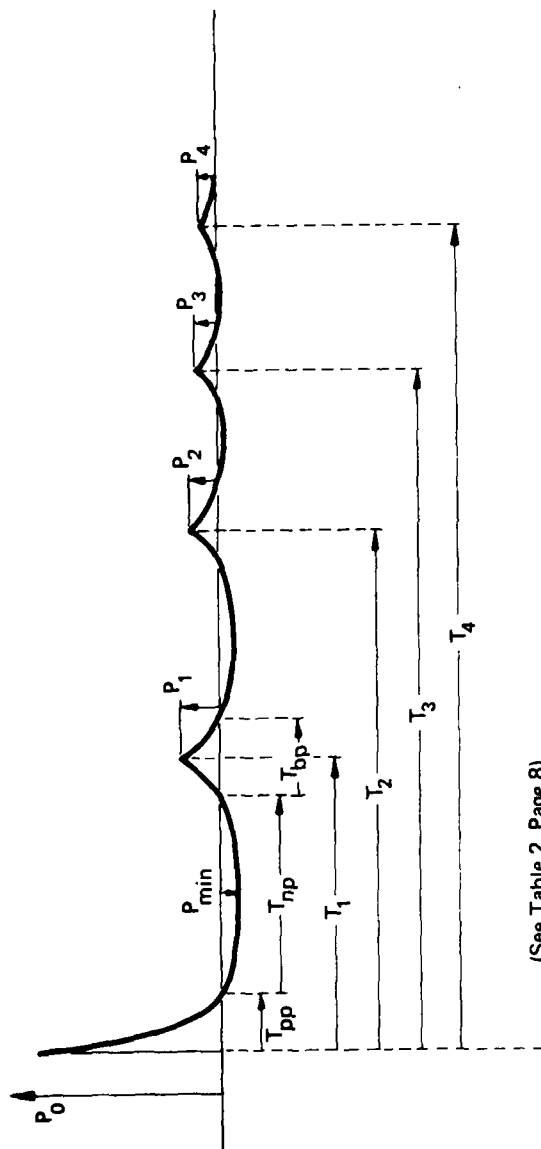


FIGURE 20  
 SYNTHETIC OCEAN BOTTOM IMPULSE  
 RESPONSE versus GRAZING ANGLE ALIGNED  
 ON SPECULAR REFLECTION CALCULATED FROM BOTREF

ARL:UT  
 AS-81-323  
 GI-GA  
 3-4-81

TABLE I  
GEOACOUSTIC MODEL FOR FIGS. 20, AND 68-89

Depth	Velocity	Attenuation	Density
<u>(m)</u>	<u>(m/sec)</u>	<u>(dB/m-kHz)</u>	<u>(g/cm<sup>3</sup>)</u>
0 <sup>-</sup>	1515		1.0
0 <sup>+</sup>	1485	0.02	1.4
1000 <sup>-</sup>	2485	0.02	2.4
1000 <sup>+</sup>	5200	0.01	2.5



(See Table 2, Page 8)

**FIGURE 21**  
**PARAMETERS FOR THE PRESSURE-TIME HISTORY OF THE**  
**QUASITHEORETICAL SYNTHETIC SOURCE WAVEFORM**  
 [Reproduced from Gaspin and Shuler, (1971)]

amplitude measurements, four bubble pulse delays, and three periods associated with the width of the bubble pulses that must be determined empirically. The delays between bubble pulses were found by Gaspin and Shuler to be proportional to the cube root of the charge weight and inversely proportional to the sixth root of the depth of detonation.

Although this provides a practical and convenient method for the estimation of the source spectrum, it should be noted that although an actual explosion shock wave decays exponentially the decay rate decreases markedly after a time of about 2. The shock wave has a significant amount of energy in the negative phase with the time of the first zero crossing strongly dependent on the depth of burst. The bubble pulses are also not well modeled by exponentials.

Thus, although these waveforms are useful for synthetic studies in which primarily the bubble pulse timing and amplitude must be modeled adequately, they are not accurate enough models to use in source deconvolution of real data.

#### 1.5.3 Synthesized Waveform

To derive the synthesized waveform, the effects of ghosts must be added to the source waveform. This "total source waveform" must then be convolved with the ocean bottom impulse response to obtain the synthesized waveform.

Ghost time delays can be calculated by ray tracing using the experiment geometry and the water sound speed structure. Assuming that the transfer function of the air-water interface is a negative one, the "total source waveform" is calculated by adding the source waveforms at zero delay and each ghost delay with the appropriate sign, positive or negative.

With the additional assumption that the grazing angle at the ocean bottom is the same for the first arrival and its ghost arrivals, the synthesized waveform is calculated by convolving the "total source waveform" with the impulse response. Since the bottom is assumed to be flat and laterally homogeneous, the impulse response for an  $n$  bottom bounce signal will be the Fourier transform of  $(R(\theta, \omega))^n (-1)^{n+1}$  where  $R(\theta, \omega)$  is the ocean bottom transfer function for a one bottom bounce signal.

The assumption that the impulse response for the first arrival and its ghost arrivals is the same becomes more valid as the number of bottom interactions increases.



## CHAPTER 2

### TEM FILTER EFFECTS ON ACOUSTIC DATA

#### 2.1 System Filter Effects

If the impulse response consists essentially of a specularly reflected and a refracted arrival, knowledge of the travel time difference between these components would allow for the calculation of velocity as a function of depth in the subbottom. Measuring this travel time difference from bottom loss data is difficult, for common source receiver geometries of the experiment, because source bubble pulses and the source and receiver ghosts considerably obscure the time delay of interest. In this section the arrivals of the source and receiver ghosts and source bubble pulses will be shown on time versus grazing angle plots for multiple bottom bounce acoustic signals.

Figure 22 shows the frequency representation of an acoustic signal recorded in a bottom limited ocean and Fig. 23 shows a schematic that illustrates the various filtering effects which act on the signal. It is seen that the signal consists of three filter components: the source waveform, the source and receiver ghosts, and the multiple bottom bounce impulse response.

First, consider the filtering effect of source bubble pulses on time versus grazing angle plots. Since the bubble pulse delays are dependent on source characteristics only, the effect of the source bubble pulses will be independent of grazing angle or range. Thus, the interfering

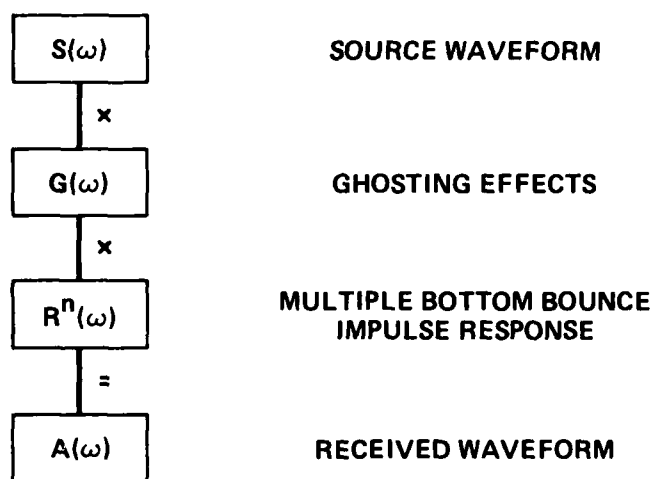


FIGURE 22  
 FREQUENCY DOMAIN REPRESENTATION  
 OF ACOUSTIC SIGNAL

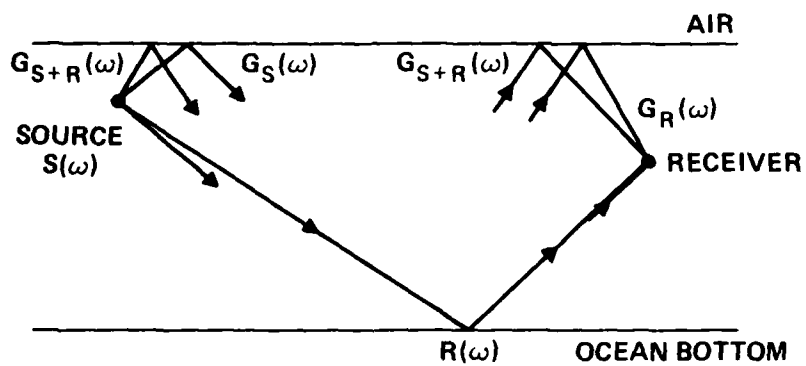


FIGURE 23  
SYSTEM FILTERING EFFECTS

effects due to bubble pulses of aligned arrivals will appear as straight lines on time versus grazing angle plots at the bubble pulse delays. In fact every event of the impulse response will have a trail of bubble pulses.

For the work done here the nominal source depths are 18.3, 91.4, and 244.1 m (or 60, 300, and 800 ft). Figure 24 shows the quasi-theoretical plots of these waveforms for the first 300 msec from the work of Gaspin and Shuler. Figure 20 shows that we are attempting to measure time delays in the impulse response which vary from 0 to about 125 msec for grazing angles between 0 and 30°. Recognizing the convolutional nature of filtering operations in the time domain, it is seen that only the 18 m source will not considerably obscure the time delay of interest.

Second, we consider the filtering effects due to ghosts. From Fig. 23 it is seen that, for each acoustic pulse generated at the source, four arrivals come in at the receiver: the arrival that is not reflected from the air-water interface, the source ghost, the receiver ghost, and the source plus receiver ghost.

The delays of these ghosts can be approximated by considering a plane wave interacting, with a free surface (see Fig. 25). This time delay is

$$t_g = \frac{2d \sin\theta}{c}$$

where  $d$  is the depth of the source or receiver,  $c$  is the water sound speed, and  $\theta$  is the grazing angle.

This delay is illustrated on a time versus grazing angle plot in Fig. 26 for depths between 12.5 and 400 m. Zero delay is aligned at

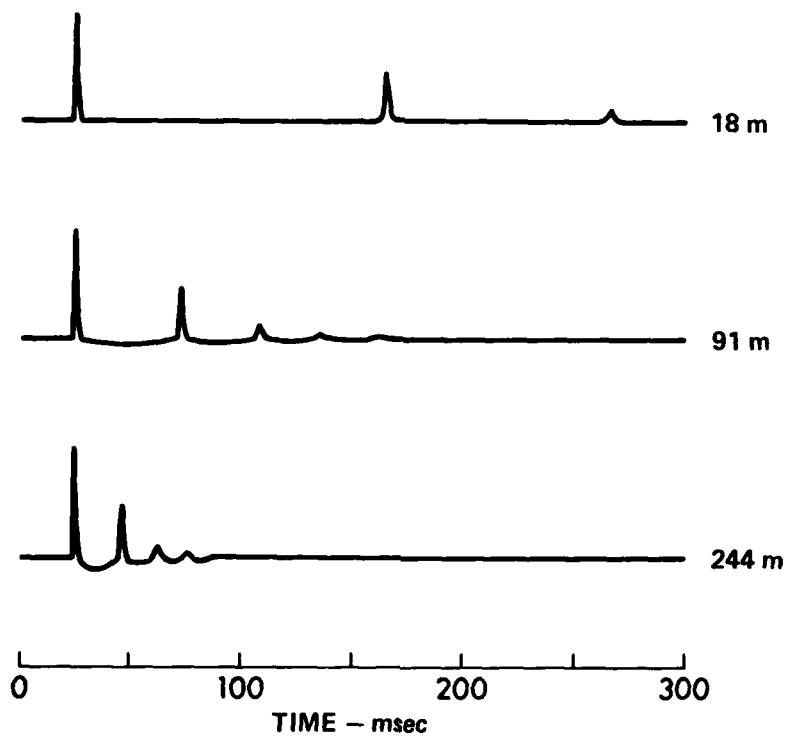


FIGURE 24  
SOURCE WAVEFORMS FOR DIFFERENT SOURCE DEPTHS

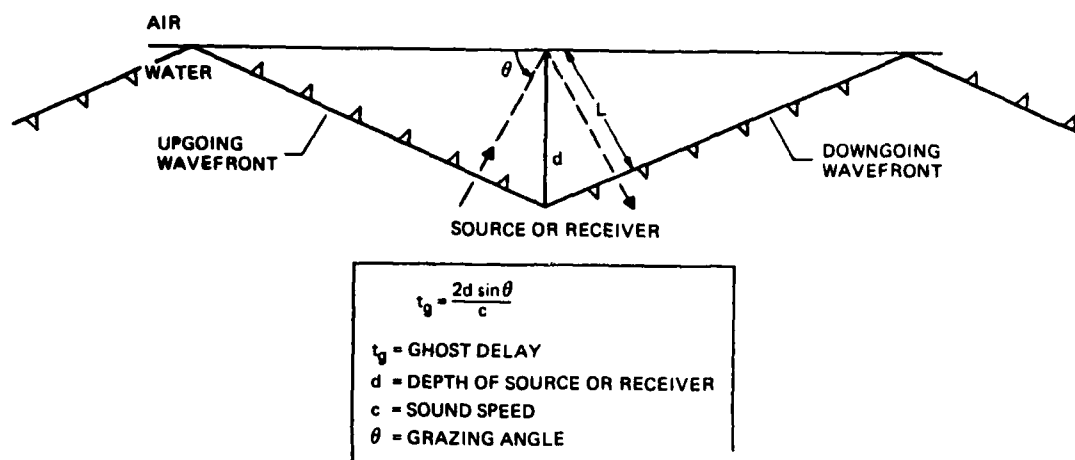


FIGURE 25  
CALCULATION OF GHOST TIME DELAY

ARL:UT  
AS-81-828  
GDI - GA  
7-28-81

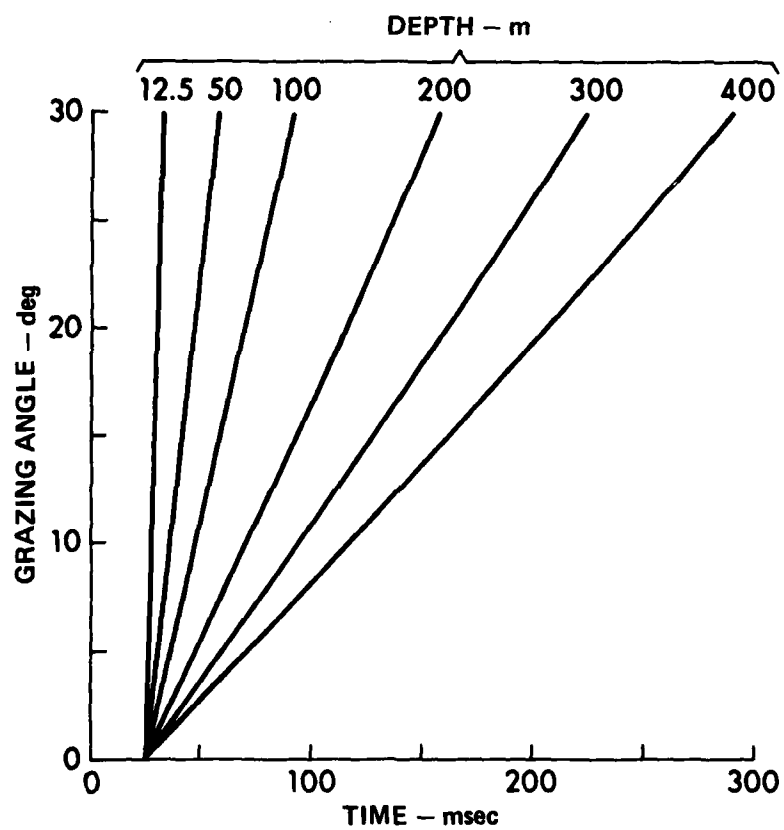


FIGURE 26  
RANGE OF TYPICAL SOURCE-RECEIVER GHOST DELAYS

ARL:UT  
AS-81-328  
GI - GA  
3 - 4 - 81

25 msec to be consistent with plots of real and synthetic acoustic signals to be shown in later sections.

Figure 27 shows the acoustic response of the ghosting effects. The source ghost response is

$$\delta(t) - \delta(t-t_S) \quad ,$$

and similarly the receiver ghost response is

$$\delta(t) - \delta(t-t_R) \quad .$$

The convolution of these filter components yields the total ghost response

$$\delta(t) - \delta(t-t_S) - \delta(t-t_R) + \delta(t-t_S-t_R) \quad ,$$

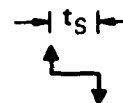
which consists of the source ghost, the receiver ghost, and the source plus receiver ghost. As expected the source ghost and the receiver ghost, which reflect from the air-water interface only once, are negative while the other two arrivals are positive. The total ghost response shows that significant interference will occur at the source ghost time delay, the receiver ghost time delay, and their sum. Since the time delay is proportional to depth, for the plane wave approximation, significant interfering energy will arrive along the lines drawn in Fig. 26 at the source and receiver depths and the sum of their depths.

The final filter needed to describe multiple bottom bounce acoustic signals is the multiple bottom bounce impulse response. The (n)



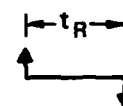
### SOURCE GHOST RESPONSE

$$\delta(t) - \delta(t - t_S)$$



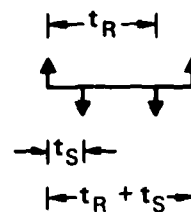
### RECEIVER GHOST RESPONSE

$$\delta(t) - \delta(t - t_R)$$



### TOTAL GHOST RESPONSE

$$\delta(t) - \delta(t - t_S) - \delta(t - t_R) + \delta(t - t_S - t_R)$$



$$t_g = \frac{2d \sin \theta}{c}$$

$\theta$  = GRAZING ANGLE

$d$  = DEPTH

$c$  = WATER SOUND SPEED

FIGURE 27  
SYNTHESIS OF TOTAL GHOST RESPONSE  
OF AN ACOUSTIC SIGNAL

ARL:UT  
AS-81-830  
GDI - GA  
7-28-81

bottom bounce impulse response is equal to the convolution of the (n-1) bottom bounce impulse response and the negative of the one bottom bounce impulse response (assuming the bottom is flat and laterally homogeneous). If the ocean bottom impulse response consists of only a specular reflection and a refracted component which has gone through a caustic, then it can be represented as a pulse followed by a pulse with a  $90^\circ$  phase shift. This is the case illustrated in Fig. 28 (BB = bottom bounce). It is seen that in this case there is a  $90^\circ$  phase shift between each of the components of the multiple bottom bounce impulse response. The fact that the leading arrival is alternately positive and negative is due to the reflection at the air-water interface between bounces. Thus, the phase of the impulse response components of multiple bottom bounce signals can be predicted.

Amplitudes can also be predicted. Consider the same case of an impulse response that consists essentially of a specularly reflected and refracted component. If we consider the delay between the components to be unity the signal can be represented in the Z domain by

$$a_1(\omega) + a_2(\omega)e^{i\pi/2Z} \quad ,$$

where  $a_1$  is the amplitude of the specular reflector,  $a_2$  is the amplitude of the refracted arrival, and Z is the unit delay between them. Dividing by  $a_1$  and recognizing that convolution in the time domain is equivalent to multiplication in the Z domain we have:

$a_1 (1+aZ)$	1BB
$a_1^2 (-1-2aZ-a^2Z^2)$	2BB
$a_1^3 (1+3aZ+3a^2Z^2+a^3Z^3)$	3BB

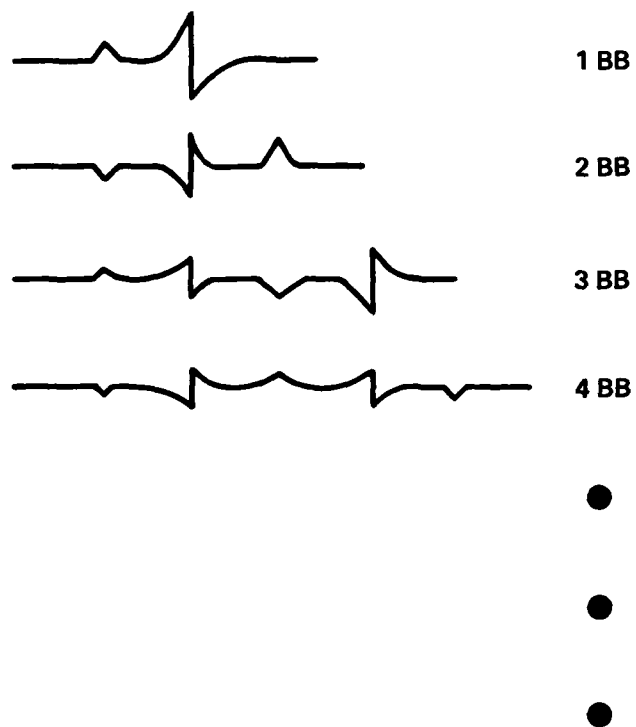


**FIGURE 28**  
**MULTIPLE BOTTOM BOUNCE IMPULSE RESPONSE**

$$a_1^4 (-1-4aZ-6a^2Z^2-4a^3Z^3-a^4Z^4) \quad 4BB$$

$$a_1^n ((1+aZ)^n(-1)^{n+1}) \quad nBB$$

where  $a = [a_2(\omega)/a_1(\omega)] e^{i\pi/2}$ . Thus, it is seen for the case where  $a_2/a_1=1$  that the impulse response will be symmetric and have its greatest contribution in the center. If  $a_2/a_1 > 1$  then the impulse response will have its larger contributions in its tail.

So it is seen that the amplitude and phase of the components of the impulse response can be predicted for multiple bottom bounce signals if the one bottom bounce impulse response is known. The fact that the phase of the impulse response components can be predicted gives encouragement that these components can be identified in the data. This would allow for the inversion of the time delay between them to velocity and attenuation profiles as a function of depth in the subbottom.

To get an idea of how the multiple bottom bounce impulse response components are delayed as a function of grazing angle, consider a model of the ocean bottom as an infinite half-space with a simple linear gradient of velocity. In this case the travel time of the refracted path in the sediment is

$$T_R = -\frac{2}{g} \ln \left( \frac{\cos \theta_R}{1 + \sin \theta_R} \right),$$

where  $g(\text{sec}^{-1})$  is the gradient and  $\theta_R$  is the transmitted angle at the interface (Ewing and Leet, 1932). In the plane wave case, assuming the

water column is locally isovelocity at the water-sediment interface, the travel time difference is

$$\Delta t = -\frac{2}{g} \ln \left( \frac{\cos \theta_R}{1 + \sin \theta_R} \right) - \frac{2}{g} \sin \theta_R \quad ,$$

(Mitchell and Lemmon, 1980.) In reality, the spreading of acoustic energy from the source is more nearly spherical than planar. The main effect of this is that the reflected and refracted components have different angles of incidence at the water-sediment interface. The plane wave assumption will be used since it provides a good estimate of the delay between the reflected and refracted components and is very easily calculated from the preceding formula. Appendix I shows a comparison between the plane wave and a very simple spherical wave model of  $\Delta t$  versus grazing angle.

The plane wave assumption is made in all of the work of the next section.

## 2.2 T- $\theta$ Plots of Multiple Bottom Bounce Acoustic Signals

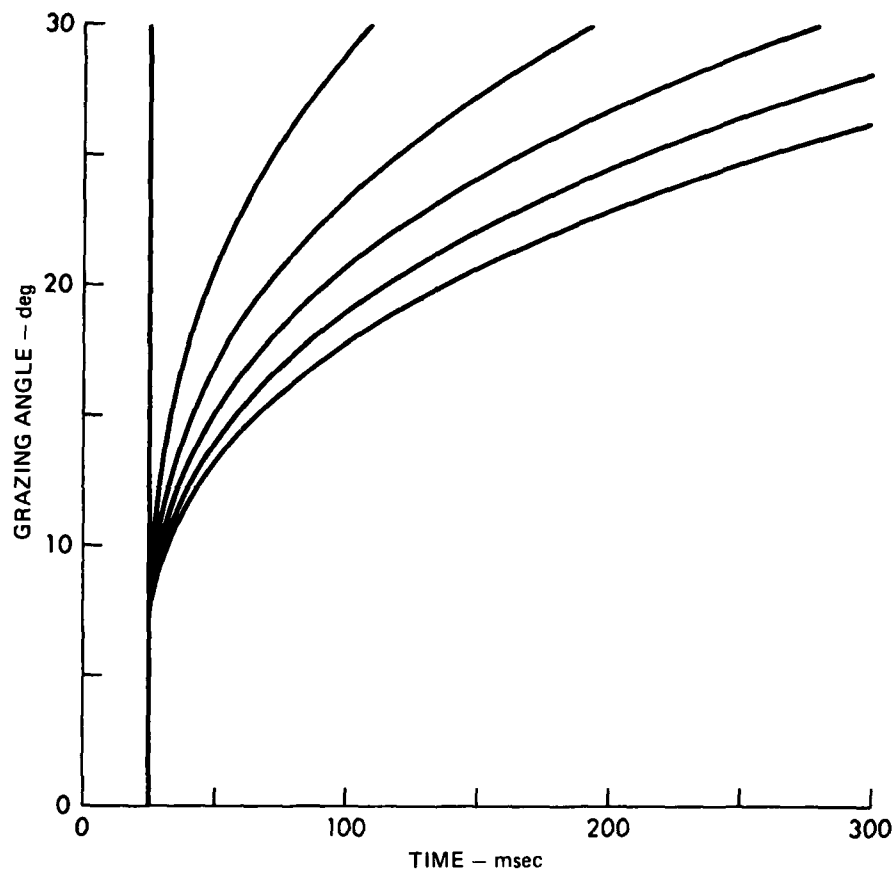
In this section the predicted travel time curves of the components of multiple bottom bounce acoustic signals will be synthesized and compared to measured signals with the first recognizable phase of the measured signals aligned at 25 msec. This will illustrate the effects of the source waveform and ghosts on travel time versus grazing angle plots of acoustic signals, and will show that these effects can often be identified and that, in general, they severely distort the ocean bottom impulse response. (The aligned arrival is not usually believed to be the first arrival of the acoustic signal since the first arrival is usually buried in the noise; rather it is the first phase that can easily be recognized on

all traces. Aligning an easily recognized phase is time consuming (~2 h). Aligning less easily recognized phases would be much more time consuming and the alignment of a particular phase would be less certain.)

Figure 29 shows the predicted travel time curves for the arrivals of a five bottom bounce impulse response assuming a plane wave model with a water-sediment sound speed ratio of 0.994 and a gradient of  $1.1 \text{ sec}^{-1}$ . This is a good first order prediction of the travel time curves of the bottom response components based on geoacoustic models proposed in the literature. The important components of the impulse response are assumed to be a single specular reflection and a single refracted component per bottom bounce, as shown in Fig. 28. Clearly, a more complicated model with subbottom reflectors will considerably complicate the travel time plot and make unambiguous identification of arrivals more difficult. Internally reflected events (or deep refracted events) are generally ignored since they are considered to be attenuated to the noise level.

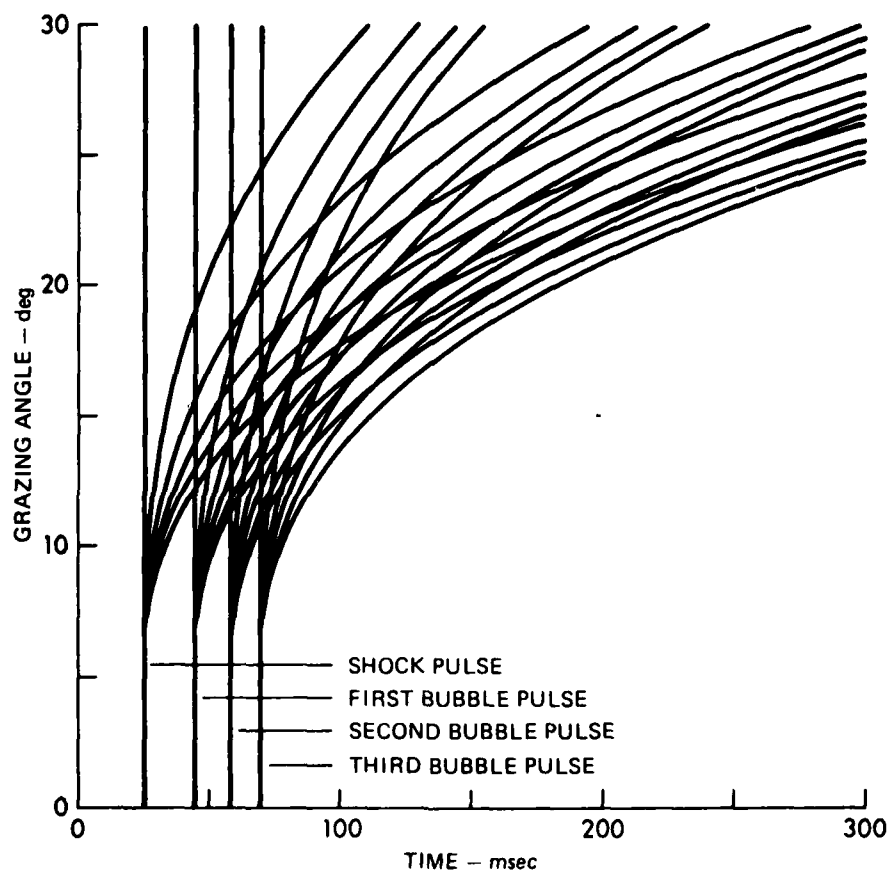
Figure 30 shows the effects of the source bubble pulses of the previous figure with a 244 m source. For all pass plots (0-600 Hz) the shock pulse would be expected to be largest with an exponential decay of the amplitude of trailing bubble pulses. For a low pass plot the first bubble pulse may be, and often is, observed to be larger than the shock pulse. In general, the second bubble pulse is very small and the third bubble pulse can generally be ignored.

Figure 31 shows the ghosting effects of the multiple bottom bounce impulse response on a travel time versus grazing angle plot. Each component of the impulse response is delayed by the ghost delays associated with the source depth, the receiver depth, and the sum of the source and



**FIGURE 29**  
**MULTIPLE BOTTOM BOUNCE IMPULSE RESPONSE**  
**DELAYS versus GRAZING ANGLE**  
 (5 BB,  $c_s/c_w = 0.994$ ,  $g = 1.1 \text{ sec}^{-1}$ )

ARL:UT  
 AS-81-832  
 GDI - GA  
 7-28-81



**FIGURE 30**  
**BUBBLE PULSE DELAYS OF MULTIPLE**  
**BOTTOM BOUNCE IMPULSE RESPONSE**  
 (244 m SOURCE)

ARL:UT  
 AS-81-833  
 GDI - GA  
 7-28-81



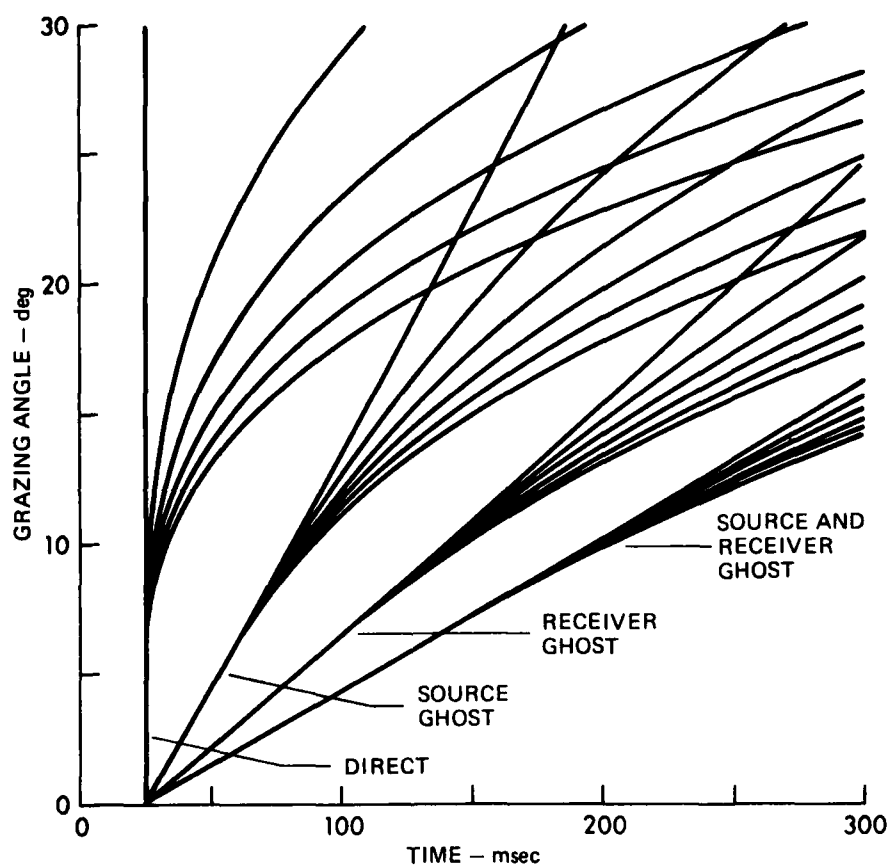


**FIGURE 31**  
**GHOST DELAYS OF MULTIPLE BOTTOM BOUNCE IMPULSE RESPONSE**  
 (244 m SOURCE, 498 m RECEIVER)

ARL:UT  
 AS-81-834  
 GDI - GA  
 7-28-81

receiver depths. The depths of the source and receiver were chosen in accordance with the nominal depths of the data that follow. Figure 32 shows the combination of all filtering effects: the source bubble pulses, ghosting effects, and the multiple bottom bounce impulse response.

Figure 33 shows data with nominal source and receiver depths of 244 and 498 m, respectively. A particular phase is aligned at 25 msec. Figure 34 shows that the aligned phase is probably not the first component of the acoustic signal. A precursor of the aligned arrival is observed with variable advance. The significance of this is that not all of the signal components will be delayed with respect to the aligned arrival at 25 msec.

Also in Fig. 34 a phase is identified that is delayed with respect to the peak aligned at 75 msec. This time delay seems to be a mirror image of the time delay of the precursor identified in Fig. 33. This gives credence to the existence of impulse response components with this time difference. Thus, delays between impulse response components apparently can be identified on aligned, otherwise unprocessed, acoustic signals. However, this time difference is more easily identified and interpreted using techniques which follow.

Returning to Fig. 33 it is seen that there are three trends of the acoustic energy on the time versus grazing angle plot. The first trend is located on a line rotated at about  $10^\circ$  with respect to the vertical; the second trend is located on a line rotated at about  $35^\circ$  with respect to the vertical, and the third trend is located on a line rotated about  $45^\circ$  with respect to the vertical. The first trend is due to refracted energy of the impulse response, while the other two trends are due to ghost energy.

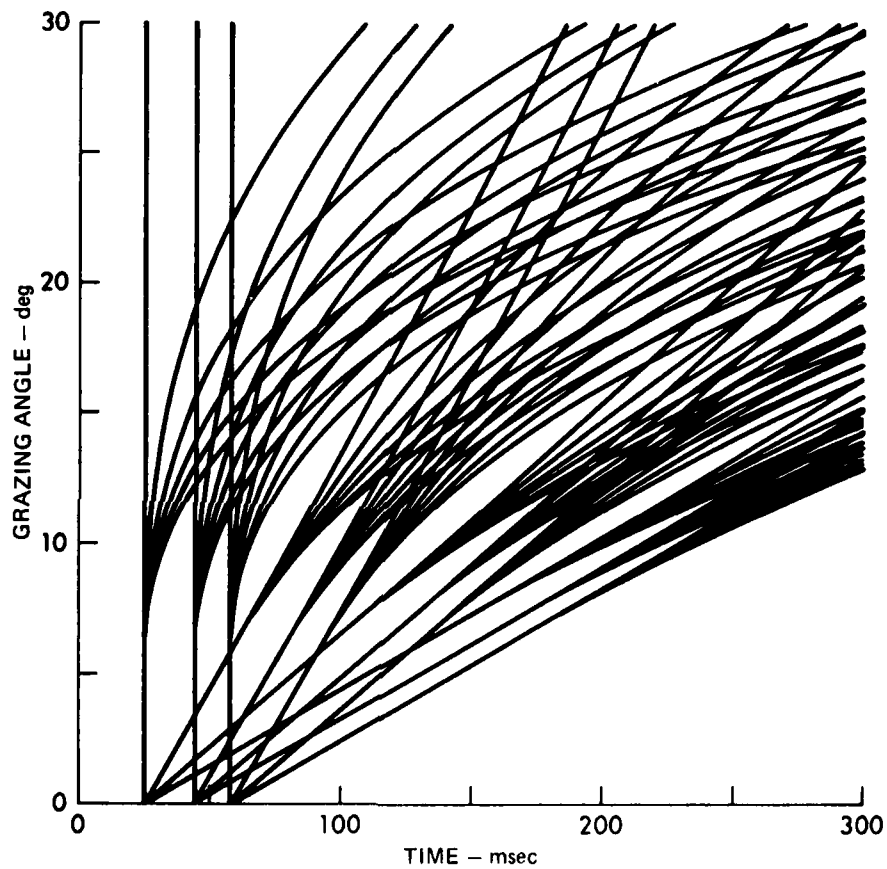


**FIGURE 32**  
**TRAVEL TIME versus GRAZING ANGLE PLOT**  
**OF TIME DELAYS BETWEEN MAIN ARRIVALS**  
**OF A 5 BB ACOUSTIC SIGNAL WITH A 244 m**  
**SOURCE AND 498 m RECEIVER**

ARL:UT  
 AS-81-835  
 GDI - GA  
 7-28-81

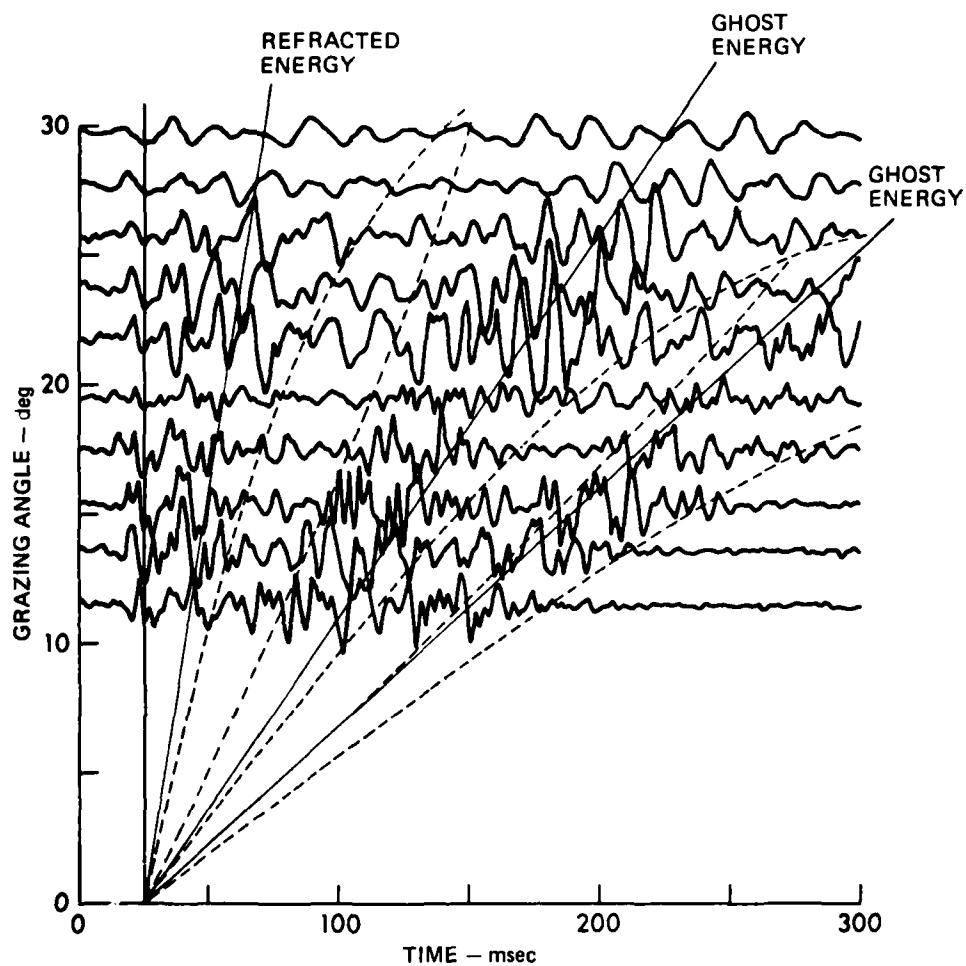
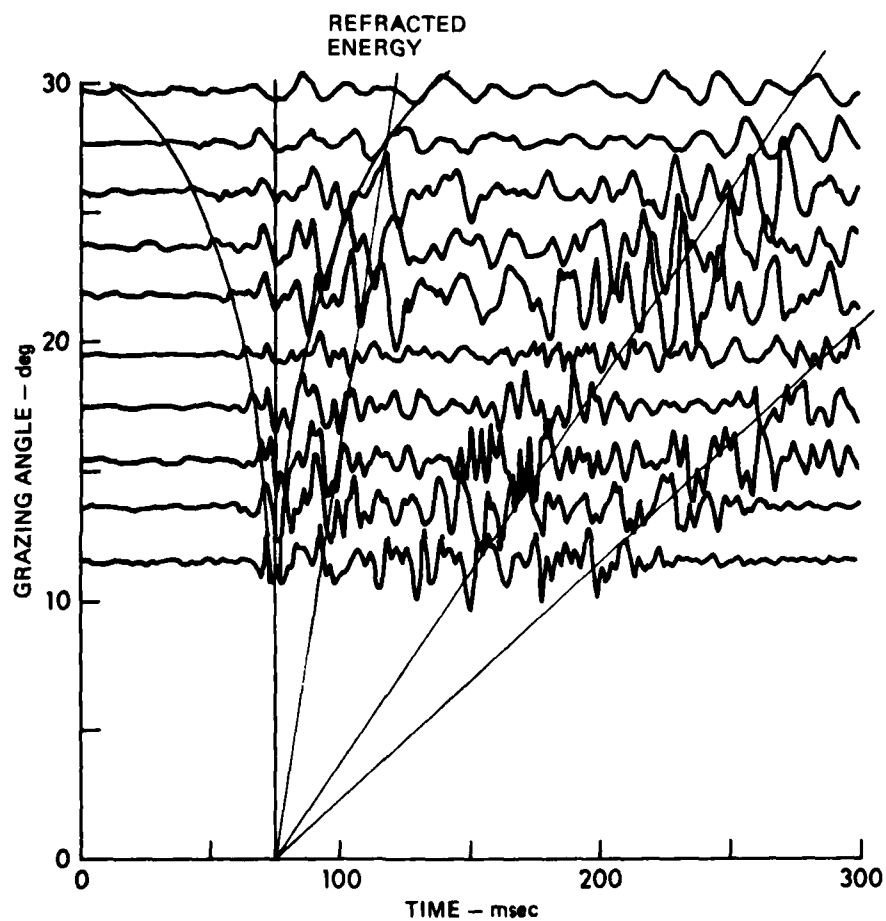


FIGURE 33  
SIX BOTTOM BOUNCE ACOUSTIC SIGNALS WITH 244 m SOURCE DEPTH  
AND NOMINAL 498 m RECEIVER DEPTH

ARL:UT  
AS-81-836  
GDI - GA  
7-28-81



**FIGURE 34**  
**SIX BOTTOM BOUNCE ACOUSTIC SIGNALS WITH 244 m SOURCE DEPTH**  
**AND 498 m NOMINAL RECEIVER DEPTH ALIGNED AT 75 msec TO**  
**REVEAL AT LEAST ONE ARRIVAL BEFORE THE ALIGNED ARRIVAL**

ARL:UT  
 AS-81-837  
 GDI - GA  
 7-28-81

Figure 35 shows the 6 BB data of Figs. 33 and 34 aligned at 25 msec with travel time curves associated with the five bottom ice impulse response ( $c_s/c_w=0.994$ ,  $g = 1.1 \text{ sec}^{-1}$ ), the source waveform, and the source and receiver ghosts. The 5 BB impulse response was used rather than the 6 BB response since at least one arrival has been tentatively identified before the aligned arrival. Thus, at least one component of the impulse response will not be delayed with respect to the aligned arrival. The nominal source and receiver depths were used to predict bubble pulse delays and source and receiver ghost delays.

From Fig. 35 it is seen that there are agreements and disagreements between the predicted travel times and the data. In particular, the vertical lines representing the bubble pulse delays of the aligned arrival agree with the bubble pulse periodicity seen in the data. Also, in agreement, the travel time curves for the source ghost overlies a significant trend of energy in the data. On the other hand, in disagreement, there is a large amount of acoustic energy predicted in the lower right hand corner of the plot where the data show none. Also, in disagreement, there is a large arrival at about 90 msec at  $30^\circ$  grazing angle that is not predicted by the travel time curves. The first disagreement is due to the fact that the nominal receiver depth is in error. The second disagreement is probably due to the fact that the a priori choice of gradient is in error.

Figure 36 shows data recorded at the same receiver, but due to an 18 m source. The advantage of the 18 m data is in the identification of filter components such as the receiver ghost and the bubble pulses. Thus, with the 18 m source data it will be easier to show that the nominal

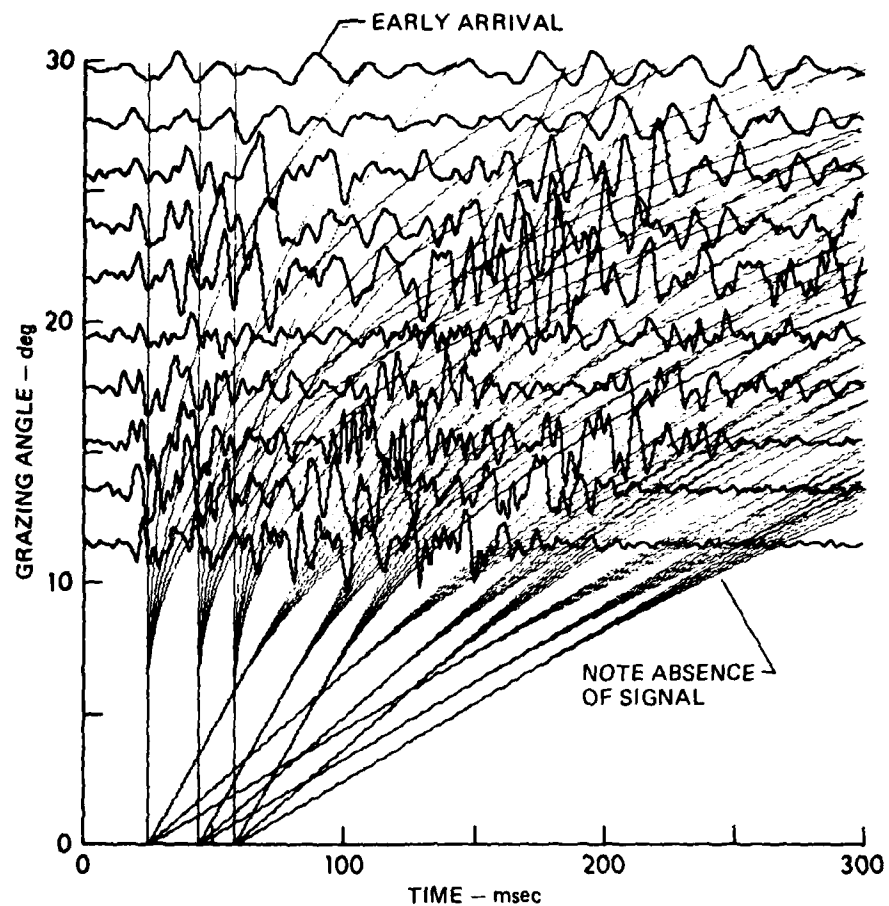


**FIGURE 35**  
**SIX BOTTOM BOUNCE ACOUSTIC SIGNALS WITH**  
**PREDICTED DELAYS BETWEEN MAIN ARRIVALS**  
**ASSUMING NOMINAL SOURCE RECEIVER DEPTHS**

ARL:UT  
 AS-81-838  
 GDI - GA  
 7-28-81

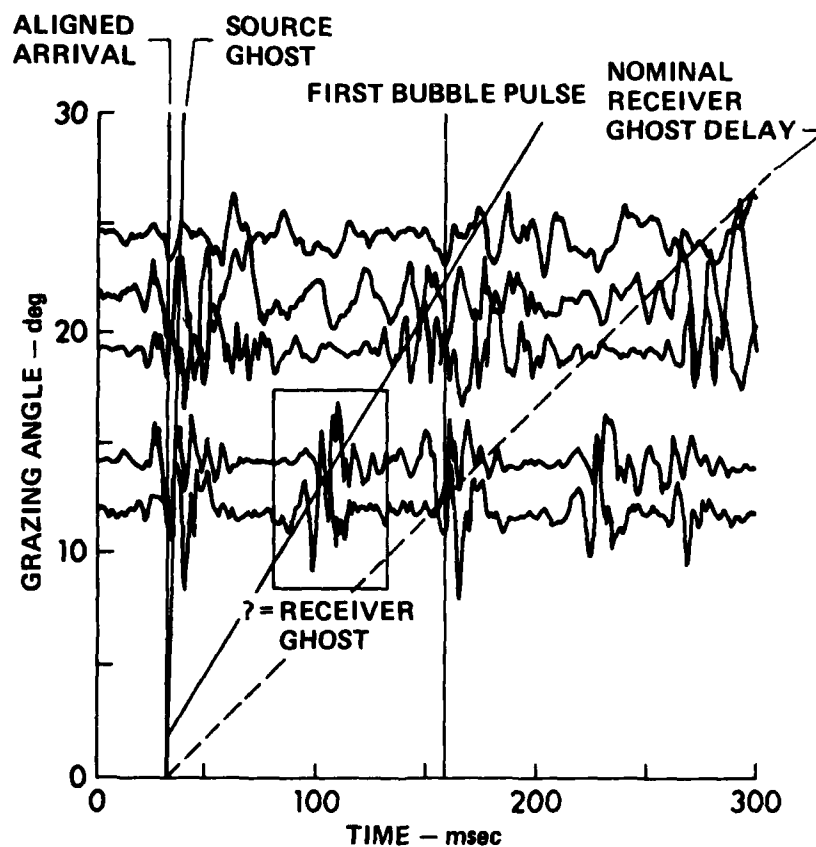


FIGURE 36  
FIVE BOTTOM BOUNCE ACOUSTIC SIGNALS  
WITH 18 m SOURCE DEPTH AND NOMINAL  
498 m RECEIVER DEPTH

ARL:UT  
AS-81-330  
GI-GA  
3-4-81



receiver depth at this site is in error and that the bubble pulse delays can be identified in the data. To identify the first bubble pulse, for instance, it is seen that the negative lobe of the signal at  $25^{\circ}$  aligned at  $\sim 33$  msec is duplicated at 160 msec. Also the arrival aligned at  $\sim 33$  msec for the  $12^{\circ}$  signal is duplicated at  $\sim 158$  msec. Thus, the first bubble pulse is identified at  $\sim 158$  msec, a delay of  $\sim 125$  msec, which is close to the theoretical value. This indicates that the source was, in fact, detonated at a depth near 18 m. Next it will be shown that the receiver depth at this site is in error. The source ghost delay for an 18 m source is shown on Fig. 36 and the nominal receiver ghost delay is also shown. Since the receiver ghost has reflected from the air-water interface one time, it is of a phase opposite to the arrival that has not been reflected from the air-water interface. Therefore, since the first bubble pulse will have approximately the same amplitude and the same phase as the shock pulse, then, for the signal at  $12^{\circ}$ , the arrival at  $\sim 150$  msec should be almost canceled to zero. But it is not. Also the absence of an arrival at about 230 msec for the signal at  $19^{\circ}$  is clear evidence that the nominal receiver depth is in error.

The arrivals shown in the box in Fig. 36 are also unexplained using the nominal source and receiver depths. These arrivals are nearly the same amplitude as the aligned arrivals and careful observation leads to the conclusion that they are opposite in phase. It can also be seen for the signal at  $19^{\circ}$  that the aligned arrival is duplicated with opposite phase at about 140 msec. Thus, it is concluded that the line through these arrivals is approximately the line of the receiver ghost. This corresponds to a receiver depth of about 255 m.

Using this new, empirically derived receiver depth, travel time curves for the data with 244 m sources are shown in Fig. 37. This shows good agreement with the data except for the early arrival mentioned previously. If the model of the ocean bottom as a specular reflection and a refracted component is accurate, this arrival indicates that the sound speed versus depth increases more rapidly than the first order prediction of  $g \approx 1.1 \text{ sec}^{-1}$ .

In summary, this section has shown that trends of acoustic energy can be identified (n) travel time versus grazing angle plots of acoustic signals when a particular phase is aligned. The interpretation of these trends is facilitated by constructing travel time curves of the filter components of the signal and overlaying these travel time curves on the data.

Overlaying the travel time curves on the data can also reveal inconsistencies between nominal source and/or receiver depths and a priori estimates of geoacoustic structure. The true depth of the source and/or receiver can be measured from the aligned data. These measurements can be greatly facilitated by the proper choice of experimental geometry. And, in fact, clear and unambiguous identification of filter components is possible for some experimental geometries. Good estimates of geoacoustic structure from aligned data can also be greatly facilitated by carefully chosen experimental geometry.

In the next section correlation techniques will be used to measure delays in the acoustic signals as a function of grazing angle. The main advantage of these techniques is that the correlations are

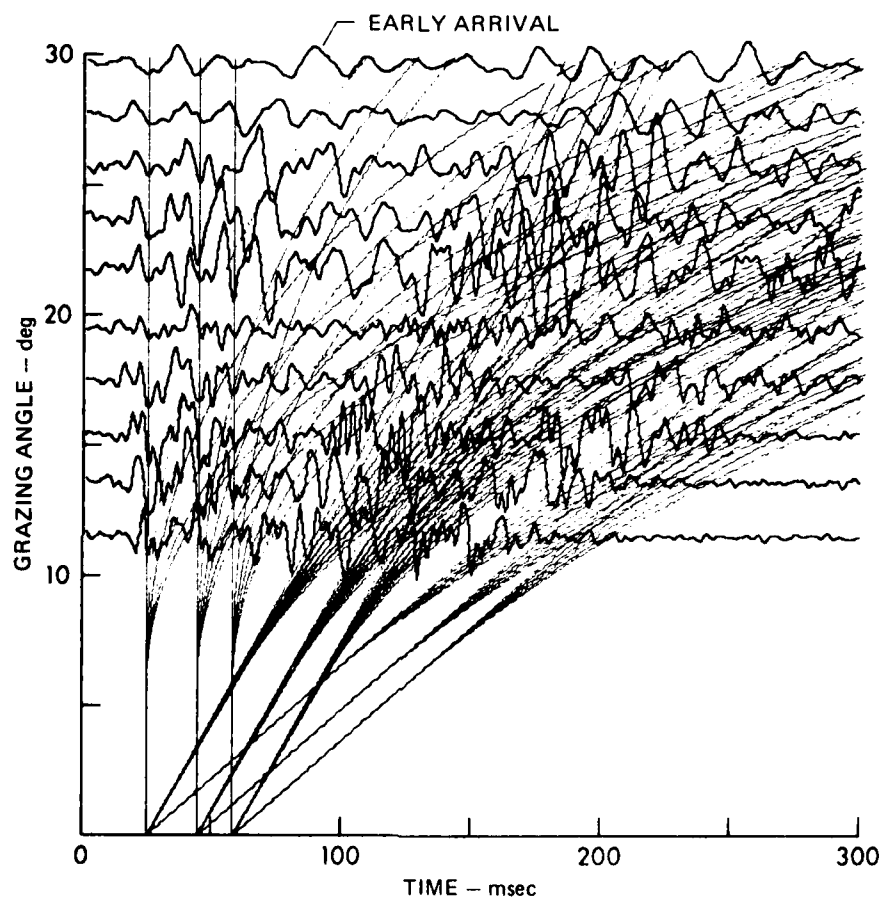


FIGURE 37  
SIX BOTTOM BOUNCE ACOUSTIC SIGNALS WITH PREDICTED DELAYS BETWEEN  
MAIN ARRIVALS ASSUMING NOMINAL SOURCE DEPTH (244 m) AND RECEIVER  
DEPTH CALCULATED FROM 18 m SOURCE DATA

ARL:UT  
AS-81-840  
GDI - GA  
7-28-81

self-aligned with respect to the zero lag value and the delays between convolutional components are more readily seen and measured.

## CHAPTER 3

### CORRELATION TECHNIQUES

#### 3.1 Correlation for Time Delay Detection

Originally, when this research was begun, it was thought that the ocean bottom transfer function could be described by the two-component model of a specularly reflected and a refracted arrival. In this case, if the time delay between these components could be found as a function of grazing angle, then velocity as a function of depth into the ocean bottom could be determined. Since the power cepstrum had been found to be useful for time delay detection of bubble pulses (Mitchell et al., 1976), it was thought that for some experimental geometries and geoaoustic structures it would also be useful in extracting the delay between the reflected and refracted components.

Later it was also decided to attempt to use the autocorrelation for detection of the impulse response delays. The autocorrelation has the advantage that it has the superposition property with respect to convolution while the cepstrum does not [i.e.,  $AC(x*y)=AC(x)*AC(y)$ ]. The power cepstrum does not have the superposition property with respect to convolution due to a logarithm operation (see Appendix II). The effect of the logarithm operation in the calculation of the power cepstrum is to give peaks at all sum and difference delays as well as at the delays in the signal. In addition, there will be peaks on the power cepstrum at all multiples of the delays in the signal and at all multiples of the sum and difference delays.

This produces a complicated pattern of cepstral components with amplitudes that are not readily predicted. Thus, the autocorrelation is initially preferred over the power cepstrum, since the superposition property allows for the amplitude and time arrival of interfering components to be more easily predicted.

### 3.2 Theory of the Autocorrelation

The autocorrelation is simply an autoconvolution in which neither of the component factors are reversed before integration. Figure 38 illustrates the value of the autocorrelation of  $f(u)$  at the point  $x$ . The autocorrelation is defined by the integral

$$P_{ff}(x) = \int_{-\infty}^{\infty} f(u) f(u-x) du \quad ,$$

which is clearly the area of the product of the function  $f$  with a shifted version of itself by the amount  $x$ . Substituting  $w=u-x$ , we have also

$$P_{ff}(x) = \int_{-\infty}^{\infty} f(w+x) f(w) dw \quad ,$$

so

$$P_{ff} = \int_{-\infty}^{\infty} f(u) f(u+x) du = \int_{-\infty}^{\infty} f(u) f(u-x) du \quad .$$

Thus, it does not matter in which direction the function is shifted to calculate the autocorrelation. This means that, if  $f$  is real, then its autocorrelation  $P_{ff}$  is even.

Another property of the autocorrelation function is that phase information is lost. This is most easily shown by considering its Fourier transform. A time signal is a real function, and therefore its

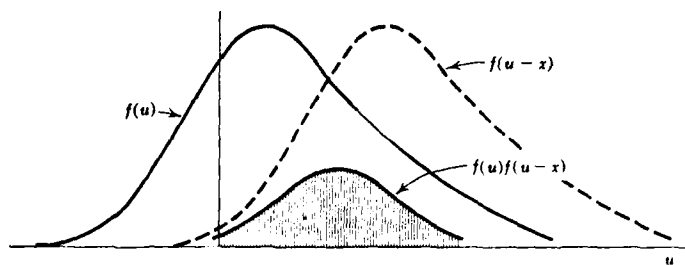


FIGURE 38  
 THE AUTOCORRELATION FUNCTION  $P_{xx} = \int_{-\infty}^{\infty} f(u) f(u-x) du$   
 IS REPRESENTED AS AN AREA IN THE FIGURE ABOVE

[Reproduced from Bracewell (1978)]

autocorrelation is even and its Fourier transform degenerates to the cosine transform which is real and even, i.e.,

$$\begin{aligned} \overline{P_{ff}(x)} &= 2 \int_0^{\infty} P_{ff}(x) \cos(2\pi xs) dx \\ &\quad - 2i \int_0^{\infty} P_{ff}(x) \sin(2\pi xs) dx \quad . \end{aligned}$$

The second integral goes to zero so the Fourier transform of the autocorrelation has no imaginary part and the phase information of the original function,  $f$ , is lost.

Finally, two other comments are warranted about the use of the autocorrelation in this work. First, the autocorrelation has the superposition property with respect to convolution: the autocorrelation of the convolution of two functions is equal to the convolution of the autocorrelations of the functions (see Appendix II). This means that the effects of coherent noise such as bubble pulses and ghosts are more easily recognized and predicted. Second, for a time series with echoes or distorted echoes, it would be expected that a contribution to the autocorrelation will occur at the time shifts corresponding to the echo delays, and, although the phase information is lost, the effect of distortion such as 90 or 180° phase shifts are apparent in the sign and shape of the autocorrelation peaks at the corresponding time delays.

### 3.3 Theory of the Power Cepstrum

The power cepstrum is the power transform of the log power spectrum of a function. The significance of this function is shown in the



following. Consider a time function which has a single echo (Kemerait, 1972).

$$x(t) = s(t) + a_0 s(t-t_0) \quad . \quad (3.3.1)$$

The power spectrum of  $x(t)$  can be written

$$\phi_x(\omega) = \phi_s(\omega) \left[ 1 + a_0^2 + 2a_0 \cos \omega t_0 \right] \quad , \quad (3.3.2)$$

and the logarithm of both sides is

$$\log(\phi_x(\omega)) = \log \phi_s(\omega) + \log \left[ 1 + a_0^2 + 2a_0 \cos \omega t_0 \right] \quad . \quad (3.3.3)$$

For  $a_0 < 1$  the second term can be approximated by  $2a_0 \cos \omega t_0$ . Thus, if  $s(t)$  is an impulse, then the log power spectrum is essentially a cosinusoidal ripple for  $a_0 \ll 1$ . The power transform of  $\log(\phi_x(\omega))$  produces a spike at the quefreny,  $t_0$ , of the ripple ( $t_0$  is the reciprocal period of the sinuosoid appearing on the log power spectrum, measured in quefrencies). In the case where  $a_0$  is not much less than one, additional terms of the series expansion are required which add spikes to the power cepstrum at integral multiples of  $t_0$ . Essentially, the same results apply for  $a_0 \gg 1$  which can be shown by dividing the second term of Eq. 3.3.2 by  $a_0^2$ . This yields

$$\phi_x(\omega) = a_0^2 \phi_s(\omega) \left[ 1 + \frac{1}{a_0^2} + \frac{2}{a_0} \cos \omega t_0 \right] \quad .$$

As  $a_0$  approaches one, the presence of multiple quefrencies is more apparent.

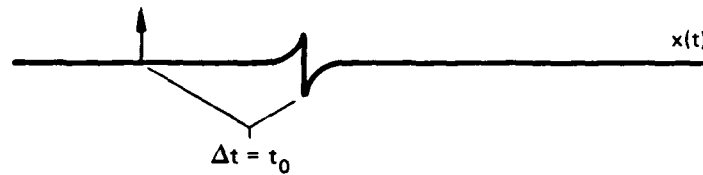
To use the power cepstrum for detecting time delays within the acoustic signals discussed in this thesis, at least two complicating effects must be considered. First, for the time delay of interest the delayed arrival has been distorted by a  $90^\circ$  phase shift. Figure 39 shows that the effect of this is to produce an even, negative sinusoidal ripple in the log power spectrum rather than a positive cosinusoidal ripple. Since the power transform of a sinusoid simply gives a spike at the frequency (or quefrequency) of the sinusoid, the power cepstrum will be unaffected by the  $90^\circ$  phase shift of the refracted component.

Second, the acoustic signals will have multiple echoes (i.e., multiple bottom bounce impulse response components, bubble pulses, and ghosts). This will have the effect of ripples in the log power spectrum at the quefrequencies associated with each delay and at all difference delays. This is complicated by the modulating effect of beating between these quefrequencies. This beating between quefrequencies is the nonlinear effect of the power cepstrum operation, giving values on the power cepstrum at all sum and difference delays.

Although, theoretically, the fact that the absolute value of the ghost amplitudes is nearly one would seem to negate the usefulness of time delay detection by the power cepstrum technique, this does not appear to be the case as shown for the synthetic and real acoustic signals that follow.

### 3.4 Synthetic Results

In this section it is attempted to model acoustic signals and their correlations for a range of relative source-receiver geometries. Figure 40 is a flowchart illustrating the format of the plots that illustrate the results. The acoustic signal is modeled in time with the



$$x(t) = s(t) + [a_0 s(t-t_0) * -\frac{1}{\pi t}]$$

$$x(t) = s(t) * [\delta(t) + a_0 \delta(t-t_0) * -\frac{1}{\pi t}]$$

$$X(f) = S(f) [1 + (a_0 e^{i\omega t_0}) (\text{isgnf})]$$

$$\Phi_{xx}(f) = \Phi_{ss}(f) [1 + (a_0 e^{i\omega t_0}) (\text{isgnf})] [1 - (a_0 e^{-i\omega t_0}) (\text{isgnf})]$$

$$= \Phi_{ss}(f) [1 + (\text{isgnf}) (2a_0) (i \sin \omega t_0) - a_0^2 (\text{isgnf})^2]$$

$$= \Phi_{ss}(f) [1 - 2a_0 (\text{sgnf}) \sin \omega t_0 + a_0^2]$$

$$\log \Phi_{xx}(f) \approx \log \Phi_{ss} - 2a_0 (\text{sgnf}) \sin \omega t_0$$

$$\text{if } s(t) = \delta(t) \text{ and } 0 < a_0 \neq 1$$

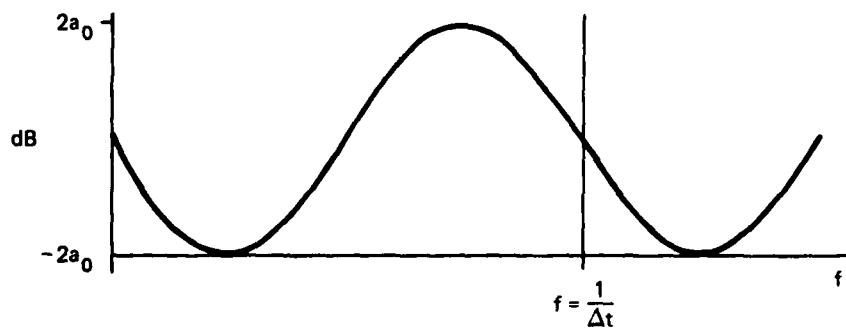
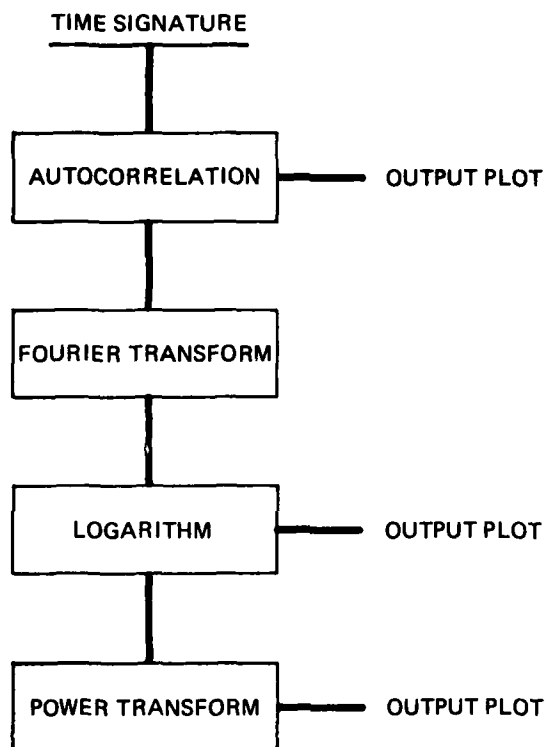


FIGURE 39  
DERIVATION OF LOG POWER SPECTRUM OF  
DELAYED PULSE WITH 90° PHASE SHIFT



**FIGURE 40**  
**BLOCK DIAGRAM SHOWING FLOWCHART OF THE CALCULATION**  
**OF THE AUTOCORRELATION, LOG POWER SPECTRUM, AND**  
**POWER CEPSTRUM OF A SIGNAL**

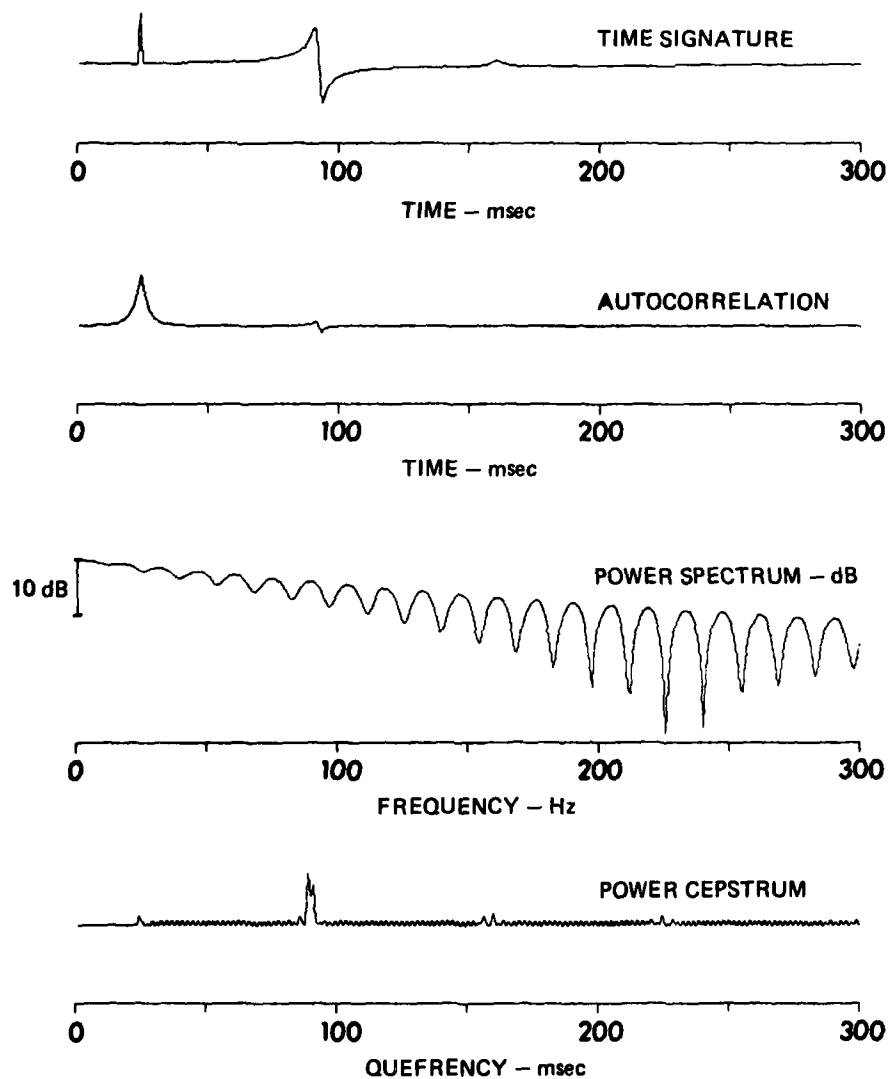
appropriate bubble pulses and ghosting effects. The synthesized waveform was derived by the method discussed in Section 1.5.

Figure 41 shows the impulse response at  $26^\circ$  predicted using the geoacoustic model shown in Table II. It is seen that there are two main components and a smaller component. The specular reflection is the first arrival, with an amplitude of about 0.25 of the incident wave. The refracted component has a  $90^\circ$  phase shift and has undergone some attenuation. The third component is a refracted wave which has reflected once from the underside of the water-sediment interface, has undergone a total of a  $360^\circ$  phase shift, and has undergone twice the attenuation of the refracted arrival (recall Fig. 16). The specular reflection was aligned at 25 msec.

The autocorrelation shown beneath the time signal reveals that an arrival which is similar in shape to the refracted waveform occurs in the autocorrelation. The middle-zero crossing of this arrival is the time delay between the reflected and refracted components. Note that the zero lag value of the autocorrelation is aligned at 25 msec.

The log power spectrum beneath the autocorrelation has some interesting features. First, the dropoff of power with increasing frequency is essentially the dropoff due to attenuation along the refracted path. It is seen that there is also a very low frequency ripple on the log power spectrum which overlies the linear dropoff due to attenuation. This low frequency component may be due to the apparent time delay between the positive and negative lobes of the refracted arrival.

The amplitude of the higher frequency ripple in the log power spectrum is frequency dependent. This is not unexpected because



**FIGURE 41**  
**TIME SIGNATURE, AUTOCORRELATION, POWER SPECTRUM, AND POWER**  
**CEPSTRUM FOR PLANE WAVE IMPULSE RESPONSE, ( $\theta_g = 26^\circ$ )**

TABLE II  
GEOACOUSTIC MODEL FOR FIGS. 41-48

<u>Depth</u> <u>(m)</u>	<u>Velocity</u> <u>(m/sec)</u>	<u>Attenuation</u> <u>(dB/m-kHz)</u>	<u>Density</u> <u>(g/cm<sup>3</sup>)</u>
0 <sup>-</sup>	1515		1.0
0 <sup>+</sup>	1515	0.02	1.7
1000 <sup>-</sup>	2515	0.02	2.4
1000 <sup>+</sup>	5200	0.01	2.5

attenuation has been included in the model. At low frequencies the refracted energy is not attenuated and  $a_0$  is much greater than one and the ripple is small. At higher frequencies the attenuation is greater,  $a_0$  approaches one, and the amplitude of the ripple increases. Eventually, a frequency is reached where the refracted energy is attenuated below the level of the reflected arrival. At this point the amplitude of the ripple begins to decrease since it is directly proportional to  $a_0$ , which decreases.

The power cepstrum of the signal shown in Fig. 41 shows that the time delay of interest is easily detected. Zero quefreny is located at 25 msec. The value of the time delay will be at the center of the two peaks at about 90 msec ( $t_0 = 65$  msec). Large cepstral peaks would also occur at the low quefrencies due to attenuation, but have been muted for the purposes of detecting the reflection-refraction delay. The first three samples of the power cepstrum are zeroed on this and all other power cepstrum plots with the exception of Fig. 53.

Figure 42 shows the effect of adding a 244 m source to the previous impulse response. It is seen that, although the impulse response is highly distorted, the time delay of interest at about 90 msec in the autocorrelation occurs with little distortion.

The effect of the source on the log power spectrum and power cepstrum is shown in Fig. 42 as well: significant new ripples associated with the first and second bubble pulses are shown in the log power spectrum. These ripples show up as spikes on the power cepstrum plot at the bubble pulse delays of about 19 and 33 msec. No significant beating between quefrencies is observed, but the amplitude of the peak associated



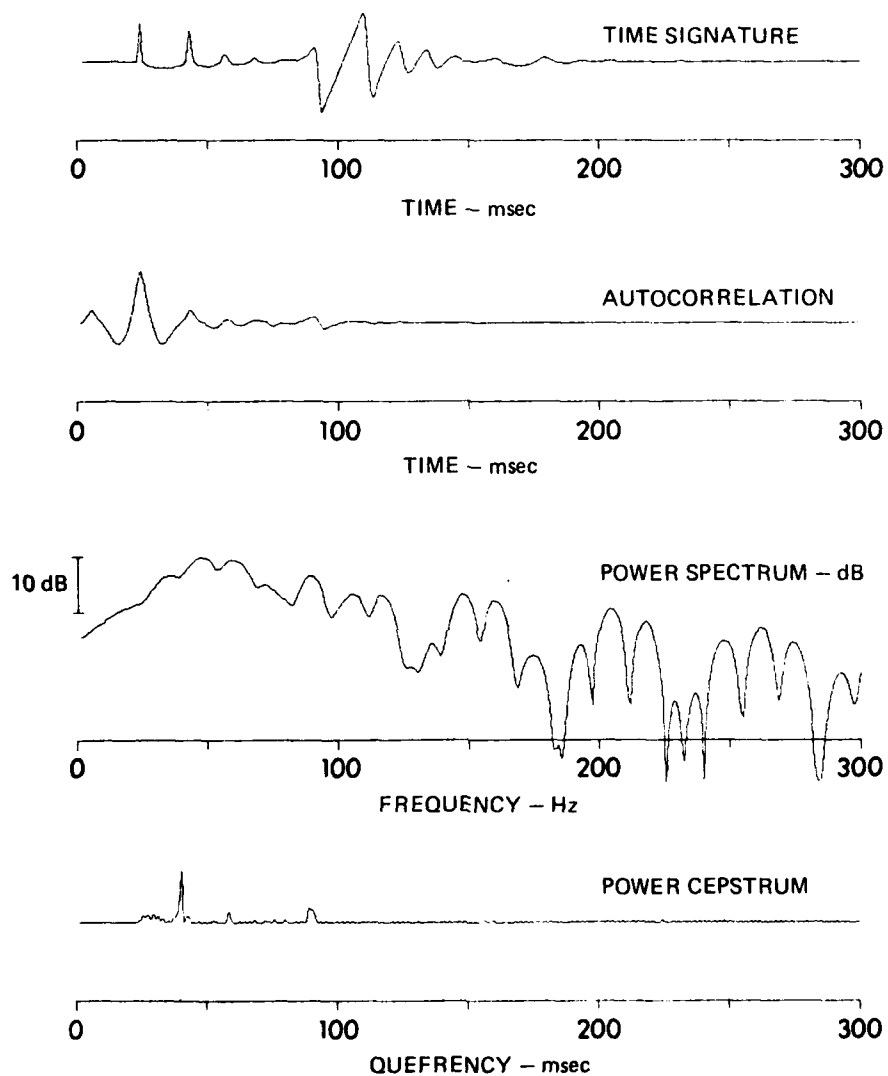


**FIGURE 42**  
**TIME SIGNATURE, AUTOCORRELATION, POWER SPECTRUM, AND**  
**POWER CEPSTRUM OF PLANE WAVE IMPULSE RESPONSE**  
**CONVOLVED WITH SOURCE WAVEFORM (244 m SOURCE)**

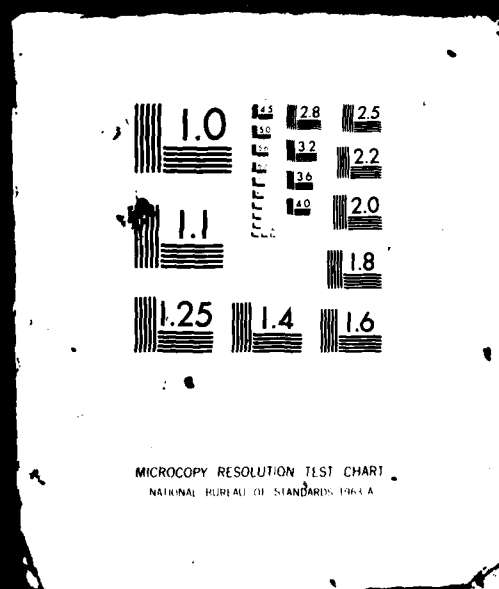
with the refracted arrival is diminished from the simple impulse response for the power cepstrum.

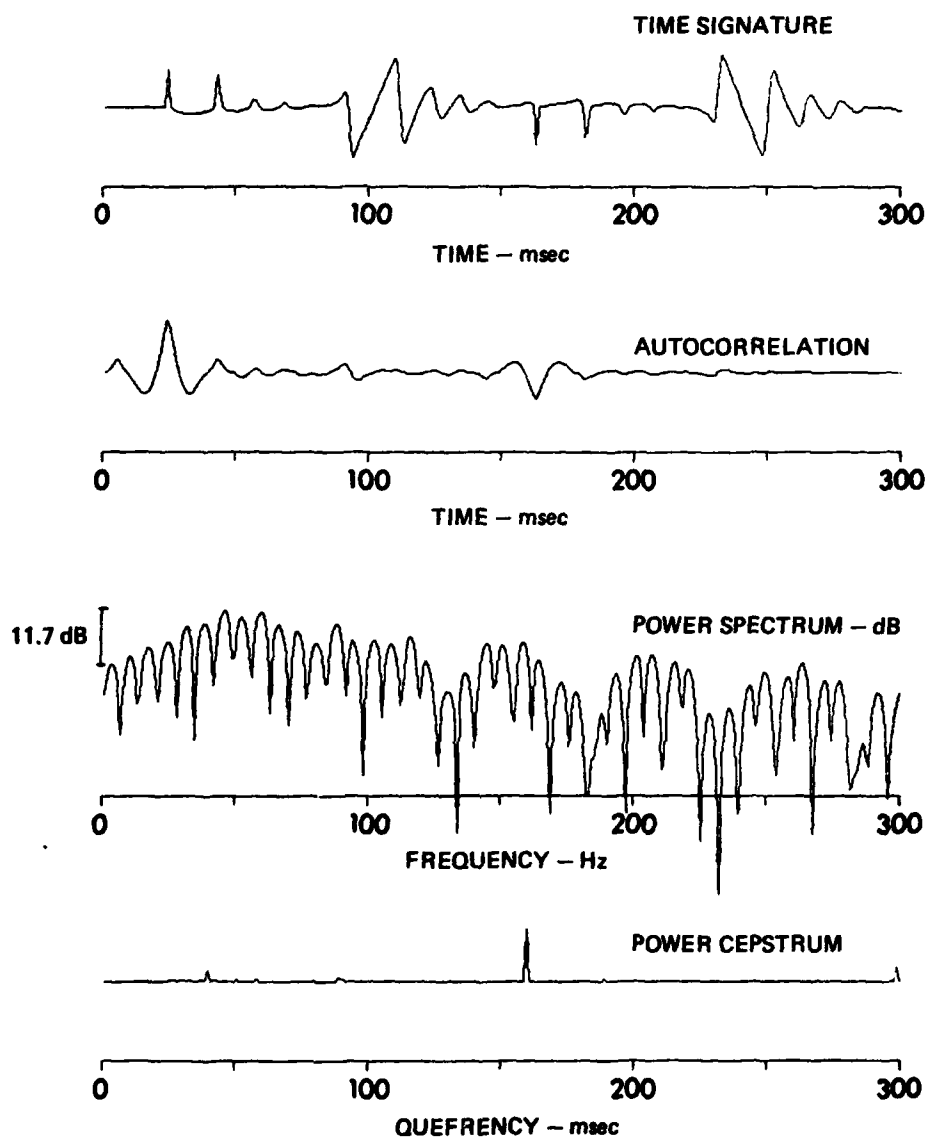
Figure 43 shows the effect of adding the 244 m ghost. No significant distortion is added to either the time or autocorrelation plots. The time delay is equally well defined in this figure as compared to Fig. 42. On the other hand, the high quefreny ripple associated with the source ghost dominates both the log spectrum and power cepstrum. The power cepstrum of this figure indicates that trace to trace adjustment of amplitude may be necessary to maximize the visibility of the desired delay. Unfortunately, the optimum trace to trace adjustment is probably difficult to predict since it is due to the complicated beating pattern of quefrenies associated with the experiment geometry and geoacoustic structure of the ocean bottom. In addition to the reduction of amplitude of the desired delay peak due to the beating of quefrenies, there appears to be a relative amplification of cepstral peaks other than the reflected-refracted peak.

Figure 44 shows the effect of including a receiver ghost and a source plus receiver ghost to the signal. In this case a shallow (75 m) receiver was chosen to observe the effect of adding a ghost between the reflected and refracted components. It is seen that this geometry (or arrival structure) considerably obstructs identification of the reflected-refracted delay. For the time, autocorrelation, and log spectrum displays, it is virtually impossible to detect the reflected-refracted delay. For the power cepstrum this is very unlikely, but perhaps on the two-dimensional  $T-\theta$  plot the arrival could be identified. The two boxed arrivals are of particular concern because they are nearly as large as the



2 OF 3  
AD-  
A11 2708





**FIGURE 43**  
**TIME SIGNATURE, AUTOCORRELATION, POWER SPECTRUM, AND POWER**  
**CEPSTRUM OF PLANE WAVE IMPULSE RESPONSE CONVOLVED WITH**  
**SOURCE WAVEFORM AND SOURCE GHOST RESPONSE**

ARL:UT  
 AS-81-830  
 GDI - GA  
 8-5-81

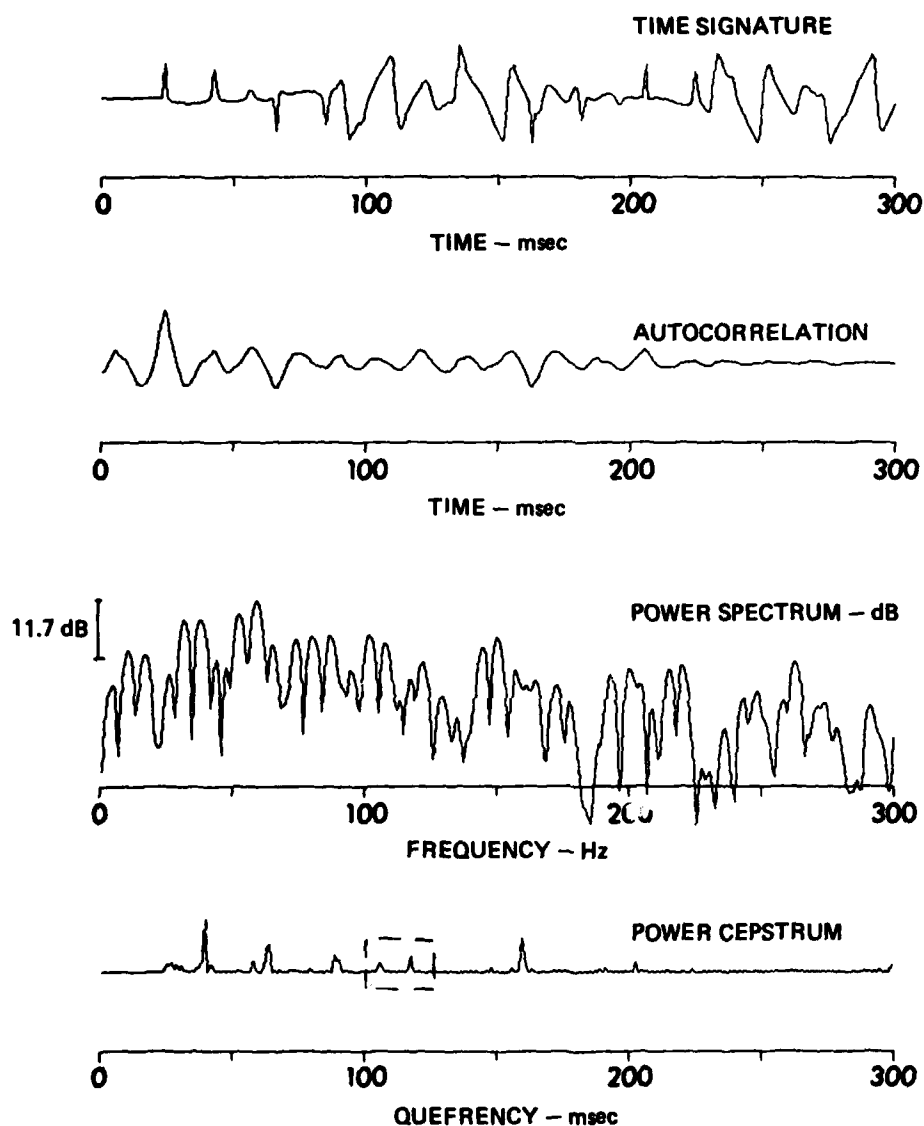
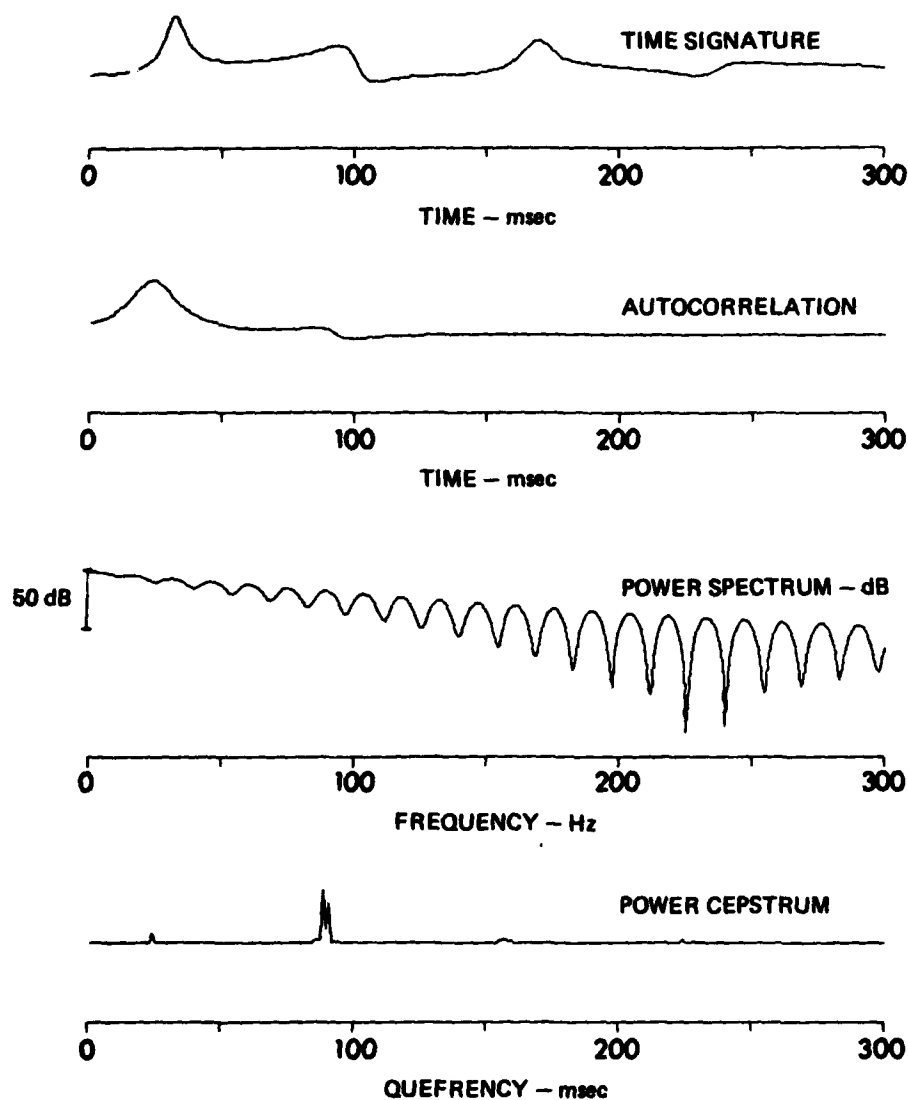


**FIGURE 44**  
**TIME SIGNATURE, AUTOCORRELATION, POWER SPECTRUM, AND POWER**  
**CEPSTRUM OF PLANE WAVE IMPULSE RESPONSE CONVOLVED WITH**  
**SOURCE WAVEFORM AND TOTAL GHOST RESPONSE (75 m RECEIVER)**

refracted arrival, but have no obvious explanation in terms of signal filter components. Actually they are beats between the other quefrequency components.

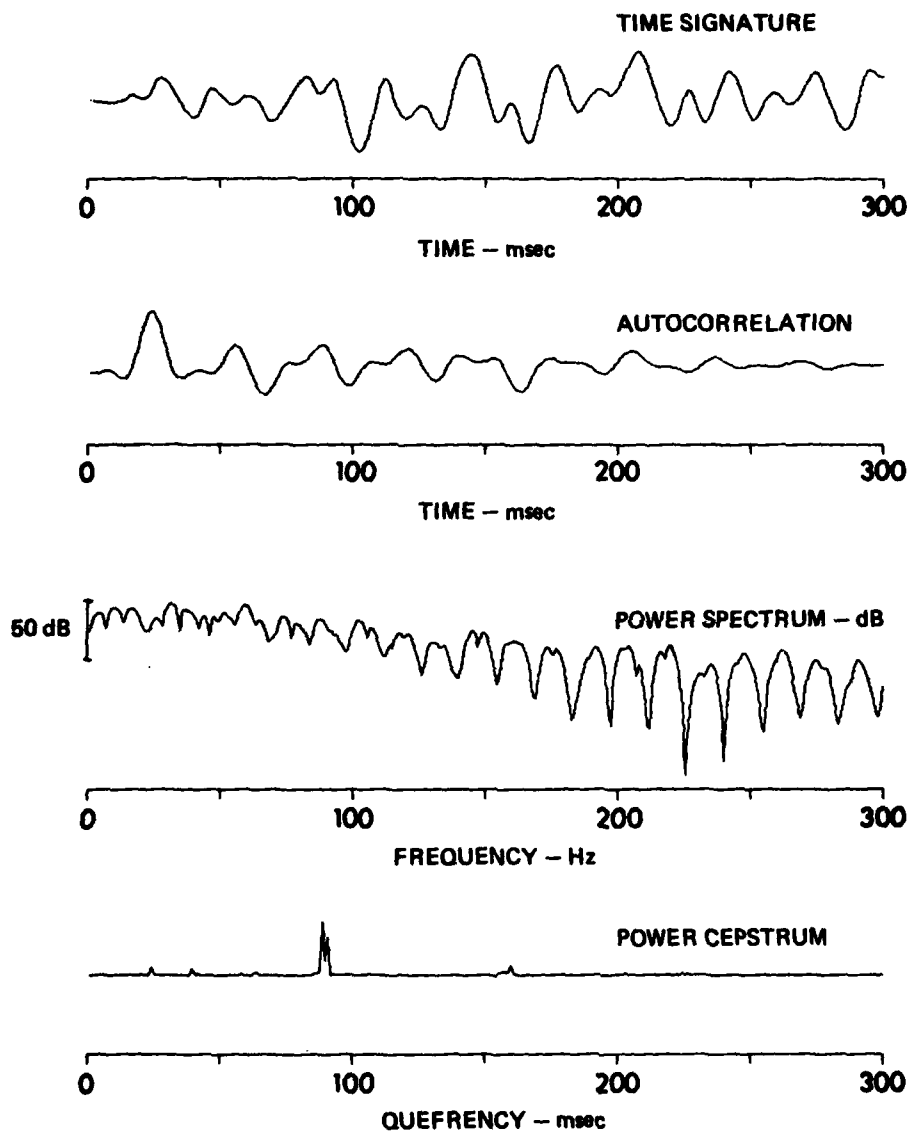
Since we often study acoustic signals that have interacted with the bottom a number of times, Fig. 45 illustrates the effect of a five bottom bounce impulse response. There is no ambiguity of the time delay associated with the reflected and refracted components in any of the figures. The greater attenuation due to more bottom refractions is evident on the time, autocorrelation, and log power spectrum. Note that the time signature and autocorrelation plots are smeared in time and the dynamic range of the log power spectrum is increased by five times. The attenuation due to the five bottom interactions of the signal shown in Fig. 45 provides a good illustration of the major advantage of the power cepstrum technique over the autocorrelation. This advantage is that the power cepstrum gives a spike at the reflection-refraction delay rather than a pulse with the crosspower spectrum of the reflected and refracted components. Thus, the power cepstrum has much greater resolving power of individual impulse response components than the autocorrelation.

Figure 46 shows the effect of a five bottom bounce signal with the source and receiver depths as in Fig. 44. It is seen that the capability of measuring the desired delay is reduced for the time plot, but dramatically improved for the autocorrelation and power cepstrum. The low pass earth filtering apparently has bolstered the reflection-refraction delay at the expense of the bubble pulse delay in the autocorrelation. This is due to greater high frequency content in the bubble pulse than in the refracted arrival. So, since attenuation is linearly dependent on



**FIGURE 45**  
**TIME SIGNATURE, AUTOCORRELATION, POWER SPECTRUM, AND**  
**POWER CEPSTRUM OF 5 BOTTOM BOUNCE PLANE WAVE**  
**IMPULSE RESPONSE ( $\theta_0 = 26^\circ$ )**





**FIGURE 46**  
**TIME SIGNATURE, AUTOCORRELATION, POWER SPECTRUM, AND**  
**POWER CEPSTRUM OF 5 BOTTOM BOUNCE PLANE WAVE IMPULSE**  
**RESPONSE CONVOLVED WITH SOURCE WAVEFORM AND TOTAL**  
**GHOST RESPONSE (244 m SOURCE, 75 m RECEIVER)**

frequency, low frequencies are preferentially passed for each bottom interaction while the high frequencies are attenuated.

The amplitude of the reflection-refraction delay is also greatly amplified with respect to other components on the power cepstrum plot as well. This is due to the fact that for synthetic signals we have infinite dynamic range, and adjacent frequency bands are affected by the attenuation in the subbottom five times as much for the five bounce signal as the one bounce signal ( $\log R^5(\omega) = 5 \log R(\omega)$ ). Thus, the amplitude of the ripples associated with the reflected-refracted delay is five times greater for the five bottom bounce signal than the one bottom bounce signal, and this effect is seen in the power cepstrum.

Figure 47 shows the effects on the time plots and frequency plot of a five bottom bounce signal with a 244 m source and a 400 m receiver. This greatly improves the ability to detect the reflected-refracted time delay in both the time and autocorrelation plots. The ability of the power cepstrum to measure the time delay of interest is about the same. In general the ability of the autocorrelation and power cepstrum to detect delays between impulse response components is greatly dependent on the source-receiver geometry.

Finally, Fig. 48 shows the time plots and frequency plot for the source-receiver geometry empirically verified in Chapter 2 for some real data. It is shown that the reflected-refracted time delay is clearly identifiable in all plots.

The geoacoustic structure also affects the ability of the autocorrelation and power cepstrum for time delay detection. Figure 49 shows an impulse response at  $26^\circ$  with an ocean bottom with the geoacoustic

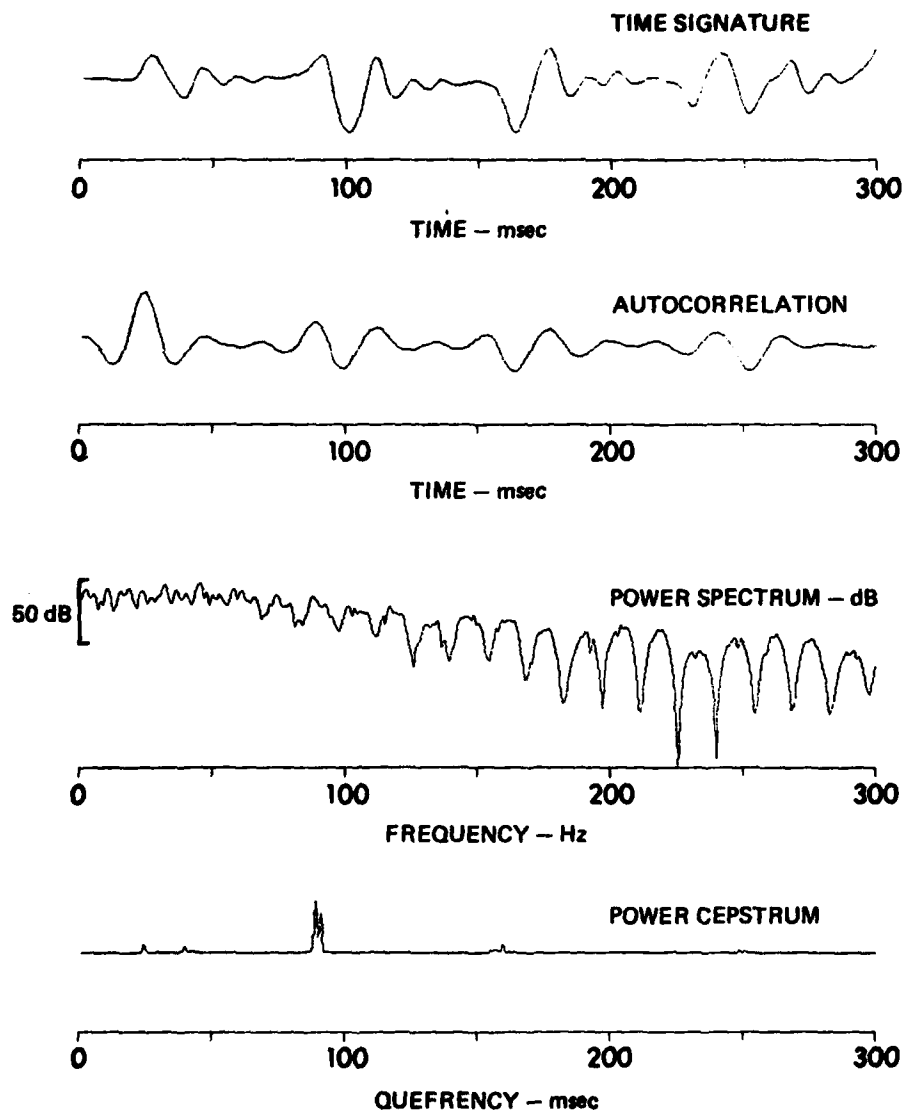


**FIGURE 47**  
**TIME SIGNATURE, AUTOCORRELATION, POWER SPECTRUM, AND**  
**POWER CEPSTRUM OF 5 BOTTOM BOUNCE PLANE WAVE IMPULSE**  
**RESPONSE CONVOLVED WITH SOURCE WAVEFORM AND TOTAL**  
**GHOST RESPONSE (244 m SOURCE, 400 m RECEIVER)**

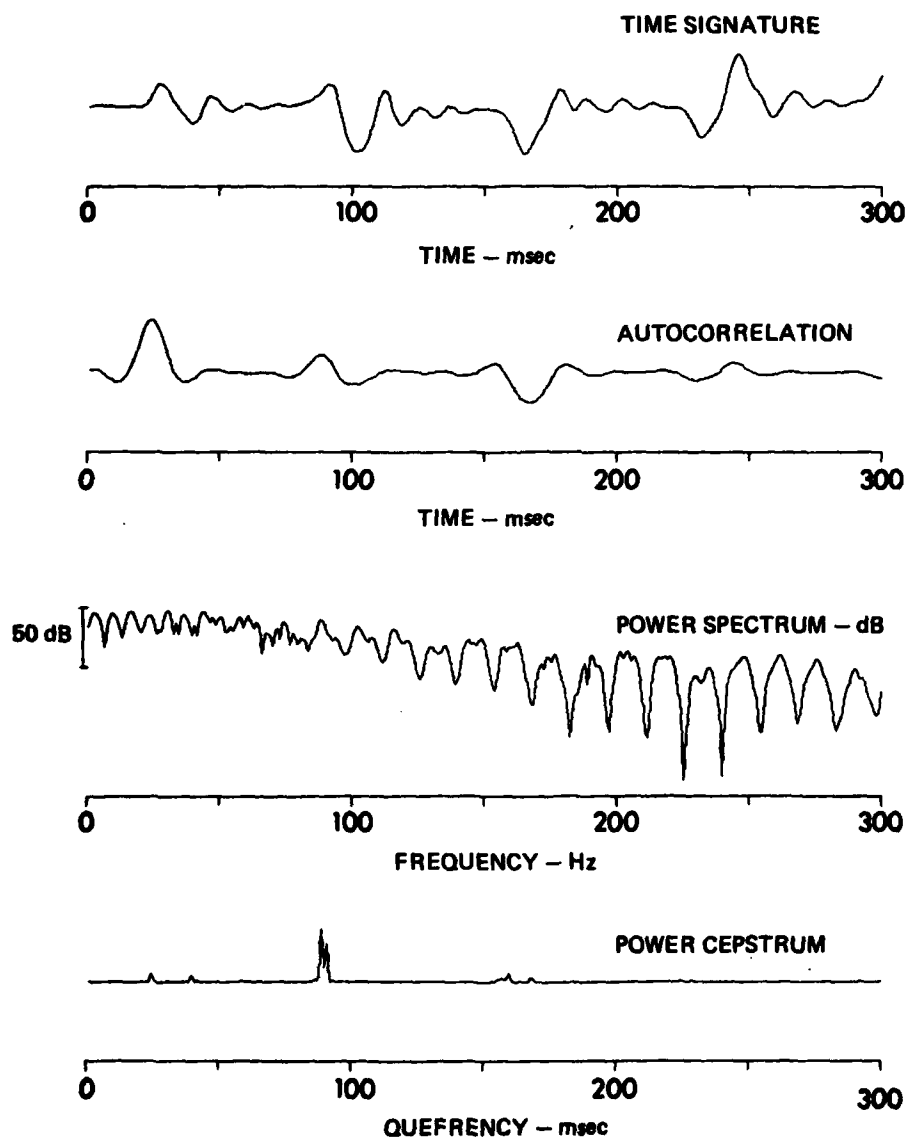


**FIGURE 48**  
**TIME SIGNATURE, AUTOCORRELATION, POWER SPECTRUM, AND**  
**POWER CEPSTRUM OF 5 BOTTOM BOUNCE PLANE WAVE IMPULSE**  
**RESPONSE CONVOLVED WITH SOURCE WAVEFORM AND TOTAL**  
**GHOST RESPONSE (244 m SOURCE, 256 m RECEIVER)**

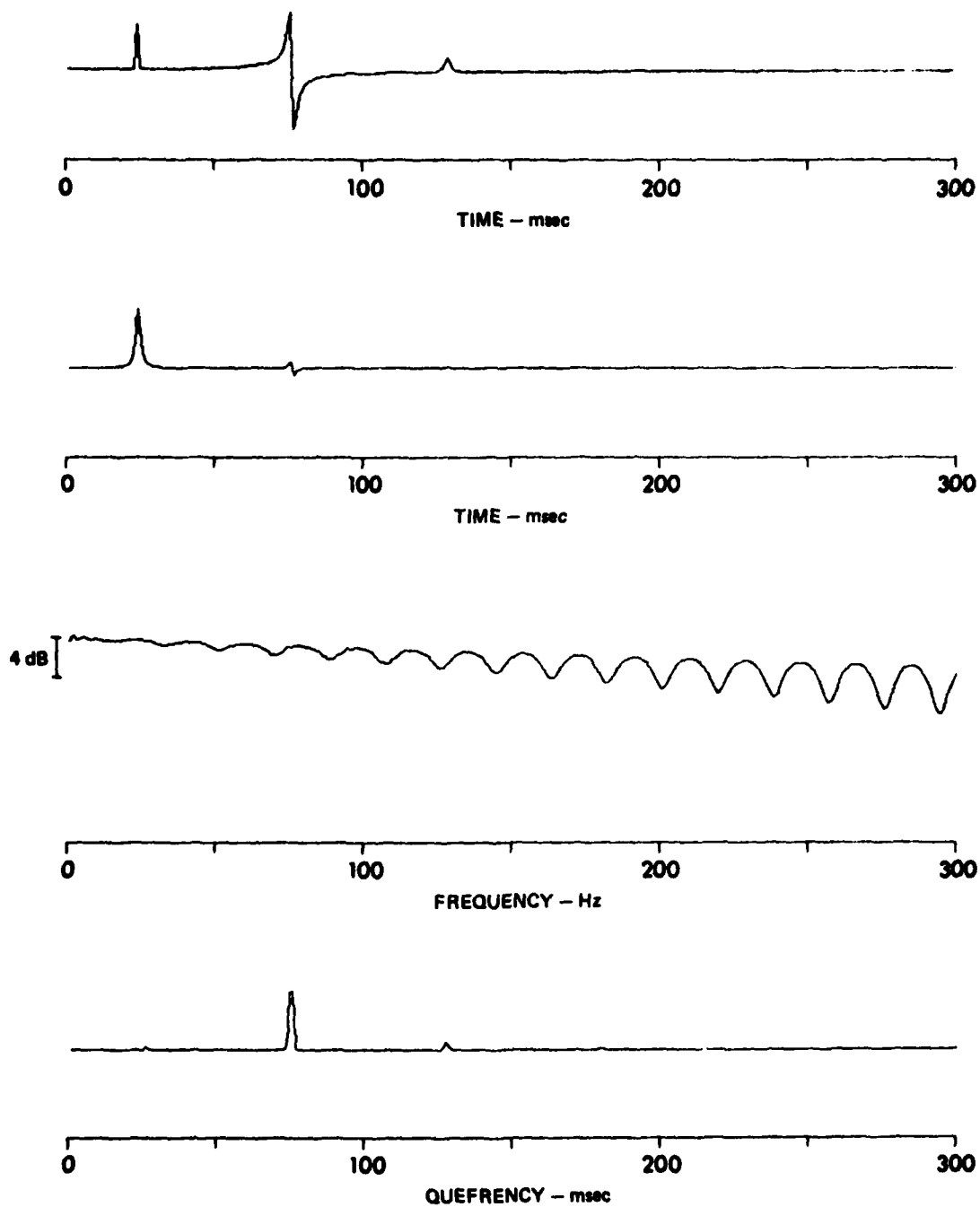


**FIGURE 49**  
**PLOT SHOWING THE IMPULSE RESPONSE, AUTOCORRELATION, POWER SPECTRUM**  
**AND POWER CEPSTRUM WITH GEOACOUSTIC MODEL HAVING SLIGHTLY HIGHER**  
**SOUND SPEEDS AND LOWER ATTENUATIONS**

ARL:UT  
 AS-81-1281  
 GDI - GA  
 9-30-81

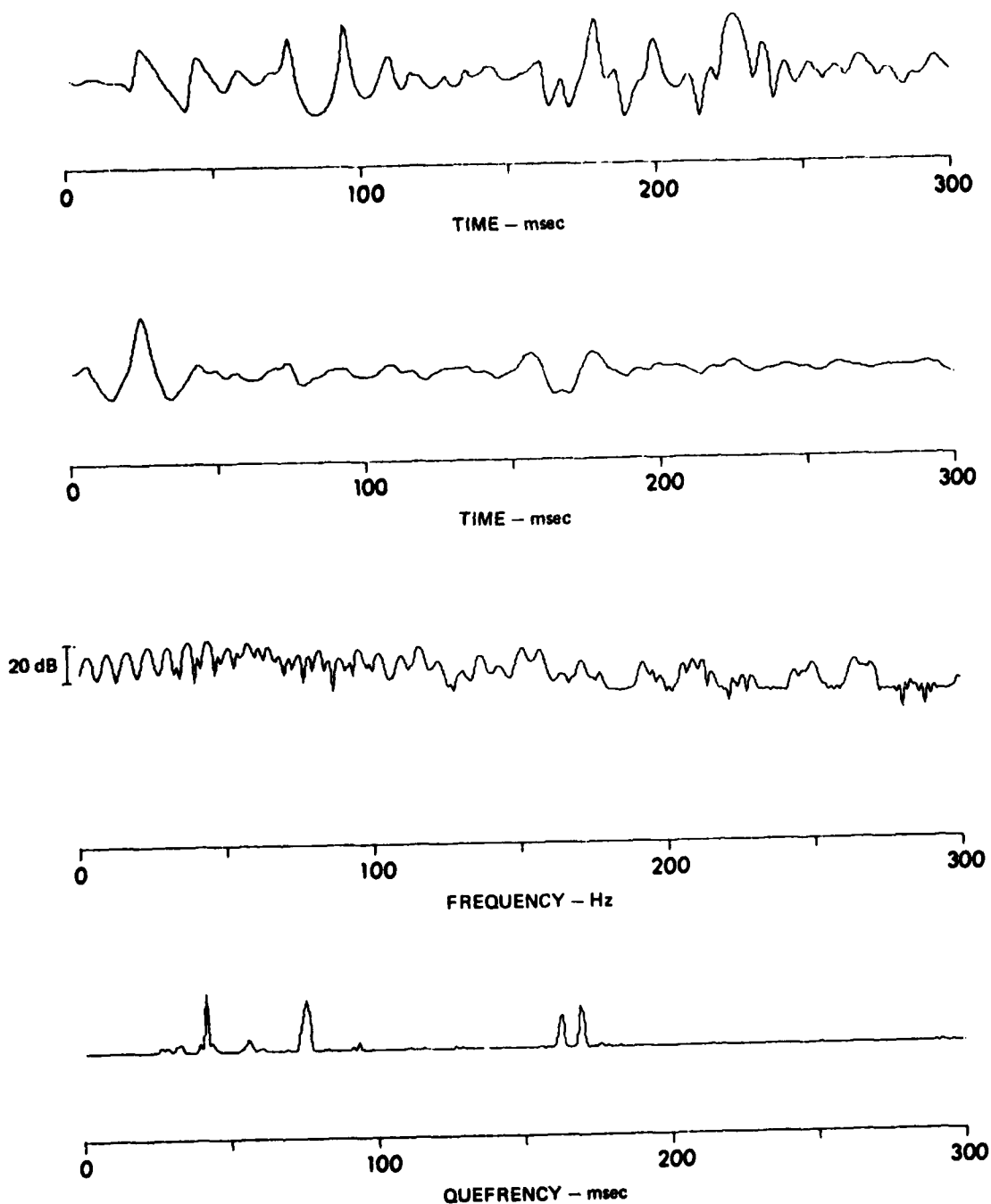
structure shown in Table III rather than that of Table II. The higher sound speeds result in shorter pathlengths of the refracted energy and the lower density at the water-sediment interface results in the specular reflection being smaller. Thus, the refracted event is larger relative to the specular reflection in Fig. 49 compared to Fig. 41. Comparing the autocorrelation and power cepstrum plots of Figs. 41 and 49, it is seen that the change in impulse responses does not affect the ability of the autocorrelations or power cepstrums in detecting the time delay of interest, although the log power spectrum indicates considerably greater dynamic range for the impulse response of Fig. 41. The effect of this difference in dynamic range on the power cepstra would be seen if they were not self-normalized. The power cepstra in these plots are normalized after the first three samples and last three samples are zeroed.

Figure 50 shows a 5 BB synthetic acoustic signal with the same source and receiver geometry as the data discussed in Chapter 2 using the impulse response shown in Fig. 49. It is seen that the autocorrelation and power cepstrum readily reveal the time delay of interest.

Comparing Fig. 48, which has the same source-receiver geometry as Fig. 50, but uses an impulse response like that of Fig. 41 rather than Fig. 49, it is seen that there are significant differences. In particular, the bubble pulse delays and the source and receiver ghost delays of the power cepstrum plot in Fig. 50 are much stronger than those in Fig. 48 relative to the reflection-refraction delay. This is due to the considerably greater dynamic range of the reflection-refraction quefrency in the log power spectrum. The greater dynamic range of the log power spectrum of Fig. 48 is due to attenuation along the refracted path. The

TABLE III  
GEOACOUSTIC MODEL FOR FIGS. 49-54

<u>Depth</u> <u>(m)</u>	<u>Velocity</u> <u>(m/sec)</u>	<u>Attenuation</u> <u>(dB/m-kHz)</u>	<u>Density</u> <u>(g/cm<sup>3</sup>)</u>
0 <sup>-</sup>	1515		1.0
0 <sup>+</sup>	1515	0.02	1.6
1000 <sup>-</sup>	2765	0.02	2.4
1000 <sup>+</sup>	5200	0.01	2.5



**FIGURE 50**  
**PLOT SHOWING THE EFFECT OF BUBBLE PULSES AND GHOSTS**  
**WITH A 5 BB IMPULSE RESPONSE CALCULATED FROM THE**  
**1 BB IMPULSE RESPONSE SHOWN IN Fig. 49**  
**244 m SOURCE, 256 m RECEIVER**

ARL:UT  
 AS-81-1284  
 GDI - GA  
 9-30-81



autocorrelation of Fig. 48 also isolates the reflection-refraction delay better than does the autocorrelation of Fig. 50. This is also due to the longer refracted pathlengths in the geoacoustic model of Fig. 48, which results in the power being more concentrated at low frequencies where the refracted energy is strong relative to the bubble pulses.

Next the effect of white uncorrelated noise will be examined on the power cepstrum. This will be done by adding some small fraction to the zero lag value of the autocorrelation. This fraction will represent the percentage of the power of the time signal which was made up of white uncorrelated noise. This only contributes to the autocorrelation integral at the zero lag value.

Figure 51 shows the effect of adding 0.01 to the zero lag value of the autocorrelation. It is seen that the effect of this is to reduce the dynamic range of the log power spectrum and this has a corresponding effect on the power cepstrum of reducing the amplitude of the peak due to the reflection-refraction delay and the bubble pulse delays. This is due to the fact that these power cepstrum peaks are more dependent on the dynamic range at the high frequencies than the ghosts are, and the fact that the high frequencies are below the mean power level of the spectrum. Figure 52 shows the effect of having 10 dB signal power excess. It is seen that the level of the reflection-refraction peak and bubble pulse peaks are further reduced and distorted.

Finally, in this section the common procedure of whitening the log power spectrum before calculating the power cepstrum is examined for synthetic plane wave data. This is accomplished by removing the slope and mean of the log power spectrum by linear regression. Figure 53

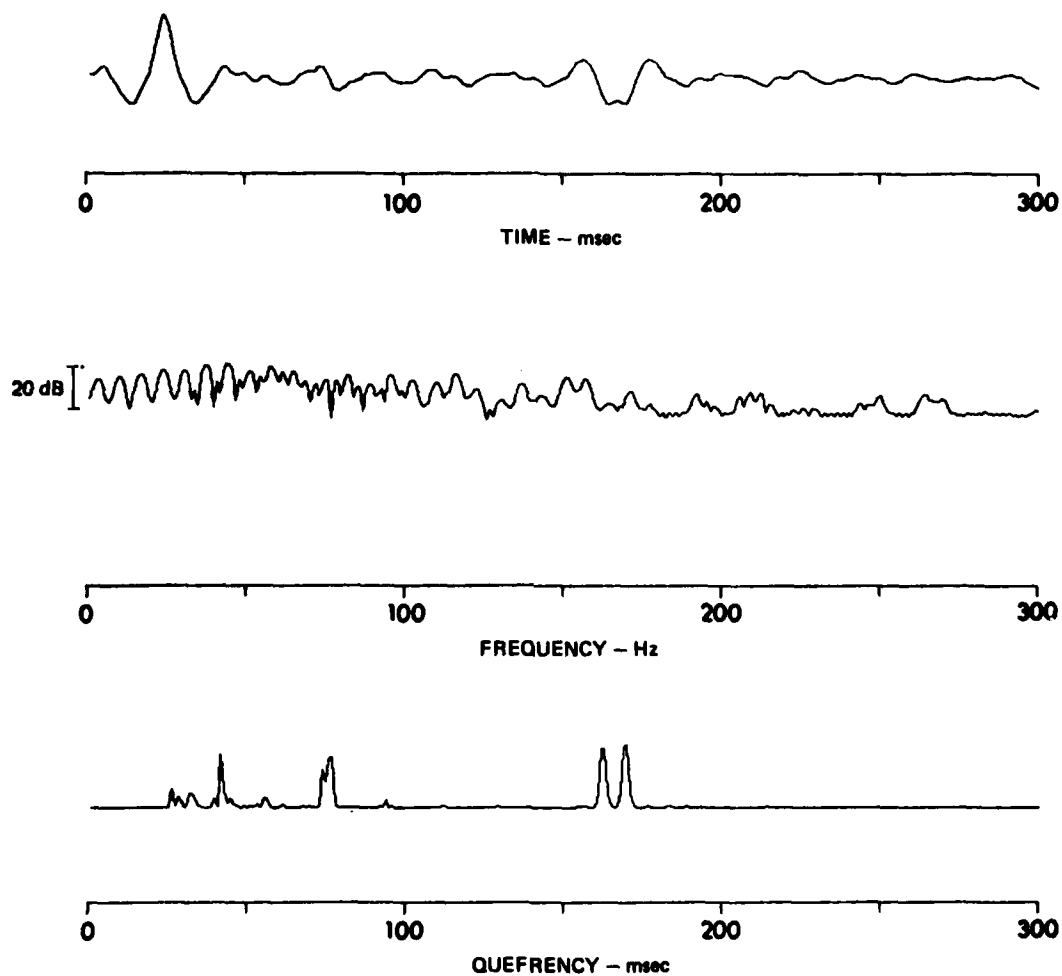


**FIGURE 51**  
**PLOT SHOWING THE EFFECT OF ADDING WHITE**  
**UNCORRELATED NOISE: 20 dB SIGNAL EXCESS**

ARL:UT  
AS-81-1283  
GDI - GA  
9-30-81

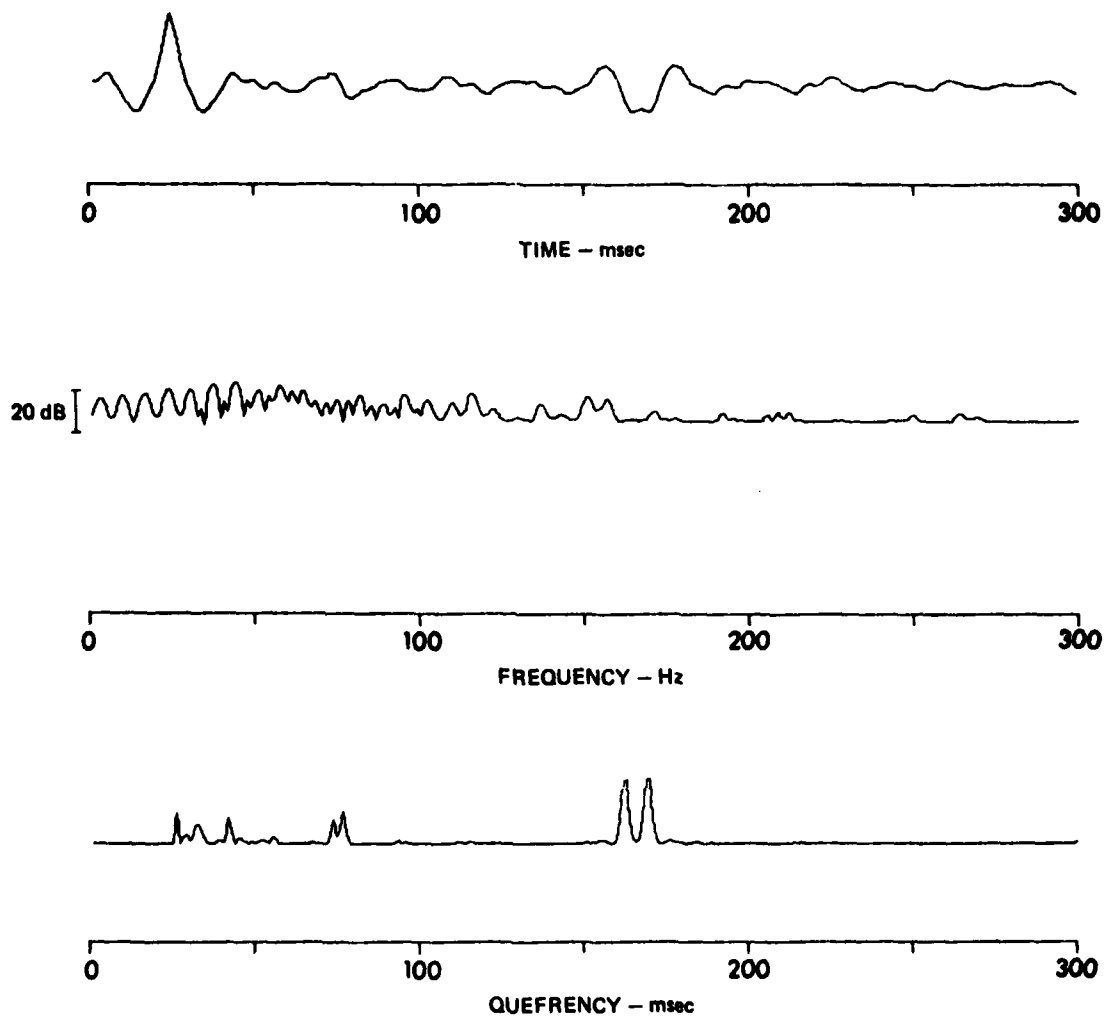


**FIGURE 52**  
**PLOT SHOWING THE EFFECT OF ADDING WHITE**  
**UNCORRELATED NOISE: 10 dB SIGNAL EXCESS**

ARL:UT  
AS-81-1282  
GDI - GA  
9-30-81

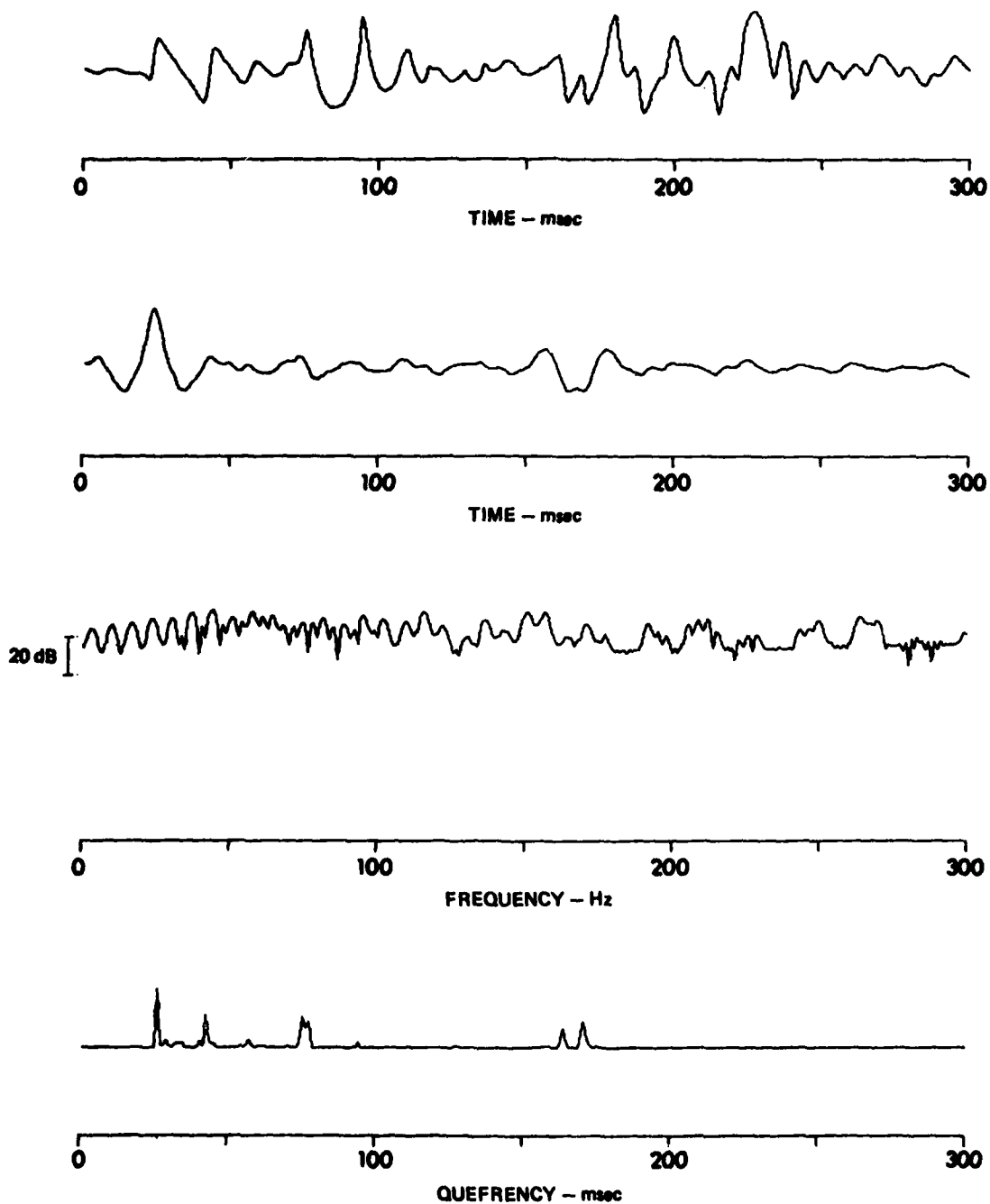


**FIGURE 53**  
**PLOT SHOWING THE EFFECT OF WHITENING THE LOG POWER SPECTRUM**  
**BEFORE CALCULATING THE POWER CEPSTRUM**  
**(NOTE: FIRST THREE SAMPLES OF THE POWER CEPSTRUM WERE NOT ZEROED)**

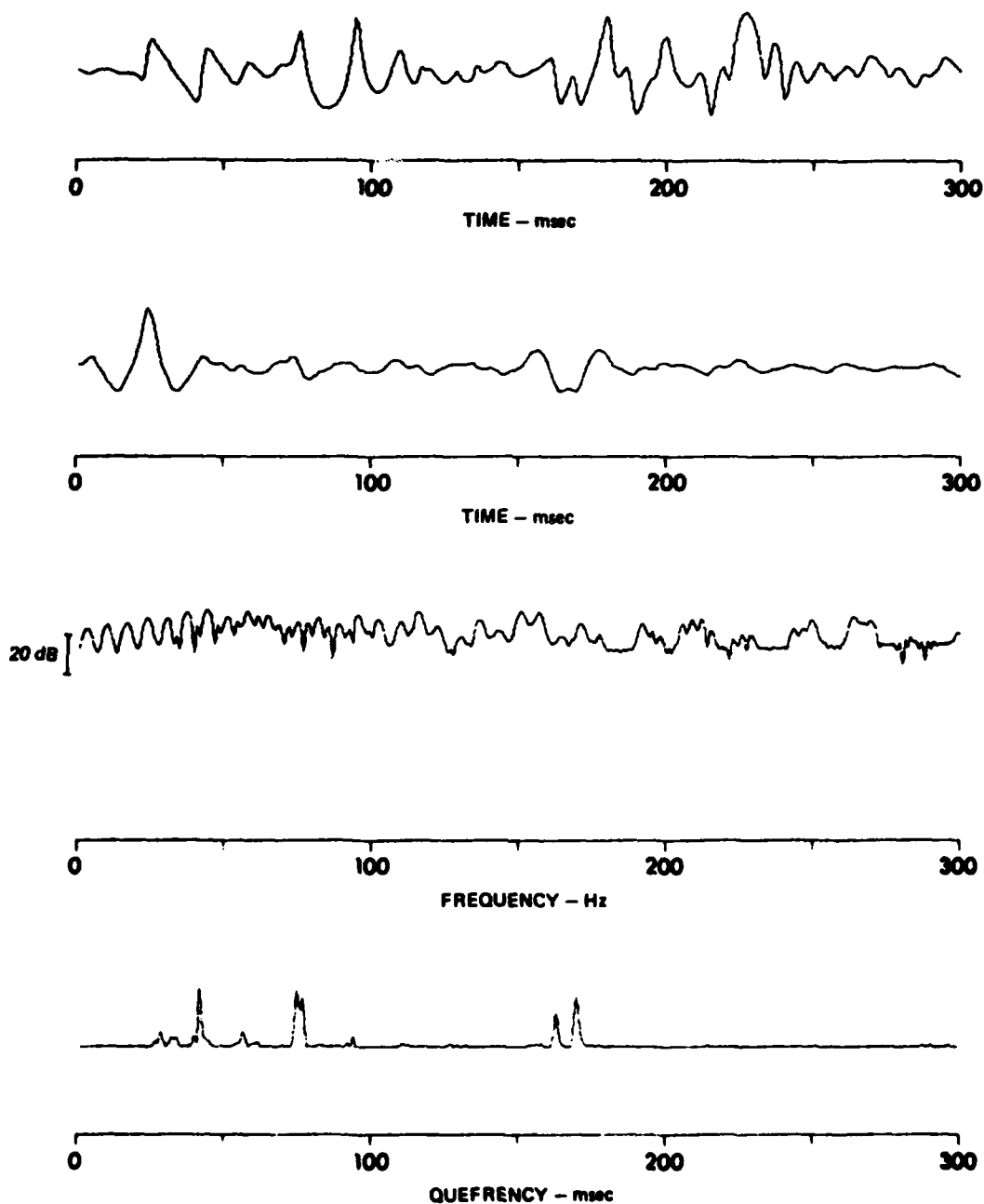
effect of whitening the log power spectrum before calculating the power cepstrum where the first three samples of the power cepstrum are not zeroed. It is seen that the bubble pulse delay, the reflection-refraction delay, and the ghost delays can be detected. The significance of this is that, ordinarily, without whitening the log power spectrum the first three samples of the power cepstrum totally dominate the plot. Therefore, one alternative to zeroing the first three samples of the power cepstrum is to whiten the log power spectrum before calculating the cepstrum.

Figure 54 shows the effect of whitening the log power spectrum before calculating the power cepstrum and zeroing the first three samples of the power cepstrum. A comparison of this figure with Fig. 50 indicates that, for this synthetic example, whitening the log power spectrum has little effect on the power cepstrum.

### 3.5 Data Autocorrelogram and Power Cepstra

In this section autocorrelations and power cepstra are calculated for real data obtained in a turbidite province. Figure 55 shows an autocorrelogram with the same source-receiver geometry as the data shown in Fig. 33. The only differences between the data shown in Fig. 33 and Fig. 55 are that the data for the autocorrelogram are sampled almost every degree and extend to  $40^\circ$  rather than  $30^\circ$ .

The source and receiver ghost delays and the source bubble pulse delays are evident on the autocorrelogram. The depth of detonation of the source has some variance and this is seen in the variance of the bubble pulse delay and source ghost delay. For these data even the second bubble pulse is observable on the autocorrelations, particularly at low grazing angles. Since the receiver is fixed, the receiver ghost delay is a



**FIGURE 54**  
**PLOT SHOWING THE EFFECT OF WHITENING THE LOG POWER SPECTRUM**  
**BEFORE CALCULATING THE POWER CEPSTRUM WITH THE FIRST THREE**  
**SAMPLES OF THE POWER CEPSTRUM ZEROED**

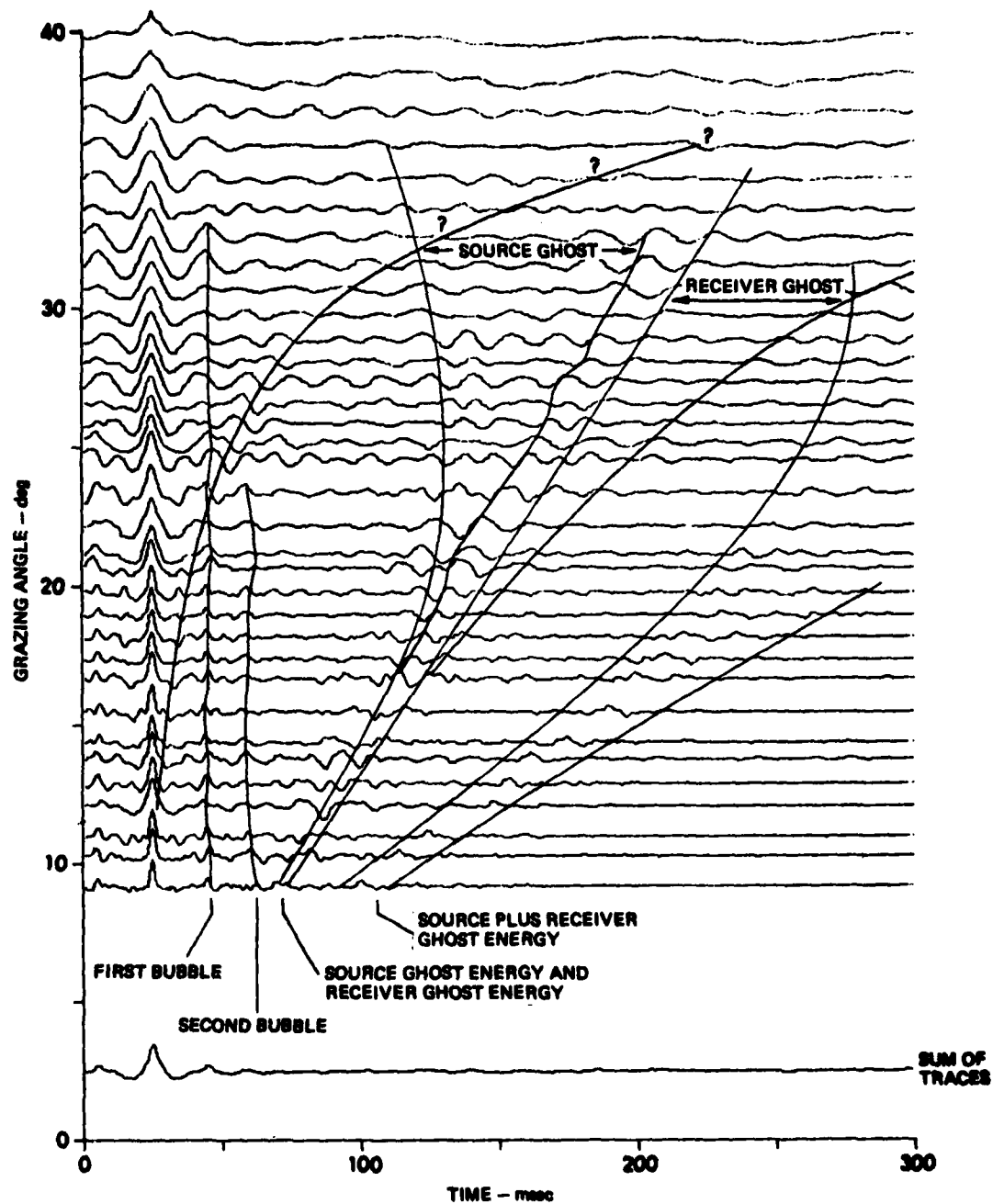


FIGURE 55  
 AUTOCORRELOGRAM FOR A TURBIDITE PROVINCE  
 CURVED TRAVEL TIMES REPRESENT THE DELAY BETWEEN  
 THE REFLECTED AND REFRACTED EVENTS  
 (244 m SOURCE, 266 m RECEIVER)

constant. The receiver ghost delay, in particular, and all other delays can best be seen by looking up the page with your eye level to the page.

The curved lines drawn on the autocorrelation plot represent the time delay between reflected and refracted energy. Currently, it is not known whether this time delay between the reflected and refracted energy is due to a specular or subbottom reflection. It is seen that this delay is well defined between about  $15-28^\circ$ . Beyond about  $32^\circ$  there is interference between the reflected-refracted time delay of the zero lag value and the ghost refracted time delay. This ghost refracted delay is the delay between the refracted component of the first arrival and the reflected arrival of the ghost. This delay bends back toward the ordinate and the event has the same shape as the reflected-refracted delay of the zero lag value.

The shape of the ghost events themselves are the negative of the zero lag value; however, this is not clearly seen in Fig. 55 since the source and receiver depths are nearly the same. The source plus receiver ghost energy is also seen in Fig. 55.

At  $2.5^\circ$  the sum of all of the autocorrelations is plotted. This provides an estimate of the autocorrelation of the source waveform assuming that attenuation is not significant, and that all events with other than zero time moveout as a function of grazing angle cancel to zero.

A significant improvement in the autocorrelogram for measuring the reflected-refracted delay is obtained by muting the time waveforms beyond the source ghost delay of the first break. This is because the bottom angles for the ghosted arrivals are greater than the arrival which has not been ghosted. Thus, the impulse response delays on the



autocorrelations, which have not had the time signals muted beyond the source ghost, give poorer resolution of the reflected-refracted event. This increased resolution of the reflected-refracted event is seen in Figs. 55 and 56.

Figure 57 shows an autocorrelogram for 18 m shot data with a receiver depth of 256 m in the same turbidite province as the 244 m shot data. The source and receiver ghosts are identifiable and the bubble pulses are apparent from the ~~zero~~ trace. The pulse at about 150 msec is the crosscorrelation of the shock pulse with the first bubble pulse, the pulse at about 200 msec is the crosscorrelation of the shock pulse with the second bubble pulse, and the pulse at about 135 msec is the crosscorrelation of the first and second bubble pulse. The variability of the bubble pulse delays indicates the variance of the depths of detonation of the source.

The reflected-refracted delay of the 18 m source autocorrelograms is the same as that on the 244 m source autocorrelograms which, of course, is expected. The 18 m shot data, however, also reveal significant reflectivity not resolved by the 244 m data. It is difficult to resolve more than one reflector since this is five bottom bounce data and some of the peaks are multiples, but a reflector which is delayed slightly from the zero log value is well defined. Thus, there appears to be a significant shallow reflector in this turbidite province. To improve the resolution of the reflected-refracted delay the time signals are muted past the receiver ghost before autocorrelating in Fig. 58.

Returning to Fig. 57, it is seen that at angles of 16, 18, and 21° the main components of the autocorrelation are reproduced for

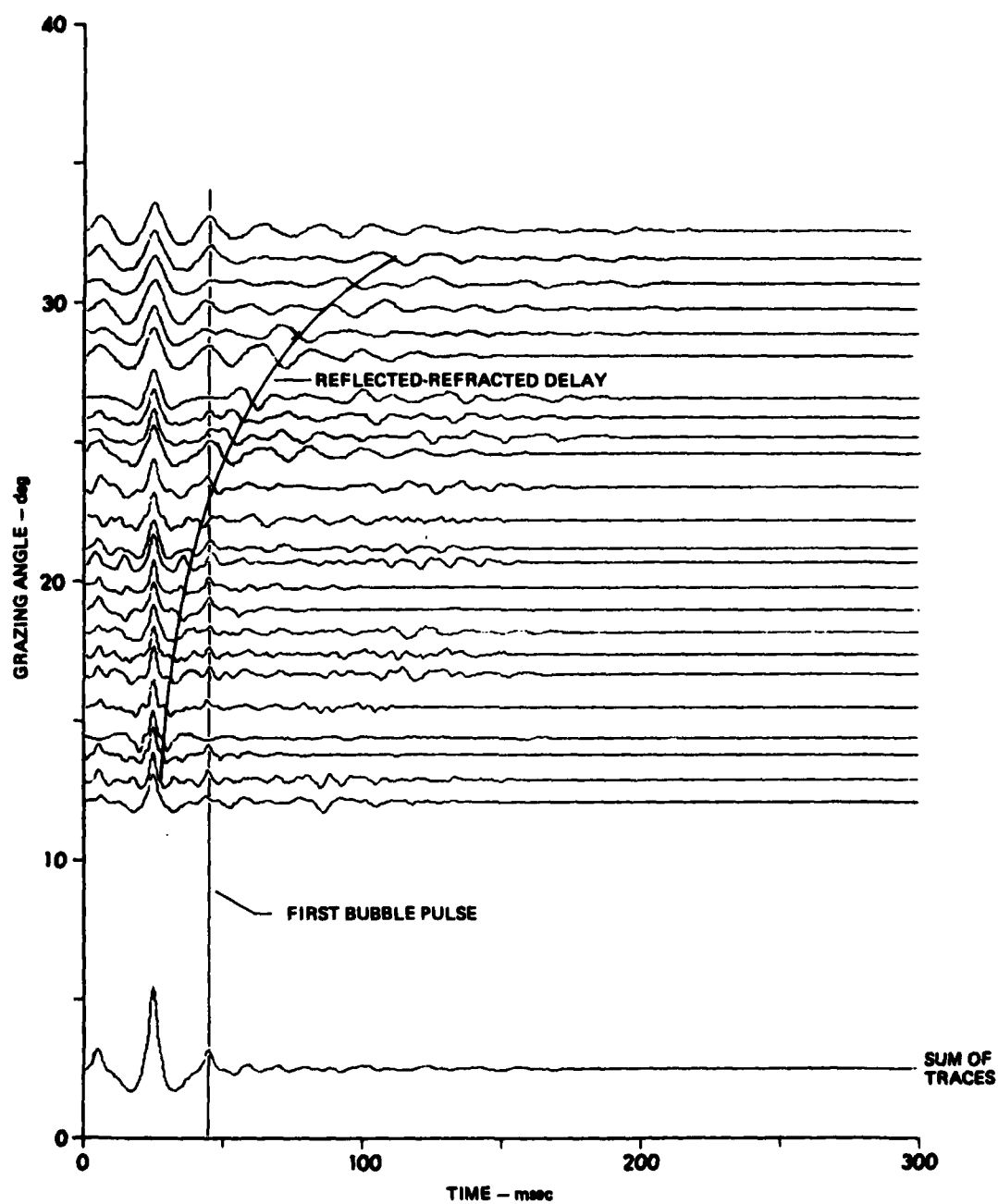


**FIGURE 56**  
**AUTOCORRELOGRAM OF THE TURBIDITE PROVINCE FOR WHICH**  
**THE TIME SIGNALS ARE MUTED PAST THE SOURCE GHOST DELAY**  
**BEFORE THE AUTOCORRELATIONS ARE CALCULATED**  
 (244 m SOURCE, 266 m RECEIVER)

ARL:UT  
 AS-81-1326  
 GDI - GA  
 10-5-81

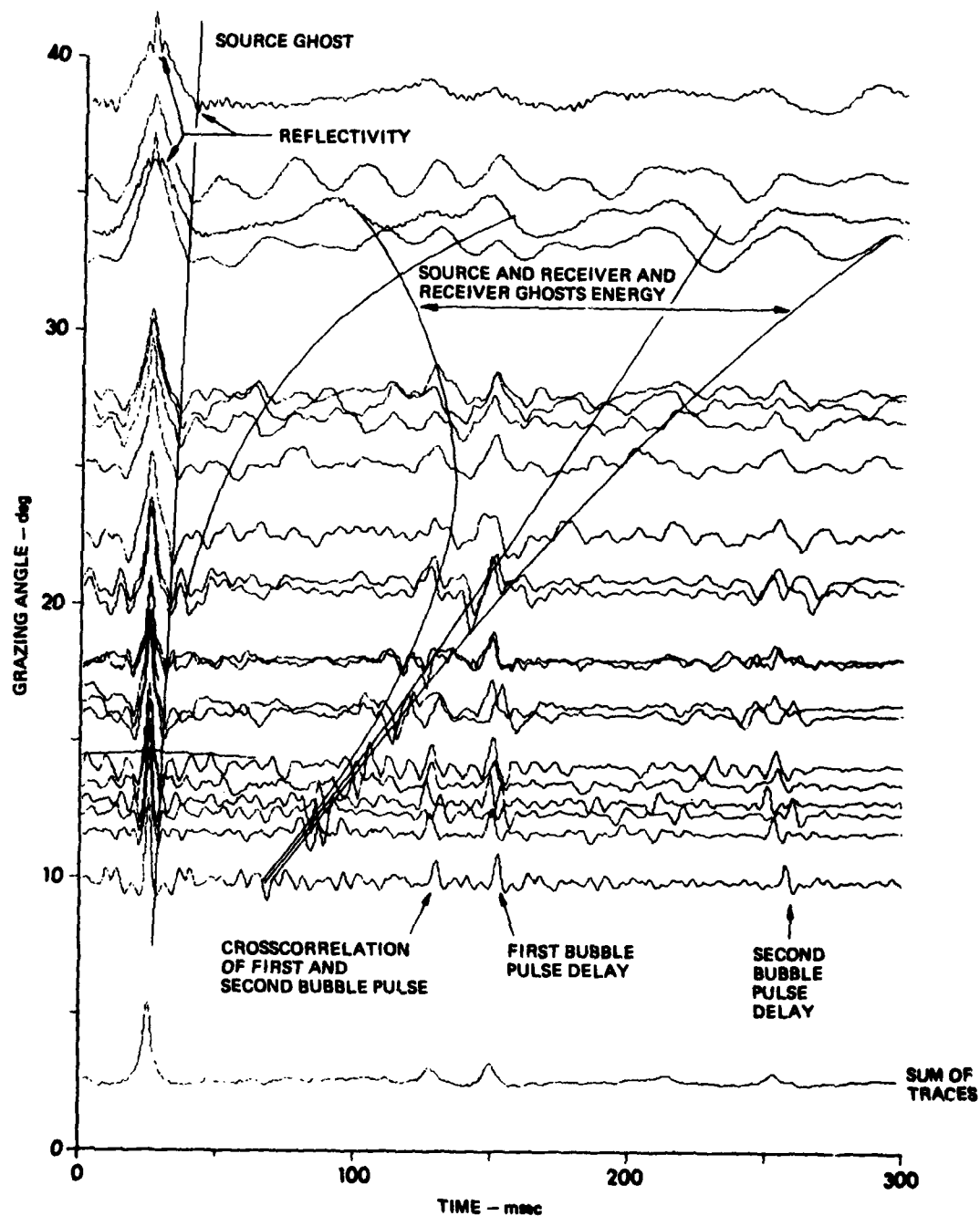


**FIGURE 57**  
**AUTOCORRELOGRAM WITH 18 m SOURCES AND 256 m RECEIVER**  
 NOTE THE APPARENT REFLECTIVITY OF SHALLOW DEPTHS  
 AND THE DOUBLE FIRST BUBBLE PULSES

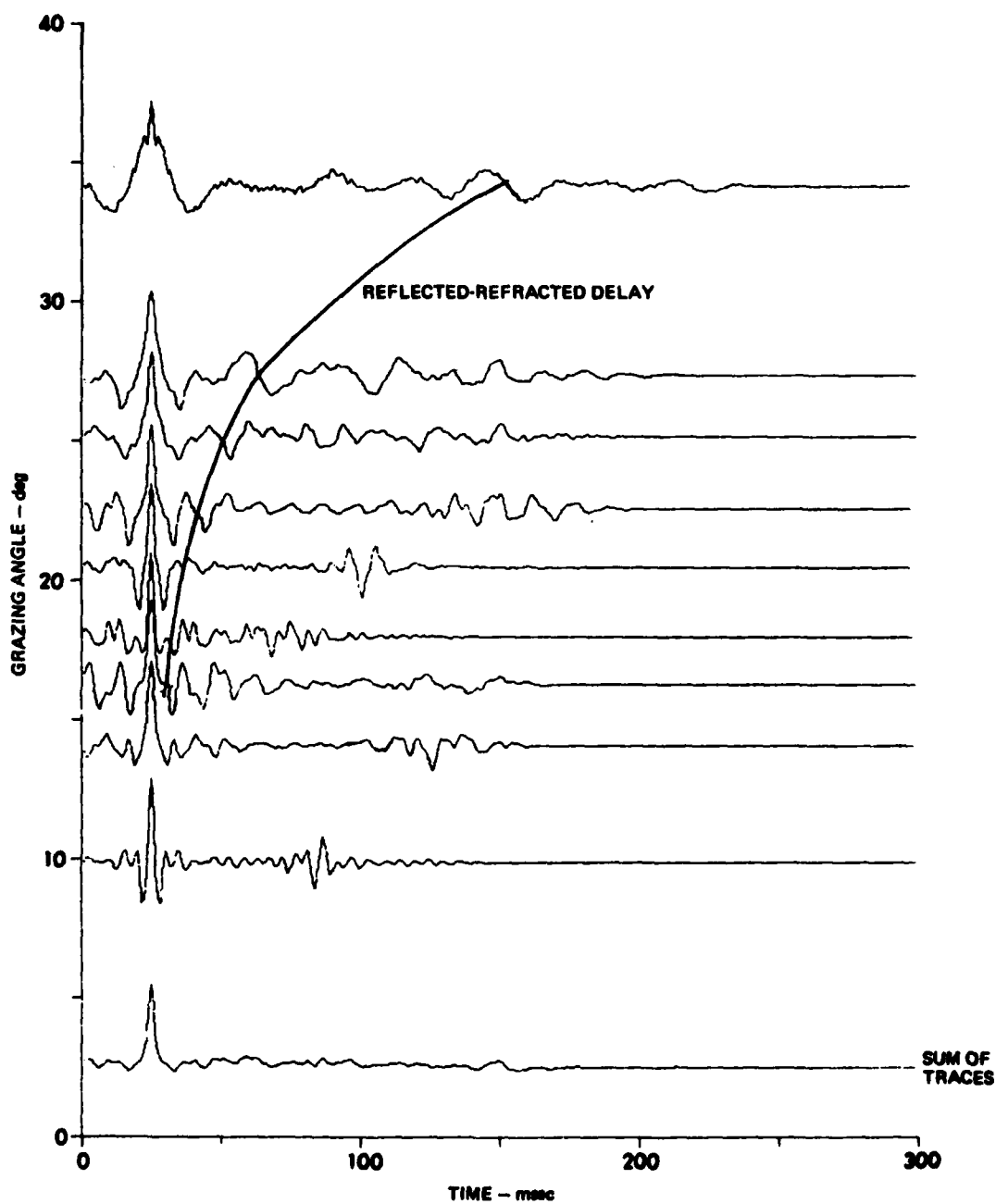


**FIGURE 58**  
**AUTOCORRELOGRAM FOR WHICH THE TIME SIGNALS**  
**WERE MUTED PAST THE RECEIVER GHOST BEFORE**  
**THE AUTOCORRELATIONS WERE CALCULATED**  
**(18 m SOURCE, 286 m RECEIVER)**

ARL:UT  
 AS-81-1328  
 GDI - GA  
 10-6-81

different shots--which is reassuring. Comparing autocorrelations at the same angle reveals the approximate noise level of a single autocorrelation.

One method of reducing the noise level of the autocorrelation and at the same time reducing the effect of bubble pulses is to sum autocorrelations at the same angle for different numbers of bottom bounces. An example of this is shown for a bottom angle of  $26^{\circ}$  in Fig. 59. It is seen here that there are similarities of the autocorrelations and differences. The similarities are due to the fact that the bottom angle and source-receiver geometries are nearly the same. The dissimilarities are due to source depth differences, slightly different bottom angles, and different bounce points on the bottom. Autocorrelations like that for the 8 BB signal are interpreted to be due to bad bounce points. The summed autocorrelation is shown at the bottom of Fig. 59. The peaks in the summed autocorrelation are readily interpreted. The first positive peak is likely the bubble pulse at the mean source depth, the second event is the reflection-refraction delay with its bubble at its tail, the third event is some combination of the ghost delays and the multiple of the reflection-refraction delay, and the waveform beyond the third event is associated with ghost energy. Thus, it appears that an autocorrelogram of summed autocorrelations would significantly facilitate time delay detection of events in the acoustic signal.

Figures 60-63 show examples of the power cepstrum applied to the data. Figure 60 shows the power cepstrums of the data shown in Figs. 55 and 56. The first three samples are zeroed for display purposes and zero quefrency is located at 0 msec. The first bubble pulse is the strongest event in Figs. 60 and 61 and the source and

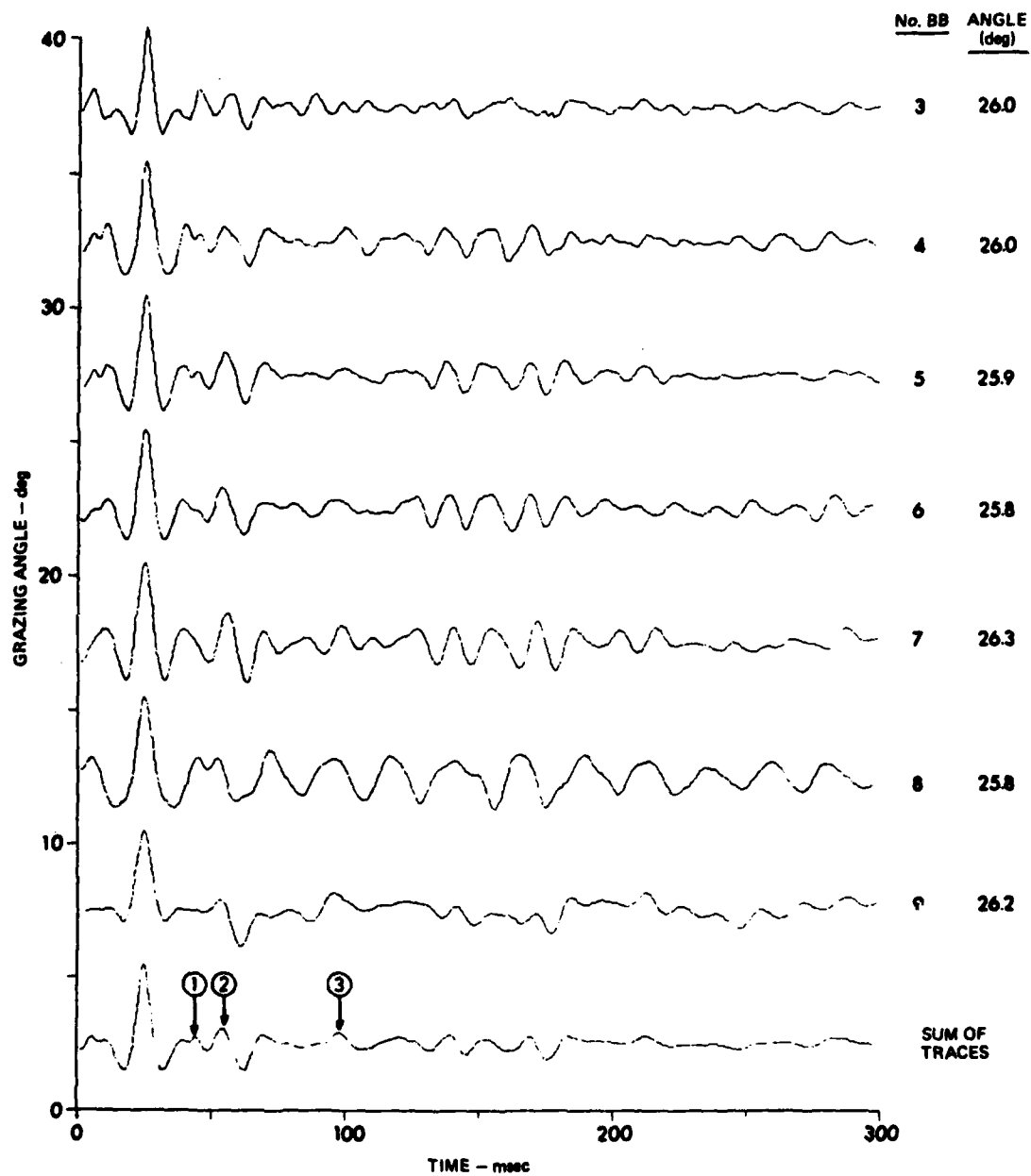
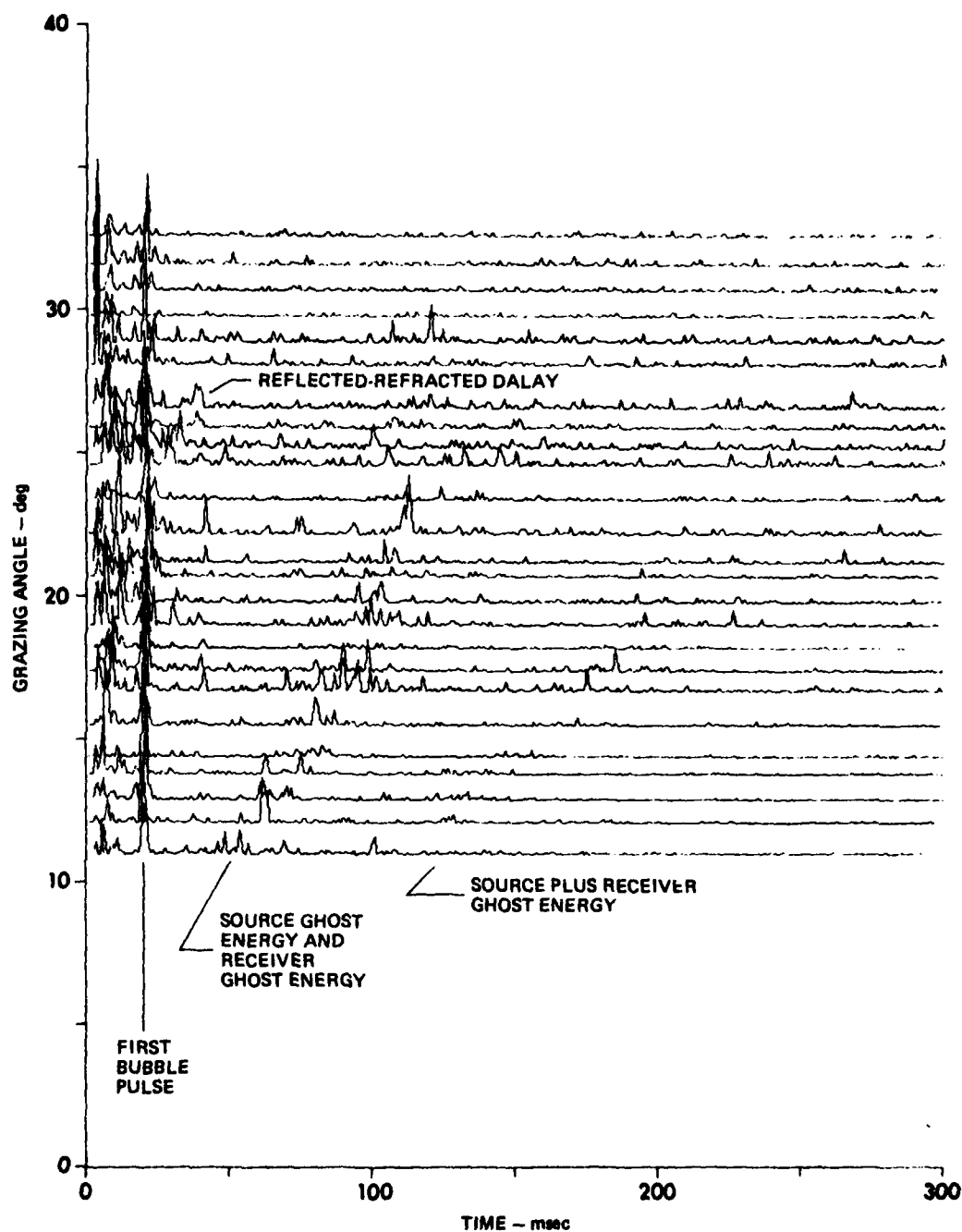
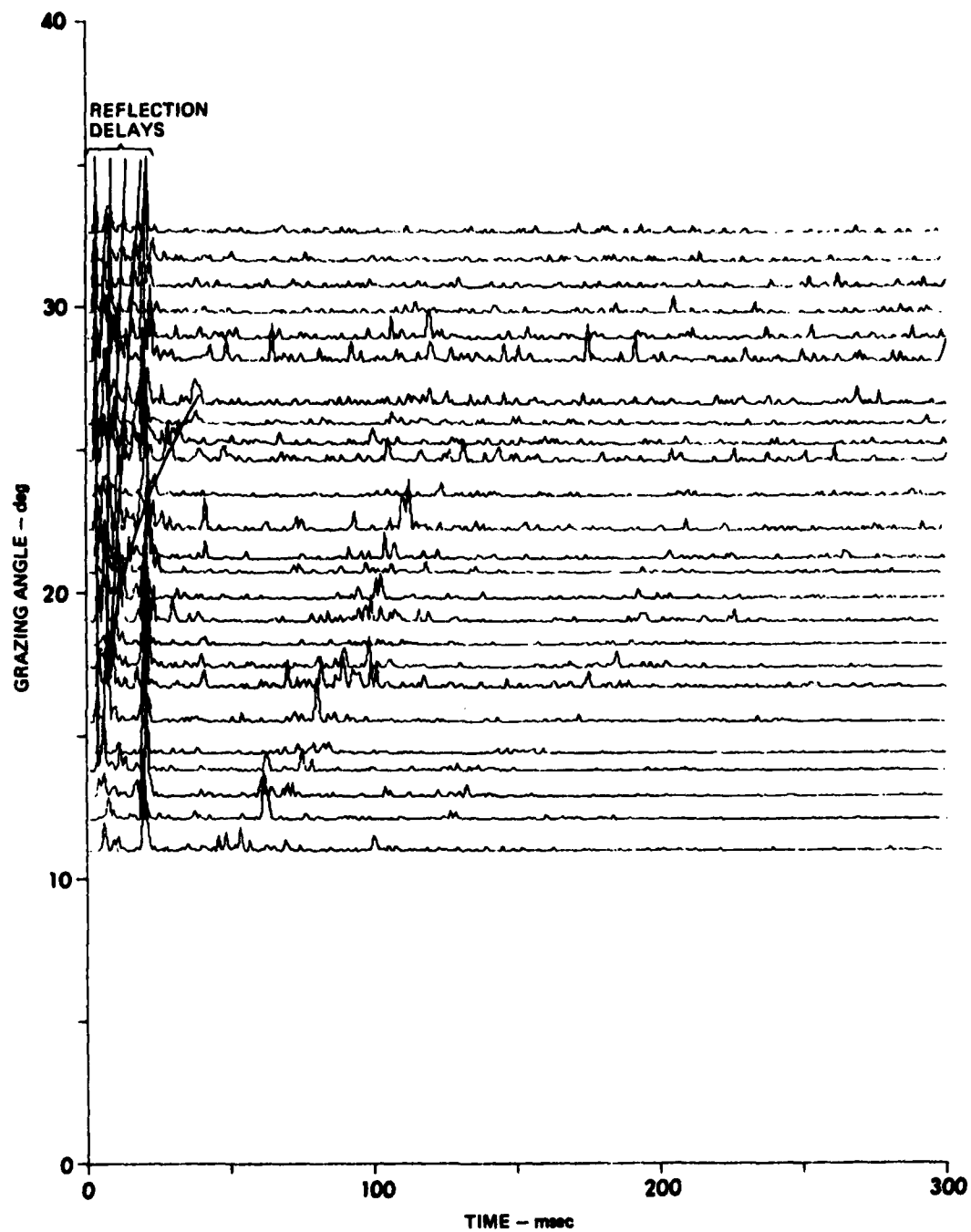


FIGURE 59  
FIGURE SHOWING AUTOCORRELATIONS WITH A  
BOTTOM ANGLE OF ABOUT 26° FOR DIFFERENT  
NUMBERS OF BOTTOM BOUNCES AND THEIR SUM

ARL:UT  
AS-81-1329  
GDI - GA  
10-5-81



**FIGURE 80**  
**POWER CEPSTRUM OF DATA IN TURBIDITE PROVINCE**  
 (244 m SOURCE, 256 m RECEIVER)



**FIGURE 81**  
**POWER SPECTRUM WHITENED BEFORE CALCULATING THE POWER CEPSTRUM**  
 (244 m SOURCE, 256 m RECEIVER)



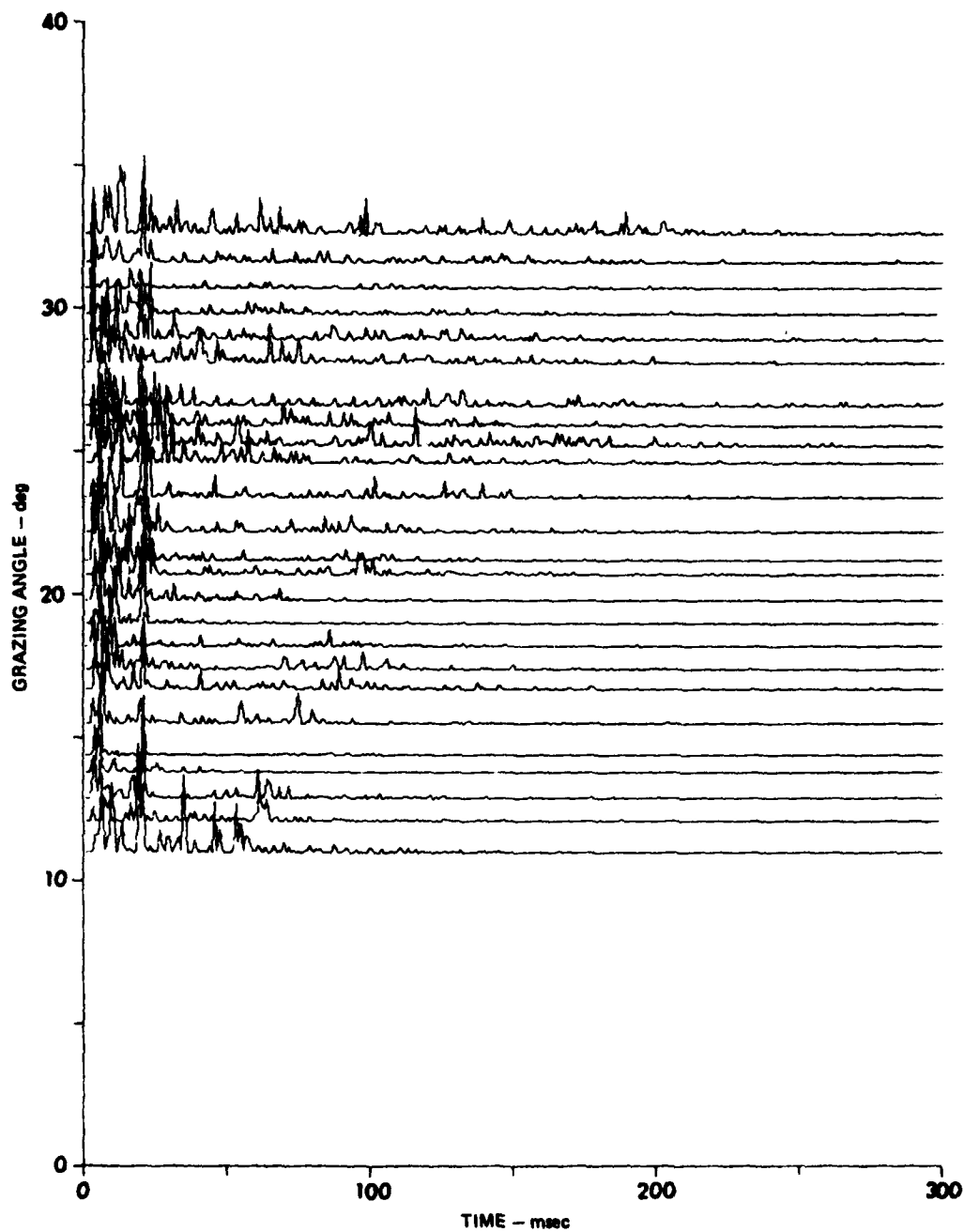


**FIGURE 62**  
**SIGNAL MUTED PAST SOURCE GHOST DELAY BEFORE**  
**CALCULATING THE POWER CEPSTRUM**

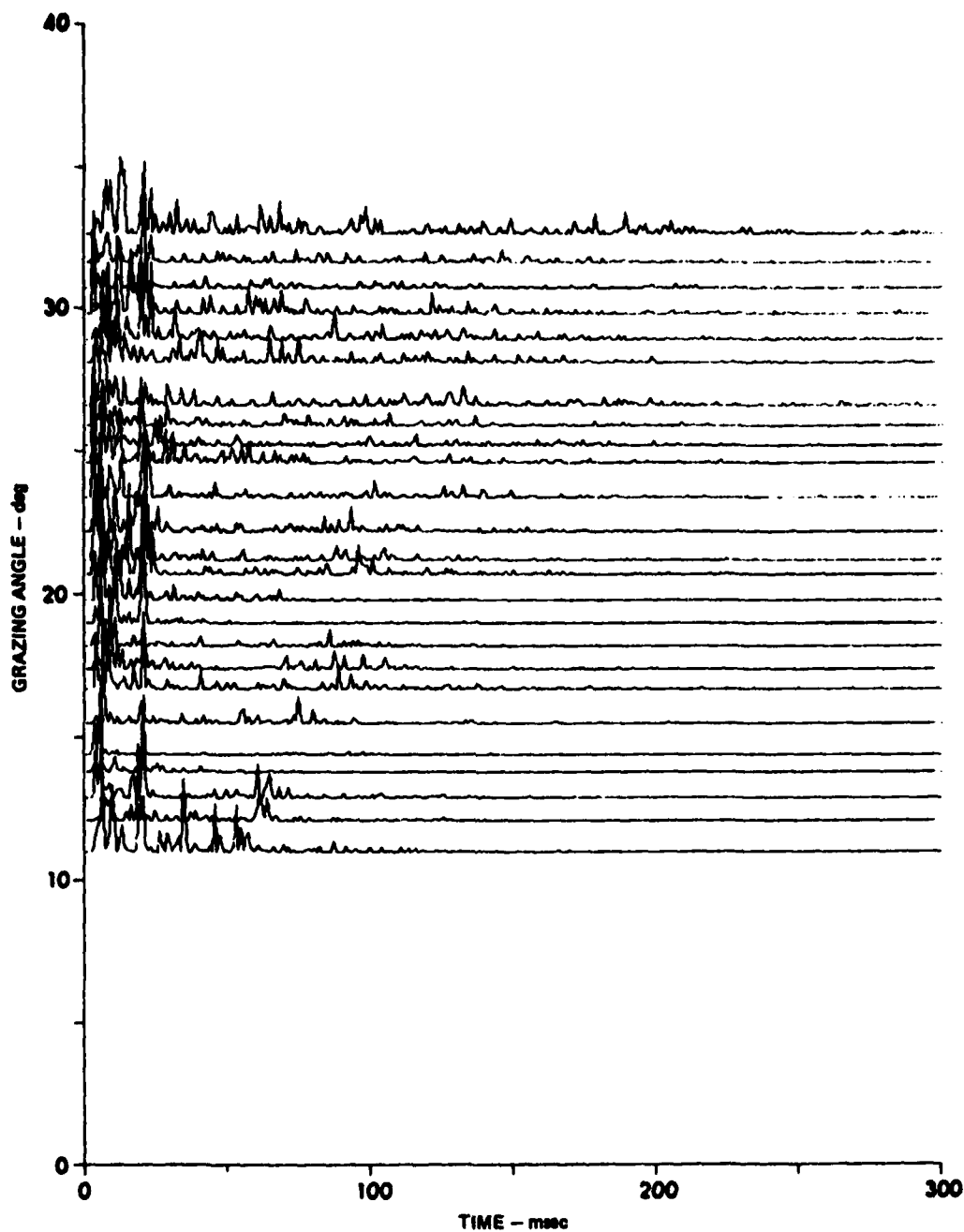


**FIGURE 63**  
**SIGNAL MUTED PAST SOURCE GHOST DELAY**  
**AND POWER SPECTRUM WHITENED BEFORE**  
**CALCULATING THE POWER CEPSTRUM**

receiver ghost energy is also evident. The source plus receiver ghost energy is less evident. The fact that the power cepstrum does not have the superposition property with respect to convolution accounts for the large amplitude variability of the ghost arrivals. This variability is due to beating between all quefrequencies of the signal. The quefrequencies that are most greatly affected will be determined by the amplitudes and periodicity of the quefrequencies which occur. Thus, interpretation of a power cepstrum or suite of power cepstra will be less exact than the autocorrelation, and will probably require some experience. Coherent noise will be less identifiable and the shape of the cepstral peaks will be less interpretable in terms of the phase of the time arrivals than for the autocorrelation.

Figure 61 shows the power cepstra shown in Fig. 60 where the power spectra were whitened before the power cepstra were calculated. Some improvement seems to have occurred. The reflection-refraction delay is as easy to detect and some subbottom reflectivity is also apparent at delays less than the reflection-refraction delay.

Figures 62 and 63 show the effect of muting the time signals past the source ghost delay before calculating the power cepstra. The reflection-refraction delay is easier to detect particularly when the power spectra are whitened before calculating the power cepstra in Fig. 63. In these figures the number of cepstral peaks at delays less than 25 msec is indicative of subbottom reflectivity; however, identification of events is not certain. The inability to identify reflection events in these plots may be due to beating between quefrequency components, or to an increase in the variance of the noise spectrum caused by muting beyond the source ghost delay of the first break.

## CHAPTER 4

### IMPULSE RESPONSE ESTIMATION USING MULTIPLE BOTTOM BOUNCE SIGNALS

#### 4.1 Impulse Response Estimation

An alternative approach to correlation for extracting geoacoustic information about the ocean bottom from acoustic data is the deconvolution of unwanted signal components (i.e., estimation of the ocean bottom impulse response by removing bubble pulses and ghosts). Debubbling has been accomplished for over ten years by frequency domain deconvolution. Hovem first introduced deconvolution of bubble pulses by measuring the source waveform and dividing the source spectrum with the spectrum of the bottom interacting signal (Hovem, 1979; Hastrup, 1969). This is described by the equation

$$I(\omega) = \frac{A(\omega)}{S(\omega)} \times G(\omega) \quad , \quad (4.1.1)$$

where

$I(\omega)$  = impulse response estimate,

$A(\omega)$  = bottom interacting signal,

$S(\omega)$  = source waveform spectrum, and

$G(\omega)$  = shaping filter taking band limitation and noise  
into account.

Santaniello et al. improved this technique by multiplying both the numerator and denominator of (4.1.1) by the complex conjugate of the source

spectrum,  $S^*(\omega)$ . This is equivalent to match filtering, which reduces the effect of uncorrelated noise. In addition, Santaniello et al. (1979) added white noise to the source power spectrum to stabilize the transfer function by preventing denominator values being near zero,

$$I(\omega) = \frac{A(\omega)S^*(\omega)}{|S(\omega)|^2 + C} \times G(\omega) \quad . \quad (4.12)$$

Dicus (1981) has improved on this technique by minimizing the squared error of the impulse response estimate for each frequency component. Dicus also shows that the deconvolution can be accomplished using a single measured source waveform by time scaling to account for source depth differences between shots.

Time domain approaches to deconvolution have been in existence in the oil industry for many years. These techniques generally employ Weiner filtering that solves for filter coefficients in the least mean square error sense which relates input to a desired output. This generally involves shaping a seismic field wavelet to an interpretive wavelet where the field wavelet is estimated statistically (Backus et al., 1977). The filter coefficients can be obtained using the Levinson algorithm and the deconvolution can be accomplished either in the time or frequency domain (Lackoff and LeBlanc, 1975). Wood et al. (1978) show that debubbling can also be accomplished using the Weiner approach in which an inverse filter is derived from a measured source waveform. The technique which follows is a Weiner approach to obtaining an estimate of the ocean bottom impulse response utilizing multiple bottom bounce waveforms that have equal source and receiver depths and equal bottom grazing angles. This deconvolution

technique will be termed multiple bottom bounce deconvolution (MBB deconvolution).

#### 4.2 Theory of MBB Deconvolution

The method used in this work to recover an estimate of the impulse response of the ocean bottom is essentially the same as the debubbling technique employed by Wood et al. (1978) except that the source waveform is replaced by an (n-1) bottom bounce waveform with the same bottom angle and source and receiver depths as an (n) bottom bounce waveform.

The flowchart reproduced from Wood et al. in Fig. 64 shows the derivation of the deconvolution filter  $D(Z)$ . This filter consists of the crosscorrelation of the (n-1) bottom bounce signal with the autocorrelation of the zero delay Wiener inverse. Clearly one would obtain a zero delay impulse if the deconvolution operator was crosscorrelated with the (n-1) bottom bounce received waveform.

$$D(Z)S^{n-1}(Z) = B(Z) B(Z^{-1}) S^{n-1}(Z) S^{n-1}(Z^{-1}) = 1 \quad .$$

There is no restriction on the phase of  $S^{n-1}(Z)$  and ghosts may be included.

This deconvolution technique can be extended to derive an estimate of the ocean bottom impulse response by deconvolving an (n-1) bottom bounce waveform, from an (n) bottom bounce waveform provided both waveforms have equal source and receiver depths and equal bottom grazing angles. This estimate involves an assumption that the ghost delays are dependent only on the source and receiver depths and the bottom grazing angles. This becomes more nearly true as the number of bottom bounces becomes large.

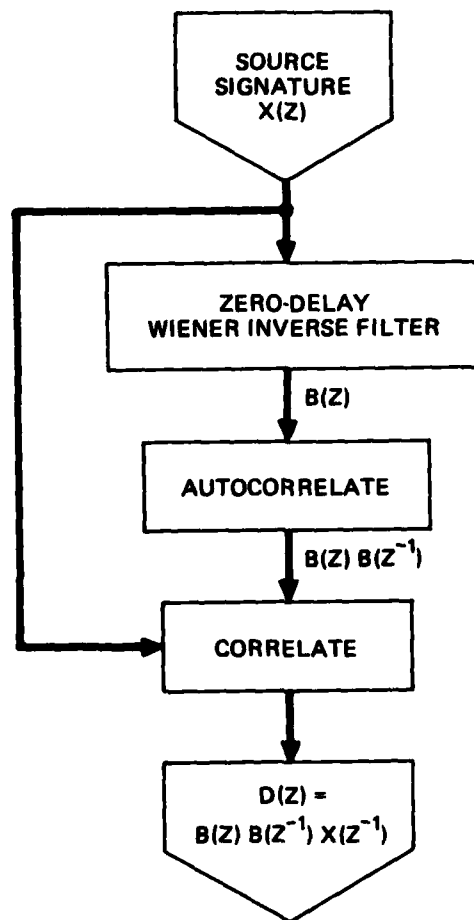


**FIGURE 64**  
**FLOWCHART FOR CALCULATION OF DECONVOLUTION FILTER,  $D(Z)$**   
 **$X(Z)$  IS THE  $(n-1)$  BOTTOM BOUNCE WAVEFORM**

[Reproduced from Wood et al., (1978)]

ARL:UT  
 AS-81-1287  
 GDI - GA  
 9-30-81

Assuming that the conditions above are met and that the ghost delays are nearly identical an estimate of the impulse response can be calculated by computing an inverse to the (n-1) bottom bounce signal in the least mean square error sense. This can be accomplished by crosscorrelating the (n-1) bottom bounce signal with the autocorrelation of its zero lag Wiener inverse and crosscorrelation of this filter with the (n) bottom bounce signal.

This can be written in the Z-domain

$$R_{n-1,n}(Z) = S^{n-1}(Z^{-1}) S^n(Z) = S^{n-1}(Z^{-1}) S^{n-1}(Z) I(Z) \quad ,$$

$$R_{n-1,n}(Z) D(Z) = B(Z) B(Z^{-1}) S^{n-1}(Z^{-1}) S^{n-1}(Z) I(Z) \quad .$$

Since  $B(Z) B(Z^{-1}) S^{n-1}(Z^{-1}) S^{n-1}(Z) \approx 1$  then  $R_{n-1,n}(Z) D(Z) \approx I(Z)$ , where  $I(Z)$  is the first bottom bounce impulse response of the (n) bottom bounce signal.

To verify that  $I(Z)$  is the impulse response of the first bottom bounce of the (n)bottom bounce signal, recall the filter representation of the (n)bottom bounce acoustic signal

$$S^n(f) = S^*(f) G_s(f) G_R(f) I^n(f) \quad ,$$

where

$S^*(f)$  = frequency spectrum of source

$G_s(f)$  = source ghost filter

$G_R(f)$  = receiver ghost filter



$I^n(f)$  = (n) bottom bounce impulse response.

If the ghost delays are assumed to be identical,

$$S^{n-1}(f) = S^*(f)G_S(f)G_R(f)I^{n-1}(f) \quad .$$

Clearly if the inverse function to  $S^{n-1}(f)$  is applied to  $S^n(f)$  the result will be an estimate of  $I(f)$ .

If the experiment geometry is set up as shown in Fig. 65 the deconvolved trace is the first bottom bounce impulse response of the (n) bottom bounce signal and thus the subbottom characteristics could be mapped in space. If the impulse response can be assumed to be space stationary, ensemble averaging can be used to improve the estimate of the impulse response versus grazing angle.

#### 4.3 Examples of MBB Deconvolution Technique

Figures 66 and 67 show examples of the deconvolution technique. In Fig. 66 an (n-1) bottom bounce synthetic waveform is deconvolved from an (n) bottom bounce synthetic waveform with equal bottom grazing angles and equal ghost delays. It is seen that the impulse response is almost perfectly recovered. The fact that it was not perfectly recovered is because the operator length was limited to the length used in real data. In practice an operator length is generally chosen to be between 100 and 250 msec. In the absence of noise an infinite operator length would be desirable due to the ghosts (which have infinite inverses); however, in the presence of noise there is a tradeoff between deconvolving predictable energy and loss of signal-to-noise ratio (S/N). The method of predictive deconvolution (Peacock and Treitel, 1969) is well suited for some of the

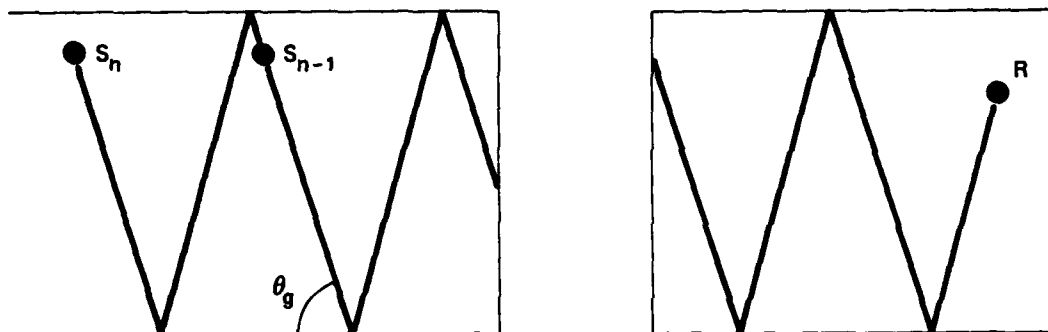


**FIGURE 65**  
**GEOMETRY FOR DECONVOLVING AN  $(n-1)$  BOTTOM BOUNCE WAVEFORM**  
**FROM AN  $(n)$  BOTTOM BOUNCE WAVEFORM**

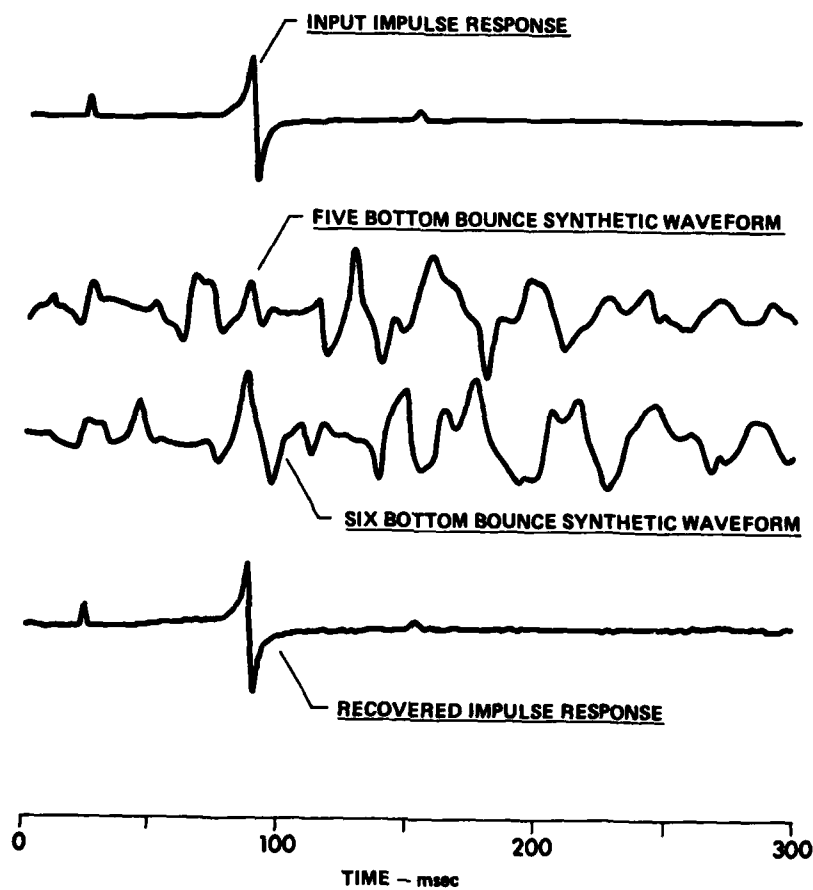


**FIGURE 66**  
**RECOVERY OF THE IMPULSE RESPONSE**  
**FROM SYNTHETIC DATA**  
 91 m SOURCE, NOMINAL 498 m RECEIVER,  $\theta = 26^\circ$

ARL:UT  
 AS-81-1289  
 GDI - GA  
 9-30-81

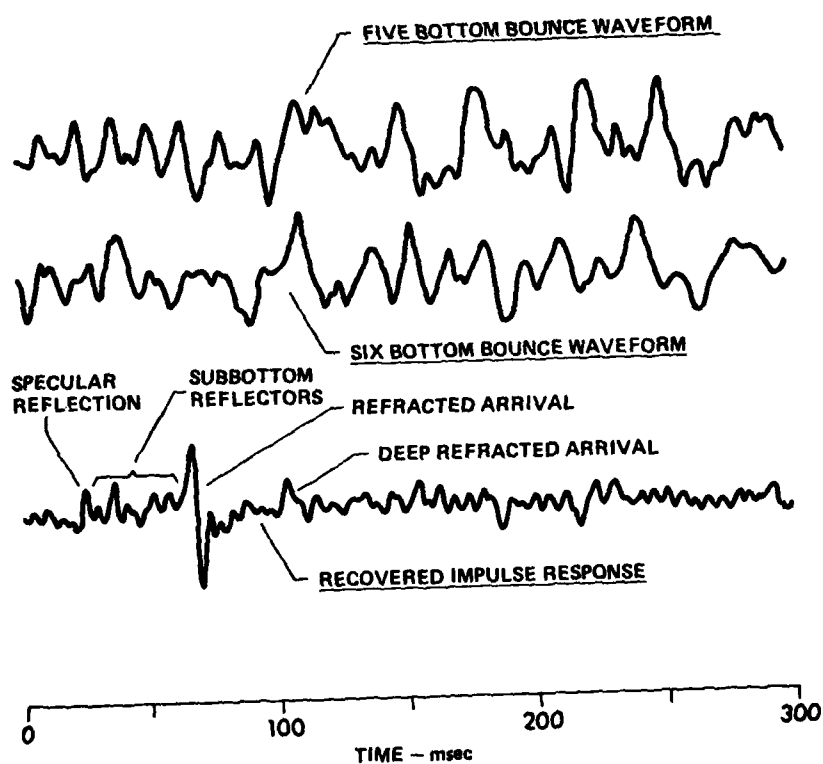


**FIGURE 67**  
**RECOVERY OF THE IMPULSE RESPONSE FROM**  
**DATA OBTAINED IN TURBIDITE PROVINCE**  
 91 m SOURCE, NOMINAL 498 m RECEIVER,  $\theta = 26^\circ$

ARL:UT  
 AS-81-1290  
 GDI - GA  
 9-30-81

geometries of interest; however, the method described here is preferable because of its ease of implementation.

Figure 67 is an example application for real data. It is seen that there is a considerably greater noise level in the deconvolved trace for real data. This is primarily due to the breakdown of the assumption that the sources were detonated at the same depth; but perhaps it is also due to the breakdown of the assumptions that the ghost delays are identical and that the angles of the (n) bottom bounce arrivals are identical to the angles of the (n-1) bottom bounce arrivals. In spite of the fact that these assumptions will always break down to some extent, Fig. 67 shows an all-pass example in which the refracted arrival is identifiable and at least two reflectors are apparent. Behind the refracted arrival there appears to be another event which may be either a deeper refraction or a multiple.

The failure of the source depths to be identical is likely to be the most common and significant source of error in deconvolution by this method. Figures 68-89 illustrate the effects of source depth differences on the deconvolution of a one bottom bounce signal from a two bottom bounce signal. Figure 68 shows the input impulse response to be used in these synthetics. Figure 69 shows the deconvolution using identical 91.4 m source waveforms. The source waveforms and impulse responses were calculated by the methods discussed in Section 1.5. Figure 70 shows that the impulse response can be recovered arbitrarily well for identical source waveforms. This is true regardless of the source depth used.

Figures 71-80 show the effect of deconvolving a 1 BB from a 2 BB waveform with 244.1 m mean source depths in which the 1 BB source waveform represents 1, 3, 5, 7, and 9% shallower depths than the 2 BB source

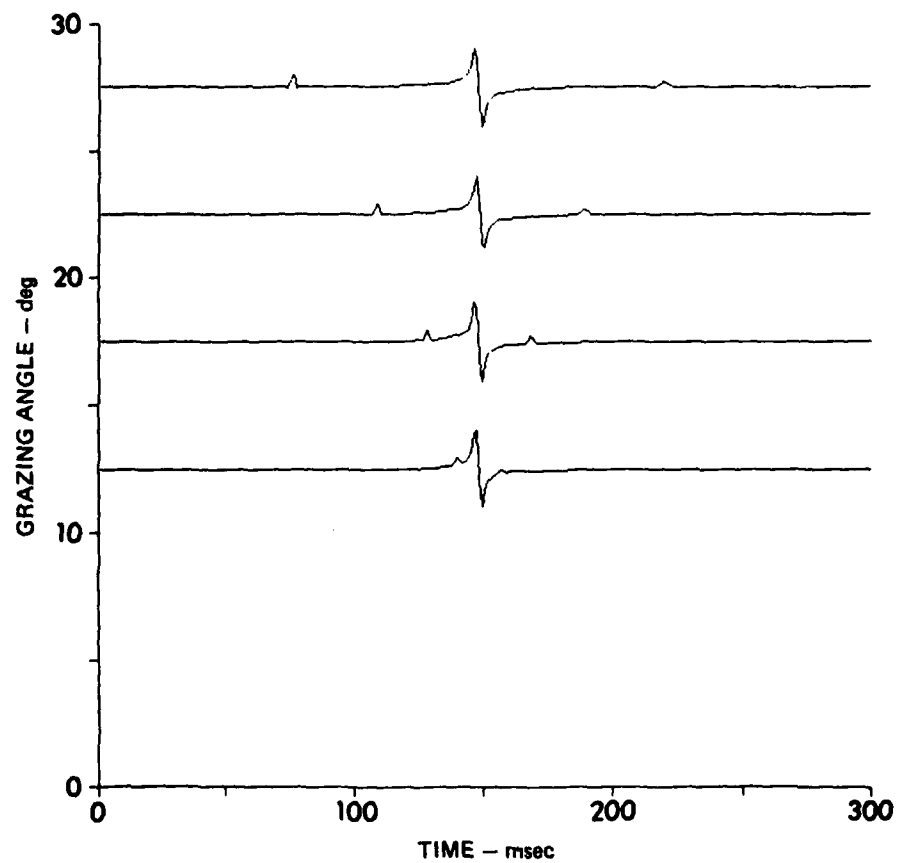


**FIGURE 68**  
**INPUT IMPULSE RESPONSE FOR SYNTHETIC DECONVOLUTION**

ARL:UT  
AS-81-1291  
GDI - GA  
9-30-81

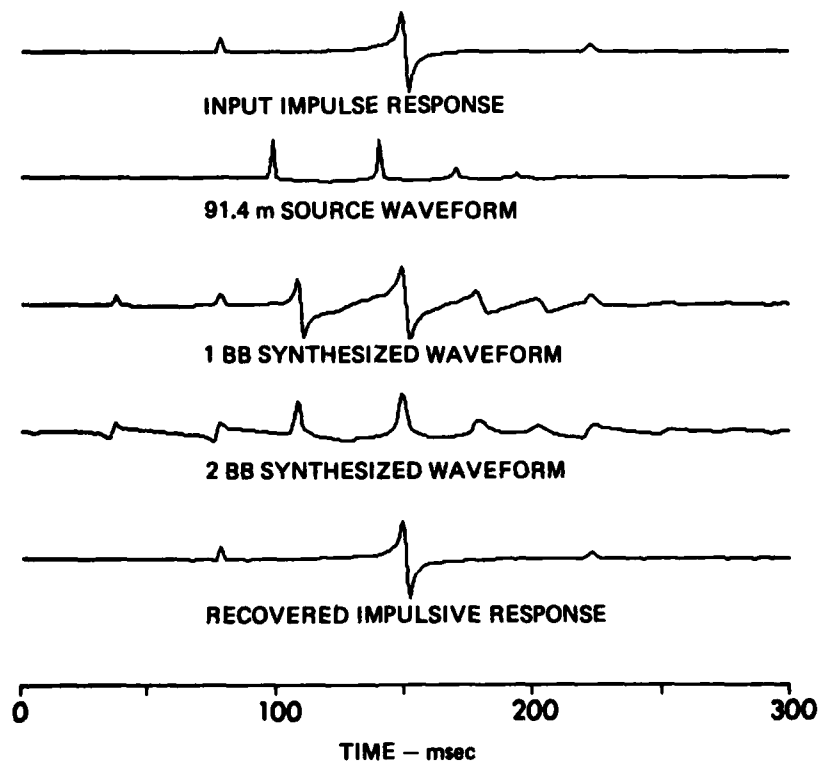


**FIGURE 69**  
**DECONVOLUTION OF  $(n-1)$  FROM  $(n)$  BOTTOM BOUNCE WAVEFORM**  
**WITH IDENTICAL SOURCE WAVEFORMS**  
**91.4 m SOURCE, GHOST IGNORED**

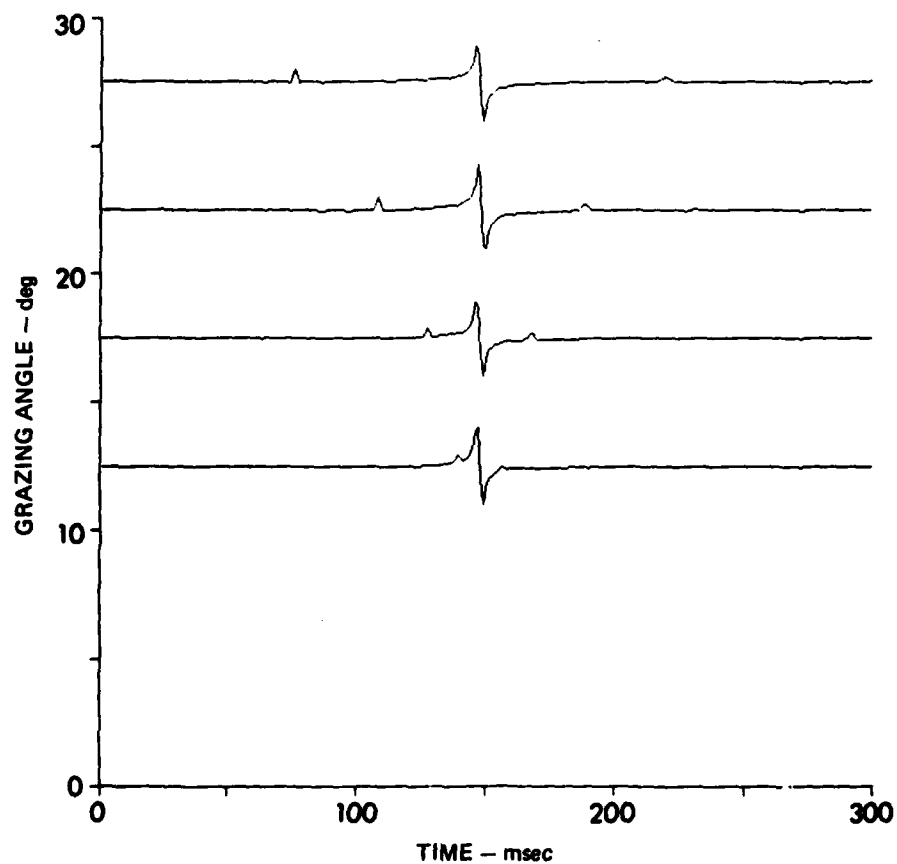


**FIGURE 70**  
**OUTPUT IMPULSE RESPONSE FOR IDENTICAL SOURCE WAVEFORMS**  
**91.4 m SOURCE, GHOSTS IGNORED**



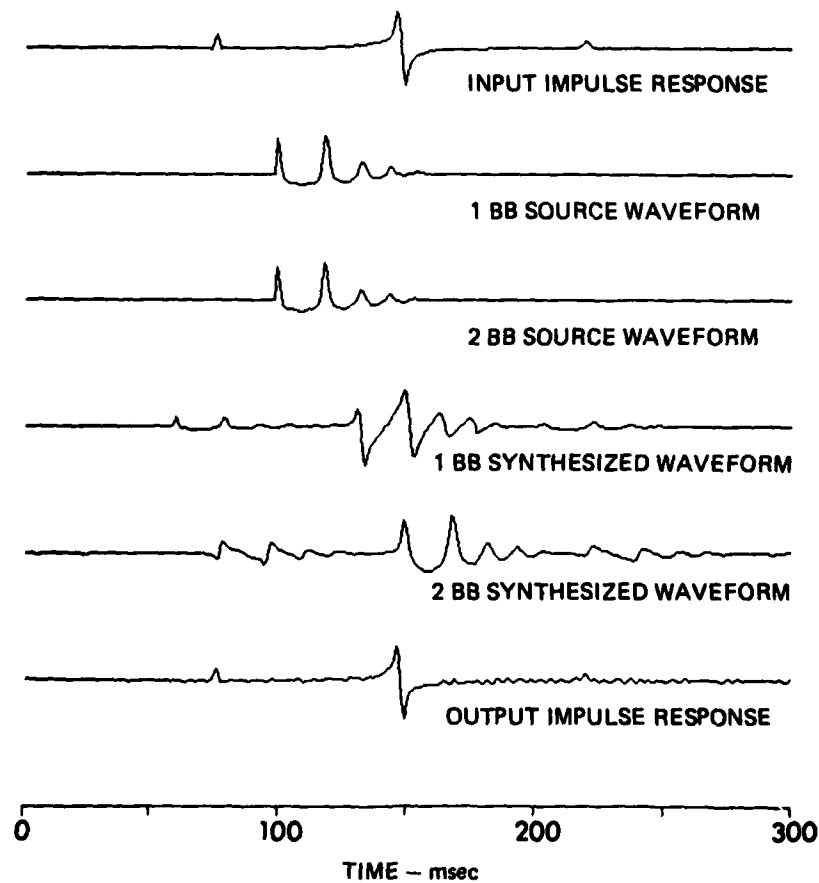


**FIGURE 71**  
**- 1% SOURCE DEPTH ERROR**  
 [(n-1) SOURCE DEPTH IS 1% SHALLOWER THAN (n) SOURCE DEPTH  
 WITH MEAN SOURCE DEPTH OF 244.1 m; GHOSTS IGNORED.]

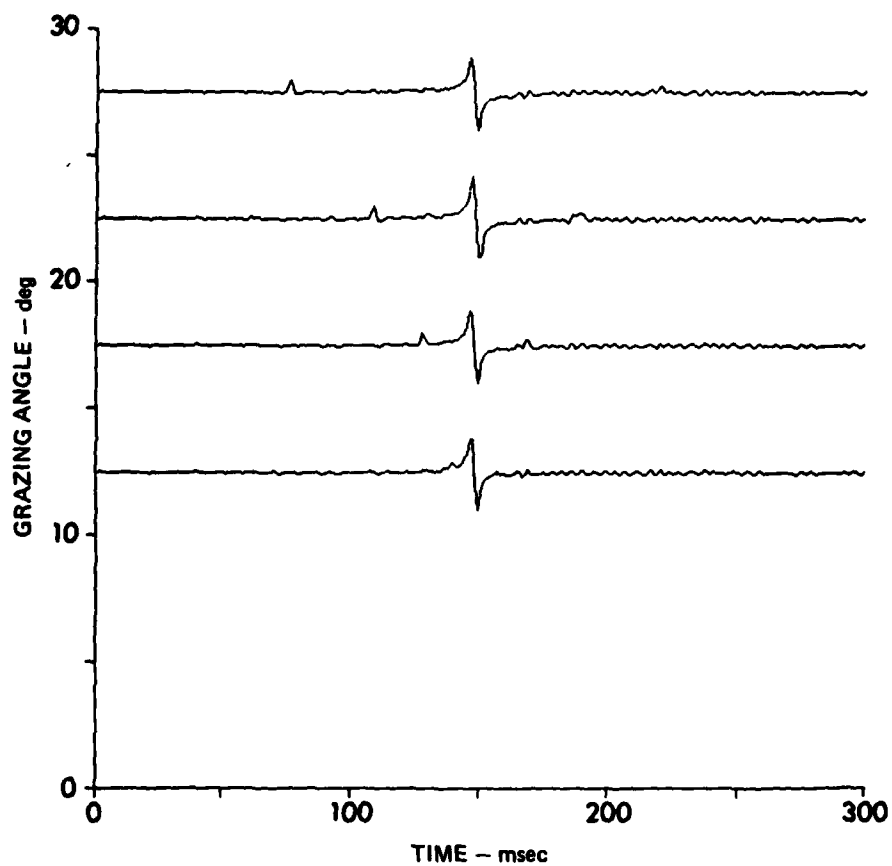


**FIGURE 72**  
**- 1% SOURCE DEPTH ERROR**  
**(244.1 m SOURCE)**

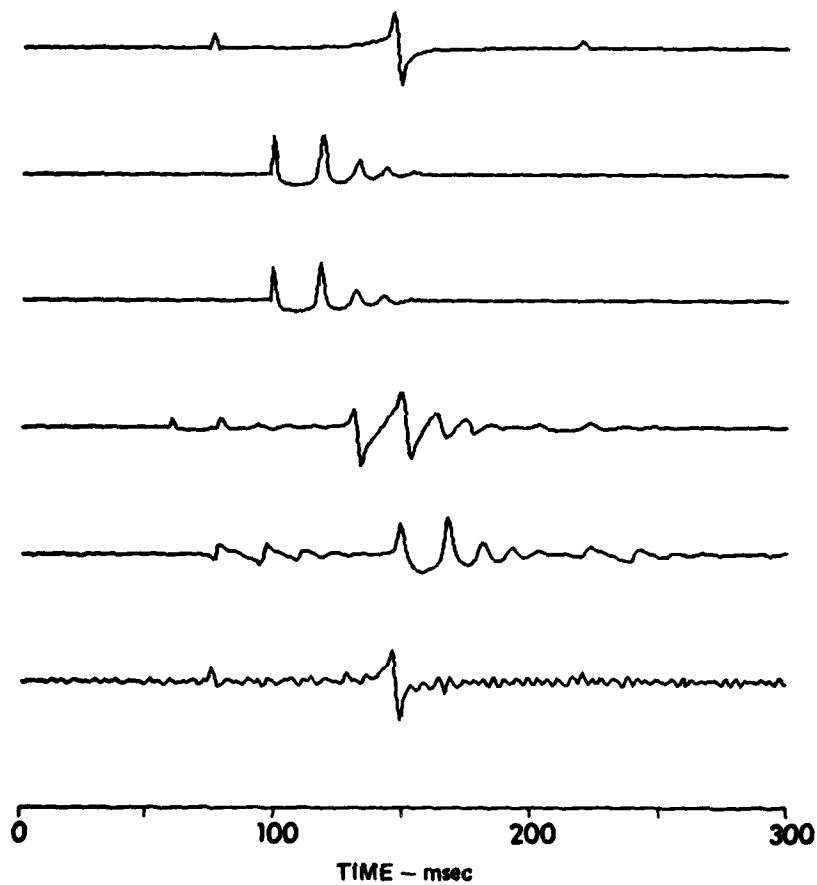


**FIGURE 73**  
**-3% SOURCE DEPTH ERROR**  
**(244.1 m SOURCE)**

ARL:UT  
AS-81-1298  
GDI - GA  
9-30-81

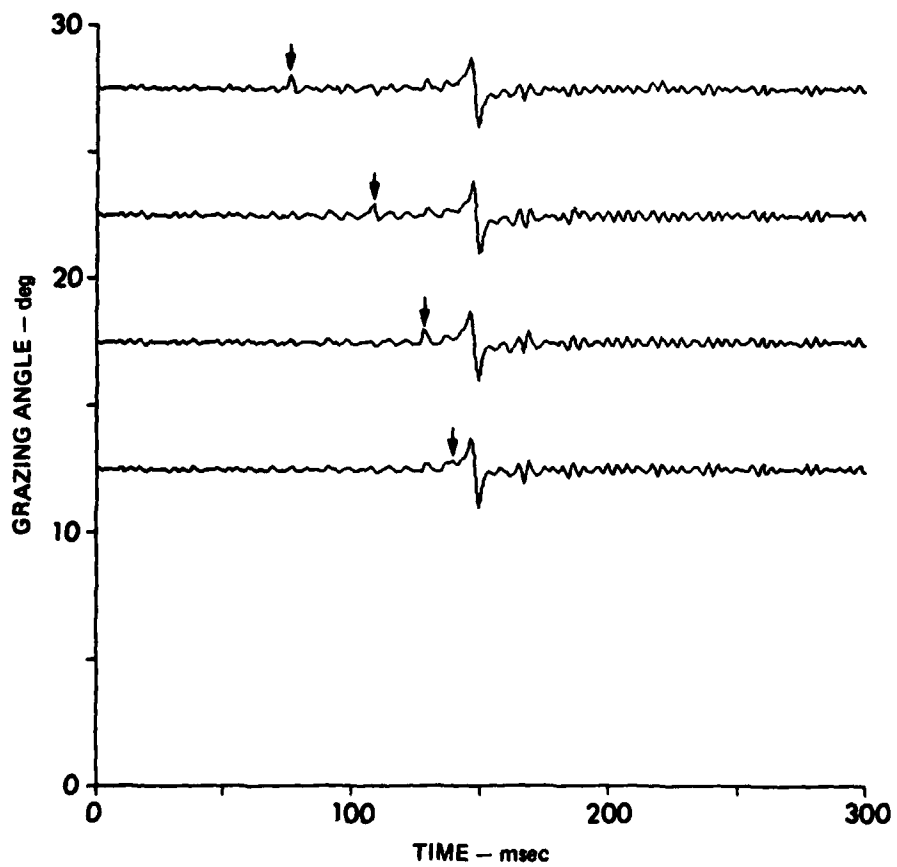


**FIGURE 74**  
**-3% SOURCE DEPTH ERROR**  
**(244.1 m SOURCE)**

ARL:UT  
AS-81-1297  
GDI - GA  
9-30-81

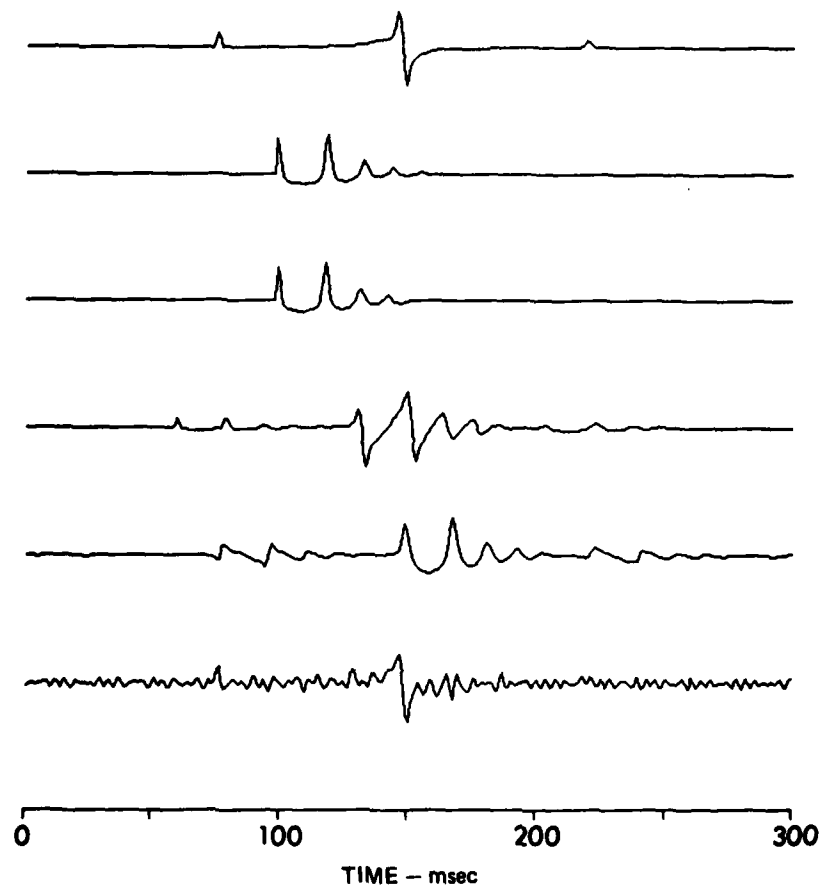


**FIGURE 75**  
**-5% SOURCE DEPTH ERROR**  
**(244.1 m SOURCE)**

ARL:UT  
AS-81-1298  
GDI - GA  
9-30-81

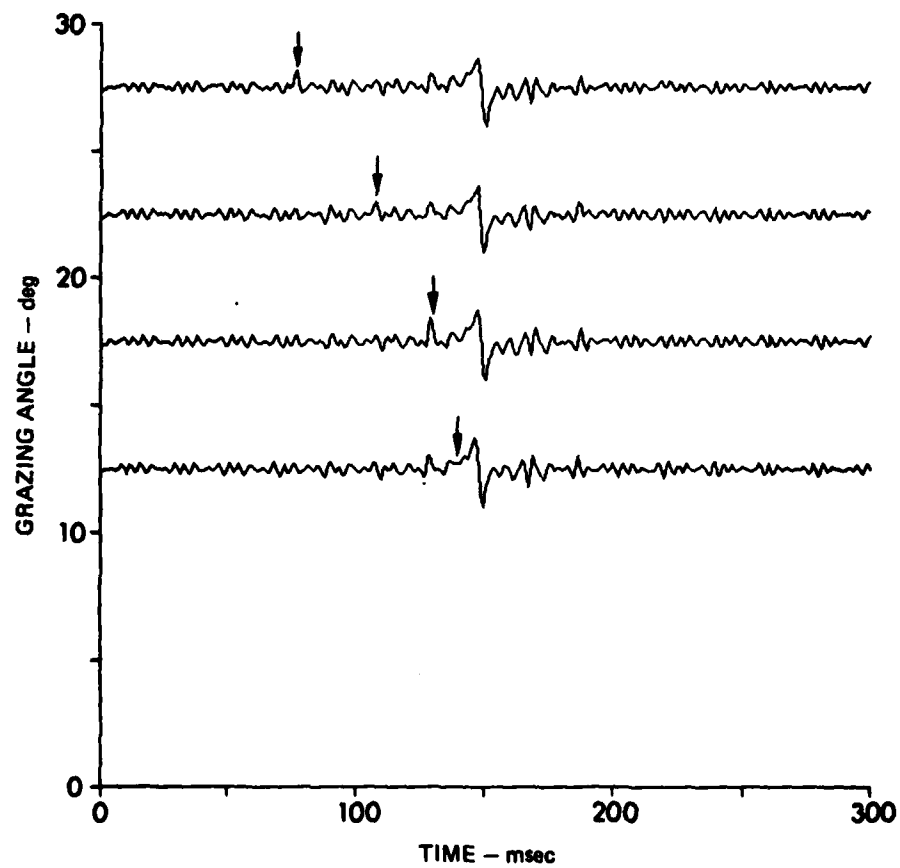


**FIGURE 76**  
**-5% SOURCE DEPTH ERROR**  
**(244.1 m SOURCE)**

ARL:UT  
AS-81-1290  
GDI - GA  
9-30-81

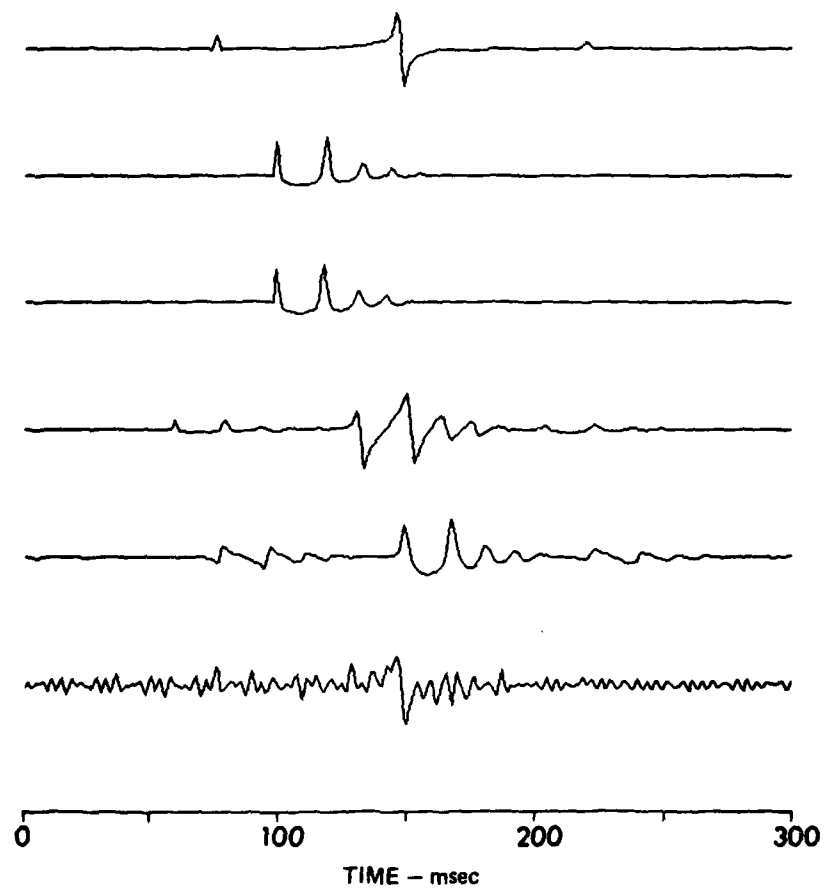


**FIGURE 77**  
**-7% SOURCE DEPTH ERROR**  
**(244.1 m SOURCE)**

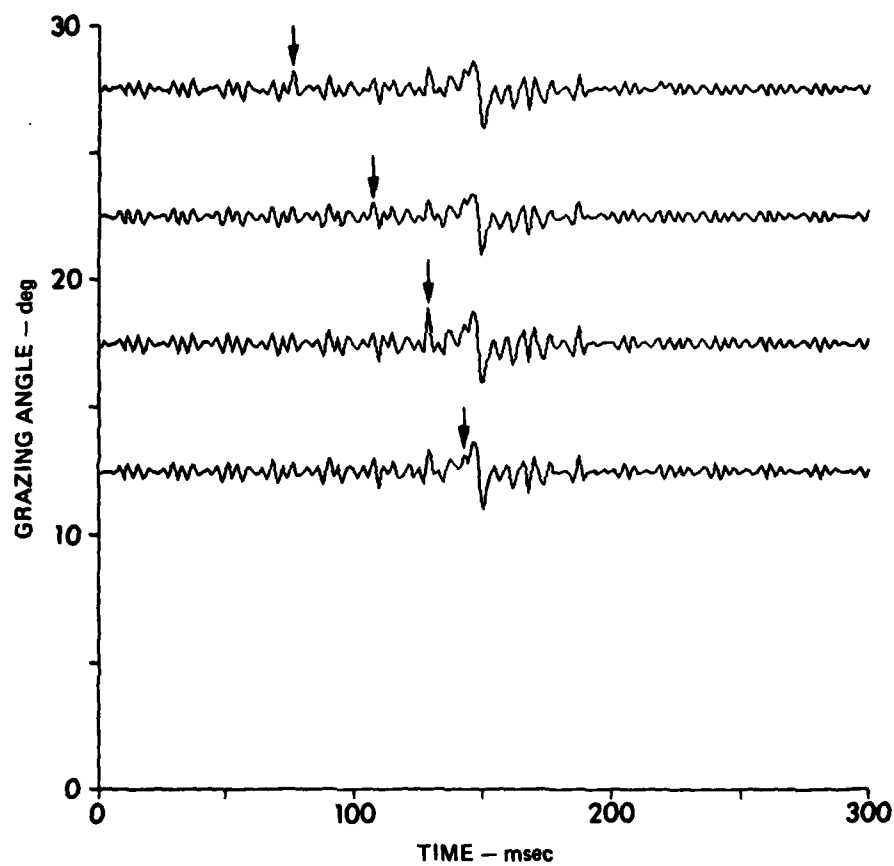


**FIGURE 78**  
**-7% SOURCE DEPTH ERROR**  
**(244.1 m SOURCE)**

ARL:UT  
AS-81-1301  
GDI - GA  
9-30-81



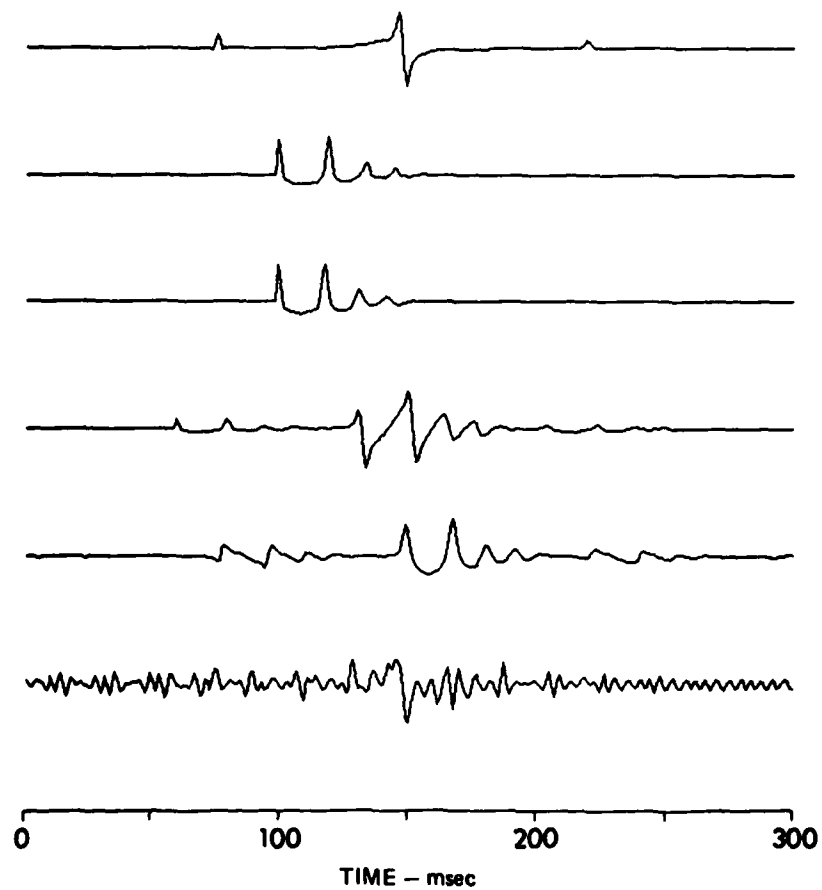


**FIGURE 79**  
**-9% SOURCE DEPTH ERROR**  
**(244.1 m SOURCE)**

ARL:UT  
AS-81-1302  
GDI - GA  
9-30-81

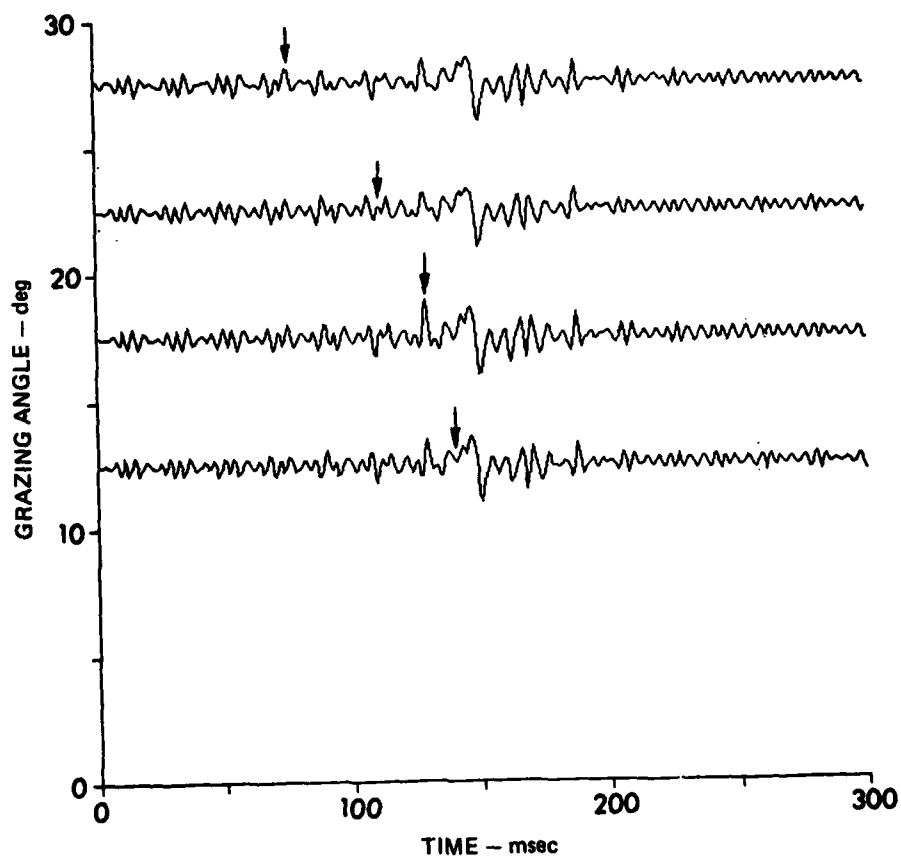


**FIGURE 80**  
**-9% SOURCE DEPTH ERROR**  
**(244.1 m SOURCE)**

ARL:UT  
AS-81-1303  
GDI - GA  
9-30-81

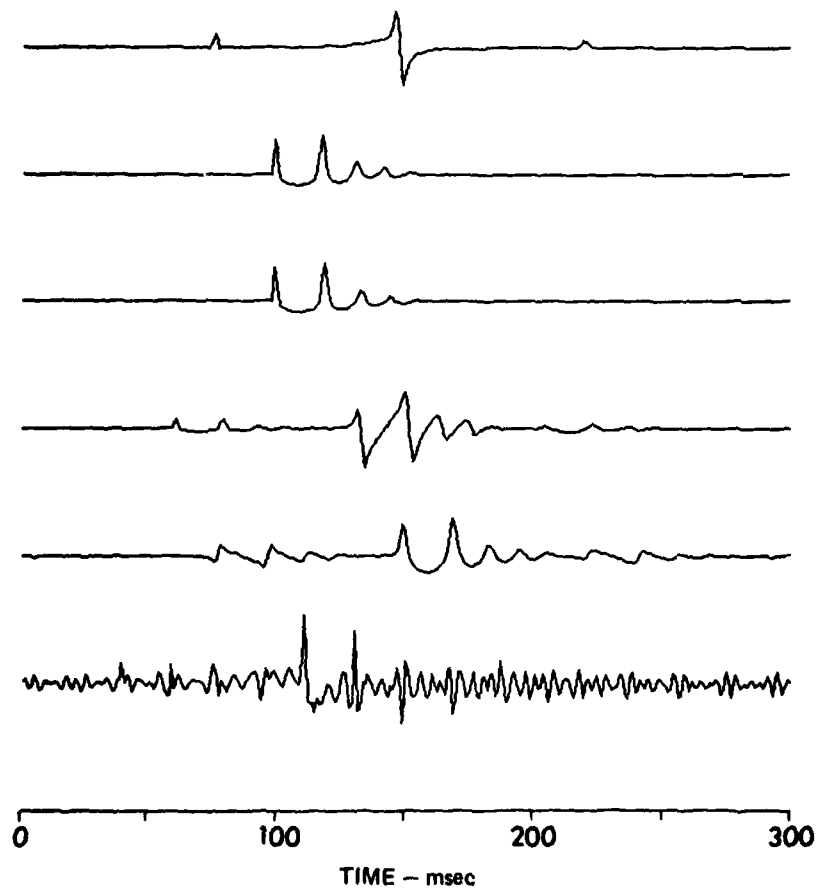


**FIGURE 81**  
**+7% SOURCE DEPTH ERROR**  
**(244.1 m SOURCE; ALL PASS)**

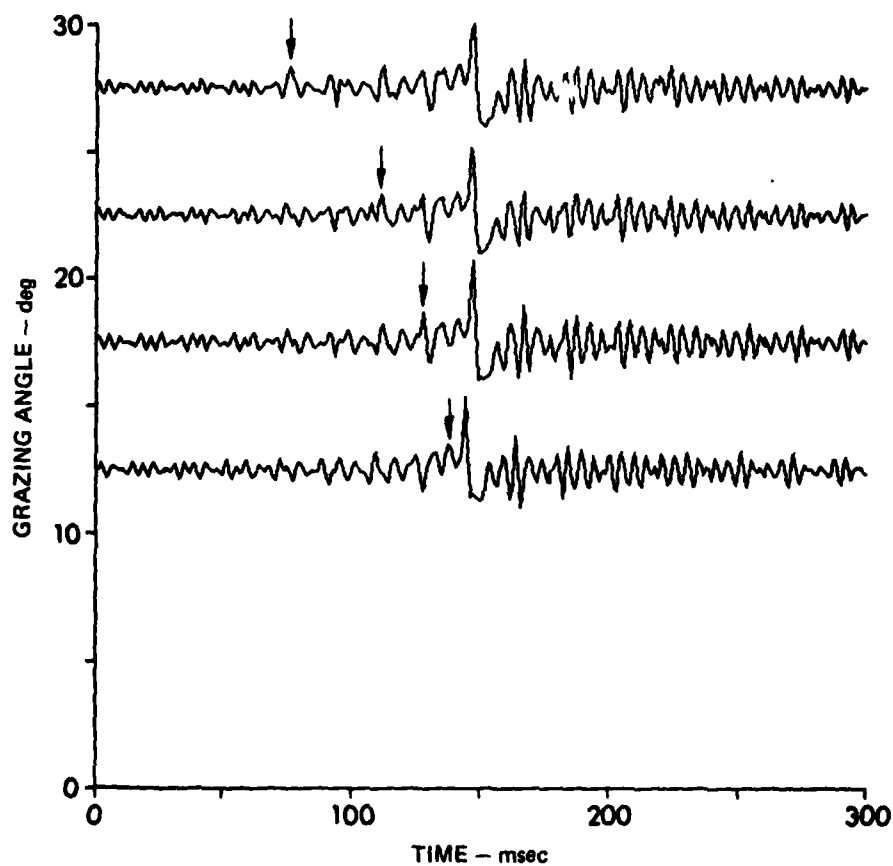


**FIGURE 82**  
**+7% SOURCE DEPTH ERROR**  
(244.1 m SOURCE; ALL PASS)

ARL:UT  
AS-81-1306  
GDI - GA  
9-30-81

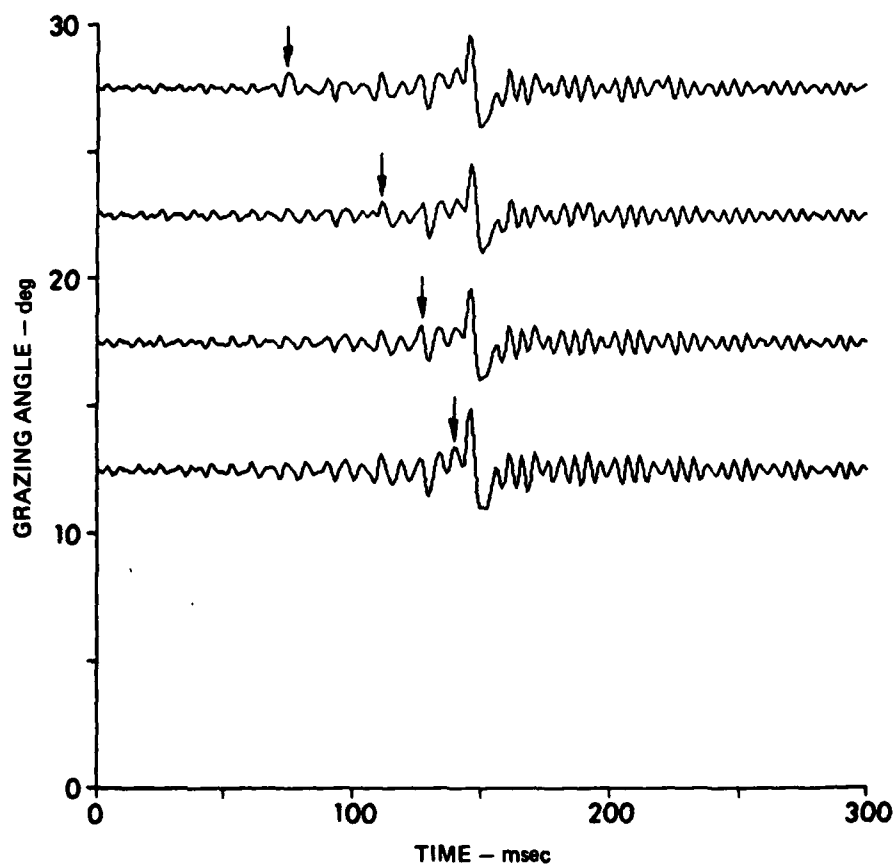


**FIGURE 83**  
**+7% SOURCE DEPTH ERROR**  
 (244.1 m SOURCE; 0-350 Hz)

ARL:UT  
 AS-81-1308  
 GDI - GA  
 9-30-81

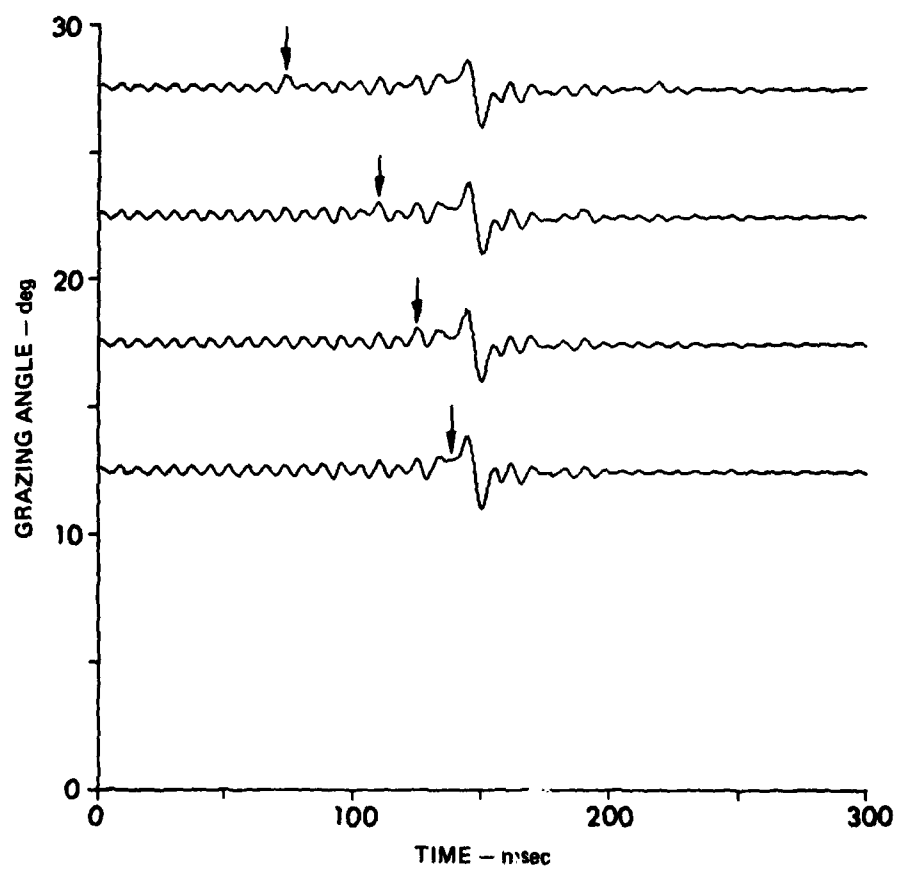


**FIGURE 84**  
**+7% SOURCE DEPTH ERROR**  
 (244.1 m SOURCE; 0-120 Hz)

ARL:UT  
 AS-81-1307  
 GDI - GA  
 9-30-81

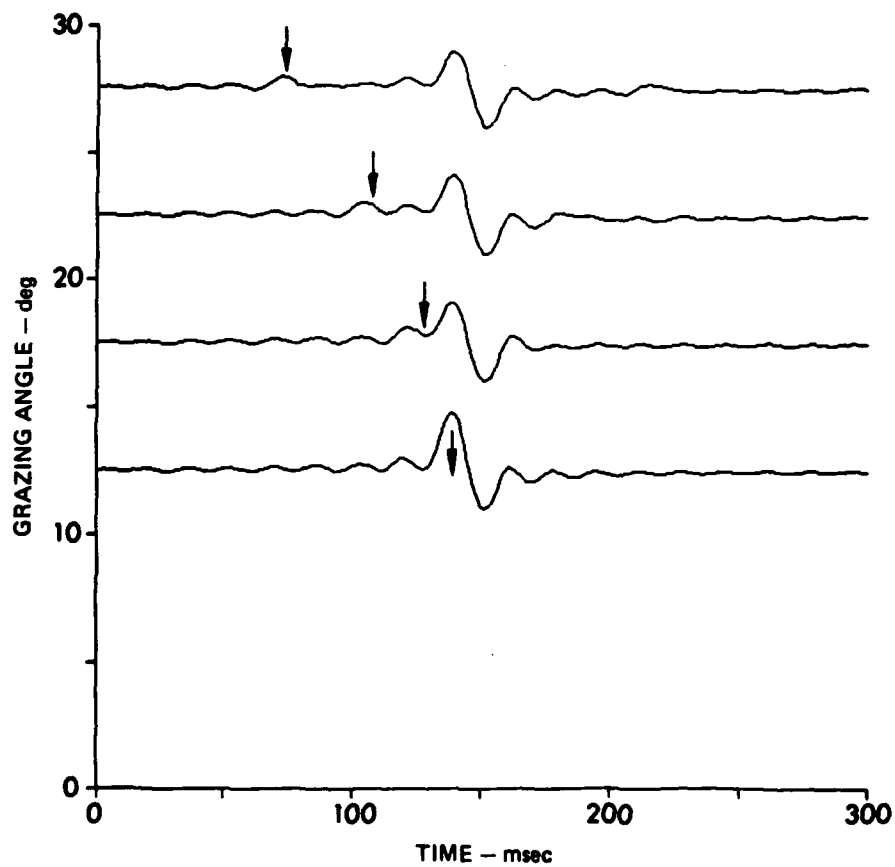


**FIGURE 85**  
**+7% SOURCE DEPTH ERROR**  
**(244.1 m SOURCE; 10-50 Hz)**

ARL:UT  
AS-81-1308  
GDI - GA  
9-30-81

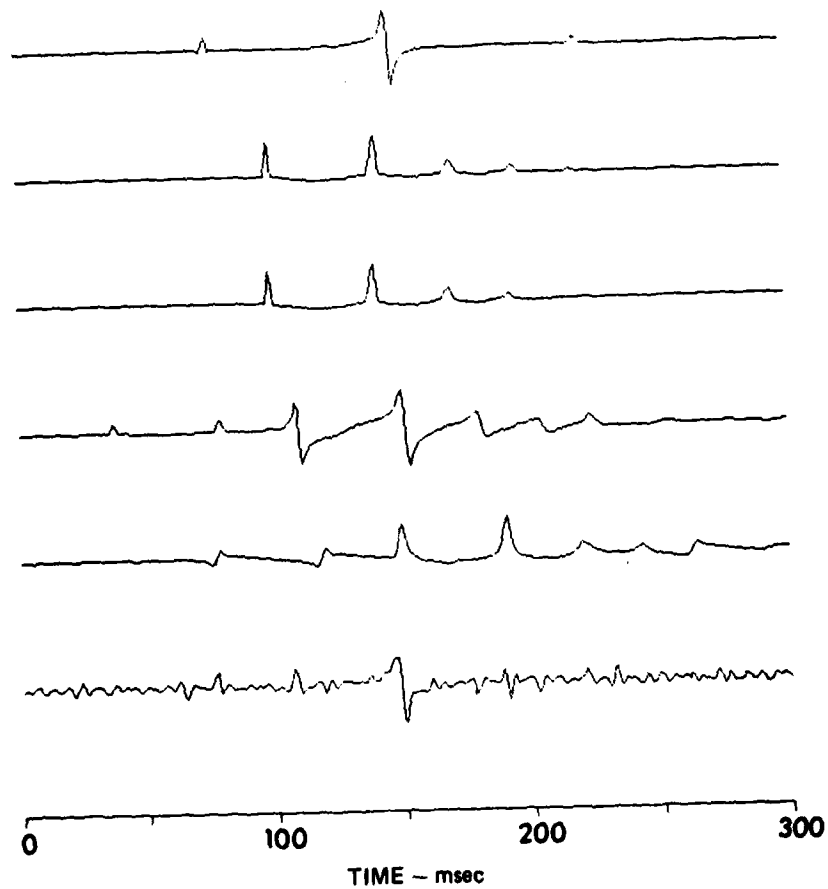


**FIGURE 86**  
**-3% SOURCE DEPTH ERROR**  
**(91.4 m SOURCE)**

ARL:UT  
AS-81-1309  
GDI - GA  
9-30-81



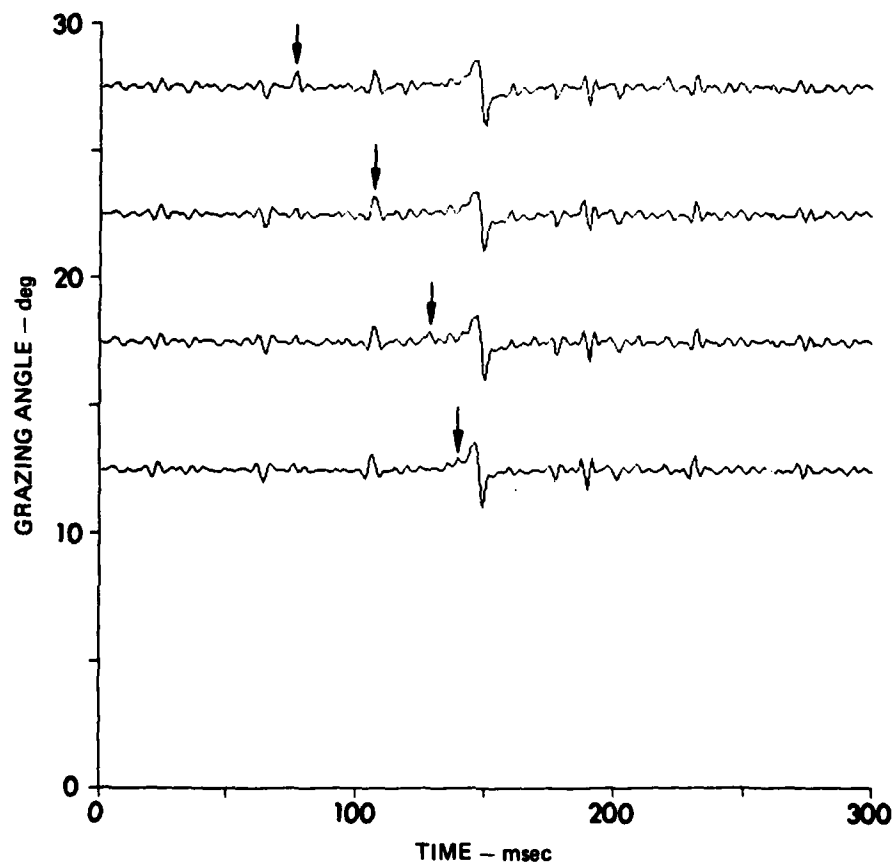


**FIGURE 87**  
**-3% SOURCE DEPTH ERROR**  
**(91.4 m SOURCE)**



**FIGURE 88**  
**-3% SOURCE DEPTH ERROR**  
**(18.3 m SOURCE)**

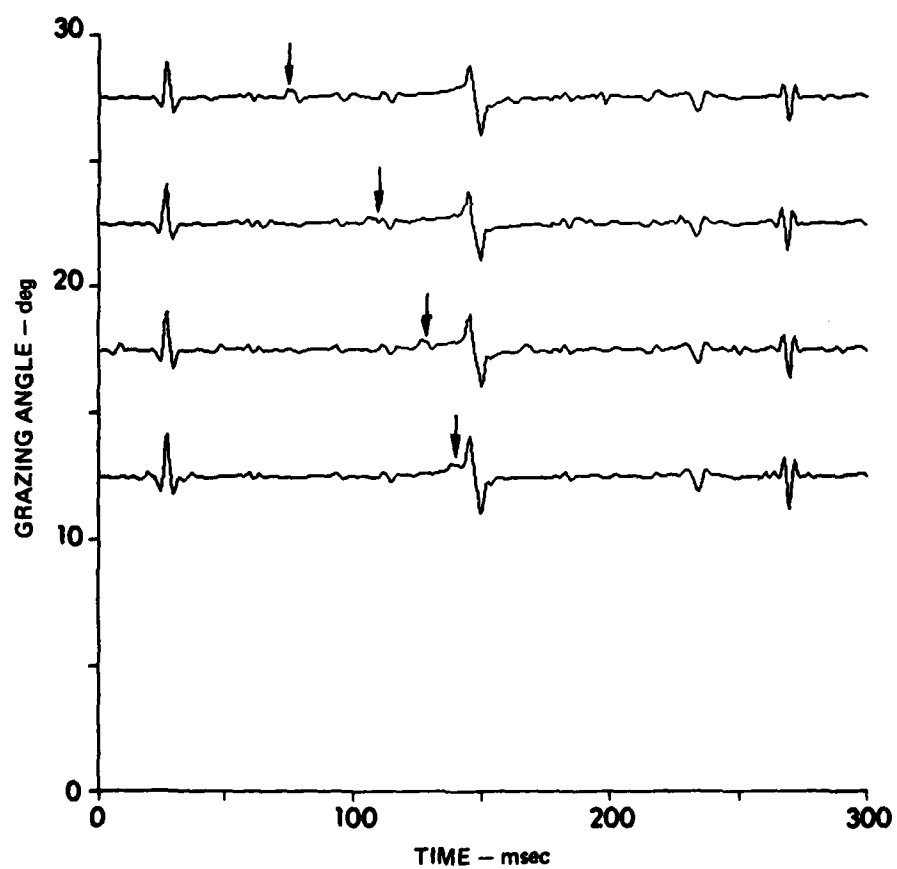


**FIGURE 89**  
**-3% SOURCE DEPTH ERROR**  
**(18.3 m SOURCE)**

ARL:UT  
AS-81-1312  
GDI - GA  
9-30-81

waveform. It is seen for all-pass deconvolution of sources with mean depths at 244 m that the deconvolution cannot tolerate greater than about 3% source depth differences.

However, as shown in Figs. 81-85, bandpass filtering reduces the noise level at the cost of resolution. Figures 81 and 82 show an all-pass deconvolution of waveforms with mean source depths of 244.1 m in which the 1 BB source waveform represents 7% deeper detonation than the 2 BB source waveform. It is seen that without a priori knowledge of the impulse response the specular reflection is not detectable. Figures 83-85 show bandpasses of 0-350 Hz, 0-120 Hz, and 10-50 Hz, respectively, and it is seen that the reflected event is progressively easier to detect although the resolution decreases.

Figures 86-89 show the effects of source depth differences of 3% for mean depths of 91.4 m and 18.3 m. It is seen that 3% source depth differences make the specular reflection almost undetectable.

Finally, Fig. 90 shows an example of the deconvolution of five bottom bounce waveforms from six bottom bounce waveforms. The same multiple bottom bounce data as shown in previous sections of this report were used. The experiment geometry was a 244.1 m source and a 256 m receiver. A flat bandpass was applied from 40-160 Hz. This clearly identified the refracted arrival and a reflected arrival, although it is ambiguous whether this is the specular reflection or a subbottom reflection. The delay between these two components is the reflection-refraction delay recovered by the correlation techniques. The relative advance of the specular reflection expected a priori for this turbidite province is also shown in the figure. The data not clearly support identification of an arrival at these times. Energy

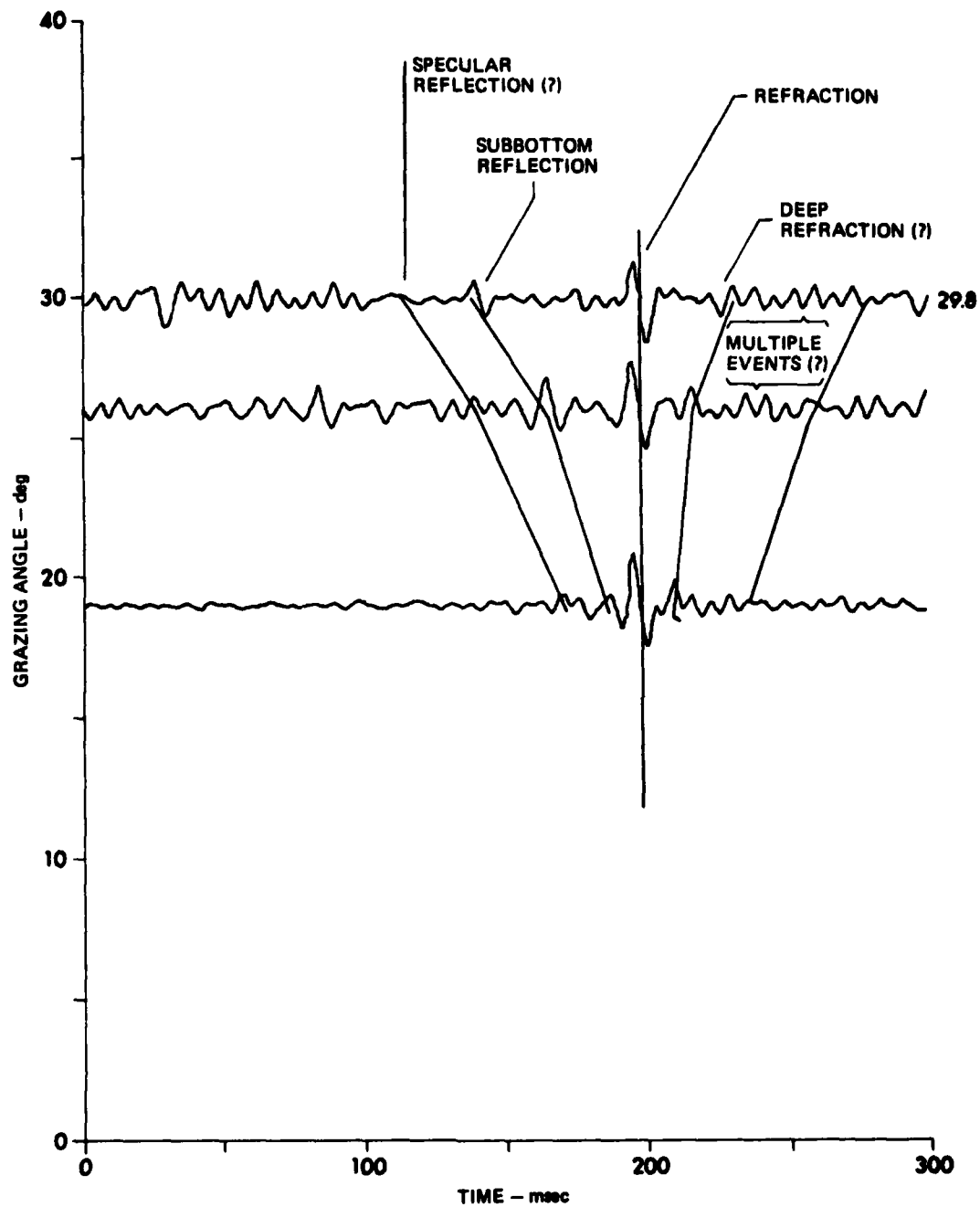


**FIGURE 90**  
**EXAMPLES OF DECONVOLUTION OF FIVE BOTTOM BOUNCE WAVEFORMS**  
**FROM SIX BOTTOM BOUNCE WAVEFORMS IN TURBIDITE PROVINCE**  
 (244.1 m SOURCE DEPTH; 256 m RECEIVER DEPTH; 40-160 Hz FLAT BANDPASS)

trailing the refracted arrival is tentatively identified as due to a deeper refraction and multiple reflection events.

## CHAPTER 5

### GEOLOGIC INFERENCES

In the past sections the correlation techniques and the impulse response estimation technique imply that two components dominate the bottom return, a refracted component and a reflected component. The reflected component may be either the specular reflection or a subbottom reflection. If it is a subbottom reflection then the geoacoustic structure in this province is significantly different than that predicted a priori on the basis of other seismic evidence and coring data (Hamilton and Bachman, personal communication). On the other hand, if the reflected component is the specular reflection, it will be shown that the velocity profile for the upper few hundred meters in the subbottom is significantly greater than that predicted a priori. Of course the correlation techniques and the impulse response estimates indicated that it is likely that there are other components of the ocean bottom transfer function besides the single reflection and the refracted component. Although these other arrivals are ignored in obtaining estimates of velocity and attenuation as a function of depth, it will be seen that the results imply that there are more than two components.

The technique used here to determine the velocity profile from the time delay between the reflected and refracted components is due to Focke (1981) and makes use of a computer program written by Smith (1981). The method is essentially one of ray tracing the reflected and refracted

paths and recognizing that the ray parameter is the reciprocal of the velocity at the turning point of the refracted arrival, i.e.,

$$\frac{\partial t}{\partial r} = p = \frac{1}{C_v} \quad , \quad (5.1)$$

where  $C_v$  is the vertex velocity,  $r$  is the range, and  $t$  is the time.

In the present study, since the arrival time of the refracted path is not known, but rather the time difference between the reflected and refracted components, Eq. (5.1) becomes

$$\frac{\partial \Delta t}{\partial r} = p(\theta_w) - p(\phi) = \frac{\cos(\theta_w)}{C_w} - \frac{\cos(\phi)}{C_w} \quad ,$$

where  $\phi$  is the reflection angle,  $\theta_w$  is the refraction angle, and  $C_w$  is the water sound speed at the bottom. The travel time differences were determined from the correlation techniques of Section 3.5 using, in particular, Fig. 56.

The refraction angle is then found using

$$\cos(\theta_w) = C_w \frac{\partial \Delta t}{\partial r} + \cos(\phi) \quad .$$

The range through the sediment for the refracting ray will be the difference between the ranges for reflected and refracted paths through the water determined by ray tracing.

$$r(\theta_w) = R(\phi) - R(\theta_w) \quad .$$



The travel time through the sediment is determined in the same manner.

$$\tau(\theta_w) = \Delta t(\phi) + T(\phi) - T(\theta_w) \quad .$$

Since the time delay in the water column can be calculated for any given angle, knowledge of the time difference between the reflected and refracted arrivals allow for the sound speed to be determined for a range  $r$  associated with an angle  $\theta_w$  related to a depth  $h$ ,

$$h = \frac{r \sin \theta_w}{2(\cos \theta_w + 1)} \quad .$$

The sound speed at this depth can be calculated from Eq. (5.1).

The result of this procedure for the travel time differences between the reflected and refracted components indicated in previous sections is shown in Fig. 91. It is seen that the sound speeds indicated from the multiple bottom bounce signals is greater than that predicted a priori for the upper 200 m of sediment. This sound speed profile was constrained at the water-sediment interface to be the sound speed determined a priori from coring data in this region. Without this constraint the data indicated a sound speed at the water sediment interface of about 1560 m/sec, which is a sound speed ratio at the water-sediment interface of 1.03 rather than 1.00. Regardless of which surface value is used the sound speed profiles determined from the time delays of the multiple bottom bounce data merge after about 40 m into the subbottom.

The velocity profile indicated in Fig. 91 for the multiple bottom bounce data can be interpreted in terms of three layers with linear

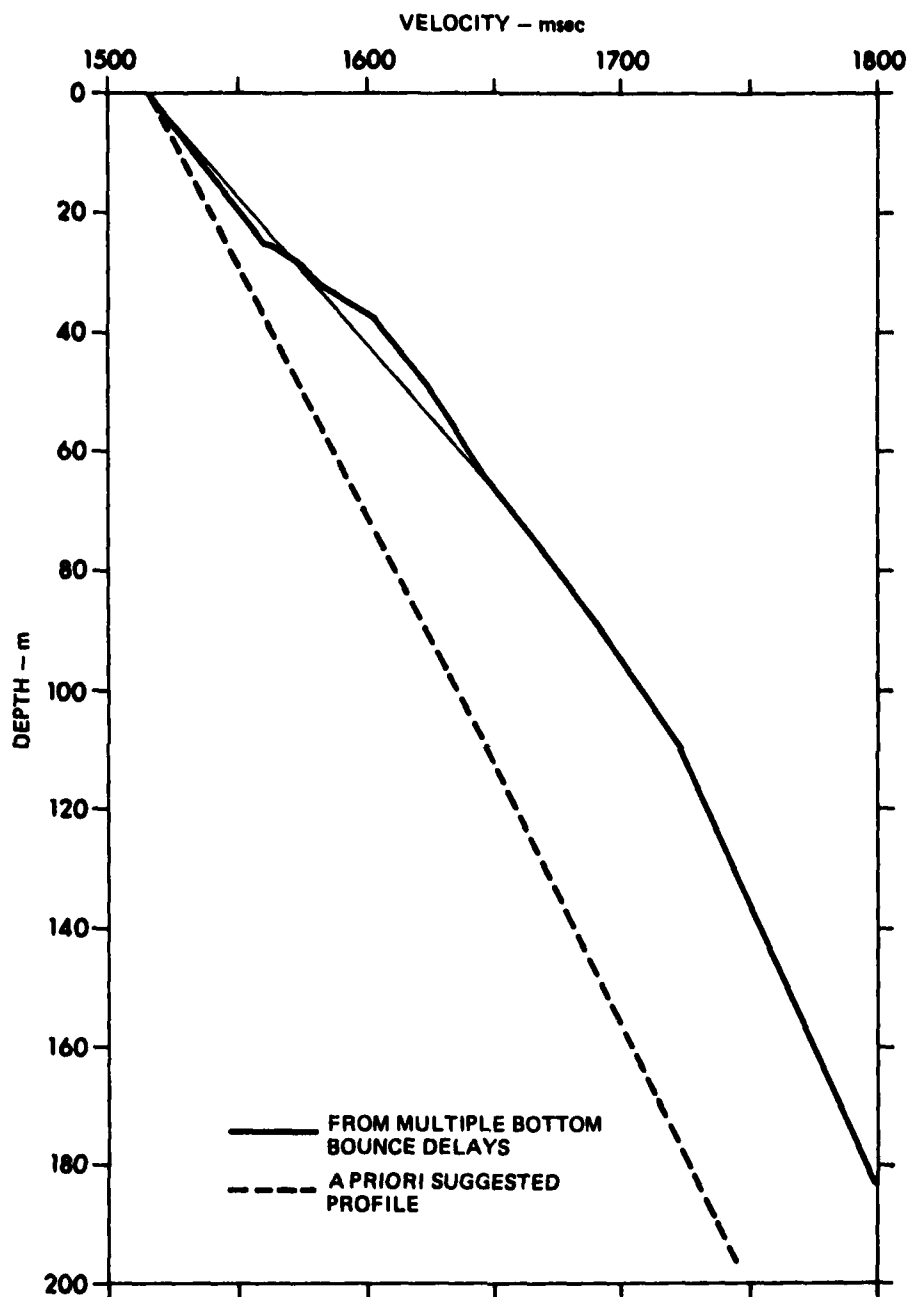


**FIGURE 91**  
**VELOCITY PROFILE OBTAINED BY INVERTING TIME DELAYS**  
**BETWEEN REFLECTED AND REFRACTED EVENTS OBSERVED**  
**IN THE AUTOCORRELATIONS OF MULTIPLE BOTTOM BOUNCE**  
**ACOUSTIC SIGNALS MEASURED IN A TURBIDITE PROVINCE**

gradients that vary continuously across the interfaces. The first layer varies from 1515 m/sec at the surface to 1640 m/sec at 60 m, a gradient of  $2.08 \text{ sec}^{-1}$ . The third layer varies from 1715 m/sec at 110 m to 1800 m/sec at 185 m, a gradient of  $1.13 \text{ sec}^{-1}$ .

This certainly is not the only interpretation of the variation of sound speed as a function of depth from this profile, particularly in the upper 60 m, but it is a fairly simple model and matches most of the curve. Using this velocity profile, an attenuation profile for the turbidite province was calculated from the bottom loss data using the method of Mitchell and Focke (1980).

Figure 92 shows the attenuation profile calculated. It is seen that the attenuation varies from 0.050 at the surface to about 0.015 at a depth of about 160 m. The darker line represents the interpreted attenuation curve for the attenuation values calculated for each of five frequency bins of 25, 50, 100, 200, and 400 Hz. At shallow depths the interpreted curve should be biased with respect to the higher frequency bins since it is difficult to measure the low loss involved at the lower frequencies. At the greater depths the interpreted curve should be biased with respect to the lower frequency bins since the higher frequencies will be attenuated to the noise level. For all frequency bins other than 400 Hz the attenuation curves are close together below 50 m. Above 50 m there are large variations of attenuation as a function of depth. This is interpreted as evidence of unmodeled reflectivity in the upper 50 m of sediment. Periodic occurrence of reflectors in the subbottom would act as a high pass filter of the ocean bottom transfer function while reflections due to sharp, but continuous, changes in impedance with depth act as low pass filters.

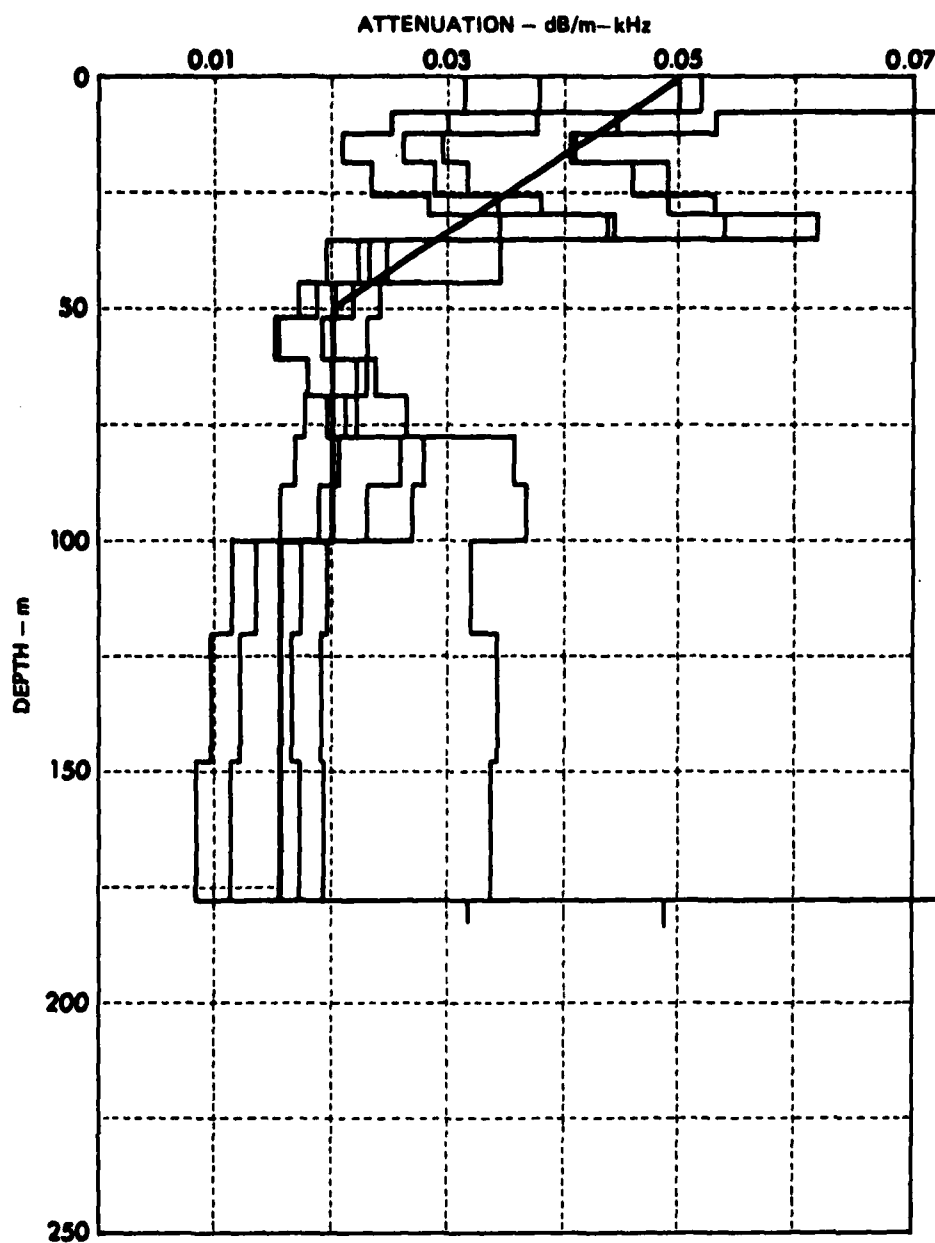


**FIGURE 92**  
**ATTENUATION PROFILE OBTAINED FROM MULTIPLE**  
**BOTTOM BOUNCE ACOUSTIC SIGNALS MEASURED IN**  
**A TURBIDITE PROVINCE USING THE VELOCITY**  
**PROFILE SHOWN IN Fig. 91 AND BOTTOM LOSS DATA**

Table IV shows a geoacoustic model derived from the velocity and attenuation profiles of Figs. 91 and 92. The densities were calculated from the velocity-density relationships of Hamilton for terrigenous sediments. Below 180 m the geoacoustic model was found by connecting a line between the geoacoustic parameters at this depth with the parameters suggested a priori at 1231 m for this province. Presumably, there is a reflector at this depth identified in other seismic work.

Table V shows the geoacoustic model derived a priori for this province. It is seen that this model suggests a gradient at the surface of about  $1.15 \text{ sec}^{-1}$  and attenuation values that are almost an order of magnitude greater than those predicted from the multiple bottom bounce data. Note also that no subbottom reflectors are identified above 1231 m.

In the rest of this section autocorrelograms and power cepstra will be calculated synthetically from the geoacoustic models shown in Tables IV and V. Comparing the synthetic results to the data autocorrelograms and power cepstra lead to the expected conclusion that the synthetics calculated from the geoacoustic model derived from the multiple bottom bounce data agree with data correlations better than those derived using the a priori model. However, it is also found that there are significant differences between data correlations and the synthetic correlations calculated with the new geoacoustic model.

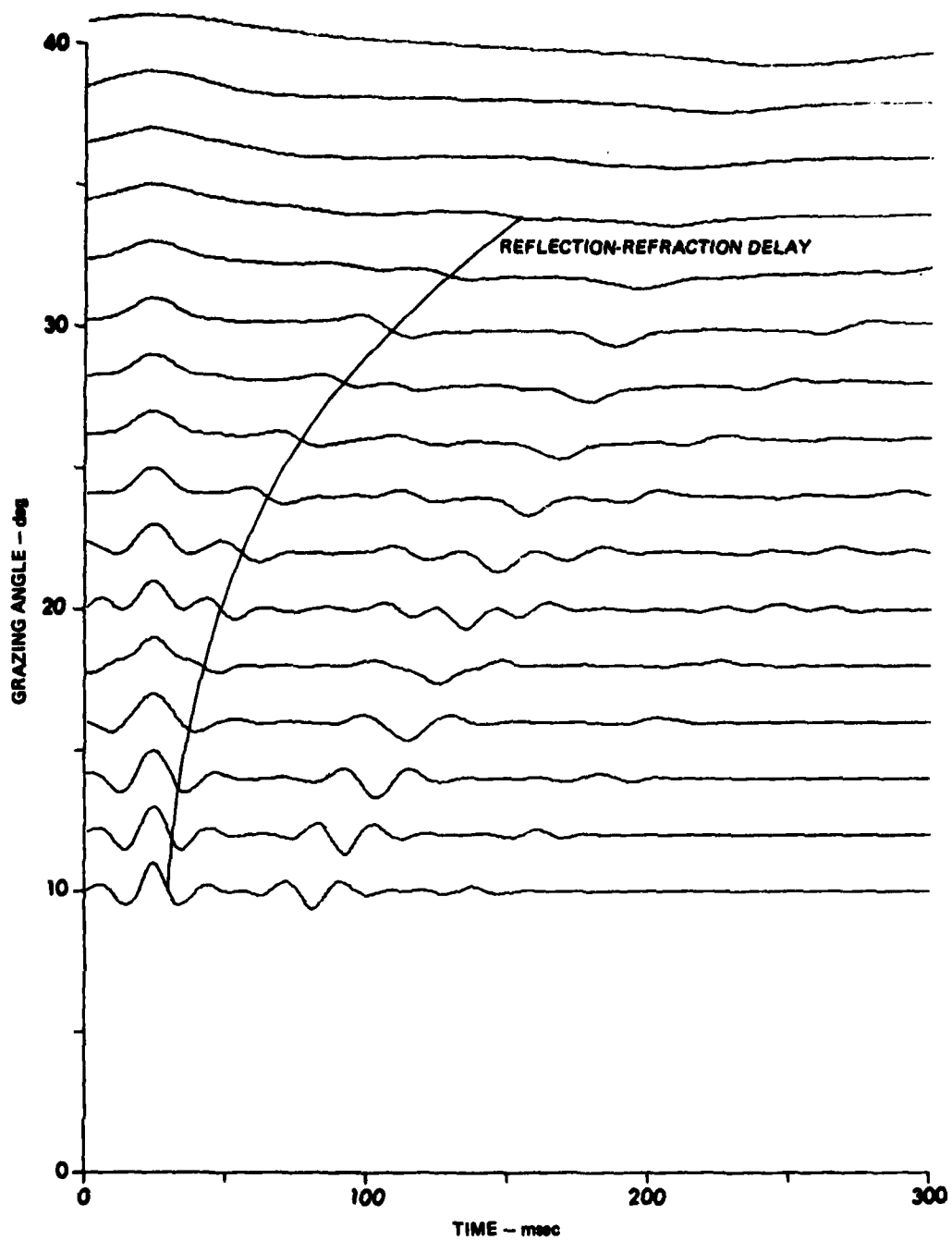
Figure 93 shows a synthetic autocorrelogram calculated from the a priori geoacoustic model. The reflection-refraction component and the ghost components of the acoustic signals can be observed on the autocorrelogram as in the data autocorrelogram shown in Fig. 55. However, there are some significant differences between the autocorrelograms.

TABLE IV  
NEW GEOACOUSTIC MODEL DERIVED  
FROM MULTIPLE BOTTOM BOUNCE ACOUSTIC DATA

<u>Depth (m)</u>	<u>Velocity (m/sec)</u>	<u>Attenuation (dB/m-kHz)</u>	<u>Density (g/cm<sup>3</sup>)</u>
0-	1514.5		1.04306
0+	1515	0.048	1.59
60	1640	0.020	1.67
110	1715	0.017	1.76
185	1800	0.015	1.85
1231-	2443	0.02	2.26
1231+	2565	0.02	2.30
1724	2900	0.02	2.40
2217	3735	0.02	2.49
2217	3400	0.02	2.52
2270	3685	0.02	2.57
3820-	3975	0.02	2.61
3820+	4600	0.02	2.50

TABLE V  
GEOACOUSTIC MODEL SUGGESTED A PRIORI  
(Shear Waves Ignored)

<u>Depth</u> <u>(m)</u>	<u>Velocity</u> <u>(m/sec)</u>	<u>Attenuation</u> <u>(dB/m-kHz)</u>	<u>Density</u> <u>(g/cm<sup>3</sup>)</u>
0-	1514.5		1.04306
0+	1515	0.10	1.59
100	1638	0.11	1.67
200	1750	0.12	1.80
300	1851	0.13	1.91
400	1943	0.14	2.02
500	2026	0.14	2.10
600	2101	0.12	2.13
700	2168	0.11	2.15
800	2230	0.10	2.18
900	2286	0.08	2.20
1000	2337	0.07	2.22
1100	2385	0.06	2.24
1200	2429	0.05	2.25
1231-	2443	0.05	2.26
1231+	2565	0.05	2.30
1724	2900	0.03	2.40
2217-	3235	0.02	2.49
2217+	3400	0.02	2.52
2770	3685	0.02	2.57
3820-	3975	0.02	2.61
3820+	4600	0.02	2.50



**FIGURE 93**  
**SYNTHETIC AUTOCORRELOGRAM USING A PRIORI GEOACOUSTIC**  
**MODEL SHOWN IN TABLE V**



First, the synthetic autocorrelogram is much more dominated by lower frequencies than the data autocorrelogram. This is clear evidence that the attenuations used in the a priori model are too high. In addition, although the delays of the ghosted components are nearly the same for the two autocorrelograms, the reflection-refraction delay is considerably different. This indicates that the plane wave assumption made for the calculation of the ghost delays in the synthetic data is approximately valid, but that the velocity profile in the sediment is inaccurate. Thus, the expected conclusion is reached that the velocity and attenuation profiles calculated for this region a priori are inconsistent with the data.

Figures 94 and 95 show synthetic power cepstra using the a priori model. It is seen that the ghosts and reflection-refraction delays can be detected and that whitening the power spectra before calculating the power cepstra has little effect on the synthetic power cepstrum plots. The amplitude variation of those components as a function of grazing angle is dependent somewhat on attenuation along the refracted path as evident in the autocorrelogram, Fig. 93. On the other hand, some of these variations such as those that go from high amplitude to low amplitude back to high amplitude again are due to the coupling between frequency components. This illustrates the major disadvantage of the power cepstrum, which is especially significant as the number of components in the ocean bottom transfer function becomes large (beating patterns become very complicated and amplitude variations become hard to predict).

On the other hand, the major advantage of the power cepstrum over the autocorrelation is that a single spike represents the time delay between components with an amplitude determined by the average dynamic

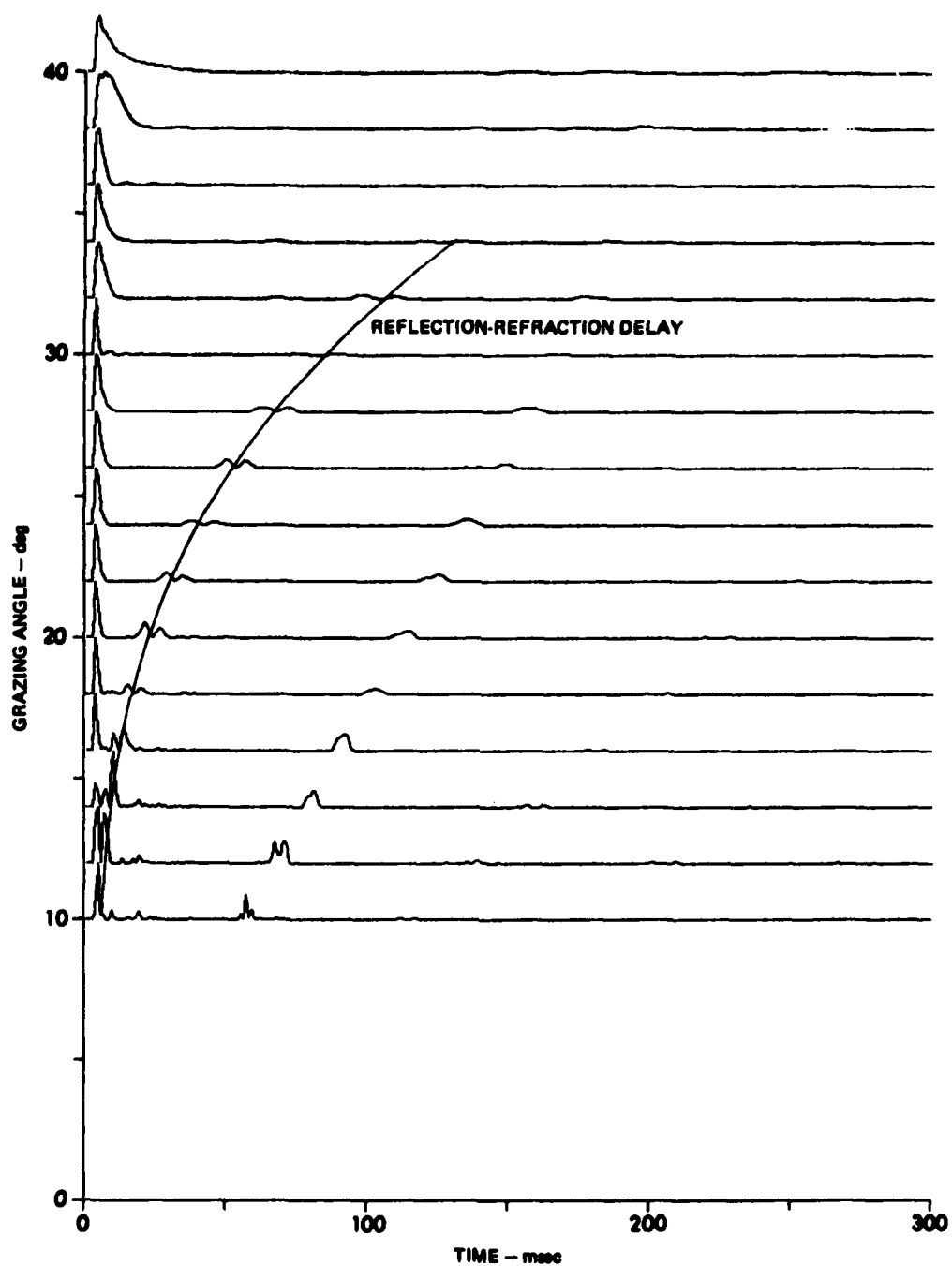


**FIGURE 94**  
**SYNTHETIC POWER CEPSTRA USING A PRIORI GEOACOUSTIC MODEL**

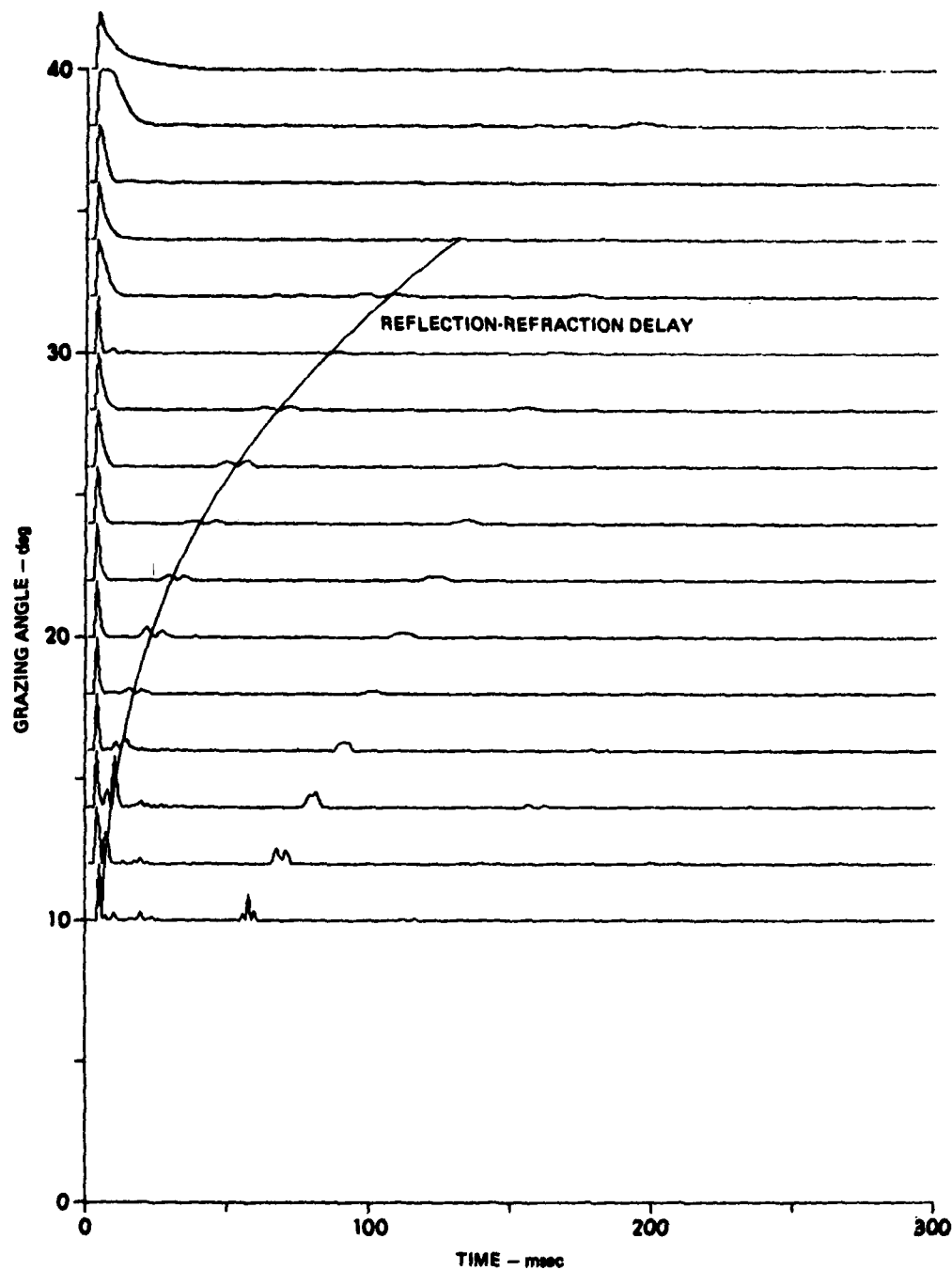


**FIGURE 95**  
**SYNTHETIC POWER CEPSTRUMS USING A PRIORI GEOACOUSTIC MODEL**  
**WITH WHITENED POWER SPECTRA**

range of the ripple. For some signals this makes the time delay easier to detect using the power cepstrum than using the autocorrelation, which gives a pulse at the time delay between components with a power spectrum determined by the crosspower spectrum of the impulse response components. Thus, if the correlated energy of the impulse response is dominated by low frequencies the delay will be hard to resolve in the autocorrelation. This effect can be seen by comparing Figs. 93 and 94 where the reflection-refraction delay is detected easier on the power cepstrum than the autocorrelation for angles less than  $16^\circ$ .

Comparing the synthetic power cepstra calculated using the a priori model (Figs. 94 and 95), with the data power cepstra (Figs. 60-63), it is seen that there are some significant differences. First, there are many more cepstral peaks in the data than in the synthetics. This is believed to be due primarily to shallow reflections, for instance in the upper 50 m, although it may also be due to the effects of beating between quefrequencies and additive random noise, which may be colored.

Second, many of the peaks found both in the data and in the synthetics are of notably different amplitudes and shapes. For instance, the first bubble pulse peak in the data is very large, whereas the first bubble pulse peak is barely visible in the synthetics. Also the large peak at very low quefrequencies is much broader in the synthetics than in the data. Finally, the peak associated with the reflection-refraction delay is not bimodal nearly as soon in the data as in the synthetics. All of these effects are believed to be due primarily to the fact that the attenuation values in the a priori model are too high. The fact that the ghost delays

are more poorly defined in the data is believed to be due to greater subbottom reflectivity and an attendant increase in quefreny beating.

Figures 96-98 show the synthetic correlations using the new geoacoustic model shown in Table IV. There are some similarities and some important differences.

Comparing the autocorrelograms, Figs. 55 and 96, it is seen that the main components of energy in the autocorrelogram of the data are reproduced in the synthetic autocorrelogram. The quiet regions on the autocorrelogram of the data are quiet on the synthetic autocorrelogram. This shows that the source-receiver geometry is well modeled in the data and the main components of the ocean bottom transfer function are modeled.

There are, however, some significant differences between the autocorrelograms. First the autocorrelations of the data at angles less than about  $26^{\circ}$  have significantly greater high frequency content than the synthetic autocorrelations at the same angles. This indicates that the attenuation values for the new geoacoustic model are too high at the shallow depths.

The occurrence of high frequencies at low angles for the data autocorrelogram may be due to reflections at shallow depths. The occurrence of reflections has the effect of a high pass filter since low frequencies do not see reflectors spaced considerably closer than their wavelengths. Reflectors, if they occur, must be modeled if an accurate attenuation profile is to be determined.

Another difference between the data and synthetic autocorrelograms is the time delay between the reflected and refracted components at angles greater than about  $30^{\circ}$ . This is due to the fact that

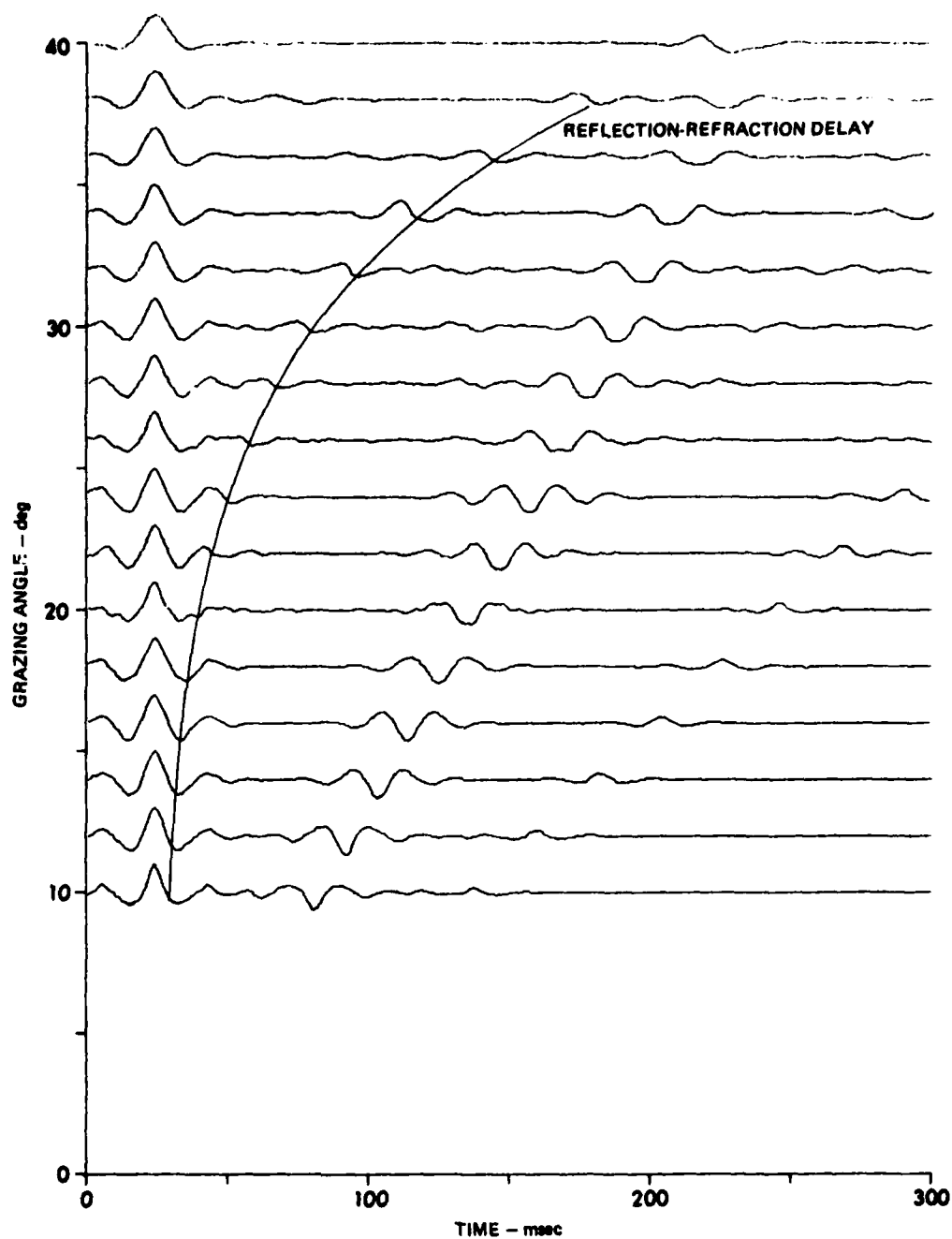


FIGURE 98  
SYNTHETIC AUTOCORRELOGRAM USING NEW GEOACOUSTIC MODEL  
PRESENTED IN TABLE IV DERIVED FROM DATA CORRELOGRAMS

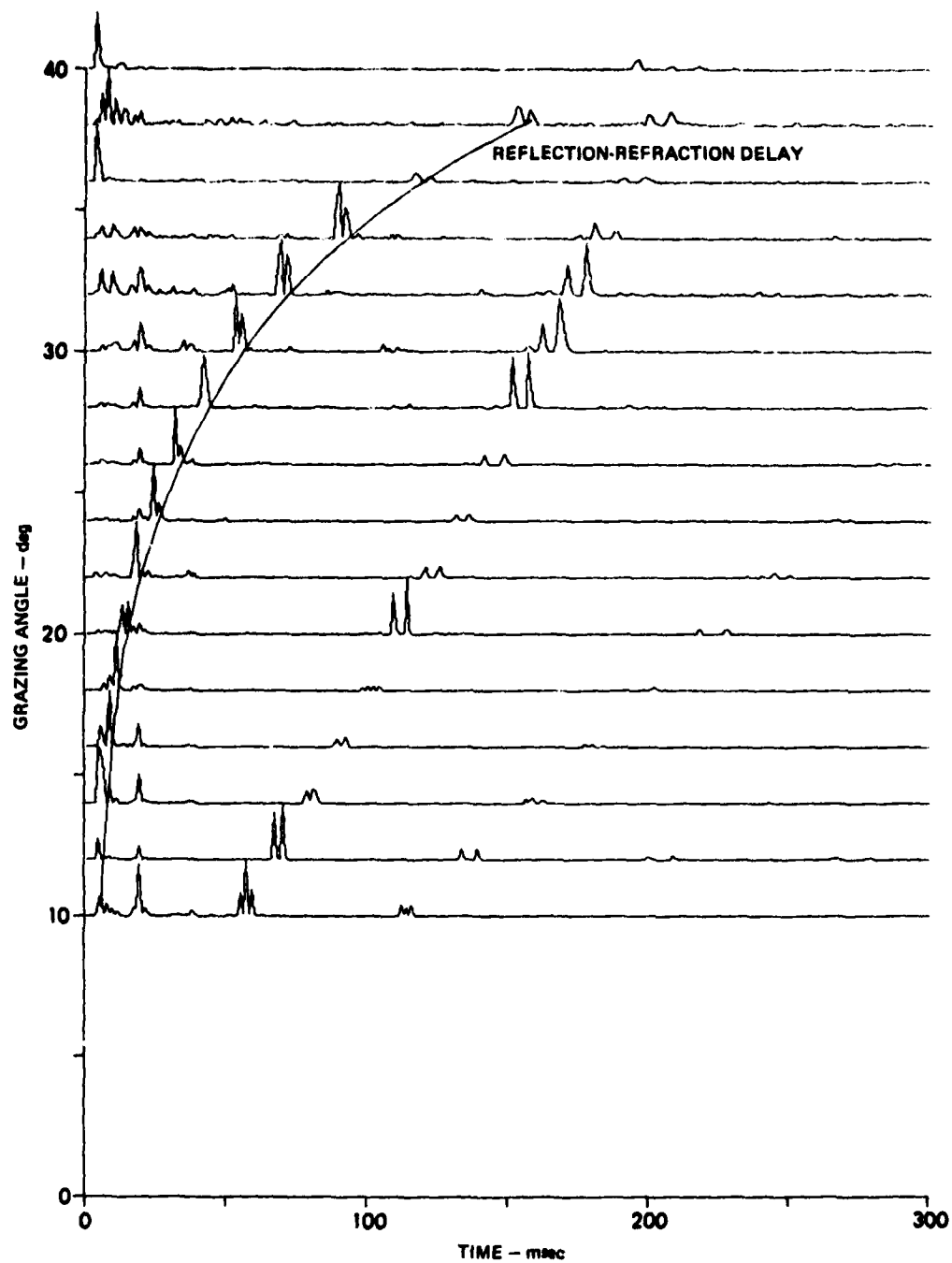


FIGURE 97  
SYNTHETIC POWER CEPSTRA USING NEW GEOACOUSTIC MODEL

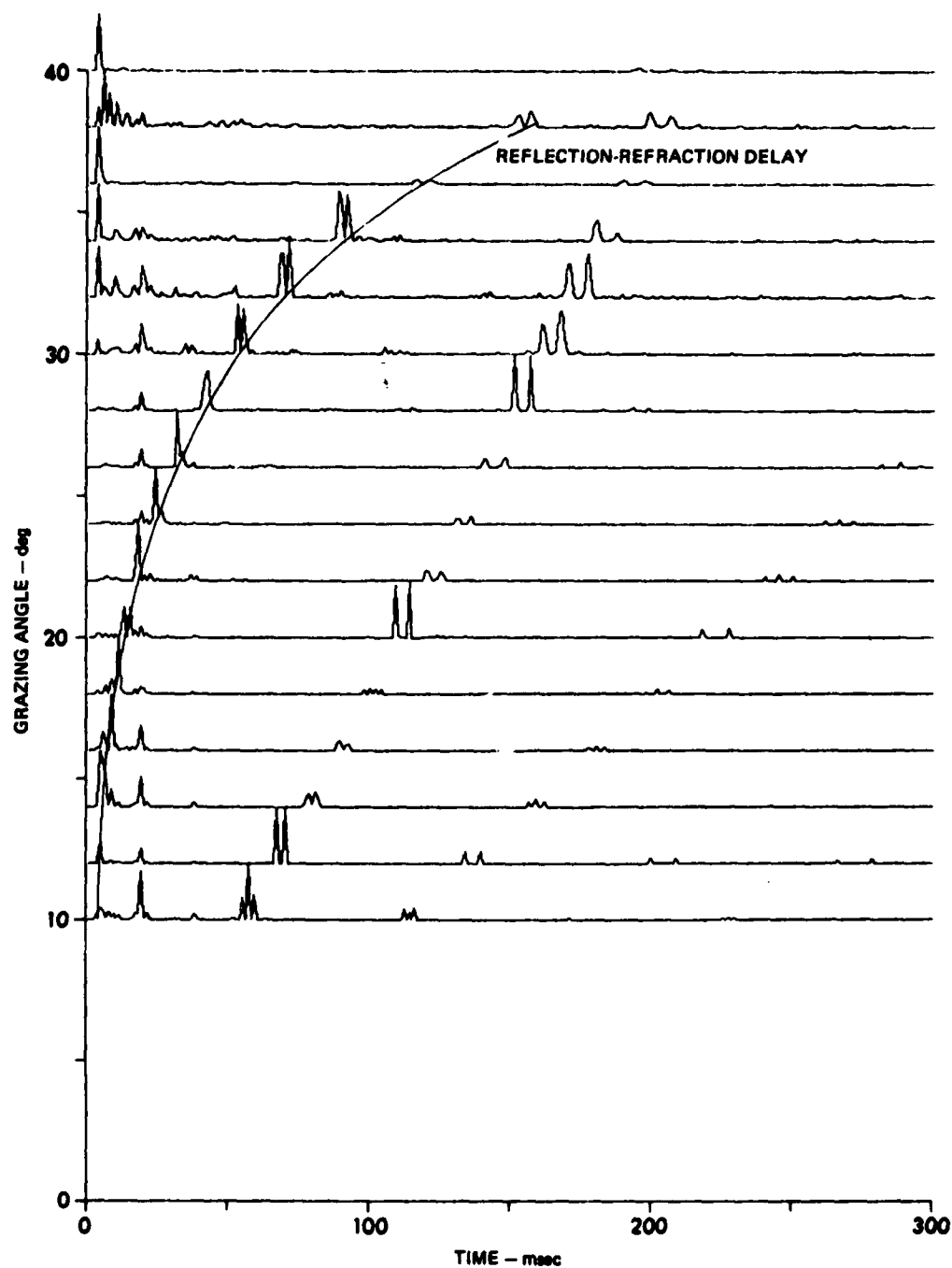


FIGURE 98  
SYNTHETIC POWER CEPSTRUMS USING NEW GEOACOUSTIC MODEL  
WITH WHITENED POWER SPECTRA



the reflection-refraction delay for the synthetics was calculated on the basis of a plane wave assumption which breaks down at the higher angles. In addition, for real data with spherical wavefronts, there is a minimum range or maximum grazing angle for which a refracted arrival will occur (Spofford, 1980). Thus, the reflection-refraction delay of the synthetic autocorrelogram can be detected for angles up to almost  $40^{\circ}$ , while the reflection-refraction component of the data autocorrelogram cannot be seen beyond about  $32^{\circ}$ . The failure of the reflection-refraction component to occur could be due to the fact that no refraction component occurs beyond that angle or to the fact that it is attenuated below the noise level.

Finally, in this section, the synthetic power cepstra using the new geoacoustic model (Figs. 97 and 98) will be compared to the data power cepstra. The amplitudes of the peaks of the main cepstral components of the synthetic power cepstra are in much better agreement with the data than the synthetic power cepstra derived using the a priori model. For instance, the amplitude of the bubble pulses, the relative amplitude of the ghost components, and the amplitude and shape of the reflection-refraction component are more nearly the same than they are for the a priori model. Even the relative highs and lows in the amplitudes of the ghost components (due to beating) is duplicated in the new model, especially at angles between about  $10$  and  $18^{\circ}$ . This agreement is due to the lower attenuations assumed in the new model.

The differences between the synthetic power cepstra and the data are primarily that there are many cepstral peaks in the data at delays where there are none in the synthetics. This is believed to be due to

reflections and their multiples and to beating between quefrequencies associated with these components.

In summary, the new geoacoustic model is an improvement over the previous model for this region since it improves the match of the delay between the two main components of the ocean bottom impulse response and the frequency content of the autocorrelations as a function of grazing angle. However, it is still deficient in two areas. First, the attenuation values may be still lower at the shallow depths than those calculated earlier in this section and, second, there may be one or more subbottom reflectors at the shallow depths. Accurate determination of the attenuation coefficient is dependent on knowledge of the occurrence of reflecters.

## CHAPTER 6

### CONCLUSIONS AND RECOMMENDATIONS

#### 6.1 Conclusions

In the first chapter of this thesis an overview of bottom loss collection was given and the state-of-the-art knowledge of geoacoustic parameters for different ocean environments was presented. It was emphasized that even in the deep ocean the physical and geologic processes are complicated and variable, thus giving considerable variability to geoacoustic structure. This variability is seen by examining physical properties of geologic cores taken in relatively close proximity, by comparing bottom loss curves in seemingly similar ocean environments, and by comparing deconvolved acoustic measurements, which reveal variable and quite significant subbottom reflectivity structure (Hastrup, 1970; Herstein et al, 1979; Santaniello et al, 1979; Chapman, 1980; Tyce et al, 1980; Dicus, 1981). Topographic effects such as the depth and nature of the basement also greatly affect bottom loss. In shallow water it would be expected that topographic effects would also greatly influence bottom loss. It would be expected that the geoacoustic structure would be even more complex and variable in shallow water than in deep water.

In Chapter 2 it was shown that multiple bottom bounce acoustic signals can be described by a series of linear filters which include bubble pulses and ghosting effects. The effects of ghosts and bubble pulses can often be identified on the acoustic data and, in general, they severely

distort the ocean bottom impulse response. For this reason it is difficult to extract information on the geoacoustic properties of sediments in the ocean bottom from the unprocessed acoustic signals. It has been shown that the ghosts and bubble pulses can be adequately identified and that the nominal source and receiver depths can be checked. It was found that, in the data discussed in this report, the actual receiver depth ( $\sim 255$  m) was considerably less than the nominal value (498 m).

The two correlation techniques investigated in this work, the autocorrelation and power cepstrum, greatly facilitate analysis of the acoustic signals. The ghost delays are detectable in many cases even with experimental geometries that were not favorable for their detection, and an estimate of the variance of the source depth is obtainable from the bubble pulse delay. In addition, inferences into the geoacoustic structure are obtainable from the correlations; a delay associated with a reflected and the refracted component is detectable. Initially the autocorrelation is preferable to the power cepstrum since it has the superposition property with respect to convolution, and thus is easier to interpret than the power cepstrum. Coherent noise such as ghosts and bubble pulses are more easily recognized, the amplitudes of events are less variable, and the shapes of events are more interpretable in terms of the phase of the time arrivals. All of these characteristics are due to the fact that the power cepstrum has a nonlinear, logarithmic operation and therefore there is coupling between cepstral components. This is what causes the unpredictable variability of the amplitude of the cepstral components. Also, the shapes of events are not duplicated on the power cepstrum causing some difficulty in recognizing signal

components, and the power cepstrum is significantly degraded by uncorrelated noise.

It was found, however, that for much synthetic and real data the power cepstrum was as good and better than the autocorrelation for measuring time delays between components of the ocean bottom impulse response. This is due to the fact that the power cepstrum gives a single spike at the time delay between components with an amplitude determined by the dynamic range of the ripple, whereas the amplitude of the autocorrelation is determined by the crosspower spectrum of the components, which may be highly dominated by low frequencies leading to poor resolution. Thus, especially at low grazing angles where the S/N ratio is high and the time delay between components is small, the power cepstrum may be preferable.

The method of deconvolving an  $(n-1)$  bottom bounce signal from an  $(n)$  bottom bounce signal is appealing due to the ease of implementation. It has been shown to be effective in estimating the main components of the impulse response over a fairly limited bandwidth. Criteria that are crucial for this method of deconvolution are nearly identical source and receiver depths, and sufficient number of bottom bounces that the ghost angles are nearly identical between the  $(n)$  and  $(n-1)$  bottom bounce waveforms.

In the turbidite region examined in this study there appear to be two main components of the impulse response--a reflected event and a refracted event. It is not known whether the reflector is the specular reflector or a subbottom reflector, but in either case the results imply that the geoaoustic structure is significantly different than that previously predicted. If the reflector is the specular reflector then the

sound speed increases with depth much more rapidly than previously predicted; otherwise, there is a significant discontinuity or a sharp increase of impedance with depth that was previously not modeled.

In addition there is evidence from the power cepstrum and 18 m source autocorrelations that there is significant subbottom reflectivity. The attenuation profiles at different frequencies seem to confirm significant reflectivity in the upper 40 m of the subbottom. This is consistent with the recent work of Tyce et al. (1980) that indicates strong reflectors of the order of the specular reflector up to 40 m below the water-sediment interface. The S/N ratio of the deconvolved traces is not sufficient to identify with confidence the reflectivity implied by the autocorrelations and power cepstra.

Assuming that the identified reflector is the specular reflector, the gradient at the surface is higher ( $g \sim 2.1$ ) than that generally assumed ( $g \sim 1.2$ ), although gradients at the surface greater than  $1.2 \text{ sec}^{-1}$  have been measured recently, e.g.,  $1.6 \text{ sec}^{-1}$  (Shirley, 1978; Tucholke, 1980) and  $1.8 \text{ sec}^{-1}$  (Dorman, 1981). For the data shown here the gradient decreases to about  $1.13 \text{ sec}^{-1}$  at about 180 m depth. This gives an average gradient of about  $1.5 \text{ sec}^{-1}$  for the upper 100 m. This is not greatly different from the value of  $1.35 \text{ sec}^{-1}$  recently reported by Dinapoli nor those used by Spofford to fit bottom loss curves of  $g_0 = 1.7 \text{ sec}^{-1}$  and  $g(500) = 1.34 \text{ sec}^{-1}$ .

(Bottom Interacting Ocean Acoustics, 1980).

The attenuation values which were derived to model the autocorrelations of the data indicate that  $k$  ranges from about 0.05 to 0.01 dB/m-kHz, which is within the range measured by Mitchell and Fooke

(1980), although these values are an order of magnitude less than those measured by some others (Hamilton, 1976, 1980); Jacobson, 1981). Chapman (1980) showed that low frequency bottom loss measurements in the Tufts abyssal plain implied an attenuation coefficient of 0.002 dB/m at 160 Hz ( $k \sim 0.013$ ) and Spofford (1980) required an attenuation coefficient which varied from 0.019 at the surface to 0.119 at 500 m to fit bottom loss curves. Thus, it is concluded that the attenuation and sound speed profiles derived from the bottom loss data are not unreasonable with respect to the state-of-the-art knowledge of these parameters.

It is concluded that the autocorrelation, power cepstrum, and multiple bottom bounce deconvolution techniques are valuable tools for the extraction of geoacoustic information from multiple bottom bounce signals.

## 6.2 Recommendations

There are several recommendations that can be made on the basis of this work. First, it is recommended that the bottom loss curves be recalculated for this site using the empirically derived receiver depths. The difference between the nominal and empirical ghost time delays will be particularly significant at the higher grazing angles and this error will be reflected in the scalloping in the frequency domain.

Second, it is recommended that study of the correlation techniques continue. A particularly interesting study would be to compare autocorrelograms over a range of passbands for different ocean basins where multiple bottom bounce autocorrelations of the same source and receiver depths and bottom grazing angles are summed. Muting along the source or receiver ghost delay before autocorrelating would be worthwhile in improving the resolution of correlated events. Study of power

cepstra for different ocean basins would also be of value, particularly in examining subbottom reflectivity.

Third, improvement of the deconvolution technique is needed. It would be worthwhile to apply the technique of Dicus (1981), especially if a good estimate of the source spectrum can be obtained by measuring the source waveform without interference of ghosts or bottom interacting signals. The shot depth variation can be monitored by the correlation techniques. If a good estimate of the source spectrum is not available, then significant improvement of the impulse response estimate might be obtained by posing the problem as predictive deconvolution with operator length less than one.

In addition a few recommendations can be made with regard to the experimental geometry. First, deeper sources ( $>400$  m) would greatly facilitate study of the acoustic signals. This would allow for accurate muting of the data beyond the source ghost, especially if time separation between impulse response components with ghost components occurs. Also, the resolution of the impulse response estimate would be increased since the time delay between bubble pulses is almost inversely proportional to depth, and so the errors of the bubble pulse delays are almost inversely proportional to source depth errors. Thus, the model breakdown noise of the deconvolution procedure will be restricted to higher and higher frequencies as the source detonation depth increases.

Alternatively, the deconvolution procedure could be improved greatly by substantial reduction of the variance of the source detonation depths. This could be done by improving the quality of the pressure transducers. A cost effectiveness study would need to be made to choose between



increasing the pressure transducer quality or increasing the source detonation depth.

If the desired data product is an impulse response estimate versus range and angle then the source should be detonated in even increments of range assuming that the water depth and sound speed is invariant with range. The size of the increment is dependent on the water depth and sound speed and the desired range and angle sampling. This would allow for an optimum estimate of the impulse response for multiple bottom bounce signals in which the source spectrum is not known. Of course, conventional techniques could be used if the source spectrum is known or can be estimated accurately (Wood et al., 1979; Dicus, 1981). The deconvolved trace would be an estimate of the multiple bottom bounce impulse response with its source and receiver ghosts. The ghosts could be removed by predictive deconvolution if they are not time separated from the impulse response components. An estimate of the one bottom bounce impulse response could be attempted by taking the  $n$ th root of the spectrum of the  $(n)$  bounce impulse response estimate.

Finally, the whole problem of determining the factors which influence angle dependent bottom loss would be greatly facilitated by use of array data, for instance, in a multiship experiment such as ESP (expanding spread) or fixed, large offset shooting. Tau-p processing, for instance, could then be used to model the arrival structure as a function of grazing angle, which determines frequency dependent bottom loss as a function of grazing angle.

## APPENDIX I

All of the travel time curves calculated for the overlays in Chapter 2 make use of the plane wave assumption. For travel paths in the water column this is a very good approximation to reality. On the other hand, paths through the sediment, especially at high grazing angles, are more accurately modeled assuming spherical wavefronts. In this section, a comparison of travel time curves based on the plane wave assumption are compared to a spherical wave model in an ocean model with an isovelocity water layer.

Figure A-1 shows the travel time difference curves for the impulse response of a six bottom bounce waveform with a gradient of  $1.5 \text{ sec}^{-1}$ , a sound speed ratio of one, and a water depth of 3600 m. The solid curves are the travel time curves for the plane wave assumption and the dashed curves are derived assuming spherical waves with source and receiver at the top of the water column. It is seen that the travel time curves agree very well for signals which have interacted with the bottom only a few times at angles less than  $25^\circ$ . For grazing angles greater than  $25^\circ$  and for signals which have interacted with the bottom several times, the travel time curves have significant differences.

Figure A-2 shows a phenomenon for spherical waves that does not occur for plane waves; namely, at very low angles spherical wave travel refracted through the sediment arrive sooner than reflected paths. For the same parameters as used in Fig. A-1, except  $c_s/c_w=0.98$ , it is seen that the reflected and refracted paths arrive at the same time at  $10^\circ$ . This angle

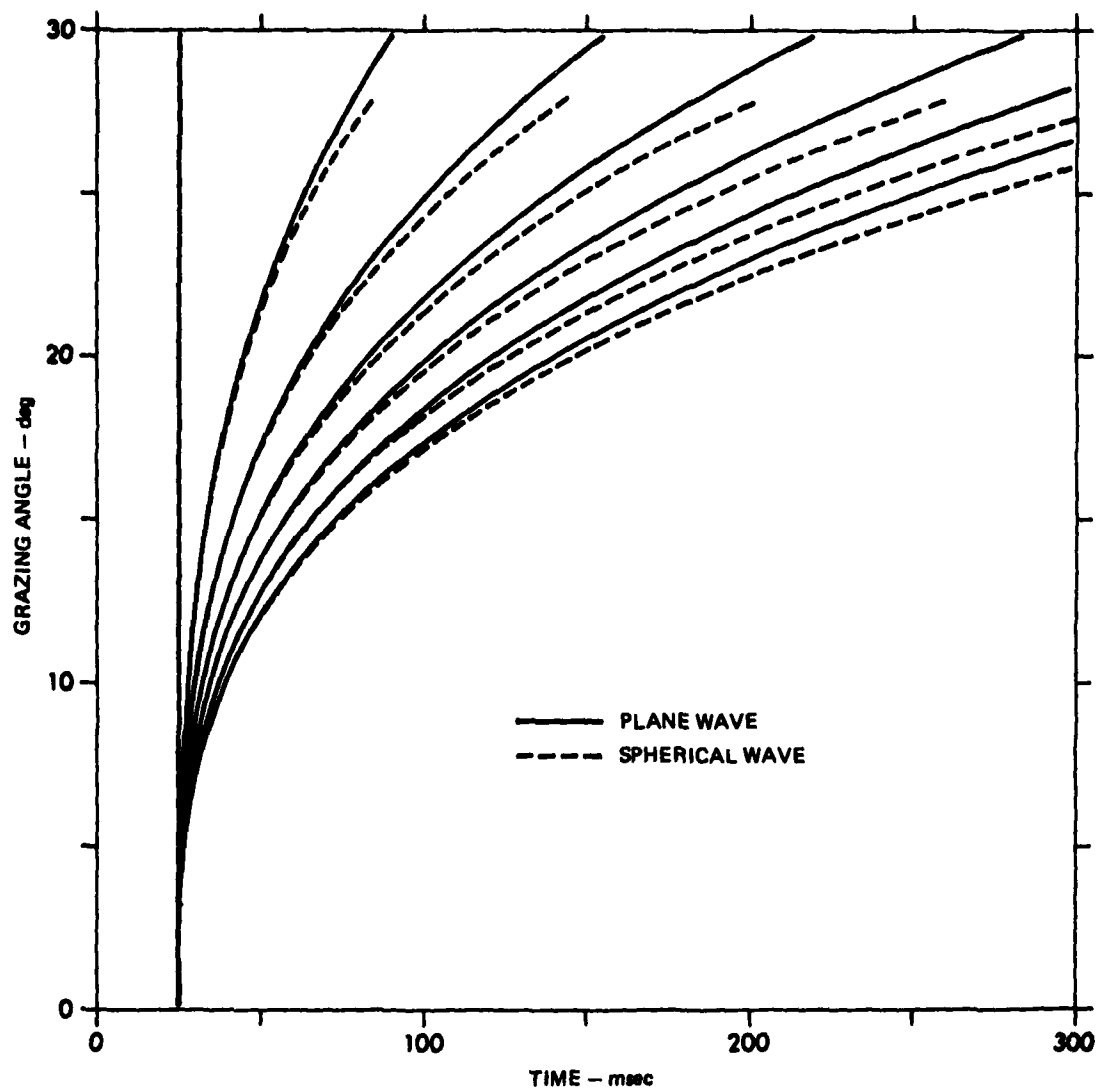
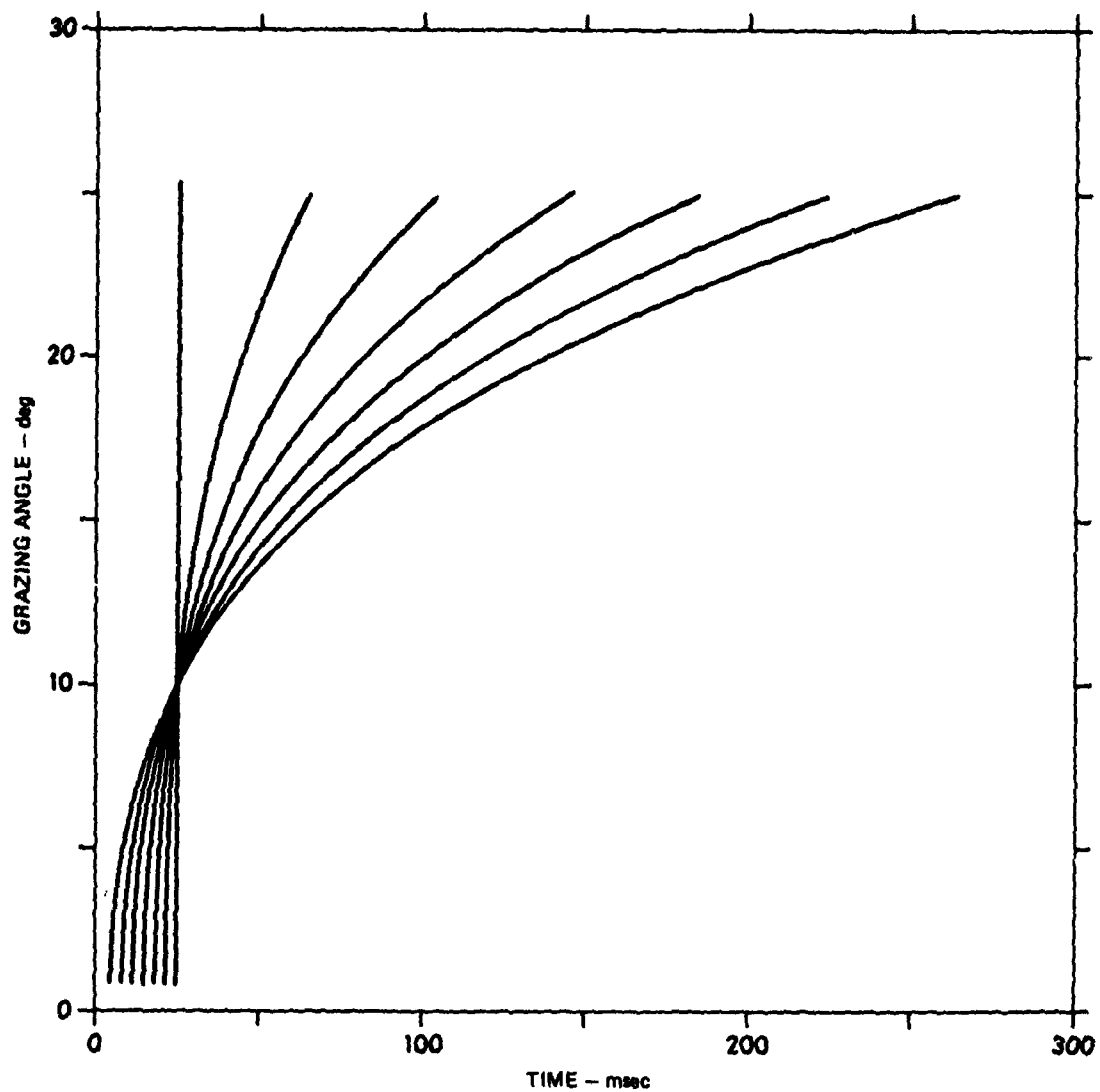


FIGURE A-1  
TRAVEL TIME DIFFERENCE CURVES FOR PLANE WAVES AND SPHERICAL  
WAVES ASSUMING AN ISOVELOCITY WATER COLUMN  
( $c_p/c_w = 1$ ;  $g = 1.5 \text{ sec}^{-1}$ ;  $d = 3600 \text{ m}$ )



**FIGURE A-2**  
**TRAVEL TIME DIFFERENCE CURVES FOR OCEAN BOTTOM WITH SOUND SPEED**  
**RATIO AT THE WATER-SEDIMENT INTERFACE LESS THAN ONE ASSUMING**  
**SPHERICAL WAVE FRONTS AND ISOVELOCITY WATER LAYER**  
 ( $c_s/c_w = 0.98$ ;  $g = 1.5 \text{ sec}^{-1}$ ;  $d = 3600 \text{ m}$ )

AD-A112 708

TEXAS UNIV AT AUSTIN APPLIED RESEARCH LABS

F/6 21/1

SOME APPROACHES TO THE ANALYSIS AND INTERPRETATION OF WIDE-ANGL--ETC(U)

FEB 82 G D INGRAM

N00014-78-C-0329

UNCLASSIFIED

ARL-TR-82-11

NL

3-3

A 2 708



END

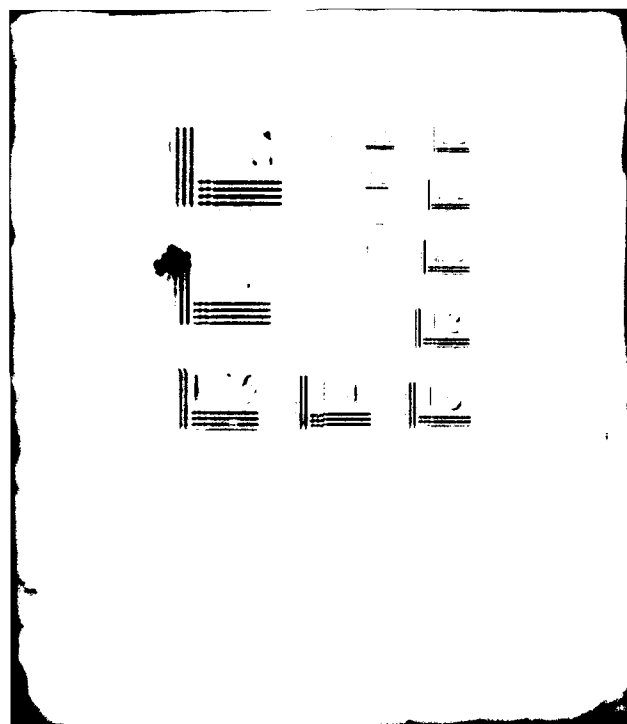
DATE

FILED

4 82

DTIC





will be dependent on the source-receiver geometry and the sound speed structure. With the plane wave assumption the refracted arrival will never arrive before the reflected arrival. For spherical waves the refracted arrival may arrive before the reflected arrival at both low angles and at high angles, dependent strongly on source-receiver geometry and the sediment sound speed structure.

Finally, in connection with spherical wave fronts it should be mentioned that there is a minimum range for a given source-receiver geometry and bottom sound speed structure at which a refracted arrival will occur (Spofford, 1980).

## APPENDIX II

It is desired to show that the autocorrelation has the superposition property with respect to convolution and that the power cepstrum is not. Consider the autocorrelations of the functions  $w(t)$  and  $y(t)$ .

$$P_{ww}(t) = \int_{-\infty}^{\infty} w(u) w(u-t) du$$

$$P_{yy}(t) = \int_{-\infty}^{\infty} y(u) y(u+t) du$$

$$P_{ww}(t) * P_{yy}(t) = \int_{-\infty}^{\infty} \left[ \int_{-\infty}^{\infty} w(u) w(u-x) du \right] \left[ \int_{-\infty}^{\infty} y(u') y(u'+t-x) du' \right] dx$$

Set  $u' = -u$ , in second inner integral; then

$$\begin{aligned} P_{ww}(t) * P_{yy}(t) &= \int_{-\infty}^{\infty} \left[ (-1) \int_{-\infty}^{\infty} w(u) w(u-x) y(-u) y(t-u-x) du \right] dx \\ &= \int_{-\infty}^{\infty} (-1) \left[ \int_{-\infty}^{\infty} w(u) y(t-u-x) du \right] \left[ \int_{-\infty}^{\infty} w(u-x) y(-u) du \right] dx \end{aligned}$$

Set  $u' = u-x$  in second inner integral.

$$\begin{aligned} P_{ww}(t) * P_{yy}(t) &= \int_{-\infty}^{\infty} (-1) \left[ \int_{-\infty}^{\infty} w(u) y(t-u-x) du \right] \left[ \int_{-\infty}^{\infty} w(u') y(-u'-x) du' \right] dx \\ &= \int_{-\infty}^{\infty} (-1) \left[ w(t-x) * y(t-x) \right] \left[ w(-x) * y(-x) \right] dx \end{aligned}$$

Finally set  $x' = t-x$ ,



$$P_{ww}(t) * P_{yy}(t) = \int_{-\infty}^{\infty} [w(x') * y(x')] [w(x'-t) * y(x'-t)] dx'$$

Let  $w(t) * y(t) = z(t)$ .

$$P_{ww}(t) * P_{yy}(t) = \int_{-\infty}^{\infty} z(x') z(x'-t) dx' = P_{zz}(t) \quad .$$

Thus, the convolution of the autocorrelations of two functions is equal to the autocorrelation of the convolution of two functions, and the autocorrelation has the superposition property with respect to convolution.

Taking the Fourier transform of the convolution of the autocorrelations yields a product of two power spectrums. The logarithmic operation, however, does not have the superposition property with respect to multiplication; therefore, the power cepstrum does not have the superposition property with respect to convolution.

# BIBLIOGRAPHY

Backman, R. T., and Hamilton E. L., 1980. "Sediment Sound Velocities from Sonobuoys: Arabian Fan," J. Geophys. Res. 85, 849.

Backus, M. M., 1959. "Water Reverberations, Their Nature and Elimination," Geophysics 24, 233.

Backus, M. M., N. S. Neidell, and R. E. Sheriff, 1977. "The Convolutional Model - A Review," in The Stationary Model of the Reflection Seismogram: S. E. G. Continuing Education Symposium, N. S. Neidell (ed.), Houston, Texas.

Barash, R., 1968. "Evidence of Phase Shift at Caustics," J. Acoust. Soc. Am. 43, 378.

Bertagne, A. J., 1980. "Seismic Stratigraphic Investigation - Western Gulf of Mexico," Master's Thesis, The University of Texas at Austin.

Bogert, B. P., M. J. R. Healy, J. W. Tukey, 1963. "The Quefreny Analysis of Time Series for Echoes: Cepstrum, Pseudo-Autocovariance, Cross-spectrum and Saphe Cracking," Proceedings of Symnposium on Time Series Analysis, M. Rosenblatt (ed.) (John Wiley & Sons, New York), Ch. 15, p. 209.

Bottom-Interacting Ocean Acoustics, 1980. W. A. Kuperman and F. B. Jensen (eds.) (Plenum Press, New York).

Bracewell, R. N., 1978. The Fourier Transform and Its Applications (McGraw-Hill Book Company, St. Louis, Missouri).

Bryan, G. M., 1980. "The Hydrophone-pinger Experiment," J. Acoust. Soc. Am. 68, 1403.

Cervený, V., and R. Ravindra, 1971. Theory of Seismic Head Waves, (University of Toronto Press, Buffalo, New York).

Chapman, N. R., 1980. "Low Frequency Bottom Reflectivity Measurements in the Tufts Abyssal Plain," in Bottom-Interacting Ocean Acoustics, W. A. Kuperman and F. B. Jensen (eds.) (Plenum Press, New York).

Christensen, R. E., J. A. Frank, and W. H. Geddes, 1975. "Low-Frequency Propagation via Shallow Refracted Paths Through Deep Ocean Sediments," J. Acoust. Soc. Am. 57, 1421.

Claerbout, J., 1976. Fundamentals of Geophysical Data Processing (McGraw-Hill Book Company, New York).

Discus, R. L., 1976. "Preliminary Investigations of the Ocean Bottom Impulse Response at Low Frequencies," U. S. Naval Oceanographic Office Tech. Note TN 6130-4-75.

Dicus, R. L., 1981. "Impulse Response Estimation with Underwater Explosive Charge Acoustic Signals," J. Acoust. Soc. Am. 70, 122.

Dorman, L. M., and R. S. Jacobsen, 1981. "Linear Inversion of Body Wave Data--Part I: Velocity Structure from Traveltimes and Ranges," Geophys. 46, 138.

Ewing, M., and L. D. Leet, 1932. "Seismic Propagation Paths," Geophysical Prospecting AIME, 245.

Ewing, M., and L. D. Leet, 1932. "Comparison of Two methods for Interpretation of Seismic Time-distance graphs Which are Smooth Curves," Geophysical Prospecting AIME, 263.

Focke, K.C., 1980. personal communication and interoffice memorandum, ARL:UT.

Fryer, G. J., 1978. "Reflectivity of the Ocean Bottom at Low Frequency," J. Acoust. Soc. Am. 63, 35.

Gaspin, J. B., and V. K. Shuler, 1971. "Source Levels of Shallow Underwater Explosions," NSWC Tech. Report 71-160, Naval Surface Warfare Center, White Oak, Silver Spring, Maryland.

Hamilton, E. L., 1980. "Geoacoustic Modeling of the Sea Floor," J. Acoust. Soc. Am. 68, 1313.

Hamilton, E. L., 1978. "Sound Velocity-Density Relations in Sea-Floor Sediments and Rocks," J. Acoust. Soc. Am. 63, 366.

Hamilton, E. L., 1976. "Sound Attenuation as a Function of Depth in the Sea Floor," J. Acoust. Soc. Am. 59, 528.

Hamilton, E. L., and R. T. Bachman, personal communication.

Hamilton, E. L., D. G. Moore, E. C. Buffington, P. L. Sherrer, and J. R. Curray, 1974. "Sediment Velocities from Sonobuoys: Bay of Bengal, Bering Sea, Japan Sea, and North Pacific," J. Geophys. Res. 79, 2653.

Hampton, L., S. K. Mitchell, and R. R. Gardner, 1978. "Acoustic Bottom Loss Measurement Using Multipath Resolution," Proceedings EASCON '78 IEEE Meeting, Washington, D.C., 24.

Hanna, J. S., 1973. "Short-Range Transmission Loss and the Evidence for Bottom-Refracted Energy," J. Acoust. Soc. Am. 53, 1686.

Harris, F. J., 1978. "On the Use of Windows for Harmonic Analysis with the Discrete Fourier Transform," Proc. IEEE 66, 51.

- Hastrup, O. F., 1970. "Digital Analysis of Acoustic Reflectivity in the Tyrrhenian Abyssal Plain," J. Acoust. Soc. Am. 47, 181.
- Hawker, K. E., and T. L. Foreman, 1978. "A Plane Wave Reflection Loss Model Based on Numerical Integration," J. Acoust. Soc. Am. 64, 1470.
- Helmberger, D. V., G. Engen, and P. Scott, 1979. "A Note on Velocity, Density, and Attenuation Models for Marine Sediments Determined from Multibounce Phases," J. Geophys. Res. 84, 667.
- Herstein, P. D., R. K. Dullea, and S. R. Santaniello, 1979. "Hatteras Abyssal Plain Low Frequency Bottom Loss Measurements," NLONLAB NUSC Tech. Rpt. 5781, Naval Underwater Systems Center, New London Laboratory, New London, Connecticut.
- Hill, M. N., 1952. "Seismic Refraction Shooting in an Area of the Eastern Atlantic," Phil. Trans. R. Soc. London A244, 561.
- Hovem, J. M., 1970. "Deconvolution for Removing the Effects of the Bubble Pulses of Explosive Charges," J. Acoust. Soc. Am. 47, 281.
- Jacobson, R. S., G. G. Shor, Jr., and L. M. Dorman, 1981. "Linear Inversion of Body Wave Data--Part II: Attenuation Versus Depth Using Spectral Ratios," Geophys. 46, 152.
- Kanasewich, E. R., 1975. Time Sequence Analysis in Geophysics (The University of Alberta Press, Edmonton, Canada).
- Karig, D. E., 1971. "Structural History of the Mariana Island Arc System," Geol. Soc. Am. Bull. 82, 323.
- Kemerait, R. C., and D. G. Childers, 1972. "Signal Detection and Extraction by Cepstrum Techniques," IEEE Trans. Inf. Theory IT-18, 755.
- Lackoff, M. R., and L. R. LeBlanc, 1975. "Frequency-domain Seismic Deconvolution Filtering," J. Acoust. Soc. Am. 57, 151.
- Le Pichon, X, J. Ewing, and R. E. Houtz, 1978. "Deep-sea Sediment Velocity Determination Made While Reflection Profiling," J. Geophys. Res. 73, 2597.
- Mathews, J. E., 1980. "Heuristic Physical Property Model for Marine Sediments," J. Acoust. Soc. Am. 68, 1361.
- Mitchell, S. K., N. R. Bedford, and M. R. Weinstein, 1976. "Determination of Source Depth from the Spectra of Small Explosions Observed at Long Ranges," J. Acoust. Soc. Am. 60, 825.
- Mitchell, S. K., K. C. Focke, J. A. Shooter, and N. R. Bedford, personal communication.

Mitchell, S. K., J. J. Lemmon, K. C. Focke, M. M. McSwain, personal communication.

Mitchell, S. K., and J. J. Lemmon, 1979. "A Ray Theory Model of Acoustic Interaction with the Ocean Bottom," J. Acoust. Soc. Am. 66, 855.

Mitchell, S. K., and K. C. Focke, 1980. "New Measurements of Compressional Wave Attenuation in Deep Ocean Sediments," J. Acoust. Soc. Am. 67, 1582.

Mitchell, S. K., N. R. Bedford, and G. E. Ellis, 1980. "Multipath Analysis of Explosive Source Signals in the Ocean," J. Acoust. Soc. Am. 67, 1590.

Morris, H. E., 1970. "Bottom-Reflection-Loss Model with a Velocity Gradient," J. Acoust. Soc. Am. 48, 1198.

Officer, C. B., 1955. "A Deep Sea Seismic Reflection Profile," Geophys. 20, 270.

Oppenheim, A. V., R. W. Schafer, and T. G. Stockman, 1968. "Nonlinear Filtering of Multiplied and Convolved Signals," Proc. IEEE 56, 1264.

Peacock, K. L., and Treitel, S., 1969. "Predictive Deconvolution: Theory and Practice," Geophys. 34, 155.

Robinson, E. A., and S. Treitel, 1967. "Principals of Digital Weiner Filtering," Geophys. Prospecting 15, 311.

Robinson, E. A., and M. T. Silvia, 1978. Digital Signal Processing and Time Series Analysis (Holden-Day, Inc., San Francisco, California).

Santaniello, S. R., F. R. Dinapoli, F. R. Dullea, and P. D. Herstein, 1979. "Studies on the Interaction of Low-Frequency Acoustic Signals with the Ocean Bottom," Geophys. 44, 1922.

Scoville, J. M., 1978. "Wavelet Processing Using Water Bottom Multiples," Master's Thesis, The University of Texas at Austin.

Shirley, D. J., and D. W. Bell, 1978. "Acoustics of In Situ and Laboratory Sediments," Applied Research Laboratories Technical Report No. 78-36 (ARL-TR-78-36), Applied Research Laboratories, The University of Texas at Austin.

Silbiger, A., 1968. "Phase Shift at Caustics and Turning Points," J. Acoust. Soc. Am. 44, 653.

Smith, T., personal communication, ARL:UT, 1981.

Spofford, C. W., 1980. "Geoacoustic Parameters from Bottom-Loss Data," in Bottom-Interacting Ocean Acoustics, W. A. Kuperman and F. B. Jensen (eds.) (Plenum Press, New York).

Tolstoy, I., 1968. "Comments on 'Evidence of Phase Shift at Caustics'," J. Acoust. Soc. Am. 43, 380.

Tucholke, B. E., 1980. "Acoustic Environment of the Hatteras and Nares Abyssal Plains, Western North Atlantic, Determined from Velocities and Physical Properties of Sediment Cores," J. Acoust. Soc. Am. 68, 1376.

Turin, G. L., 1957. "On the Estimation in the Presence of Noise of the Impulse Response of a Random Linear Filter," IRE Trans. Inf. Theory 5.

Tyce, R. C., L. A. Mayer, F. N. Spiess, 1980. "Near-Bottom Seismic Profiling: High Lateral Variability, Anomalous Amplitudes, and Estimates of Attenuation," J. Acoust. Soc. Am. 68, 1391.

Urick, R. J., 1975. Principles of Underwater Sound (McGraw-Hill Book Company, St. Louis, Missouri).

Vidmar, P. J., and T. L. Foreman, 1978. "The Effect of Sediment Rigidity on the Acoustic Reflectivity of the Ocean Bottom," EOS Trans. Am. Geophys. Union 59, 1119.

Vidmar, P. J., 1980. "The Dependence of Bottom Reflection Loss on the Geoacoustic Parameters of Deep Sea (Solid) Sediments," J. Acoust. Soc. Am. 68, 1442.

Wakely, J., Jr., 1977. "Pressure-Signature Model for an Underwater Explosive Charge," U. S. Navy Journal of Underwater Acoustics 27, 445.

Wood, L. C., R. C. Heiser, S. Treitel, and P. L. Riley, 1978. "The Debubbling of Marine Source Signatures," Geophys. 43, 715.

Worzel, J. L., Bryant, W., et. al., 1973. Initial Reports of the Deep Sea Drilling Project, Vol. X (U. S. Government Printing Office, Washington, D.C.).

Wroldstud, K., 1980. "Internal Velocity and Attenuation Measurements in Sediments from Marine Seismic Reflection Data," J. Acoust. Soc. Am. 68, 1415.

23 February 1982

DISTRIBUTION LIST FOR  
ARL-TR-82-11  
UNDER CONTRACT N00014-78-C-0329

Copy No.

1 Commanding Officer  
2 Naval Ocean Research and Development Activity  
3 NSTL Station, MS 39529  
4 Attn: Code 110  
5 Code 115  
6 Code 125L  
7 Code 300  
8 Code 320  
9 Code 340  
Code 500  
Code 520 File  
Code 530

10 Commanding Officer  
11 Naval Research Laboratory  
12 Washington, DC 20375  
Attn: Code 8100  
Code 8160  
Code 2627

13 Commander  
14 Naval Oceanographic Office  
NSTL Station, MS 39529  
Attn: Code 7300  
Code 9210

15 Naval Ocean Research and Development Activity  
Liaison Office  
Department of the Navy  
Arlington, VA 22217  
Attn: Code 130

16 Officer in Charge  
New London Laboratory  
Naval Underwater Systems Center  
New London, CT 06320  
Attn: L. King

17 Commander  
Naval Ocean Systems Center  
San Diego, CA 92152  
Attn: M. Akers

Distribution List for ARL-TR-82-11 under Contract N00014-78-C-0329 (Cont'd)

Copy No.

- 18      Commanding Officer  
         Naval Coastal Systems Center  
         Panama City, FL 32407
- 19      Officer in Charge  
         Naval Surface Weapons Center  
         White Oak Laboratory  
         Silver Spring, MD 20910
- 20      Officer in Charge  
         David W. Taylor Naval Ship Research and Development Center  
         Carderock Laboratory  
         Bethesda, MD 20084
- 21      Director  
         Naval Ocean Surveillance Information Center  
         4301 Suitland Road  
         Washington, DC 20390
- 22      Commanding Officer  
         Naval Intelligence Support Center  
         4301 Suitland Road  
         Washington, DC 20390
- Superintendent  
         Naval Postgraduate School  
         Monterey, CA 93940
- 23      Attn: Library
- Assistant Secretary of the Navy  
         RE&S  
         Department of the Navy  
         Washington, DC 20350
- 24      Attn: G. A. Cann
- Chief of Naval Operations  
         Department of the Navy  
         Washington, DC 20350
- 25      Attn: OP-02
- 26                    OP-03
- 27                    OP-05
- 28                    OP-095
- 29                    OP-096
- 30                    OP-951
- 31                    OP-952
- 32                    OP-951F
- 33                    OP-952D



Distribution List for ARL-TR-82-11 under Contract N00014-78-C-0329 (Cont'd)

Copy No.

34-35	Headquarters Naval Material Command Washington, DC 20360 Attn: CAPT E. Young/ONT
36-37	Project Manager Antisubmarine Warfare System Project Department of the Navy Washington, DC 20360 Attn: PM-4
38	Director Strategic System Projects Office Department of the Navy Washington, DC 20376 Attn: PM-1
39	Chief of Naval Research
40	Department of the Navy
41	Arlington, VA 22217
42	Attn: Code 100
43	Code 102B
44	Code 220
	Code 230
	Code 460
	Code 480
45	Commanding Officer Office of Naval Research Branch Office London FPO New York, NY 09510 Attn: Code 241
46	Commander
47	Naval Electronic Systems Command
48	Washington, DC 20360
49	Attn: PME-124
50	PME-124TA
51	PME-124/30
	PME-124/40
	PME-124/60
	Code 612
52	Commander Naval Sea Systems Command Washington, DC 20362 Attn: R. Farwell (Code 63RA)

Distribution List for ARL-TR-82-11 under Contract N00014-78-C-0329 (Cont'd)

Copy No.

	Commander Naval Air Systems Command Washington, DC 20361
53	Attn: Code 370
54	PMA-264
55	Deputy Undersecretary of Defense for Research and Engineering Department of Defense Washington, DC 20301
	Defense Advanced Research Projects Agency 1400 Wilson Boulevard Arlington, VA 22209
56	Attn: T. Kooij
57	CDR K. Evans
58	Commander Naval Oceanography Command NSTL Station, MS 39529
59	Director of Navy Laboratories Room 1062, Crystal Plaza, Bldg. 5 Department of the Navy Washington, DC 20360
	Defense Advanced Research Projects Agency ARPA Research Center Unit 1, Bldg. 301A NAS Moffett Field, CA 94035
60	Attn: E. L. Smith
61-62	Commanding Officer and Director Defense Technical Information Center Cameron Station, Building 5 5010 Duke Street Alexandria, VA 22314
	Director of Naval Matters Center of Naval Analysis Alexandria, VA 22311
63	Attn: C. E. Woods
	Applied Physics Laboratory The Johns Hopkins University Johns Hopkins Road Laurel, MD 20810
64	Attn: A. Chwastyk
65	W. L. May
66	G. L. Smith

Distribution List for ARL-TR-82-11 under Contract N00014-78-C-0329 (Cont'd)

Copy No.

67 Woods Hole Oceanographic Institution  
Woods Hole, MA 02543  
Attn: E. E. Hayes

68 B-K Dynamics, Incorporated  
15825 Shady Grove Road  
Rockville, MD 20850  
Attn: P. G. Bernard

69 Bell Telephone Laboratories, Inc.  
Whippany Road  
Whippany, NJ 07961  
Attn: J. Goldman  
70 L. F. Fretwell

71 Daubin Systems Corporation  
104 Crandon Blvd.  
Key Biscayne, FL 33149  
Attn: S. C. Daubin

72 Ocean Data Systems, Inc.  
6000 Executive Boulevard  
Rockville, MD 20852  
Attn: G. V. Jacobs

73 Planning Systems Incorporated  
7900 Westpark Drive  
Suite 600  
McLean, VA 22101  
Attn: R. S. Cavanaugh

74 Science Applications, Inc.  
P.O. Box 1303  
McLean, VA 22101  
Attn: J. S. Hanna  
75 C. W. Spofford

76 Tracor, Inc.  
Rockville Laboratory  
1601 Research Blvd.  
Rockville, MD 20850  
Attn: J. T. Gottwald

Distribution List for ARL-TR-82-11 under Contract N00014-78-C-0329 (Cont'd)

Copy No.

77	TRW Incorporated
78	7600 Colshire Drive
	McLean, VA 22101
	Attn: R. T. Brown
	I. B. Gereben
	Western Electric Company, Inc.
	P.O. Box 20046
	Greensboro, NC 27420
79	Attn: R. H. Harris
80	T. Clark
81	Office of Naval Research
	Resident Representative
	Room 582, Federal Building
	Austin, TX 78712
82	Environmental Sciences Division, ARL:UT
83	Gregory D. Ingram, ARL:UT
84	Stephen K. Mitchell, ARL:UT
85	Reuben H. Wallace, ARL:UT
86	Library, ARL:UT

**DA  
FILM**